DEPARTMENT OF PHYSICS

TECHNISCHE UNIVERSITÄT MÜNCHEN

Master's Thesis

Search for Charged Higgs Bosons in $H^+ \to W^+h$ Decays with the ATLAS Detector

Simon Grewe

CERN-THESIS-2021-095
20/07/2021

MAX-PLANCK-INSTITUT FÜR PHYSIK

DEPARTMENT OF PHYSICS

TECHNISCHE UNIVERSITÄT MÜNCHEN

Master's Thesis

Search for Charged Higgs Bosons in $H^+ \to W^+h$ Decays with the ATLAS Detector

Suche nach geladenen Higgs Bosonen in $H^+ \to W^+h$ Zerfällen mit dem ATLAS Detektor

Author:	Simon Grewe
Supervisor:	Dominik Duda
Advisor:	Hubert Kroha
Submission Date:	09.07.2021

I confirm that this master's thesis is my own work and I have documented all sources and material used.

Munich, 09.07.2021 Simon Grewe

Acknowledgments

First, I would like to thank the Max-Planck Institut für Physik and especially Prof. Hubert Kroha for giving me the opportunity to work on this interesting topic with them. During my thesis i had a great time and learned a lot.
Special thanks go to my supervisor Dominik Duda. Thank you very much for many helpful discussions and always patiently answering my question. Even under the difficult pandemic circumstances, the communication was very easy and besides your many other commitment you always took time to answer my questions and help me.
Furthermore i want to thank Sandra Kortner, for always proving very helpful comments for my talks.

Finally i want to thank my family for always supporting me!

Abstract

Various theories predicting an extended Higgs sector predict also the existence of at least one set of charged Higgs bosons. The main production mode of these new particles depends on their mass. For charged Higgs boson masses larger than the sum of the top and the bottom quark mass, the dominant production mode is expected to be in association with a top quark and a bottom quark (tbH^+).

In the alignment limit of the two Higgs-Doublet model (2HDM), heavy charged Higgs bosons with m(H^+)>m(t)+m(b) decay almost exclusively via $H^+ \to tb$. However, in other models such as the N2HDM or in Higgs triplet models e.g Georgia-Machacek model, significant branching ratios for $H^+ \to W^+h$ are possible. The latter decay mode is so far uncovered by searches at the LHC.

This thesis presents a search for charged Higgs bosons in $H^+ \to W^+h \to \ell\nu bb$ decays in final states containing multiple jets, missing transverse energy and a charged lepton. The ATLAS Run 2 dataset, corresponding to a integrated luminosity of 139 fb^{-1} of proton-proton collisions recorded at a centre of mass energy $\sqrt{s} = 13TeV$, is used. Boosted decision trees (BDTs) are used to solve the jet combinatorics, thus reconstructing the charged Higgs boson decay. Event selection criteria are developed to define signal and control regions. In addition, data driven methods are explored aiming to improve the data-to-simulation agreement in the signal and control regions. The final search sensitive is evaluated in terms of expected upper limits on the cross-section time branching ratio for the $pp \to tbH^+ \to tbWh$ process by performing a maximum likelihood fit. The expected upper limits range from 0.1215 pb, for a charged Higgs boson mass of 400 GeV to 0.0179 pb for a charged Higgs boson mass of 1600 GeV.

Contents

1. Introduction

In 2012, the Higgs boson was discovered by the ATLAS and CMS experiments at the Large Hadron Collider (LHC) [1, 2]. The Higgs boson, first predicted in 1964, was the "last missing piece", of the Standard Model (SM) of particle physics, which is now complete.

Currently, the Standard Model of particle physics is the best description of elementary particles and their interaction. It has been successfully tested numerous times to high precision [3–5]. Yet, the Standard Model cannot explain various experimental observations, e.g dark matter or the baryon asymmetry in the universe. Many theories extending the Standard Model have been proposed, aiming to deliver a more complete description of nature.

Among these, one of the most popular types of theories are Supersymmetric models [6]. A crucial part of such a theory is an extended Higgs sector, including the prediction of additional charged scalar particles. Likewise other extensions of the Standard Model predict an extended Higgs sector, and thus predict additional scalars. The observation of a charged Higgs boson would be a clear indication of physics beyond the Standard Model. Searches for charged Higgs bosons have been carried out at collider experiments and in various final states [7, 8].

One of the best studied extensions of the SM-Higgs sector is the Two Higgs Doublet Model (2HDM). In the 2HDM, the dominant decay mode of a heavy charged Higgs boson, with $m_{H^+} > m_t + m_b$, is into a top and bottom quark or into a τ lepton and a neutrino. So these decay channels have been the focus of searches at the LHC. Nevertheless other decay channels can become relevant. The decay of a charged Higgs boson into a neutral Higgs boson and a W boson $H^+ \to Wh$ may become dominant in models like the Next-to-Two-Higgs Doublet Model (N2HDM) or the Georgie-Machacek Model and has been proposed as a possible discovery channel for a charged Higgs boson at the LHC [9–12]. Yet this decay channel is so far uncovered by the ATLAS and CMS experiments.

In this thesis, a search for a charged Higgs boson decaying into a W boson and a neutral Higgs boson (with mass 125 GeV) with the ATLAS detector is presented. The focus is on the $H^+ \rightarrow Wh \rightarrow l\nu bb$ final state, where the W boson decays leptonically and the Higgs boson decays into a b quark pair, resulting in a final state containing jets, a charged lepton and missing transverse energy. At the LHC charged Higgs bosons are produced predominantly in association with a top and a bottom quark, where the subsequent decays of these particles lead to additional jets in the final state. With these additional jets in the final state the reconstruction of the H^+ decay becomes more challenging. To solve this issue boosted decision trees are trained to reconstruct the H^+ decay.

The thesis is structured in the following way: First the experimental apparatus, the ATLAS detector is described in chapter 2. Furthermore, the particle reconstruction and identification techniques used in ATLAS are described in this chapter. Different beyond the Standard Model theories that predict additional charged scalars are introduced in chapter 3. In chapter 4, the search for charged Higgs bosons is motivated by studying the branching ratios of charged Higgs boson decays for different models. Chapter 5 describes the search for charged Higgs bosons in $H^+ \rightarrow Wh \rightarrow l\nu bb$ decays using the ATLAS Run 2 dataset of proton-proton collisions recorded at a center of mass energy $\sqrt{s} = 13 TeV$. The dataset corresponds to a total integrated luminosity of $139 fb^{-1}$. The Boosted Decision Tree based method used to reconstruct the charged Higgs boson decay as well as the optimization of control and signal regions are described. Furthermore, data driven reweighting procedures trying to improve the background estimation are investigated. Expected limits on the branching ratio$\times$ cross-section for $pp \rightarrow tbH^+ \rightarrow tbWh$ are calculated by performing a maximum likelihood fit to the expected signal and background distributions of the charged Higgs boson mass. Finally, the results of this thesis are summarized and a conclusion is drawn in chapter 6.

2. The ATLAS Detector

2.1. The Large Hadron Collider

Located at CERN (Conseil Européen pour la Recherche Nucléaire) near Geneva, the Large Hadron Collider (LHC) is currently the highest energy hadron collider. With a circumference of about 27 km, it accelerates two beams of protons to a maximum center of mass energy of $\sqrt{s} = 14$ TeV. However, during Run-1, the LHC was operated at $\sqrt{s} = 7$ 8 TeV. During Run-2, between 2015 and 2018, the center of mass energy was 13 TeV. Beside protons, also heavy ions e.g. lead-ions, can be accelerated by the LHC to an energy of 2.76 TeV/nucleon.

The beams are kept on their circular trajectory by a total of 1232 superconducting dipole magnets operating at a magnetic field strength of 8.33 T. The magnets are cooled down to 1.9 K by superfluid helium. Hadrons are not injected directly into the LHC, but undergo different stages of pre-acceleration as shown in figure 2.1. There are four interaction points where the beam lines cross and the accelerated particles collide. A detector is located at each interaction point. The ATLAS [13] and CMS [14] experiments are general purpose detectors designed to perform a variety of tasks like searching for new particles and studying the Higgs boson, as well as studying heavy ion collisions. The ALICE detector [15] is specialized for the study of the gluon-quark plasma created in heavy ion collisions. Flavor physics and CP-violation are studied with the LHCb experiment [16].
The number of events per second of a certain process is given by:

$$N = L\sigma, \tag{2.1}$$

where σ is the production cross-section and L the luminosity of the collider given by:

$$L = \frac{N_b^2 n_b f_{rev} \gamma_r}{4\pi\epsilon_n \beta^*} F, \tag{2.2}$$

where N_b is the number of particles per bunch, n_b the number of bunches per beam, f_{rev} the bunch revolution frequency, γ_r the relativistic γ-factor, ϵ_n the normalized transverse beam emittance, β^* the beta function at the interaction point and F a geometric factor taking into account the beam crossing angle at the interaction point [18].

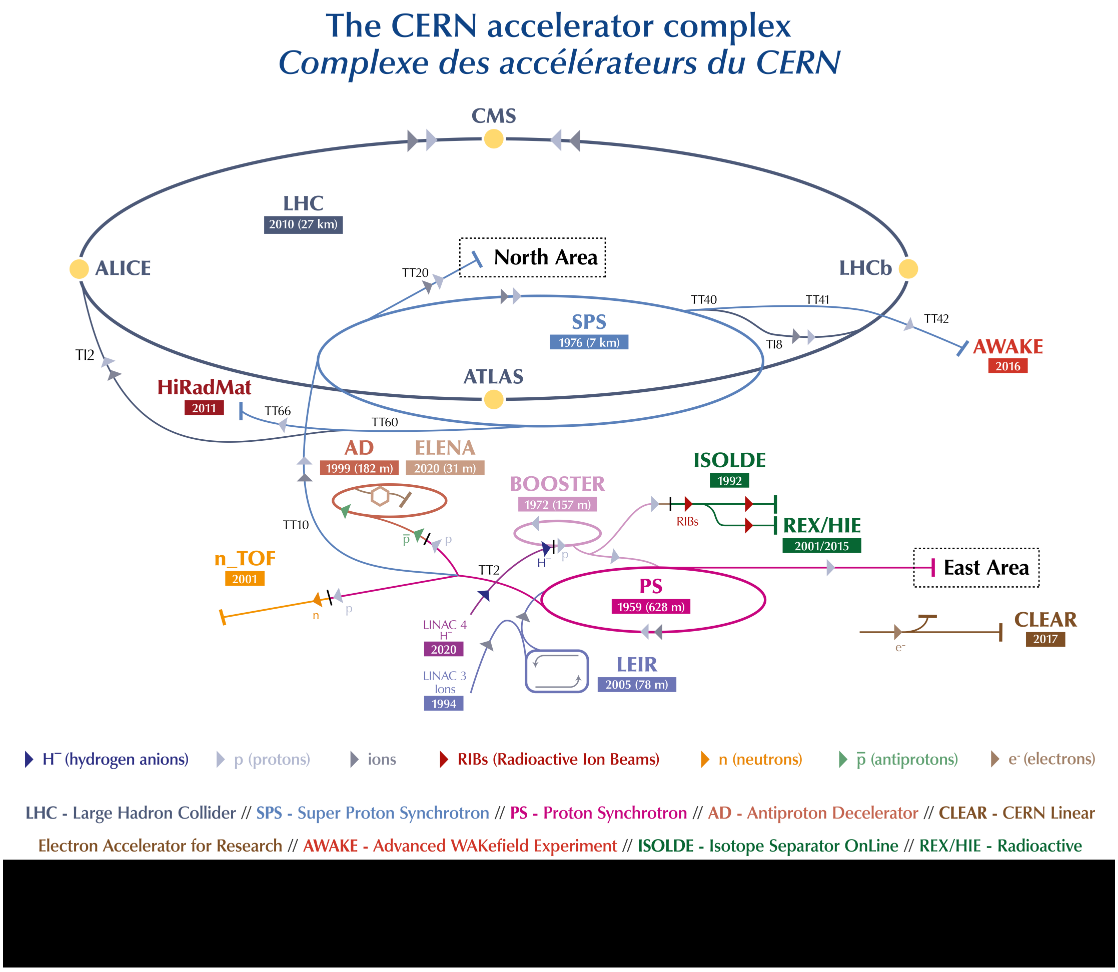

Figure 2.1.: Overview of the CERN accelerator complex and the experiments [17].

2.2. The ATLAS detector

The ATLAS (A Toroidal LHC ApparatuS) detector is one of the two multi-purpose detectors at the LHC. ATLAS is installed in a cavern about 100 m underground at the LHC point 1. The ATLAS detector is of cylindrical shape and has a diameter of 25 m and a length of 44m. It weights approximately 7000 tons.

One of the main goals of the ATLAS detector was the discovery of the Higgs boson, which was finally achieved in 2012. In addition to the search for the Higgs boson, the search program of the ATLAS experiment covers a large variety of new particles e.g. Higgs bosons beyond the Standard Model such as charged Higgs bosons and neutral pseudoscalars, new heavy gauge bosons W', Z' or supersymmetric particles. These searches cover diverse sets of final states and are sensitive up to masses at the TeV scale [13].

These benchmark processes define the performance requirements of the ATLAS detector and its subsystems: Good momentum measurements and charge identification, a high trigger efficiency, precise energy measurements for both electromagnetic and hadronic showers, good muon momentum resolution and identification are required. Furthermore, the ability to reconstruct secondary vertices for offline b-tagging capabilities is crucial. Another challenge are the conditions at the LHC, requiring fast and radiation hardened electronics [13].

2.2.1. The ATLAS Coordinate System

The origin of the coordinate system, used by the ATLAS detector and in this thesis, is the nominal interaction point. The z-axis points in the beam direction. The x-y P plane is perpendicular to the z-axis. The positive x-axis points from the origin to the middle of the LHC-ring, while the positive y-axis points upwards. The azimuthal angle Φ is measured around the beam axis and the polar angle θ is measured from the beam axis. The pseudrapidity η is defined as:

$$\eta = -\ln(\tan\frac{\theta}{2}). \tag{2.3}$$

The angular distance ΔR between two objects is given via:

$$\Delta R = \sqrt{\Delta\eta^2 + \Delta\Phi^2}. \tag{2.4}$$

2.2.2. The Inner Detector

The inner detector (ID) is the innermost subdetector of ATLAS, it extends to a radius of 1150 mm from the beamline and $\pm$ 3512 mm in the z-direction. A schematic overview of the ID is given in figure 2.2. The ID provides excellent momentum resolution and is used to reconstruct the primary and secondary vertices. The ID consists of three separate sub-detector systems and is immersed in a 2 T solnoidal magnetic field.

The first and highest granularity detection layer is the pixel detector. It covers a range of $|\eta| < 2.5$. The pixel detector consists of a total of 1744 silicon pixel sensors, each containing 47232 individual pixels of which 46080 are used. The pixel sensors are arranged in 3 layers. Each pixel is the same and has a size in $R - \phi \times z$ of 50$\times$ 400 μm^2. The pixel sensors in the barrel have a spacial accuracy of 10 μm, in the $R - \phi$ direction and 115 μm in the z-direction. In the disks, the resolution is 10 μm in the $R - \phi$ direction and 115 μm in the R-direction.

For the Run-2 data taking period an additional detection layer, the Insertable B-layer (IBL), was added to the pixel detector. It is inserted between the beam line and the pixel detector at a radius of 3.3 cm and consists also of pixel sensors. As an additional detection layer near the interaction point, the IBL improves the track reconstruction (especially for low p_T particles). In addition, the IBL improves the reconstruction of secondary vertices, thus it improves the b-tagging performance of ATLAS [19][20].

The second sub-detector is the silicon microstrip tracker (SCT). The SCT consists of 4 layers of silicon sensors in the barrel region and 9 layers in the endcaps. Each layer is composed of a set of two silicon strips, each 6.4 cm in length, daisy chained to each other. The SCT provides a spatial resolution of 17 $\mu m (R - \phi)$ and 580 μm (z).

The transition radiation tracker (TRT) is the outermost detection layer in the ID. The TRT covers the $|\eta| < 2.0$ range. The TRT consists of polyimide drift tubes (straw-tubes) of 4 mm diameter. In the barrel region the straw tubes are 144 cm long and are arranged in 73-layers. In the endcaps the straw tubes have a length of 37 cm, each endcap TRT consist of 160 layers of strawtubes. The TRT only provides $R - \phi$ directional information. Each straw tube has a spatial accuracy of 130μm [13].

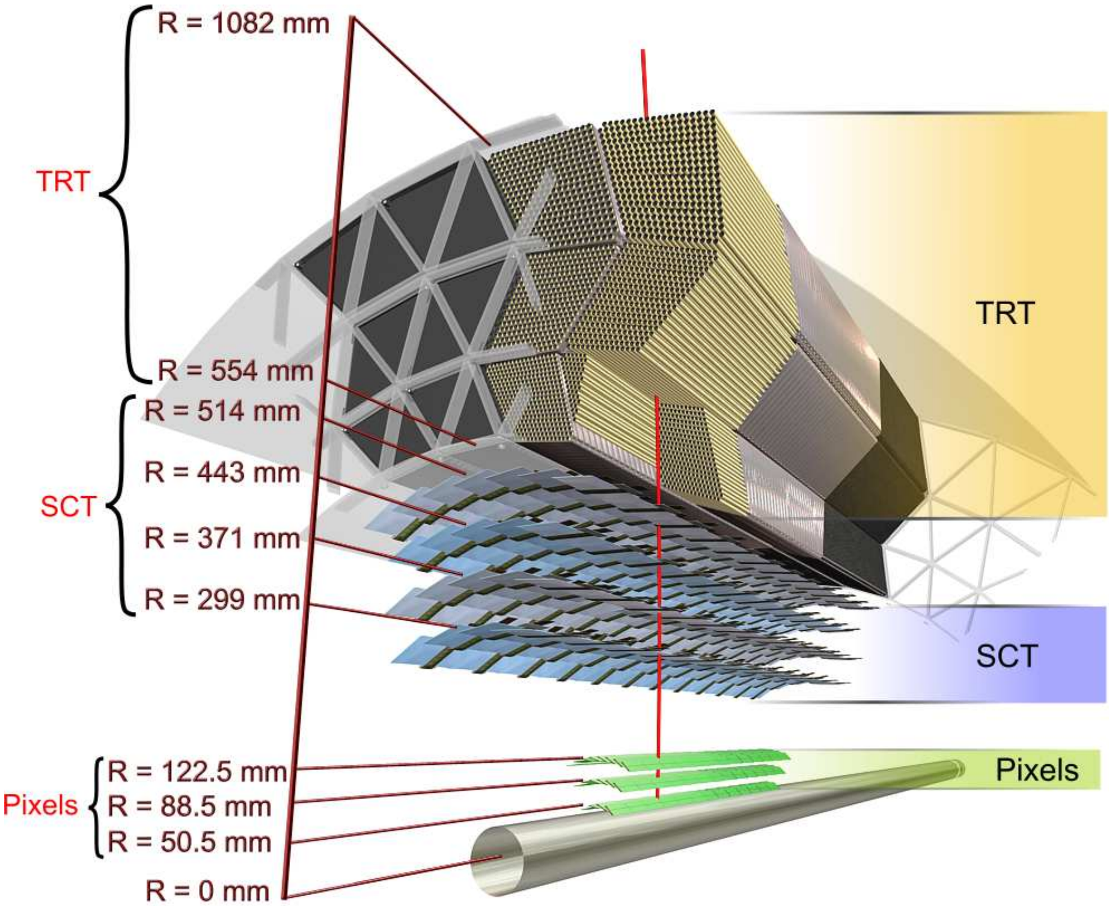

Figure 2.2.: Schematic overview of the structure of the ATLAS inner detector (ID) [13].

2.2.3. The Calorimeter

The calorimeter system is responsible to measure the energy of incoming particles. A particle entering the calorimeter will interact with the *passive/absorption* material where it will create a hadronic or electromagnetic shower of secondary particles. In the *active* material an electronically readable signal, proportional to the particle's energy, is produced by the particle shower.
A schematic overview of the ATLAS calorimeter system is presented in figure 2.3. ATLAS uses a sampling calorimeter design, where the passive material and the active material are arranged in an alternating pattern.
The ATLAS calorimeter covers a range of $|\eta| < 4.9$. The electromagnetic calorimeter offers a high granularity enabling it to measure photon and electron energies with an excellent precision. The granularity outside this range is lower, but still sufficient to reconstruct jets and to determine the missing transverse energy.
In the electromagnetic (EM) calorimeter, lead is used as the absorption material and liquid argon (LAr) is used as the active material. The active and absorbtion material are arranged in an "accordion" geometry. The EM calorimeter consists of 3 separate detectors, each housed in their own cryostat: The barrel EM-calorimeter covers a range of $|\eta| < 1.475$, while the two electromagnetic end-cap calorimeters (EMEC) cover the region $1.375 < |\eta| < 3.2$. To ensure that electromagnetic showers are contained within the calorimeter, its thickness has to be sufficient. In the barrel the EM-calorimeter has a thickness greater than 22 radiation lengths X_0[1], and $> 24X_0$ in the end-cap calorimeter. In addition, a presampler consisting of an active LAr layer, is installed in the region $|\eta| < 1.8$. The presampler is used to correct for energy loss outside the calorimeter. In the region $|\eta| < 2.5$, the electromagnetic calorimeter is segmented into 3 layers and into 2 layers everywhere else.

The hadronic calorimeter consists of a tile calorimeter and two LAr hadronic end-cap calorimeters. The tile calorimeter uses steel plates as the absorption medium and scintillating tiles as the active medium. The tile barrel covers the range $|\eta| < 1.0$ and is prolonged by the two extended barrel calorimeters, covering the range $0.8 < |\eta| < 1.7$. Behind the electromagnetic end-cap calorimeter, the hadronic end-cap calorimeter (HEC) is located. It is a liquid argon copper sampling calorimeter and covers the $1.5 < |\eta| < 3.2$ region.

In addition, the ATLAS experiment uses a Forward calorimeter (Fcalo), housed in the same cryostat behind the EMEC and the HEC. The Forward calorimeter consists of

[1]The radiation length X_0 is the average distance an electron travels in a material until its energy decreases to $1/e$ of its original energy.

3 modules. The first uses copper as the absorption material and is designed for electromagnetic measurements. The remaining two modules use tungsten as the absorption material and are designed to measure hadronic interactions. The Fcalo uses liquid argon as the active material [13].

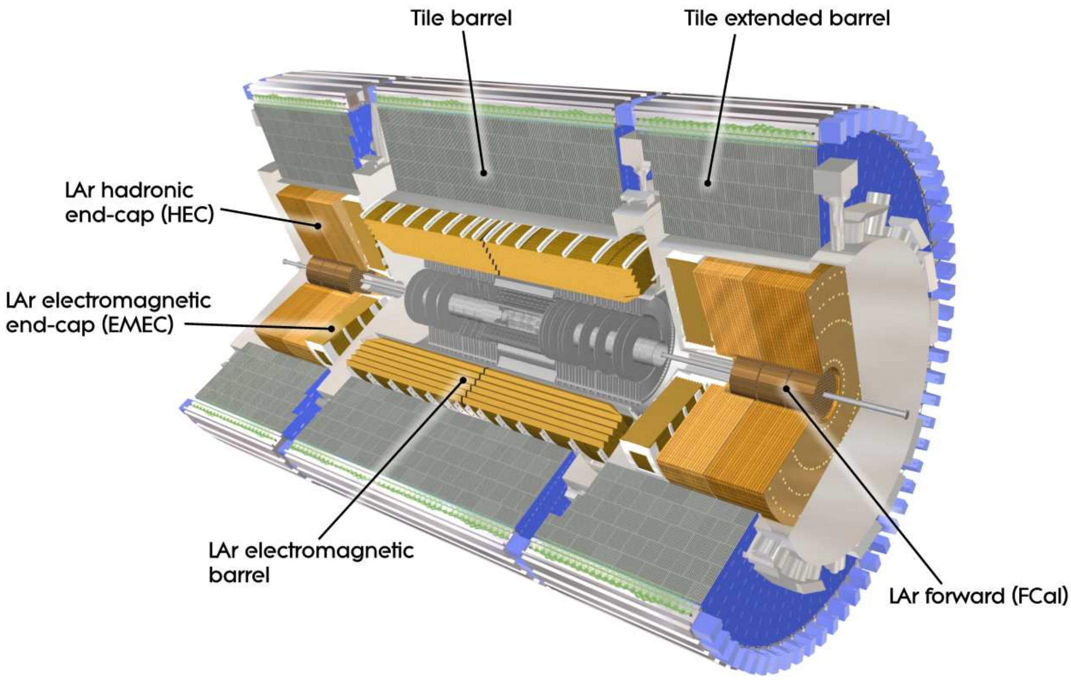

Figure 2.3.: A cutaway view of the ATLAS Calorimeter system [13].

2.2.4. The Muon Spectrometer

Muons are considerably heavier than electrons ($m_\mu \approx 200 m_e$). Thus, muons loose less energy due to bremsstrahlung and therefore are able to leave the calorimeter.

The momentum of charged particles passing the calorimeter is being measured by the Muon Spectrometer, which extends to $|\eta| < 2.7$. An overview of the structure of the ATLAS Muon Spectrometer is presented in figure 2.4. The trajectories of charged particles get bent by superconducting air-core magnets. In the barrel region ($|\eta < 1.4|$), the magnetic field stems from the large barrel toroid magnet and in the end-cap region, $1.6 < |\eta| < 2.7$, the magnetic field stems from the two end cap magnets. In the so called *transition region*, $1.4| < \eta| < 1.6$, the bending magnetic field is composed of a combination of the large barrel toroid and the end cap magnets. A high precision measurement of tracks is performed by Monitored Drift Tubes (MDTs) in the range $|\eta| < 2.0$ and by Cathode Strip Chambers (CSC) for $2.0 < |\eta| < 2.7$. The Monitored Drift Chambers are arranged in a cylindrical shape in 3 layers, while the Cathode Strip Chambers are arranged in 3 layers perpendicular to the beam axis. The Muon Spectrometer does not only measure muon tracks. Another key requirement is the ability to trigger on muon tracks, for this task fast detectors are needed. Thus, in the barrel region, Resistive-plate Chambers (RPC) are installed and in the end-caps this task is performed by Thin-gap Chambers (TGC). The Muon Spectrometer provides triggering capabilities for $|\eta| < 2.4$ [13].

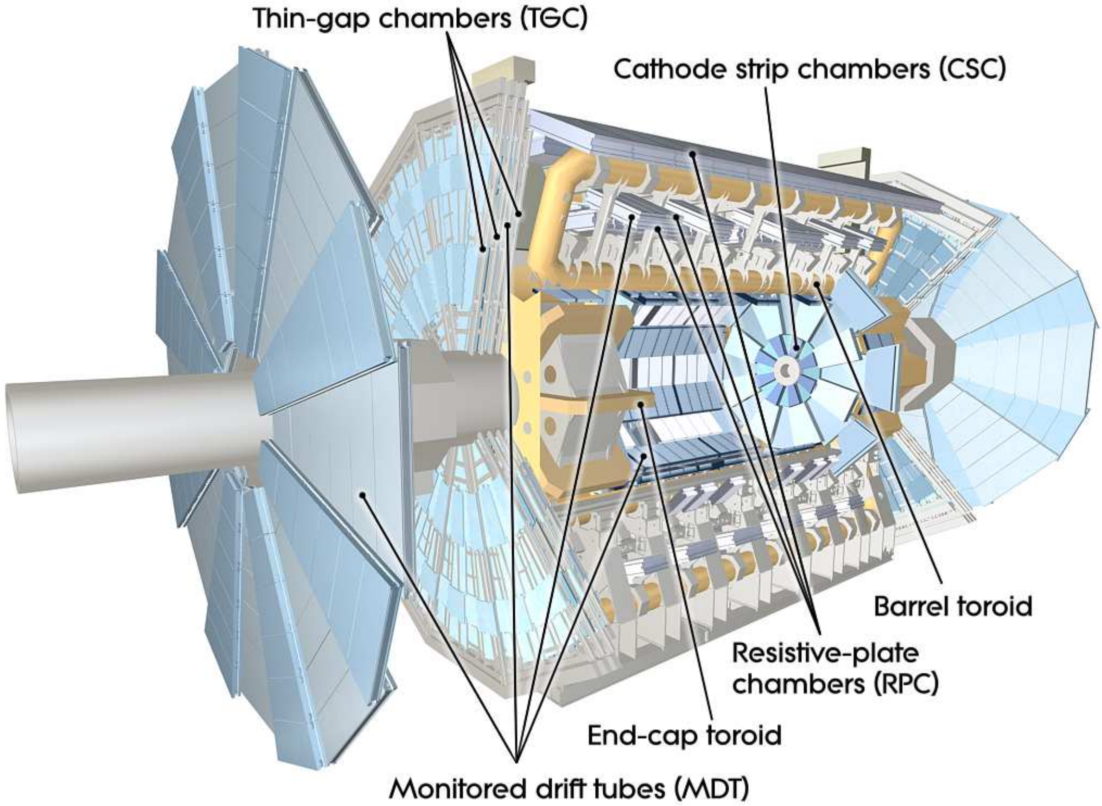

Figure 2.4.: The ATLAS Muon Spectrometer. Consisting of Monitored Drift Tubes and Cathode Strip Chambers for precision measurements of muons tracks, and Resistive-plate Chambers and Thin-gap Chambers that provide triggering capabilities [13].

2.2.5. The Trigger System

At the LHC, the proton bunches cross at a rate of about 40 kHz. To reduce the event rate to about 200Hz and only select events of interest, ATLAS employs a sophisticated trigger system. The ATLAS trigger system consists of two stages. First, events are selected by Level-1 (L1) triggers. This hardware based trigger systems can trigger on signatures of high p_T muons, electrons, photons, jets, missing transverse energy and the total transverse energy. The L1 muon triggers use reduced granularity information of the trigger chambers in the Muon Spectrometer, i.e the Resistive Plate Chamber (RPC) in the barrel region and Thin Gap Chambers (TGC) in the end-caps, to calculate the derivation of the measured muon-track to the one of an infinite momentum muon.

Information of the calorimeter gets processed by Level-1 Calorimeter triggers (L1Calo). First, the analogous detector signals get digitized and calibrated in the preprocessor. After that the data is processed in parallel by the Cluster Processor (CP), where electron, photon and τ lepton candidates can be identified, as well as by the Jet/Energy-sum Processor (JEP), that is able to identify jet candidates and calculate the total and missing transverse energy.

The final trigger decision is made by the Central Trigger Processor (CPT), which reduces the event rate to $\approx$75 kHz.
Events accepted by the L1 trigger are further selected by High-Level Trigger (HLT), which are software based. The HLT are seeded by Regions of Interest (ROI), a region in η and ϕ of the detector, identified by the L1 trigger. This step reduces the data rate transferred from the detector to the HLT. In the HLT objects are reconstructed by a software framework similar to the on used in the offline analysis. First, dedicated fast trigger algorithms are used for a first decision. Afterwards physics objects are reconstructed to a quality similar to the one used in offline analyses and the final trigger decision is formed. The HLT reduces the event rate to $\approx$ 200 Hz with each event having a size of around 1.3 Mbyte. Finally, events selected by the HLT get stored for offline analysis [13][21].

2.3. Particle Identification

2.3.1. Track Reconstruction

The tracks of charged particles are reconstructed with signals from the ID. This process is performed in multiple steps. First, *clusters* are created from the raw signals of the pixel detector and the silicon strip detector. A connected component analysis groups the raw measurements into clusters from which a *space point* is created. The energy deposit in a given cluster might not stem from a single particle, but from the interaction with multiple particles. A cluster is called *single-particle cluster* or *merged cluster*, depending on whether a single or multiple particles contribute to it. An artificial neural network is used to classify merged clusters. The efficiency for detecting clusters created by two particles is around 90% [22].

From three space-points a so-called *seed* is formed and a first estimate of the momentum, the impact parameter and the trajectory are calculated. The seed has to meet some requirements, e.g. there has to be a fourth cluster compatible with the trajectory and it also has to fulfill certain impact parameter and momentum criteria depending on the exact seed type. A track candidate is built by iteratively adding more space points compatible with the preliminary trajectory. After these stages ambiguities, i.e space points assigned to multiple track candidates, are resolved. Track candidates are ordered by their *track score*, a measure of the quality of the track, taking into account variables like χ^2 of the fit and the momentum. Track candidates that do not fulfill the quality requirements detailed in Ref. [22], are iteratively removed. Finally, a high quality fit is performed on all the remaining track candidates [22].

2.3.2. Electron Identification

Electrons[2] are reconstructed from tracks in the inner detector and clusters in the EM calorimeter. The EM calorimeter is divided into segments in $\eta \times \phi$ of size $\Delta\eta \times \Delta\phi = 0.025 \times 0.025$. For an electron candidate, an energy of $E > 2.5 GeV$ has to be deposited in an array of 3×5 of those segments. Furthermore, this energy cluster has to be spatially matched to an ID track, using a $-0.10 < \Delta\phi < 0.05$ requirement. Electron candidates are selected by a likelihood based identification procedure that takes information from the tracking and calorimeter system into account.

The likelihood identification procedure operates at four different working points:

[2] The same methods are used to reconstruct and identify positrons

"Very Loose", "Loose", "Medium"[3] and "Tight". The Loose, Medium and Tight working points require 2 hits in the pixel detector and a total of 7 hits in the pixel and silicon strip detector. The Tight and Medium working points further require a hit in the innermost layer of the pixel detector. They all require a transverse Energy (E_T) of at least 4.5 GeV. However, in the search for charged Higgs bosons only electron candidates with an $E_T > 27 GeV$ are considered.

The electron identification efficiency varies as a function of E_T. At $E_T = 40 GeV$ the electron identification efficiencies are 80%, 88% and 93% for the Tight, Medium and Loose working points, respectively. Figure 2.5 shows the electron identification efficiency as function of E_T for the different working points.
It is essential to be able to differentiate prompt electrons coming from the signal process and non prompt electrons produced in e.g semileptonic hadron decays. Signal electrons are well separated from any other object activity in their vicinity. So an isolation variable is used, allowing the distinction between signal and non prompt electrons. Two types of isolation variable are constructed, a calorimeter- and a track-based one.

For the calorimeter-based isolation variable, a cone of size ΔR is laid around the electron trajectory. The energy deposited in all the topological clusters (see. subsection 2.3.5) within the cone are summed up. This is called the *raw isolation energy* $E_{T,raw}^{isol}$. To account for the energy deposited by the electron in the calorimeter, the energy within a rectangle of size $\Delta\eta \times \Delta\phi = 0.125 \times 0.125$ is subtracted from $E_{T,raw}^{isol}$. Furthermore, $E_{T,raw}^{isol}$ is corrected to account for pileup and energy leakage into the cone. After all corrections are applied, the variable is called *fully corrected calorimeter-based isolation variable* $E_{T,col}^{isol}$.

The track based isolation variable is calculated from tracks with $p_T > 1 GeV$. Again a cone of size ΔR is built around the electron track and all the transverse momenta within the cone, excluding contributions from the electron, are summed up and corrected for bremsstrahlung emitted by the electron. This variable is called $p_{T,var}^{isol}$[23].

2.3.3. Muon Identification

At first, muons are reconstructed independently in both the Inner Detector and the Muon Spectrometer. In the Muon Spectrometer segments are constructed from hits in each chamber by a straight line fit. Track candidates are fitted from segments in different layers by a segmented seeded search algorithm. At least two matching segments are

[3] The "Medium" working point is the default.

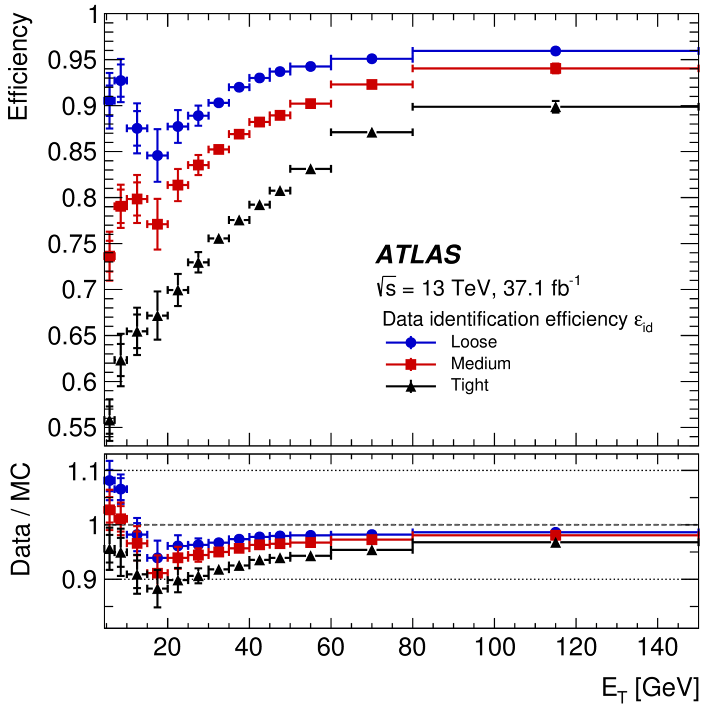

Figure 2.5.: The efficiency to identify electrons as a function of the electron transverse energy E_T at three different working points: Loose, Medium and Tight [23].

required, except in the barrel-endcap transition region, where one high-quality segment is sufficient. The final muon candidate is reconstructed from information of the inner detector, Muon Spectrometer and calorimeter. There are four different types of reconstructed muons:

- Combined muons: are reconstructed from tracks of the ID and MS. A outside-inn pattern recognition algorithm is used. The track reconstructed in the MS is extended to the ID and matched with a muon track candidate. Also an inside-out approach is used, where an ID-track is extrapolated into the MS and matched to a track.
- Segment-tagged muon: an ID track is extrapolated and matched to a segment. Muons with a low p_T or in a region of low acceptance in the MS might not leave a full track, but just a segment.
- Calorimeter-tagged muon: muon tracks in the ID are matched with an energy deposit in the calorimeter consistent with a minimal ionizing particle.

- Extrapolated muon: is only reconstructed by the track in the MS. This is useful for muons in the region not covered by the ID ($2.5 < |\eta| < 2.7$).

In order to ensure a good momentum measurement and to reject non prompt muons e.g from Kaon decays, a muon identification is performed. Four different selection criteria are available: "Loose", "Medium"[4], "Tight" and "high p_T". The muon identification efficiency, for Medium muons as a function of the muons p_T, is given in figure 2.6. For the selection, various quality measures are taken into account like the χ^2 of the fit or compatibility of the momenta measurement in the MDT and ID. Like electrons, muons produced by e.g the decay of a W-bosons are well isolated, while background muons produced by semileptonic hadron decays are not. Similar isolation variables, as described in subsection 2.3.2, are used to identify isolated muons. [24].

2.3.4. Missing Transverse Momentum

The colliding proton system has zero momentum in the lab frame. Due to momentum conservation, the sum of the transverse momenta of all objects in the detector is in principle zero. With particles not interacting with the detector (e.g neutrinos or other weakly interacting particles) their momentum should equal the missing transverse momentum E_T^{miss}. The missing transverse momentum is calculated via two components

$$E_T^{miss} = -\sum E_T^{hard} - \sum E_T^{soft}, \tag{2.5}$$

E_T^{hard} are the transverse momenta of "hard objects". These are fully reconstructed and calibrated objects i.e. muons, electrons, photons, taus and jets. The term E_T^{soft} describes "soft objects". These are the detector signals that cannot be associated with any hard object [25, 26].

2.3.5. Jet Reconstruction

Jets are reconstructed from topological clusters in the calorimeter. A topological cluster formation starts with a *proto cluster* a cell with a high signal significance ς_{cell}^{EM}

$$\varsigma_{cell}^{EM} = \frac{E_{cell}^{EM}}{\sigma_{noise,cell}^{EM}}, \tag{2.6}$$

where σ is the expected average noise and E_{cell}^{EM} the measured signal at the EM scale. A Cell with $\varsigma > 4$ is chosen as the *seed* for a proto cluster. Neighbouring cells with high cell significance of $\varsigma > 2$ are added to the *proto cluster*. This is repeated for all

[4] The "Medium" working point is the default.

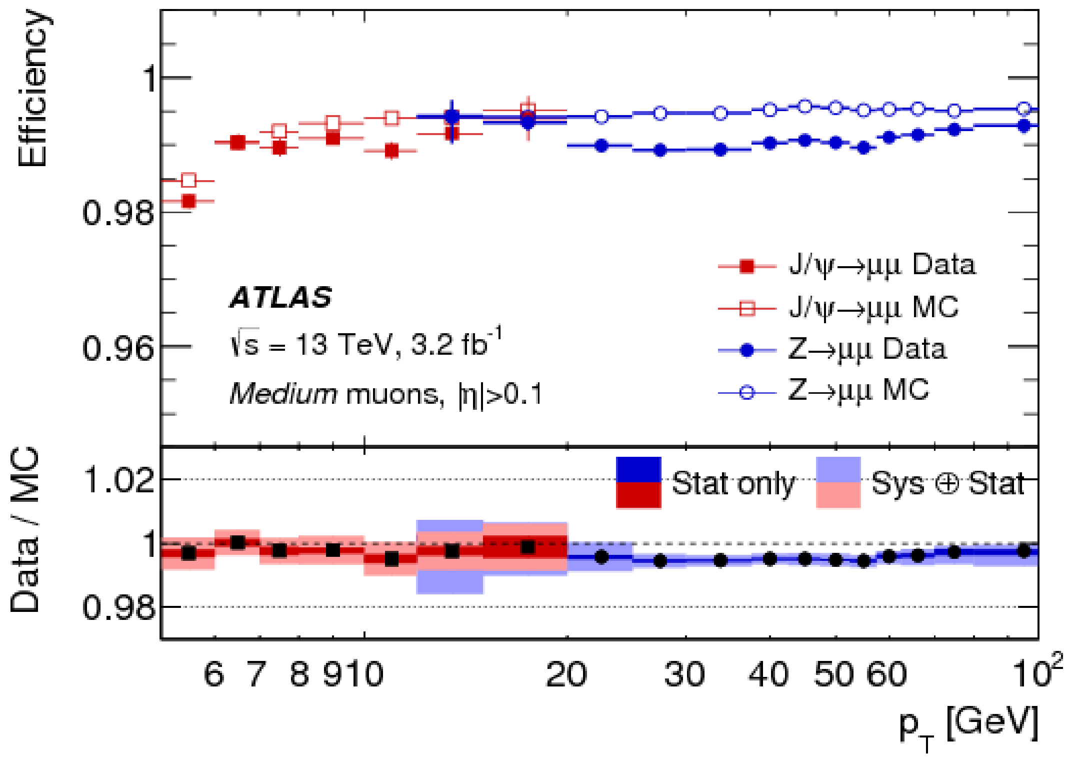

Figure 2.6.: The muon identification efficiency for the medium working point as a function of p_T and $|\eta| > 0.1$. The muon identification efficiency is determined using $J/\Psi \rightarrow \mu\mu$ and $Z \rightarrow \mu\mu$ events [24].

neighbouring cells with $\varsigma > 2$. Finally, all neighbouring cells are added [27].

4-vectors of topological clusters are the input to the anti-k_T clustering algorithm [28, 29]. The distance measure d_{ij} between two objects and d_{iB} between an object and the beam are defined as:

$$d_{ij} = min(k_{ti}^{2p}, k_{tj}^{2p}) \frac{\Delta_{ij}^2}{R^2} \tag{2.7}$$

and

$$d_{iB} = k_{ti}^{2p}, \tag{2.8}$$

with $\Delta_{ij}^2 = (y_i - y_j)^2 + (\phi_i - \phi_j)^2$, k_{ti} the transverse momentum, y_i the rapidity, ϕ_i the azimuth and R the radius parameter. The standard choice in ATLAS is R=0.4 and is used in this thesis. For the anti-k_t algorithm, the parameter $p = -1$ is used. Jets are clustered iteratively. All distances d_{ij} are calculated and the smallest one is used. If $d_{ij} > d_{Bi}$, the object is called a jet. If $d_{ij} < d_{Bi}$, the two objects are merged. This procedure is repeated until no object is left. This algorithm produces conical shaped jets, while being both infrared and collinear safe [27, 30].

2.3.6. b-Tagging

Jets originating from b quarks are of particular physical interest. A good identification of jets originating from b quarks and thus containing b-hadrons is crucial for ATLAS and allows to study e.g the Higgs boson or searches for new physics and can be used to significantly reduce the large background steaming from light-flavoured jets. B-tagging algorithms make use of characteristic properties of b-hadrons, like their long life-time, their high mass, their decay multiplicity and the hard b quark fragmentation function.

At ATLAS a variety of different low-level b-taggers are available. The IP2D and IP3D algorithm exploit the long b-hadron lifetime $\tau \sim 1.5ps$ i.e. b-hadrons travel lengths of the order of mm, before they decay leading to a secondary vertex. The IP2D and IP3D taggers use the transverse impact parameter (d_0) and longitudinal impact parameter ($z_0 \sin\theta$) to identify b-jets. The impact parameter significance is used as a discriminate between b-jets and light-flavour/c-jets. Impact parameters are defined as the distance of closest approach of a track to the primary vertex.

Another low level b-tagging algorithm used by ATLAS is based on secondary vertex finding algorithms (SV). They attempt to reconstruct the properties of b-hadron decays such as the mass or the decay length.

JetFitter is a multi-vertex reconstruction algorithm aiming to reconstruct the full b-hadron decay chain. JetFitter uses the typical topological structure of the b- and c-hadron decay to identify b-jets.

In order to achieve better performance than offered by each of the low-level-b-tagging algorithms individually, high level b-tagging algorithms have been developed. Such taggers like MV2 [31] or DL1 [31] combine outputs of low level algorithms into a single discriminant.

The MV2 algorithm is used in the search presented in this thesis. A Boosted Decision Tree (BDT) is used to build a single discriminant to distinguish between b-jets and c/light-flavour jets. Outputs of the low level taggers described above are used as an input as well as the jets p_T and η. The training of the BDT was performed with simulated $t\bar{t}$ events. The distribution of the MV2 output for b-jets, c-jets and light-flavour jets is depicted in figure 2.7 a). The background rejection, split into light-flavour and c-jet backgrounds is given in figure 2.7 b) as a function of the efficiency to identify b-jets. The MV2-tagger can operate at different efficiencies (working points) to identify b-jets. They are defined by a specific-cut on the output of the MV2-tagger. In this thesis, the 70% b-jet efficiency working point is used. At this working point the light-flavour jet rejection is 381 and the c-jet rejection is 12 [31–33].

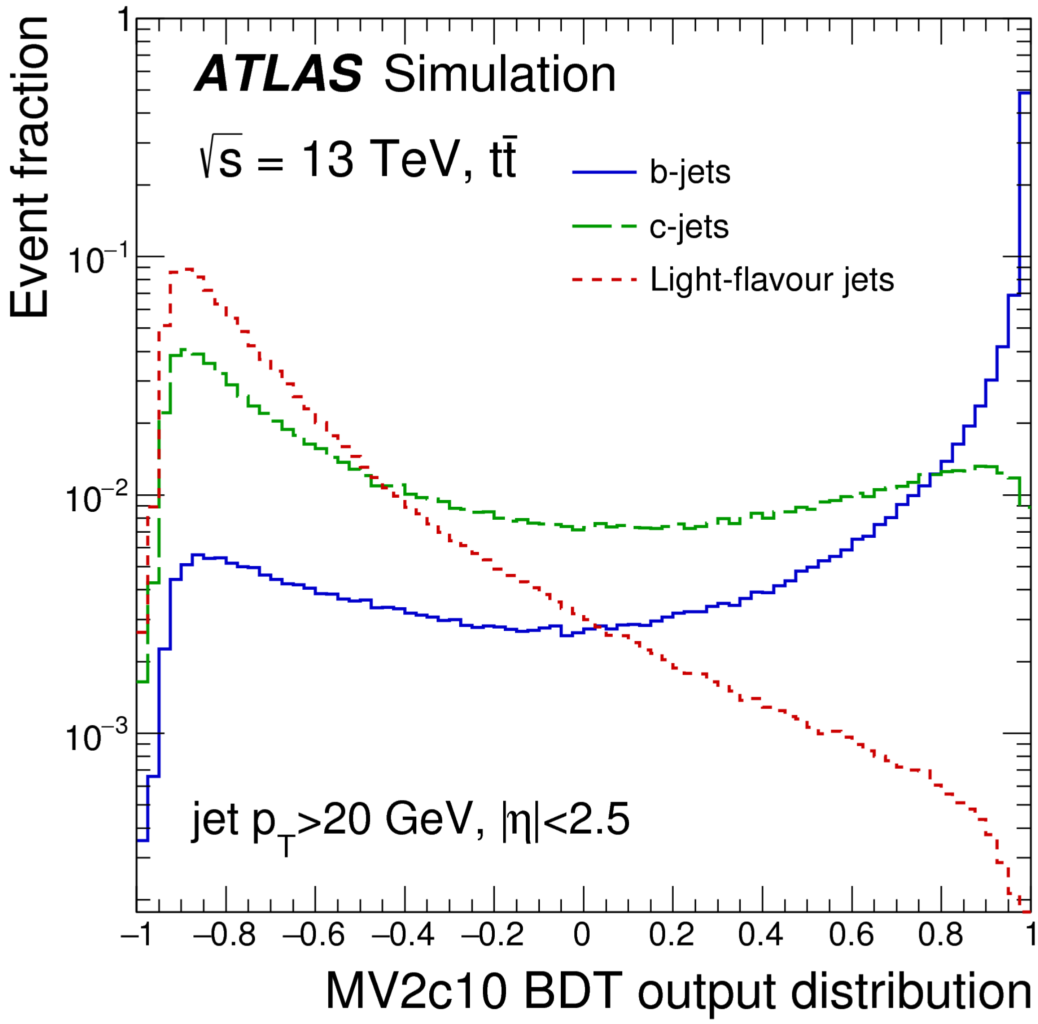

(a)

Figure 2.7.: a) The output of the MV2-algorithm for b-jets (blue), c-jets (green) and light-flavour jets (red) determined using simulated $t\bar{t}$-samples [32].

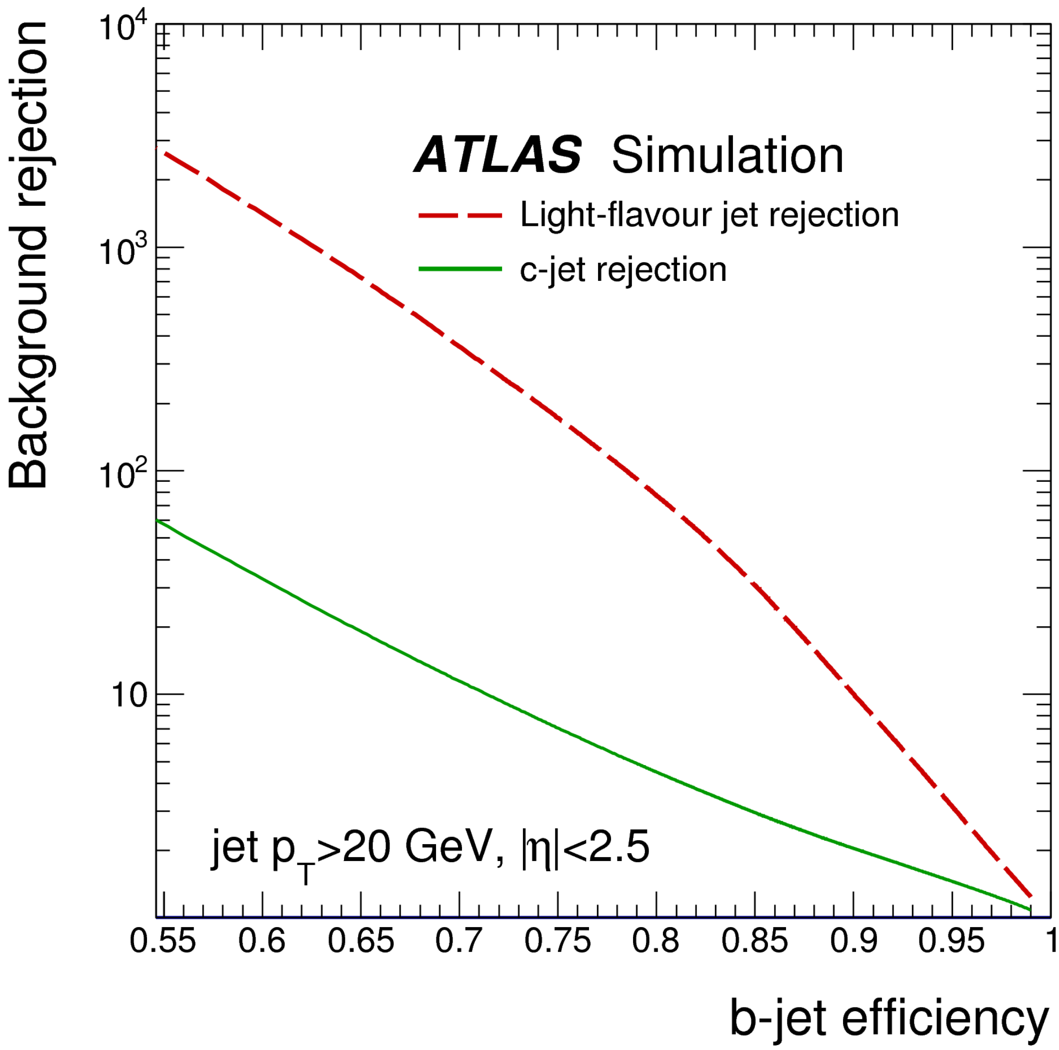

(b)

Figure 2.7.: b) The background rejection of c-jets (green) and light-flavour jets (red) as a function of the b-jet identification efficiency determined using simulated $t\bar{t}$-samples [32].

3. Theoretical Background

3.1. The Higgs Mechanism of the Standard Model

The Higgs mechanism of the Standard Model of particle physics was independently introduced by Englert and Brout [34] as well as by Higgs [35]. This mechanism explains the origin of gauge boson masses by introducing the principle of spontaneous symmetry breaking (SSB) to a gauge theory.
A complex scalar self-interacting SU(2) doublet ϕ is introduced:

$$\Phi = \begin{pmatrix} \Phi^+ \\ \Phi^0 \end{pmatrix} = \begin{pmatrix} \Phi_1 + i\Phi_2 \\ \Phi_3 + i\Phi_4 \end{pmatrix}, \tag{3.1}$$

where the upper component $(\Phi_1 + i\Phi_2)$, with weak isospin $I^0 = +1/2$, corresponds to a charged one with electric charge quantum number $Q = +1$, and hence hypercharge $Y = 2(Q - I^0) = +1$. The lower component is uncharged, so it has the quantum numbers $Q = 0$, $I^0 = -1/2$ and $Y = +1$. The simplest self interacting potential of the scalar field is given by:

$$V(\Phi) = \mu^2 \Phi^\dagger \Phi + \lambda (\Phi^\dagger \Phi)^2 \tag{3.2}$$

The SU(2)$\times$ U(1) gauge invariant scalar Lagrangian is therefore:

$$\mathcal{L}_{scalar} = (D_\mu \Phi)^\dagger (D^\mu \Phi) - \mu^2 \Phi \Phi^\dagger - \lambda (\Phi \Phi^\dagger)^2 \tag{3.3}$$

The vacuum state is the one where the potential is minimal. For $\mu < 0$ and $\lambda > 0$, the field value of the ground state is non-zero. Due to its shape, such a potential is often called "mexican hat" potential (see figure 3.1). Namely the potential will be minimal for an absolute value of Φ of:

$$|\Phi|_0 = \sqrt{\frac{-\mu^2}{2\lambda}} := \frac{v}{\sqrt{2}} \tag{3.4}$$

The minimum described by this condition is degenerate. There is an infinite number of possible vacuum states with this field value, related via gauge transformation. However, by choice of one particular phase value for the vacuum state:

$$\Phi = \frac{1}{\sqrt{2}} \begin{pmatrix} 0 \\ v \end{pmatrix}, \tag{3.5}$$

the electroweak symmetry of the Lagrangian is spontaneously broken. This is called spontaneous symmetry breaking (SSB). This process and the general shape of the potential is visualized for two instead of four dimension in figure 3.1. Field excitations

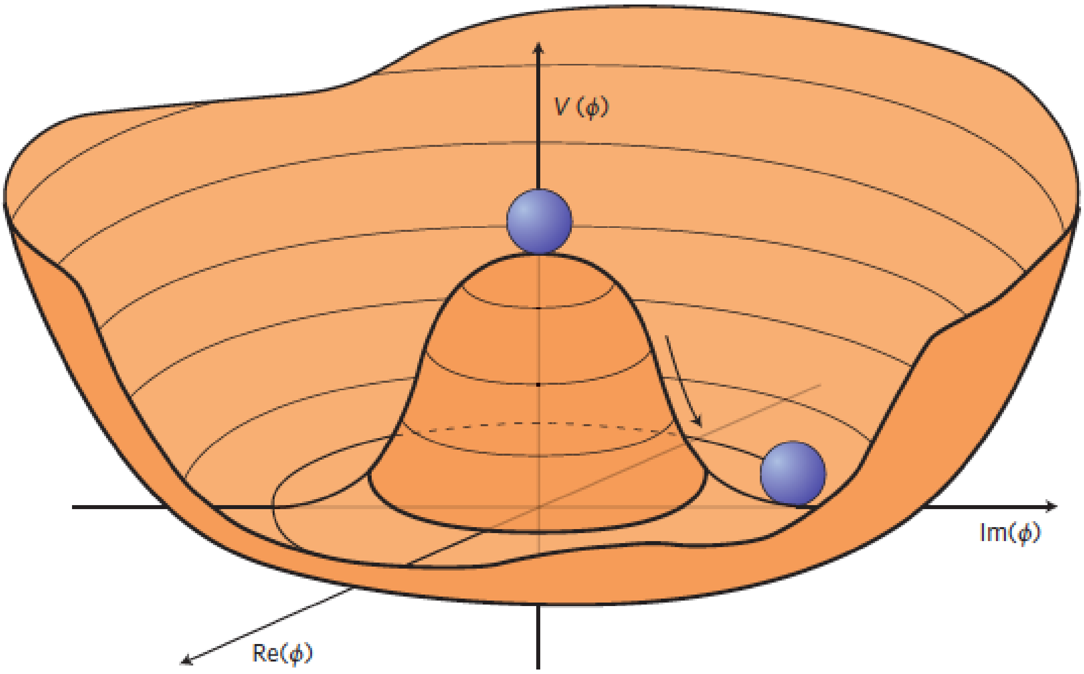

Figure 3.1.: An illustration of the Standard Model Higgs potential in two dimension instead of four. The minima of the potential are at non-zero field value on a circle of radius v arround the origin and therefore degenerate [36].

around the chosen vacuum state can be parameterised by:

$$\Phi = \exp(\frac{iT_i\xi_i(x)}{v}) \begin{pmatrix} 0 \\ (h(x)+v)/\sqrt{2} \end{pmatrix}, \tag{3.6}$$

where T_i (i=1,2,3) are the generators of SU(2). The three fields ξ_i are massless excitations, Goldstone bosons, which are unwanted as there is no physical particle they could be identified with. The field h corresponds to a massive excitation called the Higgs boson. The Goldstone bosons can be eliminated by a SU(2) gauge transformation:

$$\Phi \to U(\xi)\Phi = \exp(-\frac{iT_i\xi_i(x)}{v})\Phi. \tag{3.7}$$

The fields ξ have vanished. However, the fields ξ will not disappear completely, but will reappear in the full Lagrangian as longitudinal polarisation of the massive W and

Z bosons. This all can be seen by inserting equation 3.7 in equation 3.3 and D_μ will be the $SU(2)_L \times U(1)_Y$ gauge invariant derivative $D_\mu = \partial_\mu + ig\hat{T}W_\mu + ig'B_\mu$

$$\mathcal{L} = (\frac{1}{2}(\partial_\mu h)(\partial^\mu h)) + \frac{g^2}{8}(v+h)^2(W^1_\mu + iW^2_\mu)(W^{\mu 1} - iW^{\mu 2}) + \frac{1}{8}(v+h)^2(gW^{\mu 3} - g'B^\mu) + \mu^2 h^2 - \lambda v h^3 - \frac{\lambda}{4}h^4 \quad (3.8)$$

Substituting the physical field $W^\pm_\mu = \frac{W^1_\mu \mp iW^2_\mu}{\sqrt{2}}$ and $Z_\mu = \frac{-g'B_\mu + gW^3_\mu}{\sqrt{g^2+g'^2}}$

$$\mathcal{L} = \frac{1}{2}(\partial_\mu h)(\partial^\mu h)) + \mu^2 h^2 - \lambda v h^3 - \frac{\lambda}{4}h^4 + \frac{1}{4}g^2 v^2 W^- W^+ + \frac{1}{2}vg^2 W^- W^+ h + \frac{1}{2}W^- W^+ hh + \frac{(g^2+g'^2)v^2}{8}Z^\mu Z_\mu + ..., \quad (3.9)$$

A few things stand out: there is a massive Higgs boson with mass $m^2_{Higgs} = -\mu^2$, and furthermore there are now mass terms for the weak gauge bosons with $m_W = \frac{1}{2}gv$ and $m_Z = \frac{v}{2}\sqrt{g^2+g'^2}$.
The Higgs boson does not only interact with the weak gauge bosons, but also with the fundamental massive fermions via Yukawa couplings. The Yukawa interaction Lagrangian for the example of the electron mass eigenstate is given by:

$$\mathcal{L}_{Yukawa} = -g_e \frac{v+h}{\sqrt{2}}(\bar{e}_R e_L + \bar{e}_L e_R) = -\frac{g_e v}{\sqrt{2}}\bar{e}e - \frac{g_e h}{\sqrt{2}}\bar{e}e. \quad (3.10)$$

This holds for all other Standard Model fermions (with the exception of the neutrinos that have $m_\nu = 0$ and thus $g_\nu \propto m_\nu = 0$, in the Standard Model). The term $\frac{g_e v}{\sqrt{2}}\bar{e}e$ can be identified with the mass term of the electron with $m_e = g_e\frac{v}{\sqrt{2}}$. The term $\frac{g_e h}{\sqrt{2}}\bar{e}e$ describes the Yukawa interaction between the Higgs boson and the electron. The Higgs-fermion coupling constants are directly proportional to the fermion masses. In table 3.1 the dominant decays of the Higgs boson and their branching ratios are listed. Decays into the heavy b quarks and W bosons are the most important ones, reflecting the proportionality of the mass and the coupling strength.

Table 3.1.: The branching ratios for most dominant SM-Higgs boson decay channels

Decay mode $h \to XX$	$b\bar{b}$	WW^*	$\tau^+\tau^-$	ZZ^*	$\gamma\gamma$	$Z\gamma$	$\mu^+\mu^-$
Branching Ration[%]	58.4	21.4	6.27	2.62	0.227	0.152	0.021

In 2012, the Higgs boson was discovered by the ATLAS and CMS collaborations at the

LHC [1, 2]. It has a mass of 125 GeV. One of the discovery channels is the $h \to \gamma\gamma$ decay. The di-photon invariant mass distribution measured by the ATLAS detector is depicted in figure 3.2. There is an excess of events above the background around $m_{\gamma\gamma} \approx 126$ GeV. Combined with searches for the Higgs boson in the decays $h \to ZZ^* \to llll$ and $h \to WW^* \to l\nu l\nu$, ATLAS could excluded Higgs bosons in the mass range between 100 GeV and 583 GeV with 95% CL, except in a mass range between 122 GeV-131 GeV. At $m_h = 126.0$ GeV an excess of events, compatible with a SM Higgs boson, was observed with an significance of 5.9σ [37]. By now, several other decay modes have been observed in different production channels at the LHC. A summary of the cross-section times branching ratio values measured with the ATLAS detector at $\sqrt{s} = 13TeV$, normalized to the Standard Model expectation, is shown in figure 3.3. The properties of the Higgs boson, like spin and CP quantum numbers, agree well with the SM predictions within the experimental uncertainties. [4][38][36]

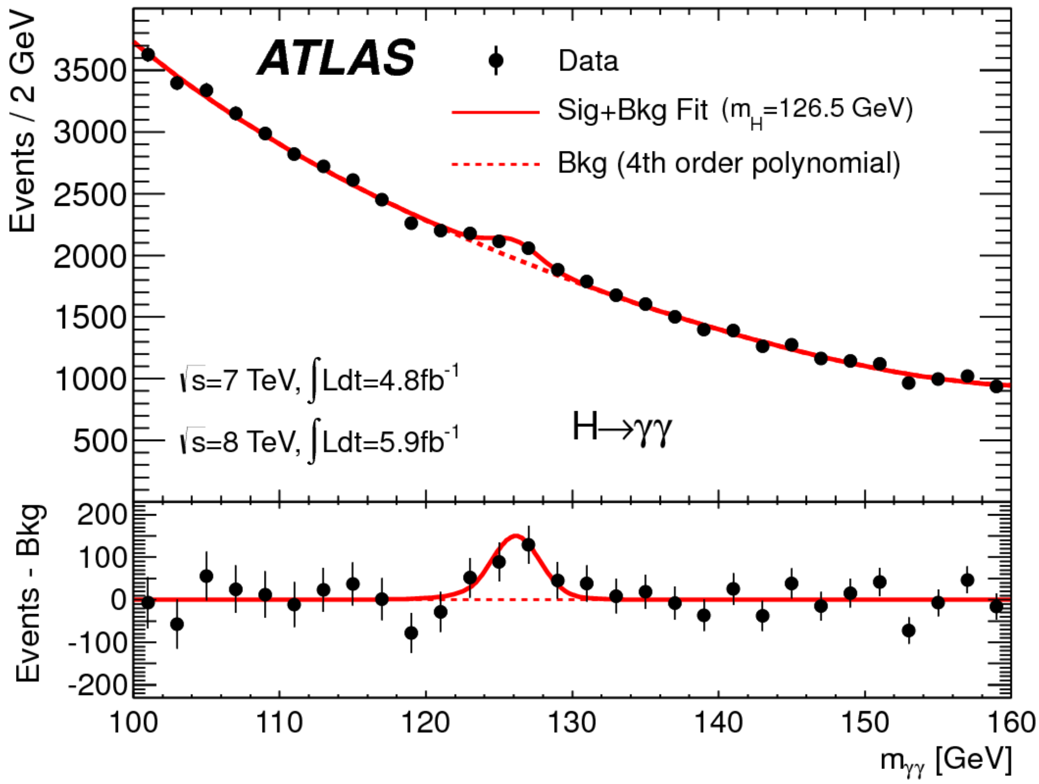

Figure 3.2.: The di-photon invariant mass distribution measured by the ATLAS experiment in 2012 at $\sqrt{s} = 7$ TeV and $\sqrt{s} = 8$ TeV. There is an excess of events at $m_{\gamma\gamma} = 126$ GeV[37].

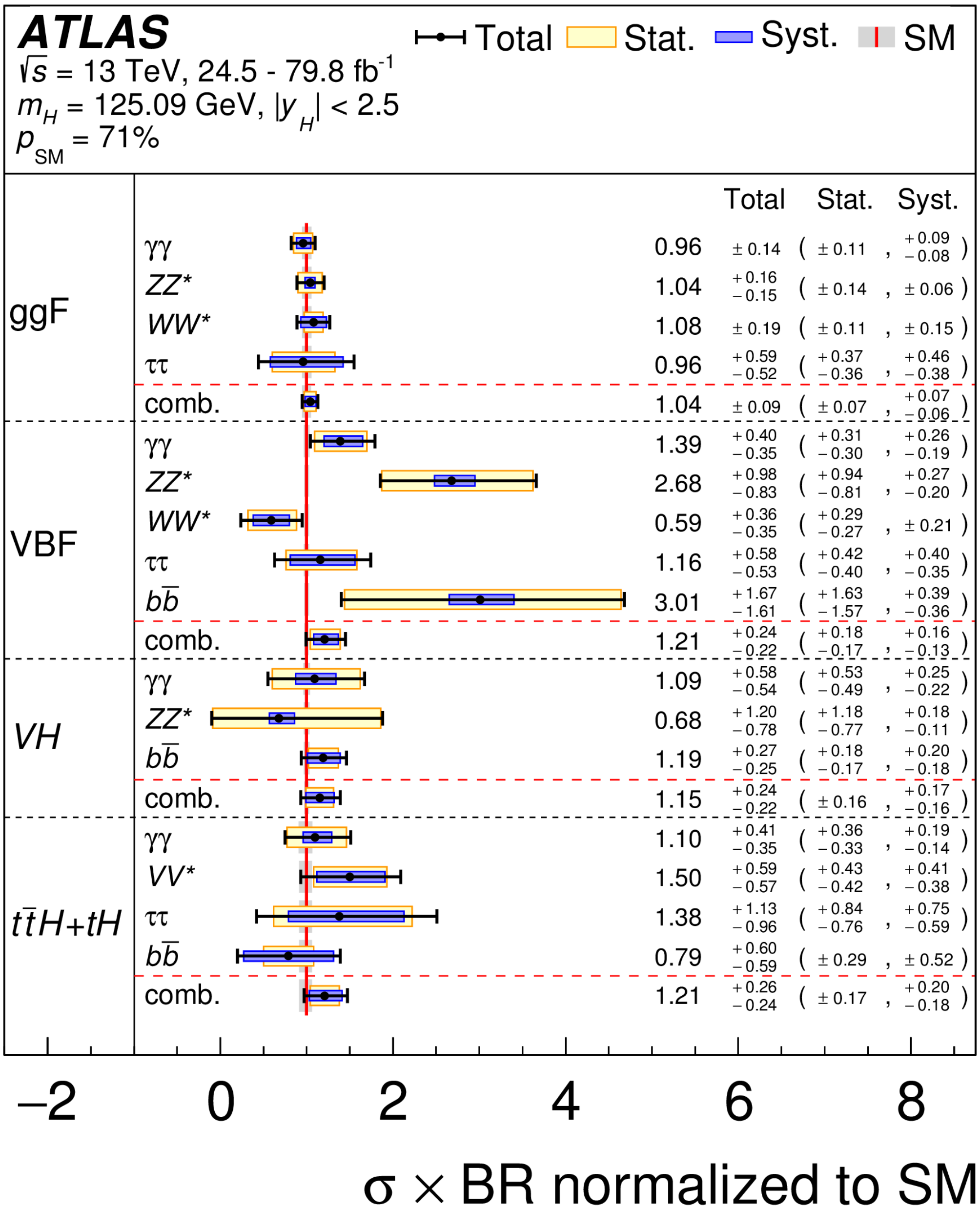

Figure 3.3.: The cross-section times branching ratio values measured by the ATLAS detector at $\sqrt{s} = 13$ TeV and normalized to the Standard Model expectations for the different Higgs boson production and the observed decay modes [39].

3.2. Extensions of the Higgs Sector

It is not clear yet whether the 125 GeV Higgs boson is the Standard Model Higgs boson, or indeed just the first observed state of an extended scalar sector. There are many proposals to extend the Higgs sector. Such models can provide solutions for problems left open by the standard model. The origin of Dark Matter [6, 40, 41], neutrino masses [41–43] and the baryon asymmetry in the universe [43–45]. Many of these theories predict additional charged scalars. In this section, a short overview of such theories that also predict charged Higgs bosons is given.

3.2.1. The Two-Higgs Doublet Model

One of the most popular and best studied extensions of the Higgs sector is the 2-Higgs Doublet Model (2HDM). It is well motivated by e.g Supersymmetrie [6], as the Higgs sector of a Minimal Supersymmetric Standard model (MSSM) is a Type-2 2HDM. Furthermore, a 2HDM can provide an additional source of CP-Violation in the weak interaction for explaining the baryon asymmetry[44–46] of the universe. A variant of the 2HDMs may play an important role in a Peccei-Quinn theory, predicting Axions, a promising Dark Matter candidate [40, 47].
The 2HDM adds a second complex $SU(2)_L$ doublet to the SM. The 2HDM potential is given by :

$$V(\Phi_1,\Phi_2) = m_{11}\Phi_1^\dagger\Phi_1 + m_{22}\Phi_2^\dagger\Phi_2 - [m_{12}\Phi_1^\dagger\Phi_2 + h.c] + \frac{1}{2}\lambda_1(\Phi_1^\dagger\Phi_1)^2 + \frac{1}{2}\lambda_2(\Phi_2^\dagger\Phi_2)^2 + \lambda_3(\Phi_1^\dagger\Phi_1)(\Phi_2^\dagger\Phi_2) + \lambda_4(\Phi_1^\dagger\Phi_2)(\Phi_2^\dagger\Phi_1) + [\frac{1}{2}\lambda_5(\Phi_1^\dagger\Phi_2)^2 + h.c.] \quad (3.11)$$

Similar to the discussion in section 3.1, the scalar fields will acquire non zero vacuum expectation values (vev) v_1 and v_2. The expansion of the fields around the vacuum state gives:

$$\Phi_{1,2} = \begin{pmatrix} \Phi^+_{1,2} \\ v_{1,2} + h_{1,2} + i\eta_{1,2}/\sqrt{2} \end{pmatrix} \quad (3.12)$$

This gives a total of 8 degrees of freedom, 3 of the 8 degrees of freedom will be absorbed into the longitudinal polarisation states of the weak gauge bosons (see section 3.1). The remaining 5 fields will manifest themselves as physical particles:

- 2 CP-even neutral Higgs bosons: h, H,
- 1 CP-odd neutral pseudoscalar: A,
- 2 charged Higgs bosons: $H^\pm$.

By definition, H is chosen to be heavier than h. Another important parameter of the 2HDM is the ratio of the vevs:

$$\tan(\beta) = \frac{v_2}{v_1}. \tag{3.13}$$

Also the squared sum of the vevs is fixed to the SM value:

$$v = \sqrt{v_1^2 + v_2^2} = 246\,GeV. \tag{3.14}$$

In general, the CP even Higgs bosons mix:

$$\begin{aligned} h &= h_1 \sin(\alpha) - h_2 \cos(\alpha), \\ H &= -h_1 \sin(\alpha) - h_2 \cos(\alpha). \end{aligned} \tag{3.15}$$

This defines the mixing angle α, another important parameter of the 2HDM. In general, one of the Higgs bosons does not have the phenomenology of a standard model Higgs boson. In order to be able to identify one of the Higgs bosons (h,H) with the 125 GeV observed state, that behaves SM-like[4], the parameter space has to fall in the so-called alignment limit. In this limit one of the CP-even uncharged particles behaves like an SM-Higgs boson would, this state can be either the light or the heavy neutral scalar. The alignment limit is defined by:

$$h \rightarrow h_{SM} : \sin(\beta - \alpha) \rightarrow 1 \tag{3.16}$$

$$H \rightarrow h_{SM} : \cos(\beta - \alpha) \rightarrow 1 \tag{3.17}$$

A priori the exact structure of the 2HDM Yukawa-sector is not determined. In a 2HDM without Flavour-Changing-Neutral-Currents (FCNC) there are four different possible 2HDM-Types defined by which of the doublets couples to the up-type quarks, down-type quarks and leptons. There are the Type I, Type II, Lepton-specific and Flipped 2HDM. Table 3.2 list which of the doublets couples to which fermions in each of the 2HDM types. By definition the up type quarks always couple to Φ_2.

Table 3.2.: The four different 2HDM types, distinguished by the coupling of Φ_1 and Φ_2 to the quarks and leptons. u are the up-type quarks, d the down-type quarks and l the leptons, i is the generation index.

	Type I	Type II	Lepton-specific	Flipped
Φ_1		d_R^i, l_R^i	l_R^i	d_R^i
Φ_2	u_R^i, d_R^i, l_R^i	u_R^i	u_R^i, d_R^i	u_R^i, l_R^i

The charged Higgs bosons interact with all SM fermions. The exact coupling depends on the 2HDM type. The Yuakawa Lagrangian for the charged Higgs bosons for one fermion generation is given by:

$$\mathcal{L}_{H^\pm} = -H^+\left(\frac{\sqrt{2}V_{ud}}{v}\bar{u}(m_u X P_L + m_d Y P_R)d + \frac{\sqrt{2}m_l}{v}Z\bar{v}l_R\right) + h.c \tag{3.18}$$

where V_{ud} correspond to the CKM-matrix element, $P_{L/R}$ the left/right handed projector and X,Y,Z constants that are depending on the particular 2HDM type. The different 2HDM types are listed in table 3.3. The couplings are proportional to the fermion masses, such that decay into the heaviest fermions, i.e top and bottom quark or a tau lepton and a neutrino, depending one the 2HDM Type and $\tan(\beta)$, dominate. Consequently searches for charged Higgs bosons focus on these decays [48–51].

Table 3.3.: Constants used in equation 3.18 to describe the Yukawa interactions of the charged Higgs boson

	Type I	Type II	Lepton-specific	Flipped
X	$\cot\beta$	$\cot\beta$	$\cot\beta$	$\cot\beta$
Y	$\cot\beta$	$-\tan\beta$	$\cot\beta$	$-\tan\beta$
Z	$\cot\beta$	$-\tan\beta$	$-\tan\beta$	$\cot\beta$

The charged Higgs boson does not only couple to the fermions but also to other bosons. The coupling constants for vertices of charged Higgs bosons with $W^\pm$ and h/H are:

$$g_{H^+hW} = \frac{g}{2}\cos(\beta - \alpha), \tag{3.19}$$

$$g_{H^+HW} = \frac{g}{2}\sin(\beta - \alpha). \tag{3.20}$$

In the alignment limit the charged Higgs bosons decouple form the SM-like Higgs boson [52–55].

3.2.2. The Next-to-Two-Higgs Doublet Model

The simplest extension of the 2HDM is the Next-to-Two-Higgs Doublet Model (N2HDM), adding an additional real singlet field Φ_S to the 2 complex doublets Φ_1 and Φ_2.
The scalar potential of the N2HDM is:

$$\begin{aligned} V(\Phi_1, \Phi_2) = m_{11}\Phi_1^\dagger\Phi_1 + m_{22}\Phi_2^\dagger\Phi_2 - [m_{12}\Phi_1^\dagger\Phi_2 + h.c] + \frac{1}{2}\lambda_1(\Phi_1^\dagger\Phi_1)^2 + \frac{1}{2}\lambda_2(\Phi_2^\dagger\Phi_2)^2 \\ + \lambda_3(\Phi_1^\dagger\Phi_1)(\Phi_2^\dagger\Phi_2) + \lambda_4(\Phi_1^\dagger\Phi_2)(\Phi_2^\dagger\Phi_1) + [\frac{1}{2}\lambda_5(\Phi_1^\dagger\Phi_2)^2 + h.c.] \\ + \frac{1}{2}m_S^2 + \frac{\lambda_6}{8}\Phi_s^4 + \frac{\lambda_7}{2}(\Phi_1^\dagger\Phi_1)\Phi_S^2 + \frac{\lambda_8}{2}(\Phi_2^\dagger)\Phi_S^2. \end{aligned} \tag{3.21}$$

The first 2 lines are the same as for the 2HDM (see equation 3.11), the last one describes the contribution of the singlet. Analogous to the 2HDM after EWSB, the doublet fields acquire a vevs v_1 and v_2, as does the singlet with a vev v_S. The scalar fields can be parametrised around the chosen vacuum state by:

$$\Phi_{1,2} = \begin{pmatrix} \Phi_{1,2}^+ \\ v_{1,2} + h_{1,2} + i\eta_{1,2}/\sqrt{2} \end{pmatrix}, \Phi_S = v_S + \rho_S, \tag{3.22}$$

leading to 6 physical states:

- 3 CP-even Higgs bosons: H_1,H_2,H_3,
- 1-CP-odd pseudoscalar: A,
- 2 charged Higgs bosons: $H^\pm$.

There is an additional scalar Higgs boson ρ_S compared to the 2HDM. The three scalar Higgs bosons mix among each other with the mixing angles α_1, α_2 and α_3. The N2HDM has a large parameter space with 12 independent parameters. For example those can be chosen as:

$$\alpha_1, \alpha_2, \alpha_3, \tan(\beta), v, v_s, m_{H1,2,3}, m_A, m_H^\pm, m_{12}^2, \tag{3.23}$$

where $\tan(\beta) = \frac{v_2}{v_1}$ follows the definition of the 2HDM.
This large parameterspace results in less stringent experimental constraints on the individual parameters compared to the 2HDM. The singlet itself does not couple to any SM particle. As it mixes with the other CP-even Higgs bosons their coupling to the SM-particles is changed wrt. the 2HDM. The coupling of the H_i to the weak gauge bosons is given by:

$$g_{H^iVV} = ig_{\mu\nu}g_{SM}c_i(\alpha_{1-3}, \beta), \tag{3.24}$$

where g_{SM} is the Standard Model coupling constant of the Higgs boson to the weak gauge bosons. Thus c is the modification factor of the coupling in the N2HDM compared to the SM. This again defines an alignment limit $c_i \to 1$ depending on which of the H_i correspond to the SM Higgs boson. The values of c for the different H_i are given in table 3.4.

Table 3.4.: The coupling modification factor of the CP-even Higgs bosons H^i to a pair fo gauge Bosons $V = W, Z$, in the N2HDM compared to the SM

c_{H^1VV}	$\cos(\alpha_2)\cos(\beta-\alpha_1)$
c_{H^2VV}	$-\cos(\beta-\alpha_1)\sin(\alpha_2)\sin(\alpha_3)+\cos(\alpha_3)\sin(\beta-\alpha_1)$
c_{H^3VV}	$-\cos(\alpha_3)\cos(\beta-\alpha_1)\sin(\alpha_2)-\sin(\alpha_3)\sin(\alpha_1)$

The coupling constants $g_{H_iWH^\pm}$ of the charged Higgs boson to a W and a CP-even Higgs boson is modified in the N2HDM and is given in table 3.5.

Table 3.5.: The coupling constants $g_{H_iWH^\pm}$ in the N2HDM

$g_{H_1WH^\pm}$:	$g/2(-\cos(\alpha_2)\sin(\beta-\alpha_1))$
$g_{H_2WH^\pm}$:	$g/2(\sin(\beta-\alpha_1)\sin(\alpha_2)\sin(\alpha_3)+\cos(\alpha_3)\cos(\beta-\alpha_2))$
$g_{H_3WH^\pm}$:	$g/2(\cos(\alpha_3)\sin(\beta-\alpha_1)\sin(\alpha_2)-\sin(\alpha_3)\cos(\beta-\alpha_1))$

All other couplings not involving a CP-even Higgs boson are the same in the 2HDM and N2HDM. Therefore, for example equation 3.18 still holds for the N2HDM as the singlet state only mixes with the CP-even Higgs bosons [56–59].

3.2.3. The Georgi-Machacek Model

Another approach in extending the Higgs sector are Higgs triplet models. Such models are often used to generate masses for the neutrinos [42, 43]. In general they do not fulfill the experimental constraints on the electroweak parameter $\rho = \frac{M_W^2}{M_Z^2 \cos^2(\Theta_W)} \approx 1$. The variant of the Higgs triplet model proposed by Georgi and Machacek [60] does not suffer from this constraint. Therefore the following discussion focuses on this model. The Georgi-Machacek model (GM) adds a real and complex SU(2) triplet ξ and χ, respectively, to the SM doublet Φ which can be described by:

$$\chi = \begin{pmatrix} \chi^0 & \xi^+ & \chi^{++} \\ \chi^- & \xi^0 & \chi^+ \\ \chi^{--} & \xi^- & \chi^{0*} \end{pmatrix} \text{ and } \Phi = \begin{pmatrix} \Phi^+ \\ \Phi^0 \end{pmatrix}. \tag{3.25}$$

As in the SM, the doublet and the triplets acquire vevs v_D and v_T, respectively. The squared sum of the vevs is fixed by the SM value $v_{SM}^2 = v_D^2 + 8v_T^2 = (246GeV)^2$. The ratio of the triplet and doublet vevs defines the Θ parameter:

$$\tan(\Theta) = \frac{2\sqrt{2}v_T}{v_D}. \tag{3.26}$$

The GM model produces a rich particle content of uncharged, charged and doubly charged Higgs bosons. The bosons are categorised as $SU(2)_L$ singlet, triplet or fiveplets:

- Singlet: H_1^0, $H_1^{0\prime}$,
- Triplet: $H_3^{\pm}$, H_3^0,
- Fiveplet: $H_5^{++/--}$, $H_5^{\pm}$, H_5^0.

When the custodial SU(2) symmetry is preserved the fiveplet and triplet states cannot mix with each other or the singlets and thus are mass eigenstates. However, the singlet states mix with the mixing angle α and thus are forming the mass eigenstates:

$$\begin{aligned} h &= \cos(\alpha)H_1^0 - \sin(\alpha)H_1^{0\prime}, \\ H &= \sin(\alpha)H_1^0 + \cos(\alpha)H_1^{0\prime}. \end{aligned} \tag{3.27}$$

The singlet states couple to the fermions as well as to the weak gauge bosons. So one of the states h or H must be identified with the 125 GeV Higgs boson as the neutral triplet states couple only to fermions pairs, but not to the weak gauge bosons, and the fiveplet states do not couple to fermions but only to weak gauge bosons pairs. Furthermore, the neutral triplet state is CP-odd.

The charged Higgs searches in this thesis thus consider the decay $H_3^+ \to (h/H)W^+$ as there is no $HH_5^+W^+$ vertex. The coupling constant for this decay are given by:

$$\begin{aligned} g_{W^+hH_3^+} &= -\sqrt{\frac{2}{3}}\frac{e}{\sin\Theta_W}(\sqrt{3}\cos(\alpha)\frac{v_T}{v} + \sin(\alpha)\frac{v_D}{v}), \\ g_{W^+HH_3^+} &= -\sqrt{\frac{2}{3}}\frac{e}{\sin\Theta_W}(\sqrt{3}\sin(\alpha)\frac{v_T}{v} - \cos(\alpha)\frac{v_D}{v}), \end{aligned} \tag{3.28}$$

where Θ_W is the Weinberg-angle.
Other possible decays of the charged Higgs boson H_3^+ are into two quarks, two leptons or a pair of other scalars. Among the decay channels of a heavy charged Higgs boson with $m(H_3^+ > m(t) + m(b))$ the dominant ones are thought to be decays into a top and bottom quark pair or into a singlet Higgs boson and a W [61]. The coupling to an up and down type quark pair is given by:

$$g_{H_3^+\bar{t}b} = \frac{\sqrt{2}}{v}V_{ud}\tan(\Theta)(m_u P_L - m_d P_R), \tag{3.29}$$

where V_{ud} is the corresponding CKM-matrix element. The H_5^+ does not have such a vertex since it does not couple to any of the SM fermions [60–64].

4. Motivation for the search for $H^+ \to W^+h$ Decays

Several direct searches for a charged Higgs bosons have been performed by the ATLAS and CMS collaborations [48–51, 65–70]. In the alignment limit of the 2HDM, the dominant decay modes of a charged Higgs boson is either into a t and b quark or into a τ and ν, depending on the mass of the charged Higgs boson and the model parameters (β, α). Thus, these decay channels have been the main focus of previous searches, while the decay $H^+ \to W^+h$ is so far uncovered. However, this decay may become important in certain models and has an experimental accessible final state. The channel $H^+ \to W^+h$ has been proposed as a promising discovery channel for a charged Higgs boson at the LHC [9–12].

In this section, the relevance of the decay $H^+ \to W^+h$ is discussed. The branching ratios (BR) of the decays $H^+ \to W^+h$ and $H^+ \to tb$ are studied in a few concrete examples of the models discussed in section 3.2. These branching ratios are studied as a function of relevant model parameters.

4.1. Branching Ratio Studies in the 2HDM

Branching ratios of a charged Higgs boson decaying into a t and b quark pair as well as into a W and h have been calculated in the 2HDM with the 2HDECAY program [71]. Following Ref. [57], the mass of the heavy neutral Higgs boson H was set to 125 GeV and the mass of the light neutral Higgs boson h to 96 GeV. A light Higgs boson of this mass may be compatible with an excess of events in the di-photon channel observed by CMS collaboration as well as with an excess in $b\bar{b}$-final states observed at LEP.

Branching ratios have been calculated for a large parameter space probing charged Higgs boson masses between 300 and 2000 GeV, $0 < \tan\beta < 40$ and $-\pi/2 < \alpha < \pi/2$. The mass of the pseudoscalar A was set to to 1.5 times the charged Higgs boson mass. Branching ratios have been calculated in all four 2HDM types. The calculated branching ratios are visualized in figure 4.1, figure 4.2 and figure 4.3.

Figure 4.1 depicts the branching ratios as a function of the charged Higgs boson mass for different values of $\tan(\beta)$ in a range between 0.25 and 7. The sub-figures a)-d) each show one of the four 2HDM types. The $\sin(\beta-\alpha)$ is set to 0.25, as this value is close to the alignment limit $\sin(\beta-\alpha) \to 0$. The branching ratios for $H^+ \to W^+h$ and $H^+ \to tb$ are (practically) independent of the 2HDM type. All the sub-figures show the same trends, which also holds true for different values of $\sin(\beta-\alpha)$. This behavior is in agreement with equation 3.18 and equation 3.20 as these are describing the most important decays for a heavy charged Higgs boson and do not exhibit any dependence on the 2HDM type.

The BR($H^+ \to tb$), for a given $\tan(\beta)$, decreases with the charged Higgs boson mass, while the BR($H^+ \to Wh$) increases slightly. At higher values of $\tan(\beta)$, the BR($H^+ \to tb$) decreases (the coupling scales with $1/\tan(\beta)$, see equation 3.18). E.g at $m_{H^+} = 400$ GeV, the branching ratio for this deacy is ≈ 0.95 at $\tan(\beta) = 0.25$ (blue dotted curve), while the branching ratio is ≈ 0.05 at $\tan(\beta) = 5$. The BR($H^+ \to hW$) goes to ≈ 0, for low values of $\tan(\beta)$ and is insignificant compared to $H^+ \to tb$. However, for large charged Higgs boson masses and large values of $\tan(\beta)$, the decay into a W and h has a higher branching ratio, than the decay into a t and b quark pair. Still the absolute value of the branching ratio is quit small with BR($H^+ \to Wh$)$\approx$ 0.075 at $\tan(\beta) = 5$ and $m_{H^+} = 2000 GeV$. While the BR($H^+ \to Wh$) first increases with increasing $\tan(\beta)$ over the hole charged Higgs boson mass range, this trend is reversed for values of $\tan(\beta) > 1$. For high values of $\tan(\beta)$ the decay mode $H^+ \to \tau\nu$ (not depicted in this graph) will be dominant.

The main dependence of the BR($H^+ \to Wh$) is on $\sin(\beta-\alpha)$. Figure 4.2 shows the BR($H^+ \to Wh$) and BR($H^+ \to tb$) as a function of $\sin(\beta-\alpha)$ at different values of $\tan(\beta)$. Each sub-figure show a different H^+ mass: 400 GeV a), 800 GeV b), 1200GeV c) and 1600 GeV d). For $|\sin(\beta-\alpha)| \to 1$, the BR($H^+ \to Wh$)) ranges up to almost 1 if $\tan(\beta) > 1$. The same is seen for all charged Higgs boson masses. While for $\sin(\beta-\alpha) \to 0$, the BR goes to 0. The BR($H^+ \to tb$) is almost independent of $\sin(\beta-\alpha)$.

However, one should keep in mind that $|\sin(\beta-\alpha)| \to 1$ is away from the alignment limit, here the state H, that in this case was identified with the 125 GeV Higgs boson decouples from the gauge bosons. So in this part of the parameter space the phenomenology of the state H is not the one of the Standard model Higgs boson.
In the alignment limit$|\sin(\beta-\alpha)| \to 0$ the charged Higgs boson does not couple to the WH decay (this will still be the case if the 125 GeV scalar is identified with the lightest Higgs boson h; in the alignment limit the charged Higgs boson decouples from the the SM-like neutral Higgs boson).

Figure 4.3 show the BR($H^+ \to hW$) and BR($H^+ \to tb$) as a function of the charged Higgs boson mass, where the sub-figures a)-d) show different values of $\sin(\beta - \alpha)$.

To conclude, the decay $H^+ \to hW$ is dominant for a non-aligned 2HDMs, while in the alignment limit this decay is unimportant. In the alignment limit, the decays $H^+ \to \tau\nu$ and $H^+ \to tb$ are dominant for a heavy Charged Higgs boson with $m(H^+) > m(h) + m(W)$. Nevertheless, for very large charged Higgs boson masses and large values of $\tan(\beta) > 1$, the decay into a h and W may have a significant branching ratio.

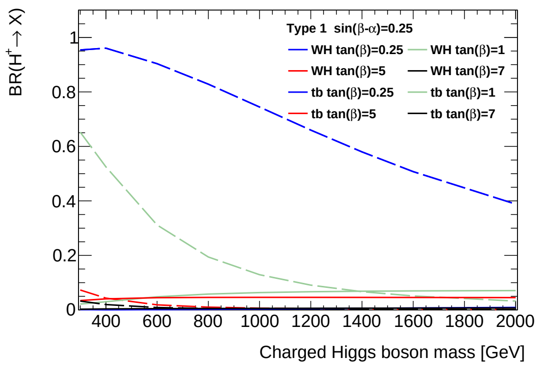

(a) Type 1

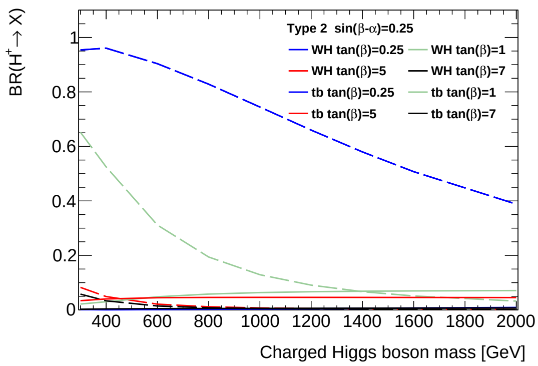

(b) Type 2

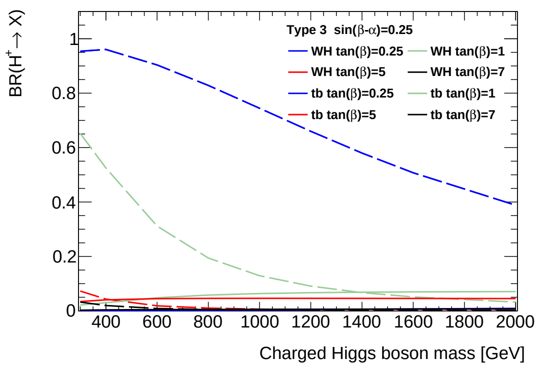

(c) Type 3

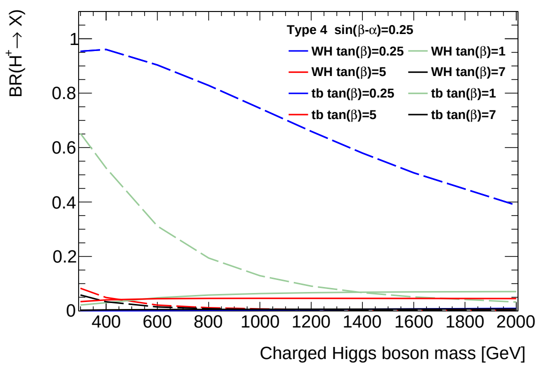

(d) Type 4

Figure 4.1.: Branching ratios for the Process $H^+ \to hW$ (solid line) and $H^+ \to tb$ (dashed line) as a function of the Charged Higgs boson mass presented for the 4 different types of the 2HDM and $\sin(\beta - \alpha) = 0.25$.

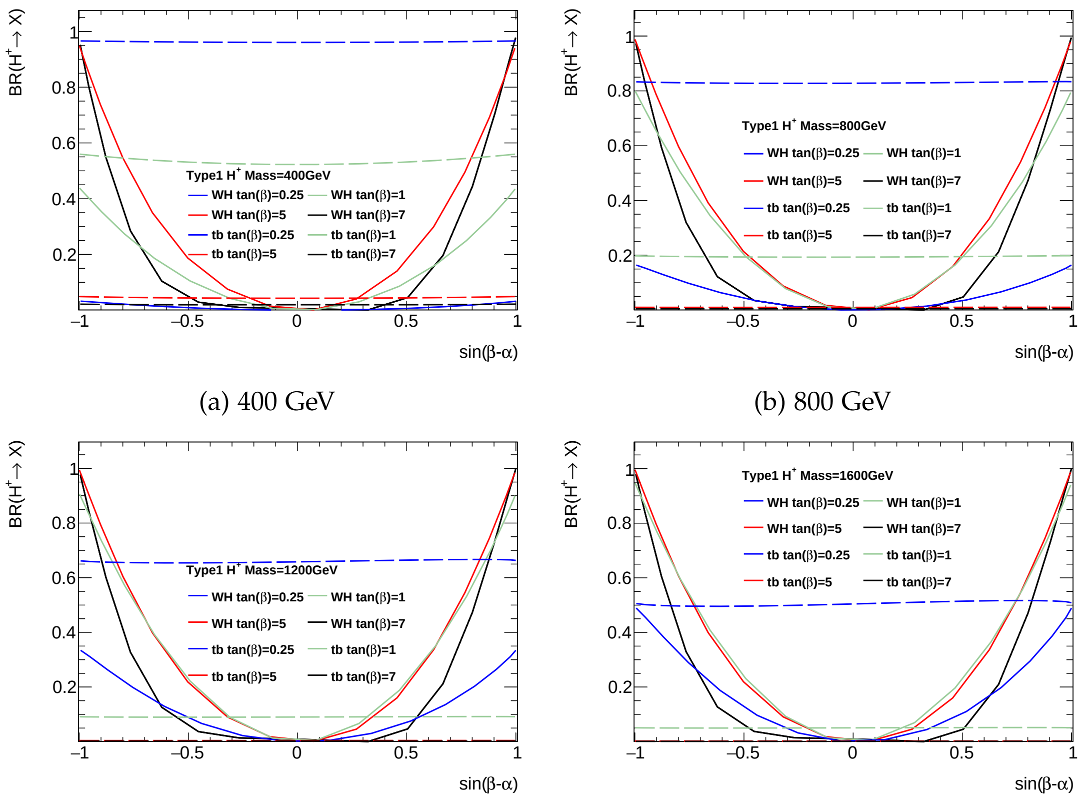

(a) 400 GeV

(b) 800 GeV

(c) 1200 GeV

(d) 1600 GeV

Figure 4.2.: Branching ratios for the Process $H^+ \to hW$ (solid line) and $H^+ \to tb$ (dashed line) as a function of the $\sin(\beta - \alpha)$ presented for different charged Higgs boson masses and $\tan(\beta)$.

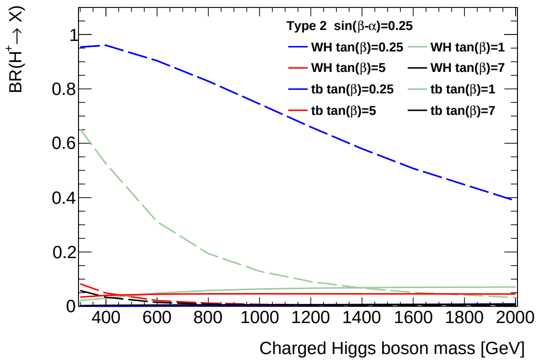

(a) $\sin(\beta - \alpha) = 0.25$

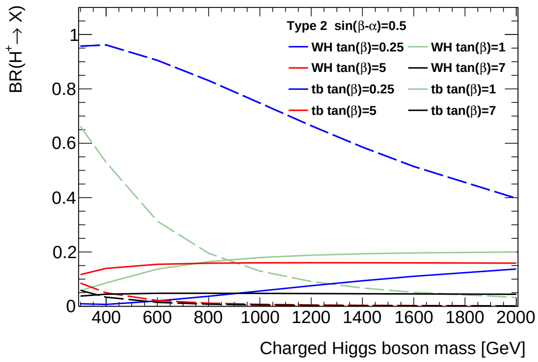

(b) $\sin(\beta - \alpha) = 0.5$

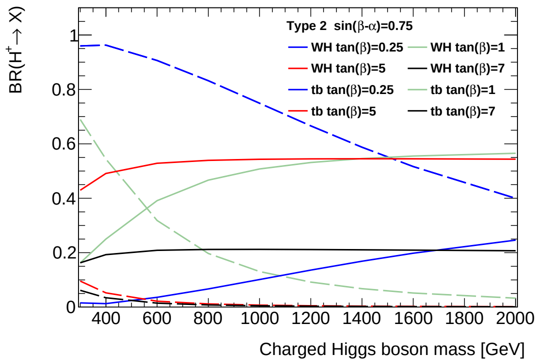

(c) $\sin(\beta - \alpha) = 0.75$

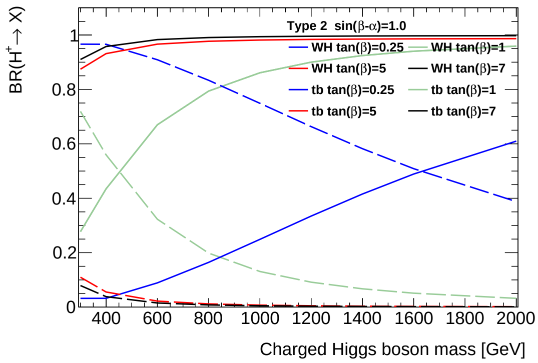

(d) $\sin(\beta - \alpha) = 1.0$

Figure 4.3.: Branching ratios for the Process $H^+ \to hW$ (solid line) and $H^+ \to tb$ (dashed line) as a function of the charged Higgs mass boson, presented for different values of $\sin(\beta - \alpha)$ in the 2HDM Type 2 model .

4.2. Branching Ratio Studies in the N2HDM

Branching ratios of the decay of a Charged Higgs boson into a W and h were calculated in a N2HDM using the program N2HDECAY[58]. The mass of the lightest CP-even Higgs boson was set to 125 GeV. The mixing angel α_3 was set to 0 as neither the coupling g_{H^+hW} of a charged Higgs boson to a W boson and Higgs boson nor the coupling of the charged Higgs boson to the fermions, depend on this parameter and thus the branching ratios should not depend on α_3 (see subsection 3.2.2). The singlet vev was set to $v_S = 246GeV$. The mass of the heavy CP-even Higgs bosons was set to $m(H_2) = 1.1 \cdot m(H^+)$ and $m(H_3) = 1.25 \cdot m(H^+)$. The mass of the pseudoscalar A was set to $m(A) = 1.25 \cdot m(H^+)$. Branching ratios have been calculated for charged Higgs boson masses between 205 GeV and 3565 GeV.

Figure 4.4- Figure 4.7 show the branching ratios as a function of α_1 and α_2. The different figures show the branching ratios for values of $\tan(\beta)$ between 1 and 40 and charged Higgs boson masses between 400-2000 GeV. The decay $H^+ \to Wh$ has a significant branching ratio over a large fraction of the parameter space. As in the 2HDM, the decay $H^+ \to Wh$ becomes more important for larger values of $\tan(\beta)$ and larger charged Higgs boson masses. For a H^+ mass of 400 GeV and $\tan(\beta) = 1$ (figure 4.4a) the branching ratios ranges up to 0.45. At a charged Higgs boson mass of 1600 GeV and $\tan(\beta) = 4$ (figure 4.6 c) the H^+ decays almost exclusively into a h and W. I.e. the branching ratio is ≈ 1 for almost the entire parameter space.

To conclude, in the N2HDM for large charged Higgs boson masses and large values of $\tan(\beta)$, $H^+ \to Wh$ is the dominant decay mode of a charged Higgs boson, for a large fraction of the parameter space. Even for light charged Higgs bosons and small values of $\tan(\beta)$, the decay $H^+ \to Wh$ acquires significant branching ratios in the N2HDM.

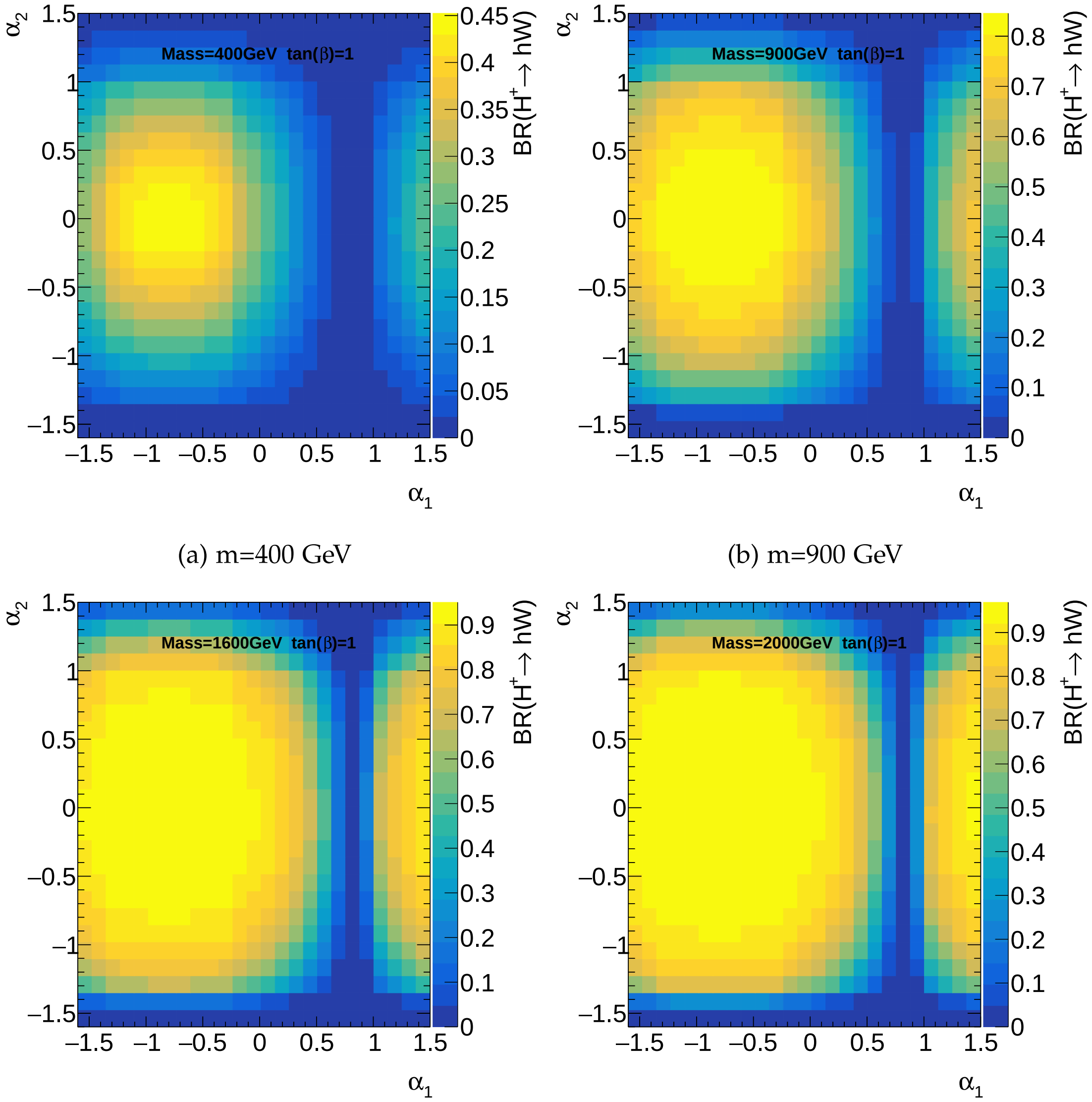

(a) m=400 GeV

(b) m=900 GeV

(c) m=1600 GeV

(d) m=2000 GeV

Figure 4.4.: Branching ratios for the Process $H^+ \to hW$ as a function of α_1 and α_2 at a $\tan(\beta) = 1$ presented for four different Charged Higgs boson masses: 400, 900, 1600 and 2000 GeV.

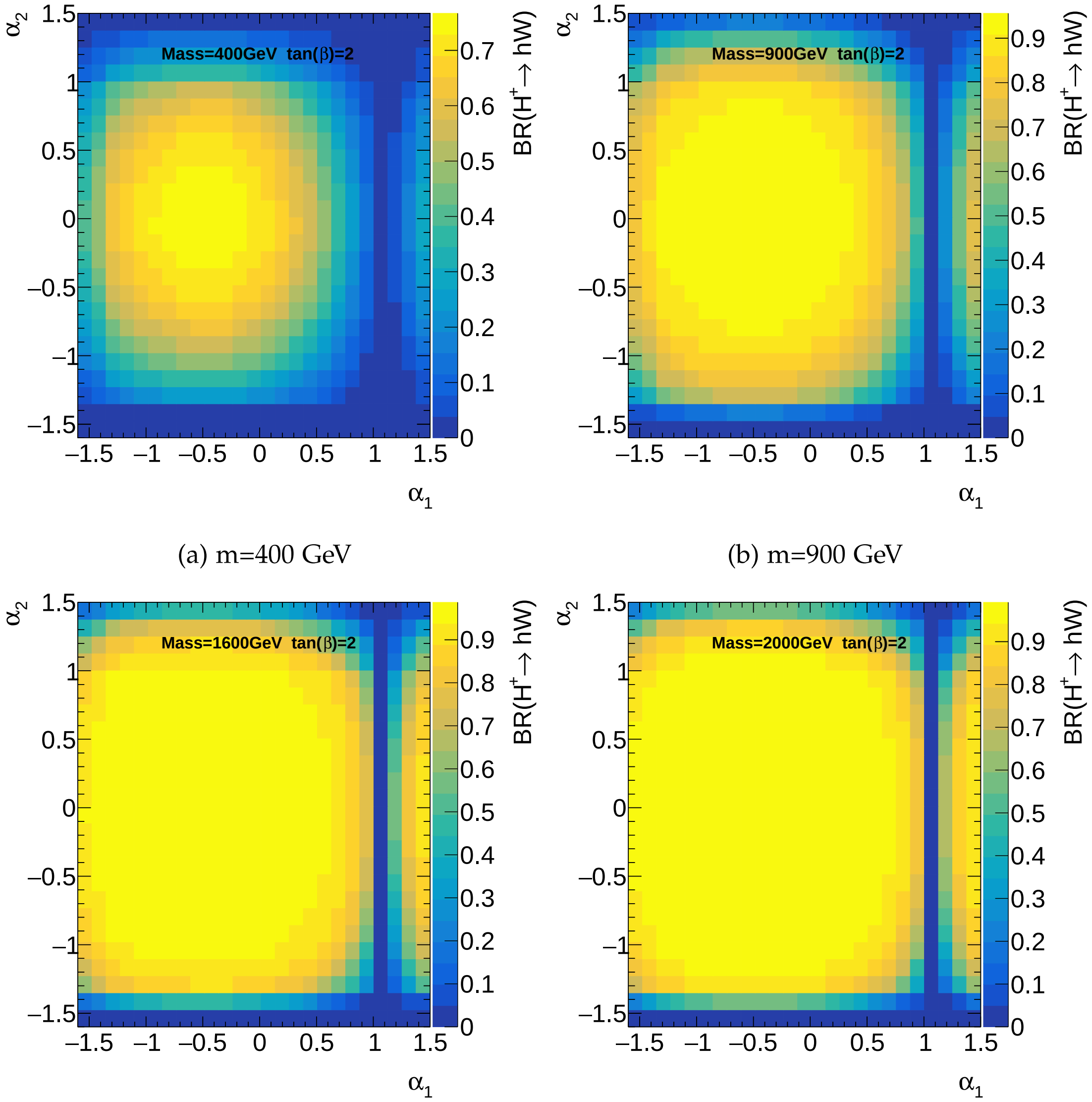

(a) m=400 GeV

(b) m=900 GeV

(c) m=1600 GeV

(d) m=2000 GeV

Figure 4.5.: Branching ratios for the Process $H^+ \to hW$ as a function of α_1 and α_2 at a $\tan(\beta) = 2$ presented for four different Charged Higgs boson masses: 400, 900, 1600 and 2000 GeV.

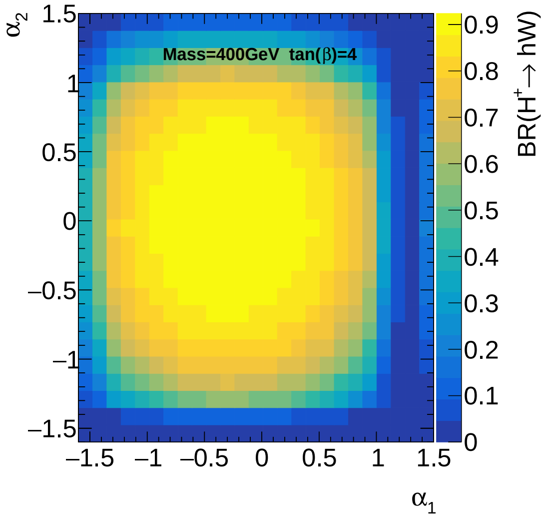

(a) m=400 GeV

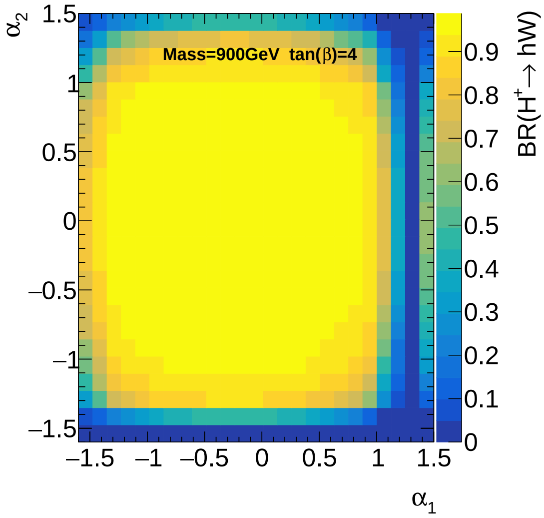

(b) m=900 GeV

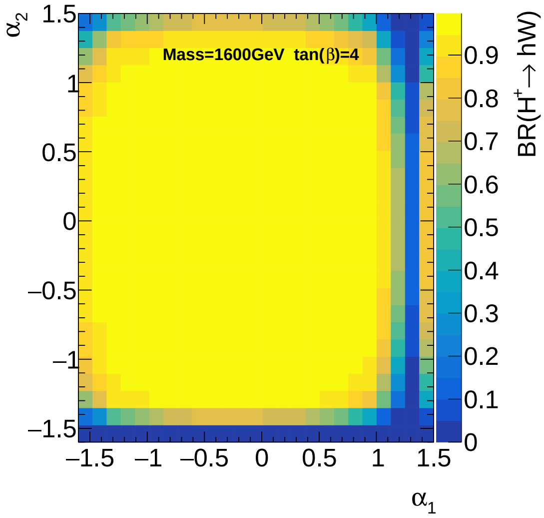

(c) m=1600 GeV

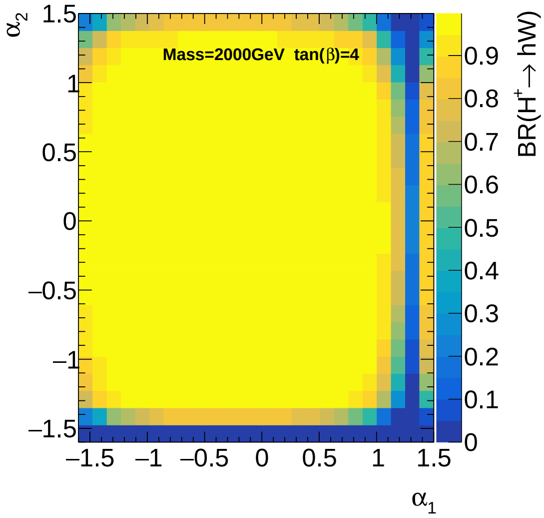

(d) m=2000 GeV

Figure 4.6.: Branching ratios for the Process $H^+ \to hW$ as a function of α_1 and α_2 at a $\tan(\beta) = 4$ presented for four different Charged Higgs boson masses: 400, 900, 1600 and 2000 GeV.

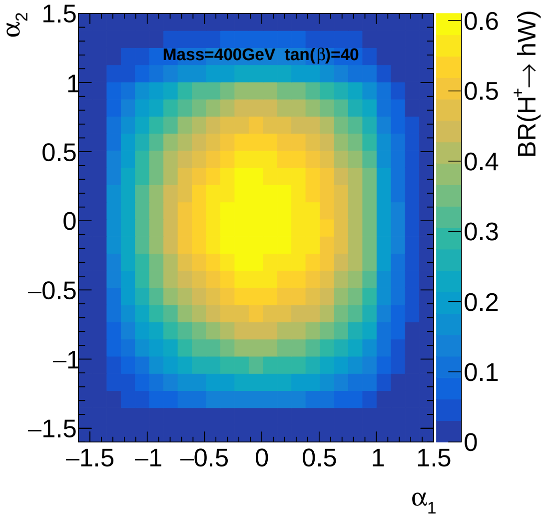

(a) m=400 GeV

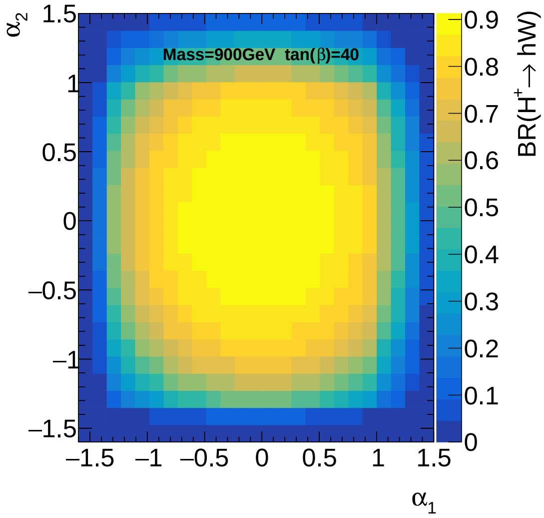

(b) m=900 GeV

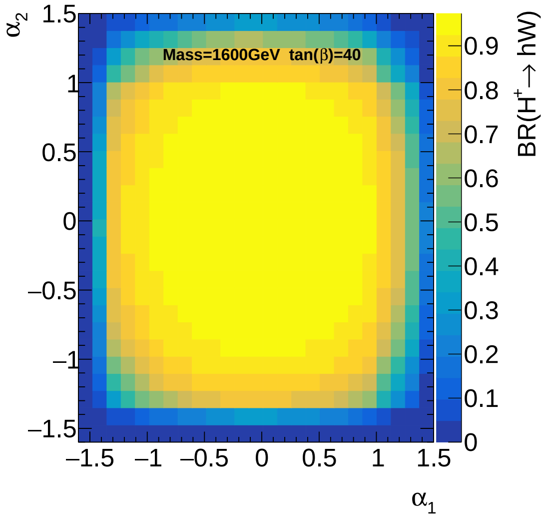

(c) m=1600 GeV

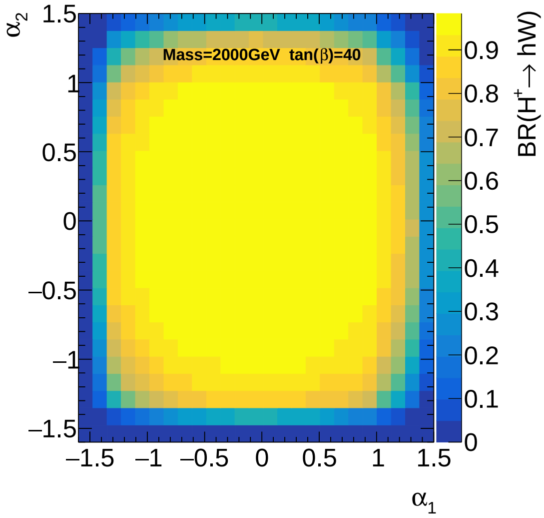

(d) m=2000 GeV

Figure 4.7.: Branching Ratios for the Process $H^+ \to hW$ as a function of α_1 and α_2 at a $\tan(\beta) = 40$ presented for four different Charged Higgs boson masses: 400, 900, 1600 and 2000 GeV.

4.3. Branching Ratio Studies in the Georgi-Machacek Model

Branching ratios and the decay width of a charged Higgs boson (H_3^+) in the Georgi-Machacek model have been calculated with the GMCALC [72] program. The branching ratios have been computed in the *H5Plane*-model [73]. The H5Plane-model is a benchmark scenario, in which the prediction of the GM-model is compatible with the observed phenomenology of the 125 GeV Higgs boson.

Figure 4.8 shows the BRs of the decay $H^+ \to Wh$ and $H^+ \to tb$ as a function of m(H^+). The sub-figures a)-e) depict the branching ratios for sin(Θ) values of 0.05, 0.1, 0.2 or 0.4. In figure 4.9, the branching ratios for the decay $H^+ \to Wh$ are presented as a function of sin(Θ), and for different H^+ masses between 439 GeV and 2010 GeV. The scanned range of sin(Θ) values varies with the charged Higgs boson mass. Not every combination of sin(Θ) and charged Higgs boson masses leads to a valid model prediction. The charged Higgs boson decay width normalized to its mass is depicted in figure 4.10 as a function of sin(Θ) and the mass.

The BR($H^+ \to Wh$) varies only slightly as a function of $\sin\Theta$. For high masses, the BR does barely depend on sin(Θ) and even for low masses the dependency is rather small. The main dependence of the BRs is on the charged Higgs boson mass. The BR($H^+ \to Wh$) increases with the charged Higgs bosons mass, while the branching ratio of the decay $H^+ \to tb$ decreases with increasing charged Higgs boson mass. For charged Higgs bosons heavier than $\approx 600GeV$, the decay $H^+ \to Wh$ becomes dominant over $H^+ \to tb$. For Charged Higgs bosons heavier than $\approx 1TeV$, the H^+ decays almost exclusively via the $H^+ \to Wh$ channel. The BRs are > 0.9 for every value of sin(Θ). But even for small charged Higgs boson masses the decay $H^+ \to Wh$ has sizable BRs. E.g at 429 GeV the H^+ has a BR of ≈ 0.26 for $\sin\Theta > 0.05$.

To conclude: In the Georgi-Machacek model, the decay $H^+ \to Wh$ is important for every charged Higgs boson mass. For charged Higgs bosons heavier than 600 GeV, the decay is the dominant one and a charged Higgs boson heavier than 1TeV decays almost exclusively into a SM-like like Higgs boson and a W boson.

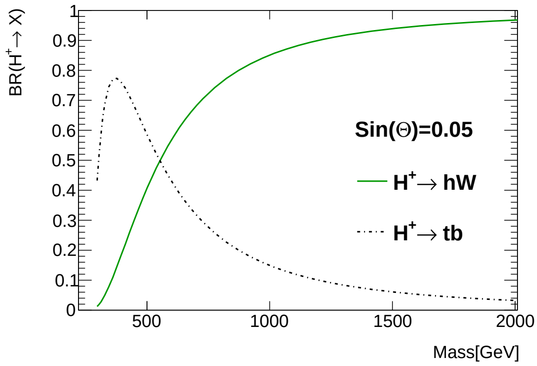

(a) $\sin\Theta = 0.05$

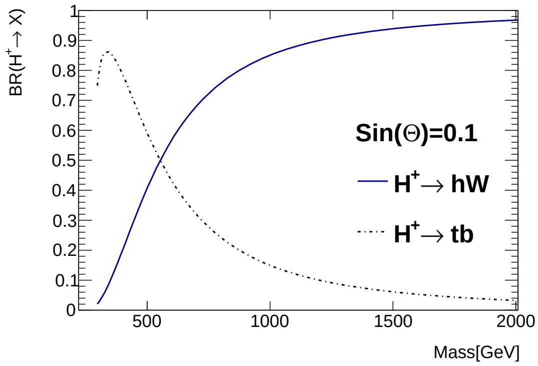

(b) $\sin\Theta = 0.1$

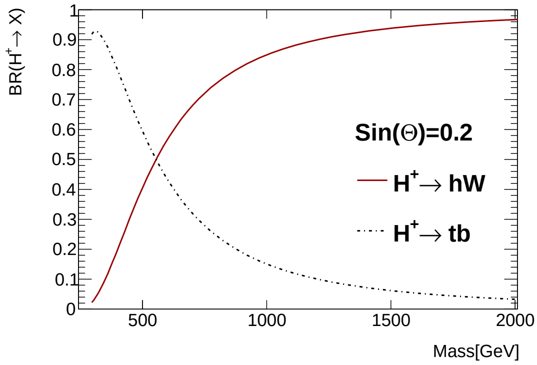

(c) $\sin\Theta = 0.2$

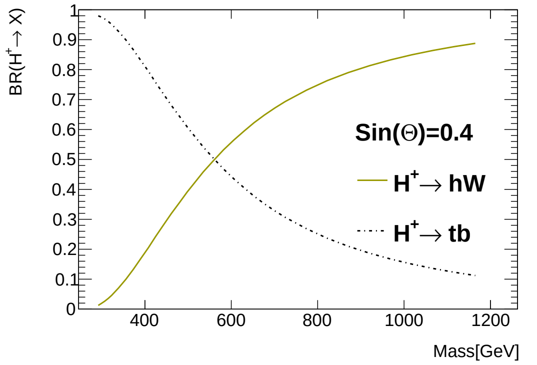

(d) $\sin\Theta = 0.4$

Figure 4.8.: Branching ratios for the decays $H^+ \to hW$ and $H^+ \to tb$ as a function of the Charged Higgs boson mass, presented for the Georgi-Machacek model for different values of $\sin\Theta$.

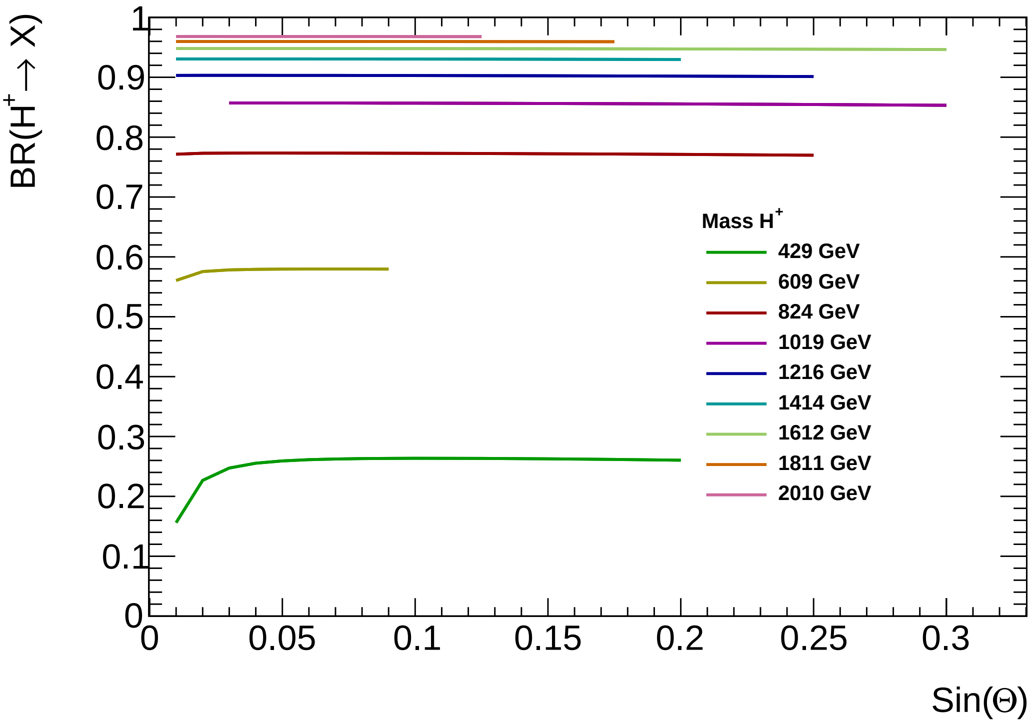

Figure 4.9.: Branching ratios for $H^+ \to hW$, in the Georgi-Machacek model as a function of $\sin\Theta$ for different Charged Higgs boson masses.

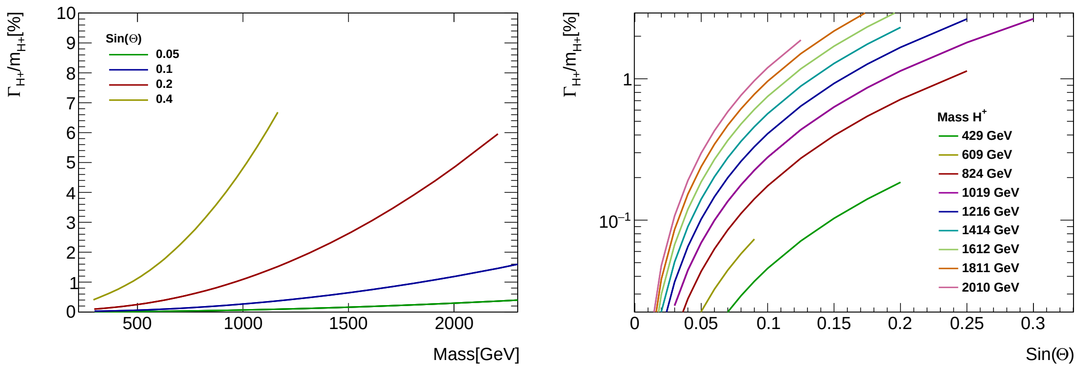

(a) (b)

Figure 4.10.: The Charged Higgs boson width normalized to its mass as a function of the Charged Higgs boson mass (a) and $\sin\Theta$ (b), in the Georgi-Machacek model.

5. Search for Charged Higgs Bosons in $H^+ \to W^+h \to l^+\nu b\bar{b}$ Decays

In this section, the search for a charged Higgs boson in the $H^+ \to Wh$ decay is discussed. First, the Monte Carlo samples and the data used in the analysis are described. The analysis will focus on the $H^+ \to Wh \to l\nu bb$ final state. A boosted decision tree is used to reconstruct the charged Higgs boson decay, which is discussed in detail in section 5.2. Section 5.3 and section 5.4 focus on the training and performance of the boosted decision tree. Events are further categorized by a cut based event selection. Its optimization is described in detail in section 5.5. Finally, data-to-simulation comparisons are presented in section 5.6. Furthermore, a data driven correction procedure, aiming to improve the background estimation, is introduced in section 5.6. The systematic uncertainties considered in the search for charged Higgs bosons are discussed in section 5.7. Finally, expected limits on the branching ratio times the cross-section are calculated in section 5.8.

5.1. The Data and the Monte Carlo Signal and Background Samples

The search for charged Higgs bosons in the $H^+ \to Wh$ decay channel is performed on proton-proton collision data recorded during the LHC Run 2 by the ATLAS detector at a center of mass energy of $\sqrt{s} = 13TeV$. The full Run 2 dataset recorded during 2015-2018 is used. Only data is used that has been recorded with all sub-detectors components being fully operational. The total integrated luminosity of this dataset is $139 \pm 2.4 fb^{-1}$ [74]. The evolution of the integrated luminosity, recorded by the ATLAS detector between 2015-2018 is depicted in figure 5.1.

The average number of interaction per bunch crossing often referred to as "pile-up" was $\langle\mu\rangle = 33.7$ during the Run 2 data taking. The mean number of interactions per bunch crossing is depicted in figure 5.1 for each year.

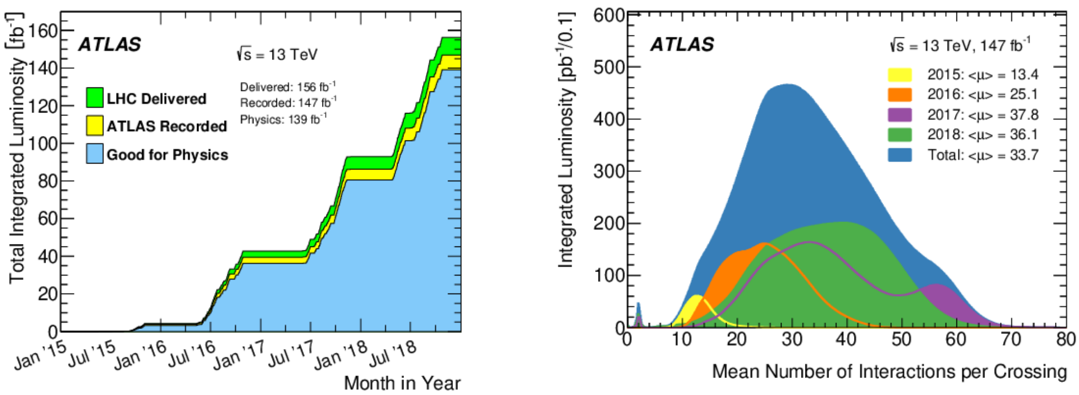

Figure 5.1.: a) The integrated luminosity measured by the ATLAS detector b) The average number of interactions per bunch crossing often referred to as "pile-up" observed by the ATLAS detector in each year [75].

Trigger strategy: Events are further selected by a high level trigger (HLT) system. A Missing Transverse Energy and a single lepton (i.e. a single electron or a single muon trigger) is used. The exact definition of the various triggers have been changed for some data taking periods. The different triggers used are summarized in table 5.1.

The name of the Missing Transverse Energy trigger describes the thresholds required for the trigger to fire. The "HLT_xe90_mht_L1XE50" trigger for example indicates a high level trigger that requires a E_T^{miss} ("xe") threshold of 90GeV, which is calculated by the "mht" algorithm [76] and is based on a L1 trigger with a 50 GeV threshold. The Missing Transverse Energy triggers used during the 2015 and 2016 runs are based on the "mht" algorithm. The E_T^{miss} is calculated as the negative transverse momentum sum from anti-k_T jets with a transverse momentum above 7 GeV. These jets are calibrated and corrected for pile-up effects.

During the 2015 Run, the E_T^{miss} threshold for the trigger was increased to 70 GeV. For the Run in 2016, the threshold was increased to 90 GeV and after the period D3 further increased to 110 GeV. The Missing Transverse Energy trigger used for the 2017 and 2018 Runs is based on the "pufit" algorithm [77]. The pufit algorithm calculates E_T^{miss} from topological clusters (see subsection 2.3.5). The topological clusters are grouped into $\eta \times \phi$ "patches", which have approximately the same size as a R=0.4 jet. The patches are corrected for pile-up contributions. Finally, the E_T^{miss} is calculated from the corrected patches. The E_T^{miss} threshold for the 2017 and 2018 Runs is 110 GeV.

As for the Missing Transverse Energy triggers, the name of the lepton triggers encode selection requirements on the lepton candidates. "HLT" denotes that it is a high-level trigger, followed by "e" for electron and "mu" for muon trigger, while the following number denotes the p_T requirement in GeV. Afterwards the working point of the likelihood-based identification requirement is defined ("lhtight", "lhmedium" or "lhloose" as described in subsection 2.3.2). Furthermore, requirements on the isolation variables ("ivarloose","iloose") are defined; "nod0" specifies that the transverse impact parameter d_0 is not used as a selection requirement.

During the 2015 Run, the electron p_T threshold ranges from 24-120 GeV depending on the identification working point. For the 2016-2018 Runs, the p_T threshold was increased to 27-300 GeV. Muons are required to have a p_T of at least 50 GeV. For the 2015 data, muons that pass the "loose" isolation requirements and have a p_T of at least 20 GeV were also considered. For the 2016, 2017 and 2018 data-taking periods, also muons satisfying the "medium" isolation requirement with a p_T over 26 GeV were used.

5.1.1. Monte Carlo Samples

Monte Carlo methods are used to model and estimate the signal and the dominant SM-background processes. Events are generated at a center of mass energy of $\sqrt{s} = 13TeV$. The response to the ATLAS detector is modeled in GEANT 4, using the full ATLAS simulation for the background samples and a fast simulation (ATLFAST) for the H^+ signal samples [78, 79]. To account for additional proton-proton collisions (pile-up) inelastic p-p interactions are modeled using PHYTIA 8 [80] and overlaid with the events in order to simulate the conditions during each data-taking period.

H^+ samples

Three samples of positively charged Higgs bosons produced in association with a top and bottom quark were simulated at masses of 400 GeV, 800 GeV and 1600 GeV. The 2HDMtypeII FeynRules model as well as the matrix element generator MadGraph5 v2.3.3 [81] in the 4-flavor scheme with the NNPDF2.3 NLO [82] parton distribution functions were used. The parton shower is modeled using PHYTIA 8.212 [80] in the A14 tune [83]. A Feynam diagram showing this H^+ production process is presented in figure 5.2.

Background samples

The different background processes considered and the generator used to produce them are listed in table 5.2. The column "Prediction order of σ_{prod}" states the perturbative accuracy in which the matrix element is calculated.

The dominant background stems from top quark pairs. The production of top quark pairs $t\bar{t}$, is modeled with the POWHEG Box 2 [84] generator, while the parton shower and hadronisation is modeled using PYHIA 8 [80] in the A14 tune [83]. The matrix element is calculated to the next-to-leading order in QCD using the NNPDF3.0 NLO [85] parton distribution function, with the hdamp [86] parameter set to 1.5 times the top mass, which was set to 172.5 GeV.

The single top quark production is modeled using the POWHEG Box 2 [84] generator to calculate the matrix element and PYTHIA 8 [80] in the A14 tune [83] to model the parton shower with the NNPDF3.0 NLO PDFs [85].

For the production of a Z boson or W boson in association with jets, SHERPA 2.2.1 [87] and the NNPDF3.0 NNLO PDFs [85] are used to calculate the matrix element at NLO accuracy in QCD for up to 2 additional parton emissions, and at LO accuracy for up to 4 parton emissions. For simulating the parton shower, SHERPA 2.2.1 [87] is used as well. The matrix elements are merged with the parton shower using the MEPS@NLO [88] formalism at a scale of $Q = 20GeV$ using the five-flavour numbering scheme.

The production of WW, ZZ and WZ boson pairs, decaying into the $llqq$, $l\nu qq$ as well as into the $\nu\nu qq$ final state, is simulated using SHERPA 2.2.1 [87] for the matrix element calculation and the parton shower and hadronisation. The NNPDF3.0 NLO PDFs [85] are used. Diagrams containing one additional emission are calculated to next-to-leading order in QCD, while diagrams containing up to 3 additional emissions are calculated at leading order in QCD.

Table 5.1.: Summery of the Trigger menus used during each data taking period.

2015 Run	2016 Run	2017 Run	2018 Run
MET trigger			
HLT_xe70	HLT_xe90_mht_L1XE50 HLT_xe110_mht_L1XE50	HLT_xe110_pufit_l1XE55	HLT_xe_pufit_xe70_L1XE50
Electron trigger			
HLT_e24_lhmedium_L1EM20VH HLT_e60_lhmedium Hlt_e120_lhloose	HLT_e26_lhtight_nod0_ivarloose HLT_e60_lhmedium_nod0 HLT_e140_lhloose_nod0 HLT_e300_ectut		
Muon trigger			
HLT_mu20_iloose_L1MU15 HLT_mu50	HLT_mu26_ivarmedium HLT_mu50		

Table 5.2.: Summary of the Monte Carlo generators used to produce the various background processes. The column "perturbative accuracy" gives the precision in QCD of the inclusive production cross-section σ_{prod} applied to the respective process. The order at which the corresponding matrix elements are calculated in the Monte Carlo is not necessarily the same as for the cross-section.

Process	Generator	Perturbative accuracy of σ_{prod}
	Vector boson + jets	
$W \to \ell\nu$	Sherpa2.2.1	NNLO
$Z \to \ell\ell$	Sherpa2.2.1	NNLO
	Top quark	
$t\bar{t}$	Poweheg+Pythia8	NNLO+NNLL
single top (s-channel)	Poweheg+Pythia8	NLO
single top (t-channel)	Poweheg+Pythia8	NLO
Wt-channel	Poweheg+Pythia8	NLO
$t\bar{t} + h$	MG5_aMC@NLO + Pythia8	NLO (QCD) and NLO (EW)
	Diboson	
$qg/q\bar{q} \to WW \to \ell\nu qq$	Sherpa2.2.1	NLO
$qg/q\bar{q} \to WZ \to \ell\ell qq$	Sherpa2.2.1	NLO
$qg/q\bar{q} \to WZ \to \nu\nu qq$	Sherpa2.2.1	NLO
$qg/q\bar{q} \to WZ \to \ell\nu q\bar{q}$	Sherpa2.2.1	NLO
$qg/q\bar{q} \to ZZ \to \ell\ell q\bar{q}$	Sherpa2.2.1	NLO
$qg/q\bar{q} \to ZZ \to \nu\nu q\bar{q}$	Sherpa2.2.1	NLO
$gg \to WW \to \ell\nu qq$	Sherpa2.2.2	NLO
$gg \to ZZ \to \ell\ell q\bar{q}$	Sherpa2.2.2	NLO
$gg \to ZZ \to \nu\nu q\bar{q}$	Sherpa2.2.2	NLO
$qg/q\bar{q} \to \ell\ell\nu\nu$	Sherpa2.2.2	NLO

5.2. Analysis Strategy

The dominant production mode of a heavy charged Higgs boson in the 2HDM [10] as well as in the GM-model [61] is in association with a top and a bottom quark. An exemplary Feynman diagram of the production process is given in figure 5.2. The Higgs boson decays dominantly into a pair of b quarks ($BR(h \to bb) \approx 58\%$). Thus, this final state will be studied in this thesis. The dominant decay mode of the W boson is either into a lepton and a neutrino (BR($W \to l\nu$)$\approx$ 30%) or into a pair of quarks (BR($W \to qq$)$\approx$ 70%). The former case will be considered here. So the decay $H^+ \to W^+h \to l\nu bb$ leads to a final state that contains multiple jets. Each of the b quarks of the Higgs boson decay will form a b-jet. Furthermore, both the top and the b quark that are produced in association with the H^+ will each lead to one additional b-jet. Moreover, the final state will contain one charged lepton and missing transverse energy (E_T^{miss}) from a neutrino.

A top quark will decay almost exclusively into a b quark and a W boson. This W boson could also decay leptonically, which would lead to a second charged lepton in the final state. Events with two charged leptons in the final state are not considered in this study, as the presence of two neutrinos would make it impossible to fully reconstruct the final state.

As only positively charged Higgs bosons are studied, the lepton produced in the charged Higgs decay chain will be positively charged, while a lepton produced in the $\bar{t}$ decay has a negative charge. Thus, the charge can be used to identify events with a leptonically decaying W^+ boson. And consequently to study the $H^+ \to l\nu bb$ final state only events with a positively charged lepton are considered.

The aim of this analysis is the reconstruction of the charged Higgs boson candidate and the use of its invariant mass (called m_{Wh} or m_{VH} in the following) as the discriminating variable against the background. A signal of the charged Higgs boson would manifest itself as a peak (bump) in the invariant mass spectrum. The H^+ will be reconstructed from a Higgs boson and the W boson. The W^+ is reconstructed via the charged lepton and the E_T^{miss}. The Higgs boson is reconstructed via two jets. As discussed above, the final state contains multiple jets, not only stemming from the Higgs boson decay, but also originating from the decays of the top quark and from the additional b-quark. To identity the jet pair originating from the charged Higgs boson decay, a boosted decision tree (BDT) is used. The BDT is a classifier, trained to identify the combination of jets and leptons originating from the charged Higgs boson decay. The BDT takes the reconstructed W boson and 2 jets as input and it outputs a value between -1 and

+1, which is called the BDT response. Values close to +1 correspond to an event being classified as signal i.e stemming from the decay of the charged Higgs boson, while BDT responses around -1 correspond to an event being classified as background. The BDT used is described in detail in section 5.3.

The response of the BDT is evaluated for very permutation of any two jet pair and the W boson in the event. The combination with the highest BDT score (called "max MVA Response" or w_{BDT}^{max} in the following) is used to reconstruct the charged Higgs boson. The Higgs boson will be reconstructed via the 2 jets chosen by the BDT in that way.

Each event will be categorized by the number of b-tagged jets. The categories are:

- 2 b-tagged jets
- 3 b-tagged jets
- 4 or more b-tagged jets

To enhance the signal over the background, which is mostly stemming from $t\bar{t}$ events, further event selection requirements are applied. These additional requirements are based on cuts on different kinematic variables. The optimization of the event selection is described in detail in section 5.5.

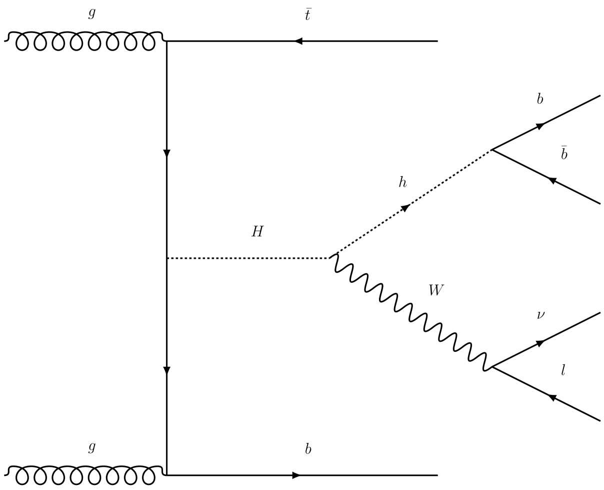

Figure 5.2.: A representative Feynman diagram of the production of a charged Higgs boson H^+ in association with a top and a bottom quark, and the subsequent decay of the charged Higgs boson into a W and the SM Higgs boson h, decaying into $l\nu$ and $b\bar{b}$, respectively.

5.3. BDT Training

A *Decision tree* is a classifier with a binary tree structure, aiming to classify an event as signal or background. At every node, a binary decision is made (e.g is $p_T > 100 GeV$ true or false ?) until an end node, the so-called *leaf*, is reached. A diagram illustrating such a structure is given in figure 5.3. At each node the selection requirement that gives the best separation between the signal and background is chosen.

The performance of the BDT as well as its stability with respect to statistical fluctuations are enhanced by introducing the concept of *boosting*. The idea of boosting is to combine multiple *weak learner*, in this case individual decision trees, into a single *strong learners*, i.e. an ensemble of trees, called a *forest*, is used instead of a single tree. The weighted outputs of all the trees are combined into a single output variable. The response of the boosted decision tree $F(x)$ can be written as:

$$F(x|P) = \sum_{m=0}^{M} \beta_m f(x, a_m); \quad P \in \{\beta_m \alpha_m\}_0^M, \tag{5.1}$$

where $f(x, a_m)$ are the response of the individual classifiers. During the boosting, the parameter P is adjusted such that the deviation of the response of the boosted decision trees to the true value y is minimized. The deviation between the true value and model response is defined by the *loss-function* $L(F, y)$. The *GradientBoost* boosting algorithm used in this thesis, uses the binomial log-likelihood as the loss function

$$L(F, y) = \ln(1 + e^{-2F(x)y}). \tag{5.2}$$

However, a boosting algorithm that minimizes this loss function cannot be obtained in a simple way. Thus, a *steepest-descent* approach is used to minimize the loss-function. The current gradient of the loss-function is calculated and afterwards a tree is built and the parameters P are adjusted to match the mean gradient. By iteratively repeating this procedure, the loss-function is minimized.

The Boosted Decision Trees provided by the toolkit for multivariate data analyses (TMVA)[89] are used.

For the BDT training, events with positive lepton charge (as the W^+ decays leptonically) and at least 4 jets are used. The signal is defined as the correct combination of final state particles stemming from the Higgs boson and the W boson decay, which will result in the correctly reconstructed charged Higgs boson. The background is defined as all wrong combination of final state particles. This is just a combinatorial background rather than a physical (stemming from SM-processes) background. The correct combination of final state particles is determined by a ΔR-based matching between generator level particles and all the reconstructed objects. The jet-jet-W combination with the smallest angular separation is chosen. In addition, the angular distance between the Higgs boson candidate (defined as the dijet pair) and the generator level Higgs boson is required to be smaller than 0.3. Furthermore, the ΔR between the W boson (reconstructed from the charged lepton and E_T^{miss}) and the generator level W boson has to be smaller than 0.3. If a jet-jet-W boson combination does not fulfill those ΔR requirements or is not the one with the smallest distance to the generator level particles, it is defined as background.

In the training, 600 trees are used and each tree has a maximum depth of 5 nodes. The boosting algorithm GradientBoost [89] is used. The separation measure is the Gini-Index[89] [1]. The learning rate is set to 0.1. And the N^{cuts} variable, i.e. the number of points in a variable range considered to find the optimal cut, is set to 40. The parameters used in the BDT training are listed in table 5.3

Table 5.3.: Hyperparameters used in the boosted decision tree training.

Parameter	Value
Separation type	Gini-Index
Learning rate	0.1
Boosting type	Gradiant
N^{Trees}	600
MinNodeSize	2%
Depth	5
N^{cuts}	40

The boosted decision trees were trained on the following features:

- invariant mass of the Higgs boson candidate (sum of two jets)
- Pseudo continuous b-tagging score of the first jet
- Pseudo continuous b-tagging score of the second jet
- $\Delta\Phi$ between the Higgs boson and the W boson candidates

[1] The separation is defined as p(1-p), with $p = n_S/(n_S + n_B)$

- p_T^{Higgs}/m_{Wh}
- p_T^W/m_{Wh}

The m_{Wh} is the invariant mass of the four-vector sum of h and W, and hence the charged Higgs boson mass. The used features are designed to be as independent as possible of the charged Higgs boson mass. Thus, the kinematic variables p_T^{Higgs} and p_T^W are normalized to the charged Higgs boson mass. Pseudo continuous (PC) b-tagging is used. A certain interval in the b-tagging score is assigned to an integer value between 0 and 4 i.e. the pseudo continuous b-tagging score. In table 5.4, the definition of the pseudo continuous b-tags are listed. Furthermore, the corresponding b-tagging efficiency (interval) is listed. The use of PC-b-tagging gives more information than a binary b-tagging selection requirement. Moreover, a BDT trained in this fashion is independent of the b-tagging working point used in the later analysis. This allows to perform studies at different working points without the need to retrain the BDT.

The boosted decision tree was trained on the sum of all three signal mass points (i.e 400 GeV, 800 GeV and 1600 GeV). This gives 194754 signal events of which 97377 are used for training and 97377 for testing as well as 4469820 background events. Again, one half of those, i.e. 2234910 events, are used for training and the other half for testing. The distributions of the variables used for training are shown in figure 5.4 separated into signal and background. The curves for the signal (blue) and the background (red) are distinct from each other, so the chosen variables allow to distinguish between signal and background, which constitutes good features to train the BDT. Figure 5.5 shows the response of the trained BDT. The response to the background is low (values around -1) and high for the signal (values around +1).

The importance of the different variables used by the BDT are listed in table 5.5. The importance is determined by counting how often a variable is used to split the tree and weighting this number by the separation gain[2] squared and by the number of events, in this node. The reconstructed Higgs boson mass (i.e the di-jet mass) is ranked the highest, however all the variables are of similar importance.

[2]the separation gain is defined as: gain(parent cell)-gain(daughter cell 1)-gain(daughter cell 2)

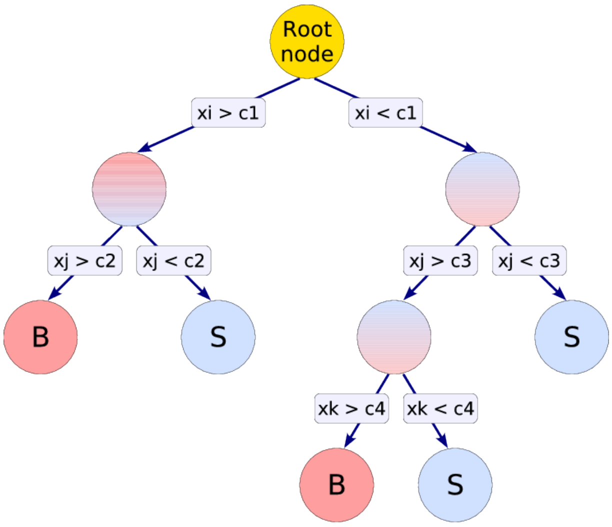

Figure 5.3.: Illustration of a decision tree. At each node, the tree is split by a simple yes/no question until a leaf is reached and the event is categorized into signal or background [89].

Table 5.4.: Definition of the pseudo continuous b-tagging categories used in the BDT training.

Pseudo-Continuous b-Tag	b-tagging score	b-tagging efficiency
0	0-0.11	100%-85%
1	0.11-0.64	85%-77%
2	0.64-0.83	77%-70%
3	0.83-0.94	70%-60%
4	0.94-1	60%

Table 5.5.: The variables used by the boosted decision tree ranked by their importance.

Variable name	Variable importance
Higgs boson mass	0.216
p_T^h / m_{Wh}	0.200
$\Delta\Phi(h, W)$	0.183
p_T^W / m_{Wh}	0.175
PC b-tag first jet	0.123
PC b-tag second jet	0.105

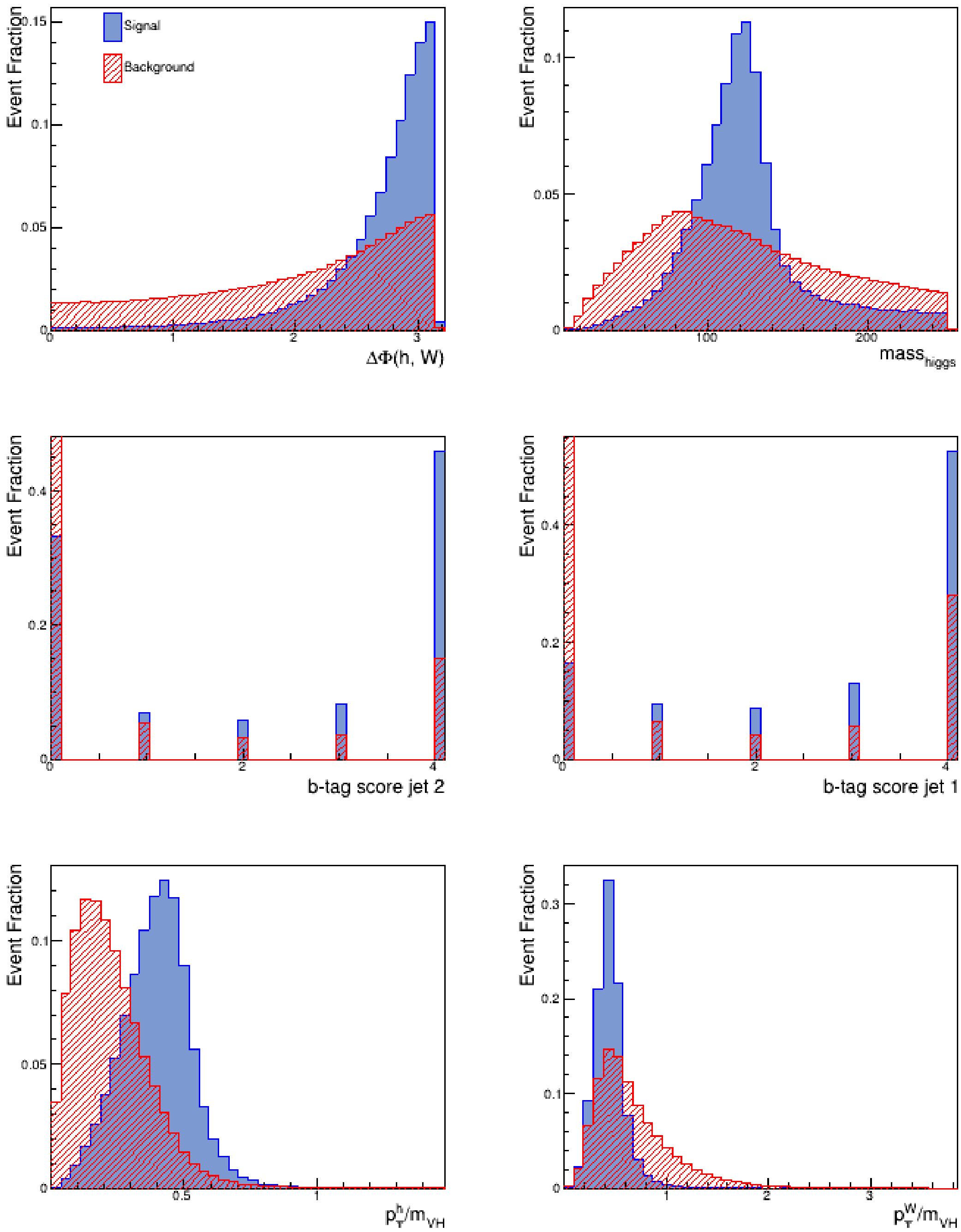

Figure 5.4.: Distribution of the variables used in the BDT training for the signal (blue) and background (red). The signal and background distributions are well separated for each variable.

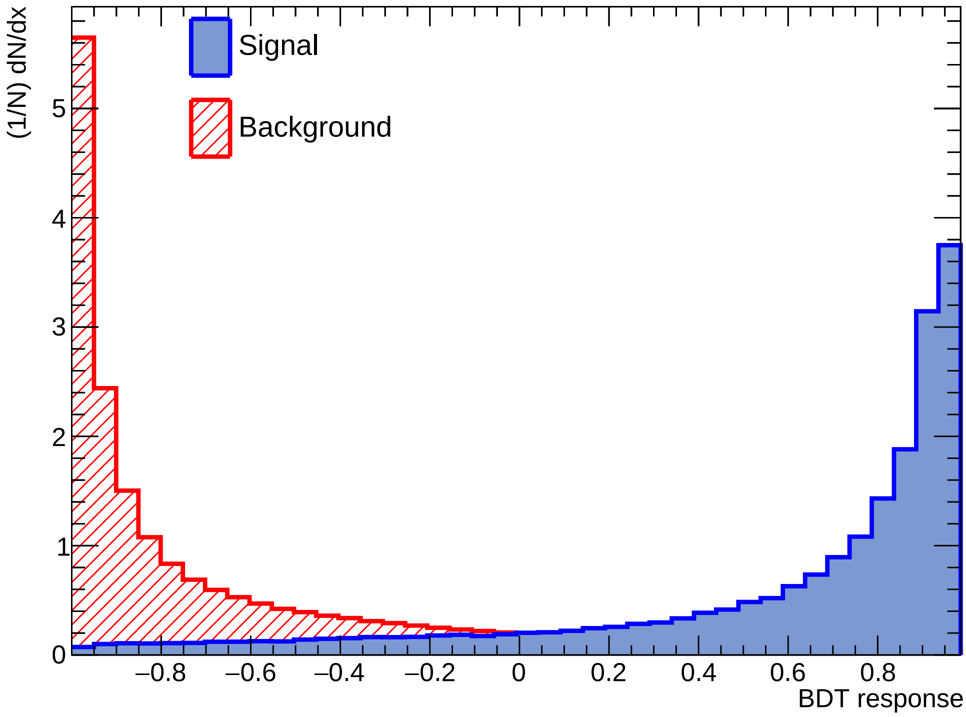

Figure 5.5.: The response of the BDT to the testing sample, separated into the response to the signal sample (blue), consisting of the correct jet-jet-lepton-MET combination stemming from the H^+ decay, as well as to the background sample (red), consisting of all the remaining jet-jet-lepton-MET combinations in the tbH^+ event.

5.4. Test of the BDT Performance

The reconstructed mass of the charged Higgs boson is presented in figure 5.6. The distributions are shown for the signal and background in each b-tagging category. The background is split into contributions stemming from top quarks and the sum of all other backgrounds. For the signal, the distributions of m_{Wh} is centered around the respective H^+ mass pole. The m_{Wh} distribution of the background peaks around 350 GeV.

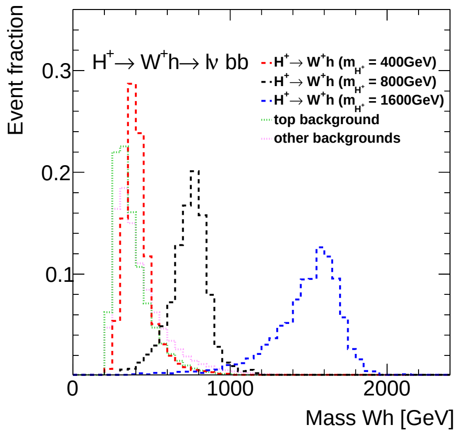

(a) 2 b-tags

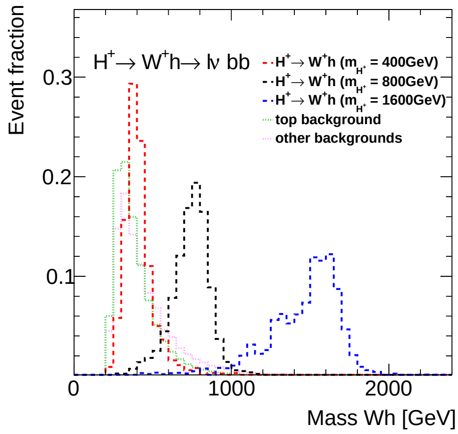

(b) 3 b-tags

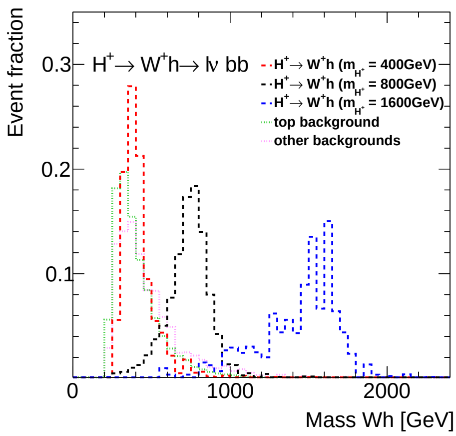

(c) 4+ b-tags

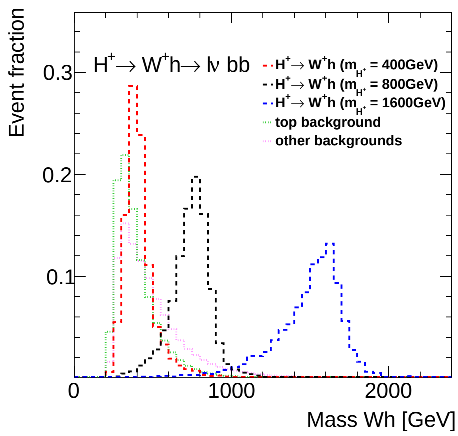

(d) Incl.

Figure 5.6.: Distributions of the reconstructed mass of the charged Higgs boson, in each of the b-tagging categories.

5.4.1. Matching Efficiency

To evaluate the performance of the BDT, the *matching efficiency* between the reconstructed charged Higgs boson and the generator level charged Higgs boson is calculated. The matching efficiency is determined by calculating the angular separation between the 4-vector of the generator level charged Higgs boson and the 4-vector of the reconstructed charged Higgs boson. If the angular separation is smaller than a given ΔR, the two objects are considered to be matched. The matching efficiency is the fraction of reconstructed charged Higgs bosons that are matched to the generator level H^+. The matching efficiency is calculated for different values of ΔR. Figure 5.7-Figure 5.8 shows the matching efficiency for ΔR requirements of 0.2, 0.3, 0.4, 0.5 and 0.6, as a function of the BDT response of the chosen jet-jet-lepton-E_T^{miss} combination (called Max MVA Response in the figures).

The matching efficiency is higher the heavier the charged Higgs boson is and rises with increasing values of the maximum BDT response. The matching efficiency decreases for tighter matching requirements. For a H^+ of mass 1600 GeV, about 95% of the reconstructed charged Higgs bosons can be matched to the generator level particles within a ΔR of 0.6, for a max BDT response above 0.9. In the BDT response inclusive region, where no selection requirement is placed on the maximal BDT response, the matching efficiency drops to about 85%. For a charged Higgs boson with a mass of 400 GeV, the matching efficiencies drop to around 61% (for a max BDT response greater than 0.9) and about 46% (when no requirements are placed on the max BDT response value). The matching efficiencies of the 800 GeV mass point lie between those of the former mass points. At max BDT response values of at least 0.9, the matching efficiency is around 89% and in the BDT response inclusive region the matching efficiency is still around 77%.

For a tight matching requirement of an angular separation of at least $\Delta R = 0.2$, the matching efficiency decreases. For example at $m_{H^+} = 1600$ GeV it is around 76% for events with a BDT response of at least 0.9 and approximately 65% in the BDT response inclusive region. For $m_{H^+} = 400$ GeV the matching efficiencies drop to about 23% and about 15%, respectively.

In conclusion, the BDT-based event reconstruction technique performs very well for the 800 GeV and 1600 GeV mass points. The performance of the 400 GeV mass point is sufficient.

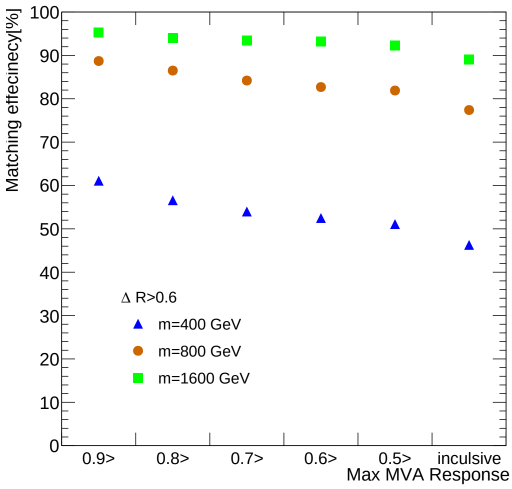

(a) $\Delta R < 0.6$

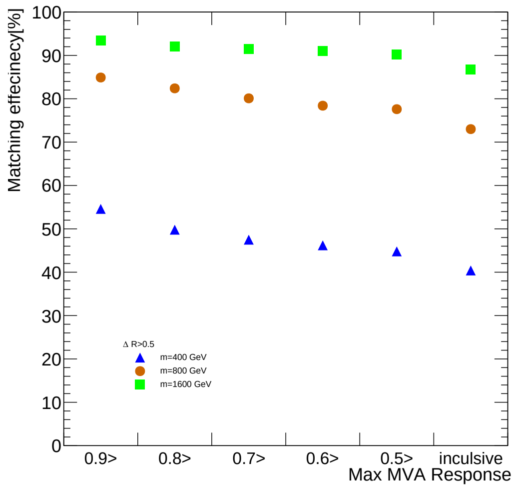

(b) $\Delta R < 0.5$

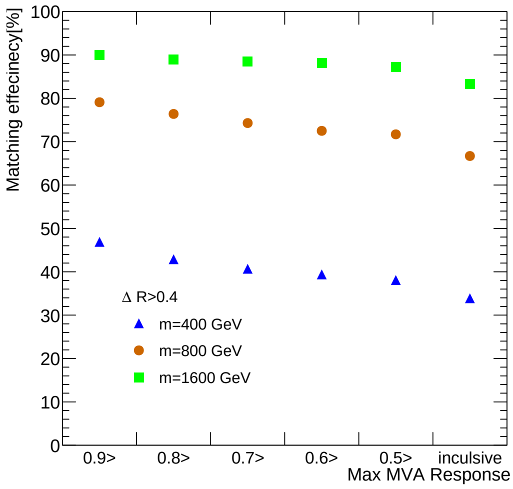

(c) $\Delta R < 0.4$

Figure 5.7.: The *matching efficiency*, i.e. the fraction of reconstructed charged Higgs boson events that can be matched to the generator level particles within a given ΔR shown as a function of the maximal BDT response.

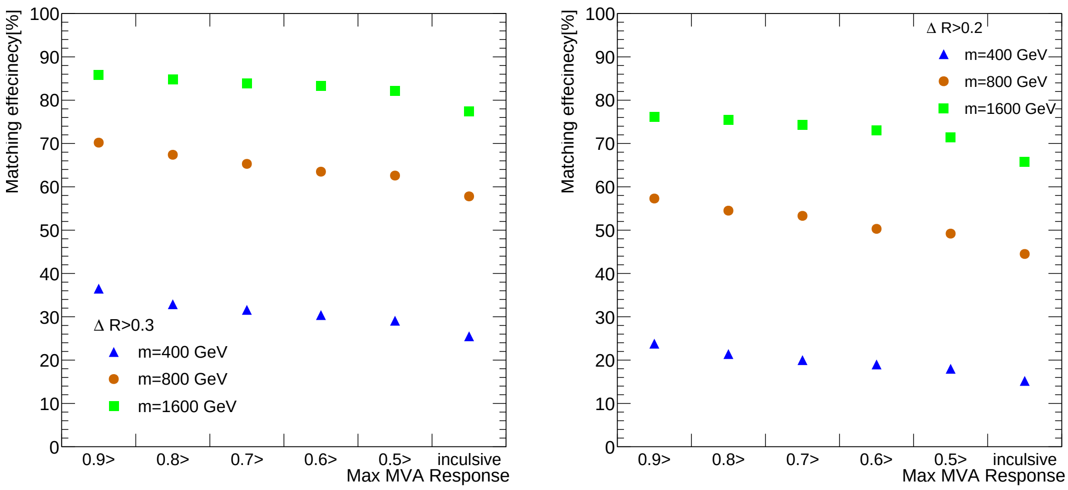

(a) $\Delta R < 0.3$

(b) $\Delta R < 0.2$

Figure 5.8.: The *matching efficiency*, i.e. the fraction of reconstructed charged Higgs boson events that can be matched to the generator level particles within a given ΔR shown as a function of the maximal BDT response.

5.4.2. Mass Resolution Studies

In order to estimate the mass resolution corresponding to the reconstruction procedure, the difference between the reconstructed charged Higgs boson mass (m_{Wh}^{recon}) and the generator level charged Higgs boson mass (m_{Wh}^{truth}) normalized to the generator level charged Higgs boson mass

$$\frac{m_{Wh}^{recon} - m_{Wh}^{truth}}{m_{Wh}^{truth}} \tag{5.3}$$

is computed. A Bukin function [90], i.e a convolution of a Gaussian and exponential functions, is fitted to the resulting distributions. The Bukin function has been chosen as it is able to fit asymmetric distributions. The σ_p parameter of the Bukin function, corresponding to the FWHM/2.35, is taken as the mass resolution. This has been done for each mass point (400 GeV, 800GeV, 1600 GeV) and separately in each b-tagging category (2Tags, 3-Tags 4+Tags). The distributions of $(m_{Wh}^{recon} - m_{Wh}^{truth})/m_{Wh}^{truth}$ with the fitted Bukin function are shown in figure 5.9-figure 5.11. The obtained values of the mass resolutions are summarized in table 5.6 with the mass resolution ranging between 10% and 17%. The mass resolution is better for higher charged Higgs boson masses. To check that the mass-resolution obtained via this method does not depend on the chosen fit-function these studies have been repeated with a Gaussian fit. The fitted Gaussian functions are depicted in subsection A.1.1. Furthermore, the mass resolution has been computed just from the Full-Width-Half-Maximum (FWHM) of the histograms without any fits being applied. In the latter case, the mass resolution is calculated as FWHM/2.35. The mass resolutions obtained in these different ways are summarized in table 5.7. The values calculated via the different methods are consistent with each other. The mass resolution obtained with the fit of the Bukin function is in general a bit smaller than the values from the Gaussian fit. The values obtained from the FWHM deviate the most from the others. The possible values of the FWHM are limited by the choice of the binning. The chosen binning for the FWHM calculation is the same as the binning in figure 5.11.

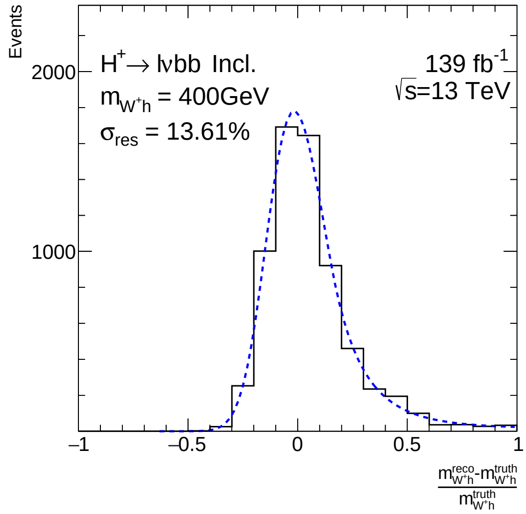

(a) $N^{\text{b-tags}} \geq 2$

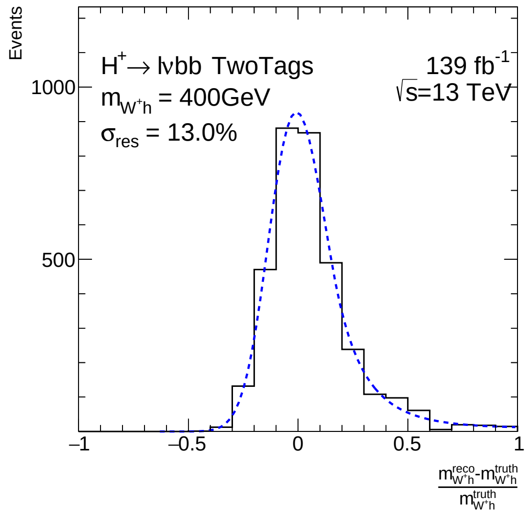

(b) $N^{\text{b-tags}} = 2$

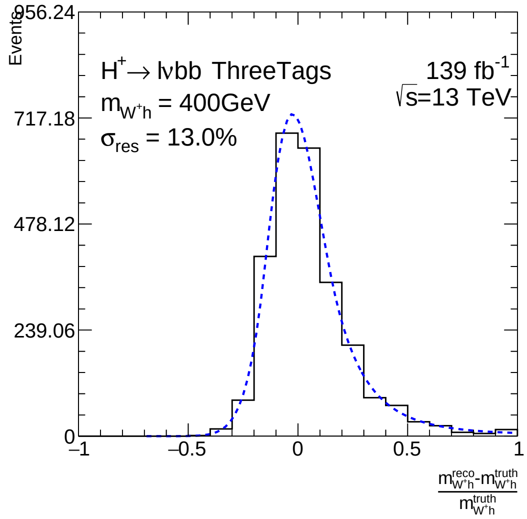

(c) $N^{\text{b-tags}} = 3$

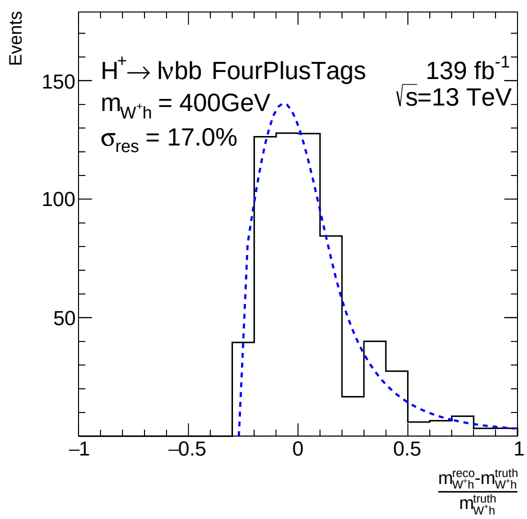

(d) $N^{\text{b-tags}} \geq 4$

Figure 5.9.: The *mass resolution*, $m_{Wh}^{recon} - m_{Wh}^{truth} / m_{Wh}^{truth}$ for the 400 GeV mass point. A Bukin function is fitted to the histograms.

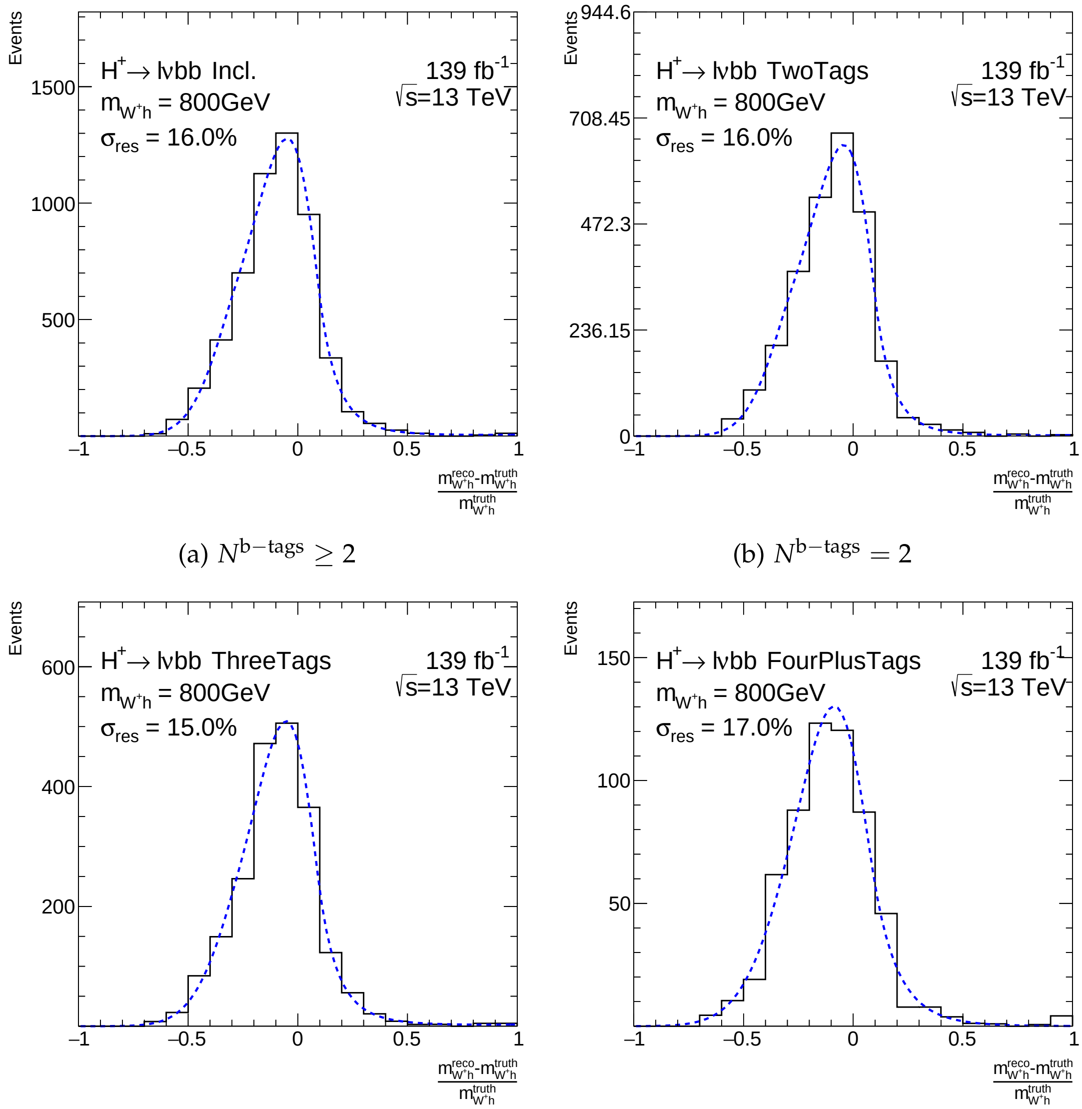

(a) $N^{\text{b-tags}} \geq 2$

(b) $N^{\text{b-tags}} = 2$

(c) $N^{\text{b-tags}} = 3$

(d) $N^{\text{b-tags}} \geq 4$

Figure 5.10.: The *mass resolution*, $m^{recon}_{Wh} - m^{truth}_{Wh} / m^{truth}_{Wh}$ for the 800 GeV mass point. A Bukin function is fitted to the histograms.

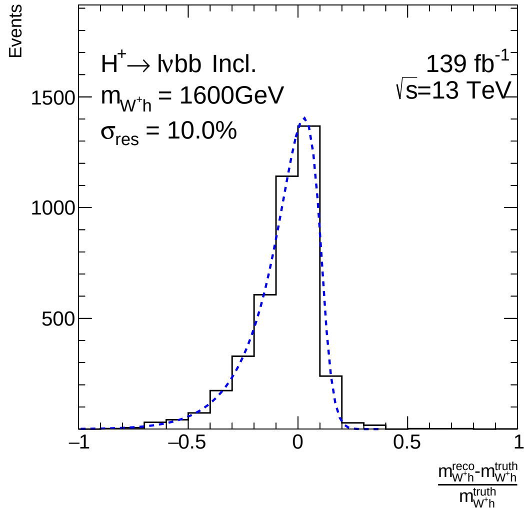

(a) $N^{\mathrm{b-tags}} \geq 2$

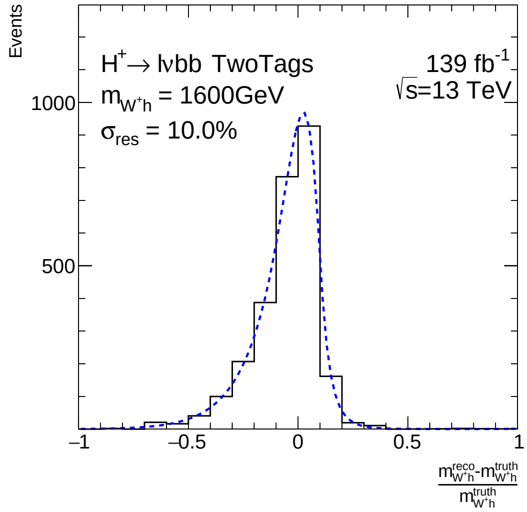

(b) $N^{\mathrm{b-tags}} = 2$

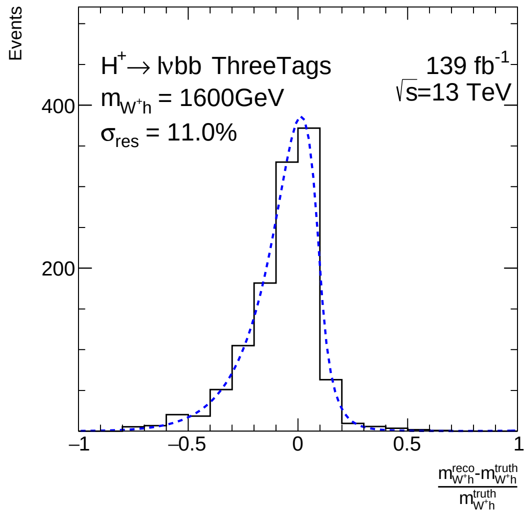

(c) $N^{\mathrm{b-tags}} = 3$

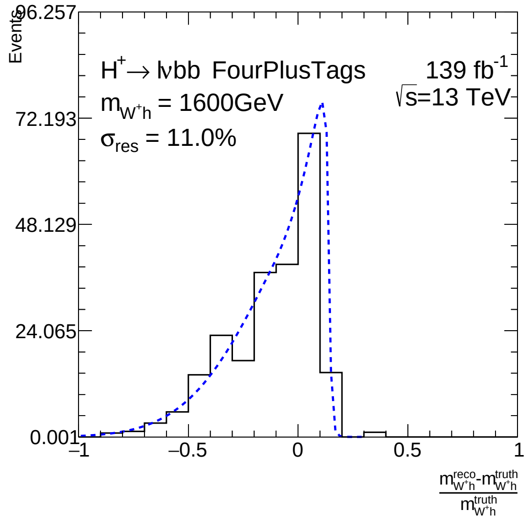

(d) $N^{\mathrm{b-tags}} \geq 4$

Figure 5.11.: The *mass resolution*, $m_{Wh}^{recon} - m_{Wh}^{truth} / m_{Wh}^{truth}$ for the 1600 GeV mass point. A Bukin function is fitted to the histograms.

The knowledge of mass resolution can be used to optimize the binning of the m_{Wh} distribution used as input for the limit setting procedure. The bin width should approximately equal the respective mass resolution. A possible m_{Wh} binning between 200 GeV and 2000 GeV would be:

$$[200, 260, 338, 437, 562, 717, 907, 1135, 1401, 1702, 2030]\,, \tag{5.4}$$

where each number denotes the lower edge of the bin in GeV. Each bin has a width of 2 times the mass resolution. The expected mass resolution between the studied mass points is obtained by a straight line fit. For this purpose the mass resolution was averaged over the b-tag categories for each mass point.

Table 5.6.: The mass resolution in each b-tagging category for H^+ masses of 400 GeV, 800 GeV and 1600 GeV.

	Two b-tags	Three b-tags	Four+ b-tags
400 GeV	13%	13%	17%
800 GeV	16%	15%	17%
1600 GeV	10%	11%	12%

Table 5.7.: Comparison of the mass resolutions.

	Bukin fit	Gaussain fit	FWHM
400 GeV 2 b-tags	13%	14%	13%
400 GeV 3 b-tags	13%	14%	13%
400 GeV 4+ b-tags	17%	16%	13%
800 GeV 2 b-tags	16%	16%	34%
800 GeV 3 b-tags	15%	16%	17%
800 GeV 4+ b-tags	17%	18%	13%
1600 GeV 2 b-tags	10%	10%	5%
1600 GeV 3 b-tags	11%	11%	10%
1600 GeV 4+ b-tags	12%	15%	10%

5.5. Event Selection and Optimization

In addition to the event reconstruction, further event selection requirements are applied, which aim for a maximum enhancement of the signal over the background, and hence increase the sensitivity of this analysis. A simple cut-based approach is chosen. In the following, the procedure of developing and optimizing the signal and control regions is described.

5.5.1. Definition of the Signal Region

The shapes of the distribution of different kinematic variables are compared between the signal processes and the most dominant backgrounds. This allows the identification of variables, with significant separation between the signal and background processes. Thus, a cut on such variables allows to enhance the signal over the background.

The background processes are split into two components. The first component contains backgrounds stemming from top quarks and the second component contains all other backgrounds. A variety of different kinematic variables was tested, namely: the missing transverse energy (E_T^{miss}), the p_T of the Higgs boson candidate, the p_T of the W boson candidate, the lepton p_T, the Higgs boson candidates mass, the number of jets(N^{Jets}), the maximal BDT response (w_{BDT}^{max}), the E_T^{miss} significance, the p_T of the Higgs boson normalized to the reconstructed charged Higgs boson mass (m_{Wh}) and the p_T of the W boson normalized to the reconstructed charged Higgs boson mass (m_{Wh}) and the angle $\Delta\Phi$ between the Higgs boson and the W boson. This has been done in the 2 b-tags, 3 b-tags, 4+ b-tags and in a b-tag inclusive region. Figure 5.12 shows the distributions for the W boson p_T (a), jet multiplicity, Higgs boson p_T and maximum MVA Response d), in the b-tag inclusive region. Figures for all other variables are given in the appendix (see subsection A.1.2). All the histograms are normalized to unity, so just the shapes are compared. The distributions of the variables shown in figure 5.12 are well separated between the signal and background processes. This holds true for the other b-tag categories. To find the optimal cut on a given variable, two measures of significance are calculated:

$$\sigma = \frac{s}{\sqrt{b}}, \tag{5.5}$$

where s is the number of signal events in the interval between the minimal/maximal value and a given cut value. The other significance definition is:

$$z_\sigma = \sqrt{2 \cdot (n \log \frac{n(b+\sigma^2)}{b^2} + n(\sigma^2) - \frac{b^2}{\sigma^2} \log (1 + \frac{\sigma^2 + (n-b)}{b \cdot (b+\sigma^2)})}, \tag{5.6}$$

where $n = b + s$ is the total number of events, s the number of signal events and b the number of background events. The significance is calculated for $\sigma = 2.5\%$, $\sigma = 5\%$ and $\sigma = 10\%$.

Both, cuts defining upper bounds (i.e all events between the minimal value and the upper bounds are considered) as well as lower bounds (i.e all events between the maximal value and the lower bounds are considered) are investigated. Figure 5.13 shows z and $s/\sqrt{b}$ in the b-tag inclusive region as a function of upper bounds on the Higgs boson transverse momentum, W boson transverse momentum, maximal BDT response and jet multiplicity for the 400 GeV mass point. The measure z tends to peak for tighter cuts than $s/\sqrt{b}$. The maximum for the $z_{2.5\%}$, $z_{5\%}$, $z_{10\%}$ distributions are identical. The optimal cuts, i.e the value where the significance peaks, is almost the same in each of the different b-tag regions. This is illustrated in figure 5.15, where the significance for the maximal BDT response scan is shown for the 400 GeV mass point within the four different b-tag categories. The distributions peak for the same value. This still holds true for all other mass points and variables. However, the optimal cut for certain kinematic variables like the Higgs or W boson p_T strongly depends on the mass of the studied charged Higgs boson, as illustrated in figure 5.14. Higher mass points benefit from tighter cuts. If the optimal cut depends on the mass point, the most conservative cut is chosen. After considering all the points discussed above, the following selection requirements are chosen to define the signal region:

- Higgs boson transverse momentum > 100 GeV
- W boson transverse momentum > 120 GeV
- $N^{Jets} > 5$
- $w_{BDT}^{max} > 0.7$

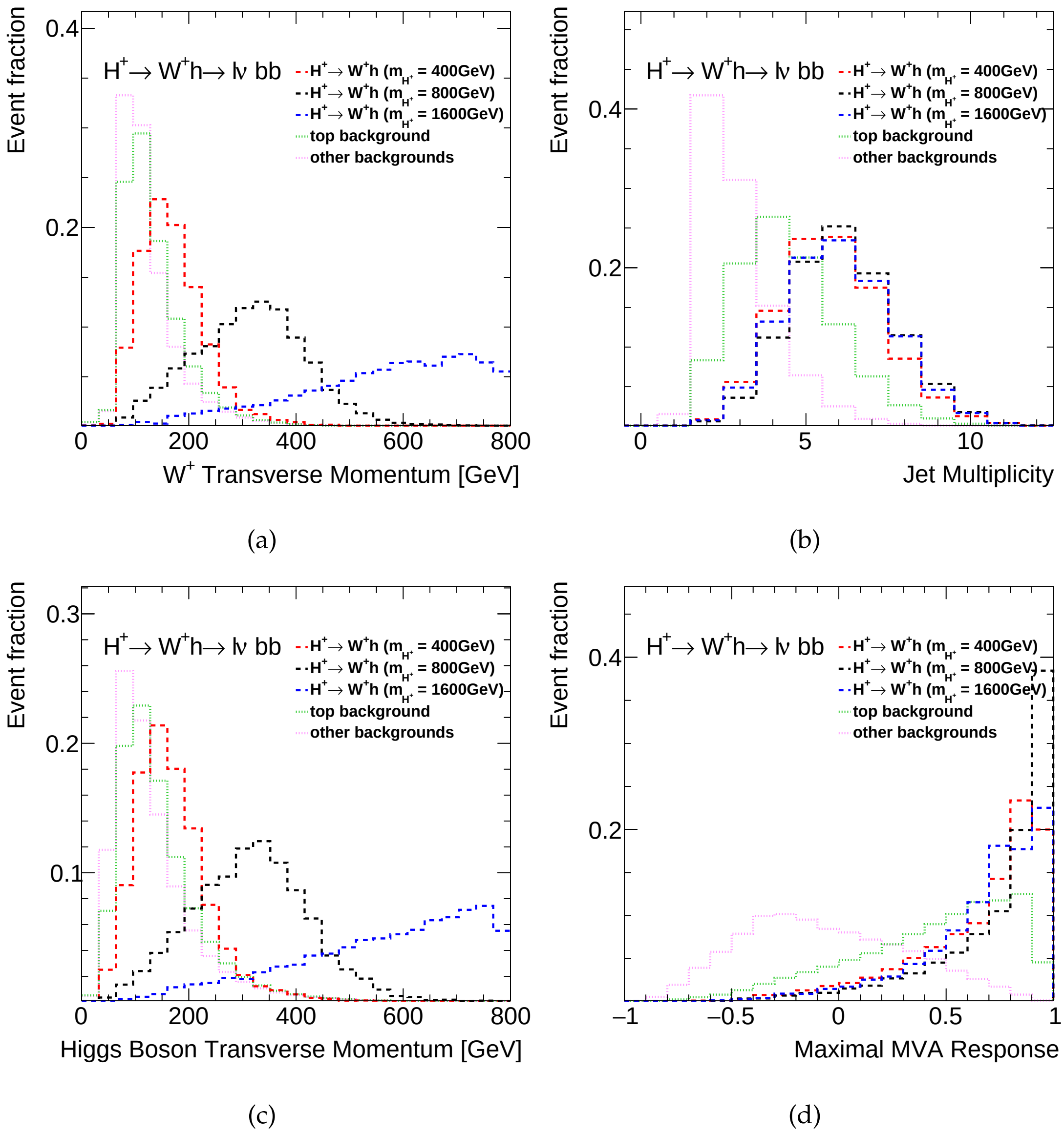

Figure 5.12.: Comparisons between the distributions of different variables. The distributions are normalized and thus show a shape comparison. The distributions are shown separately for the signal and backgrounds. These variables distinguish well between signal and background.

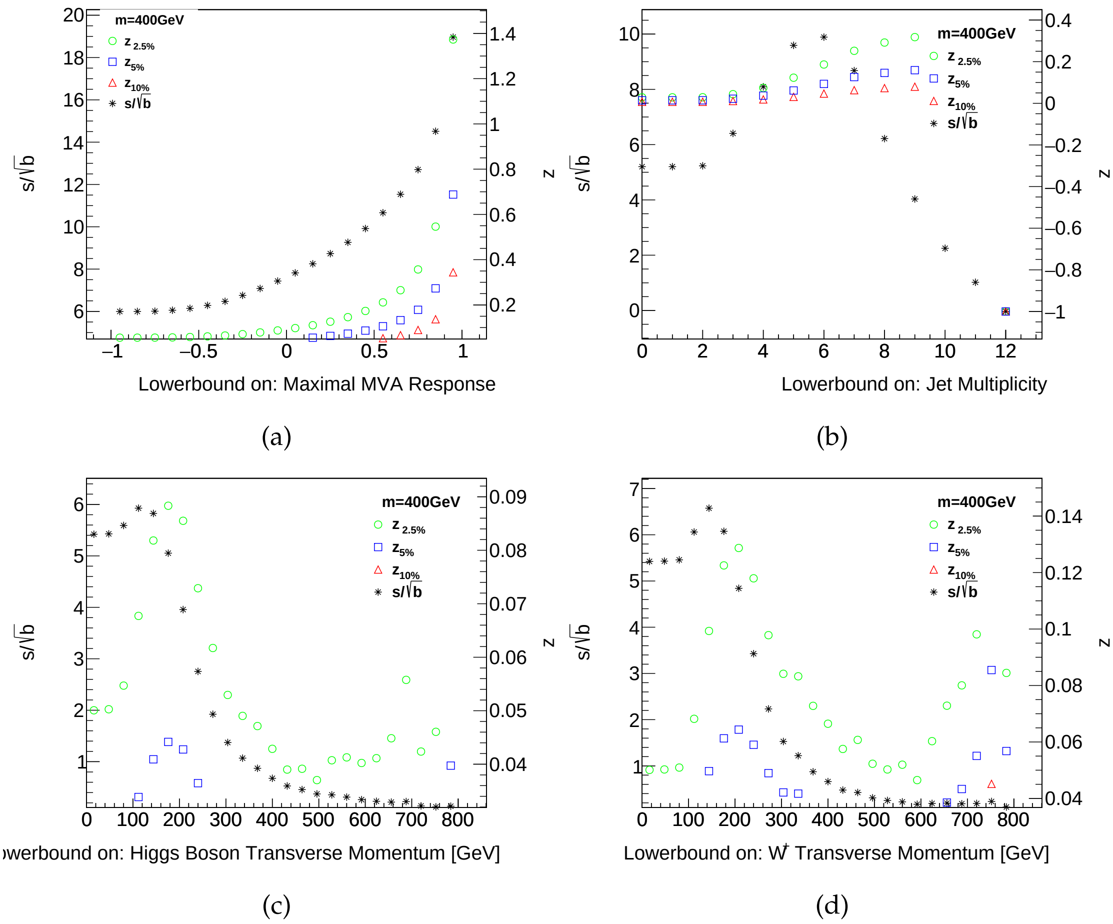

Figure 5.13.: The significance $s\sqrt{b}$, and the z measure, calculated as a function of a lower bound on different variables for a charged Higgs boson of mass 400 GeV.

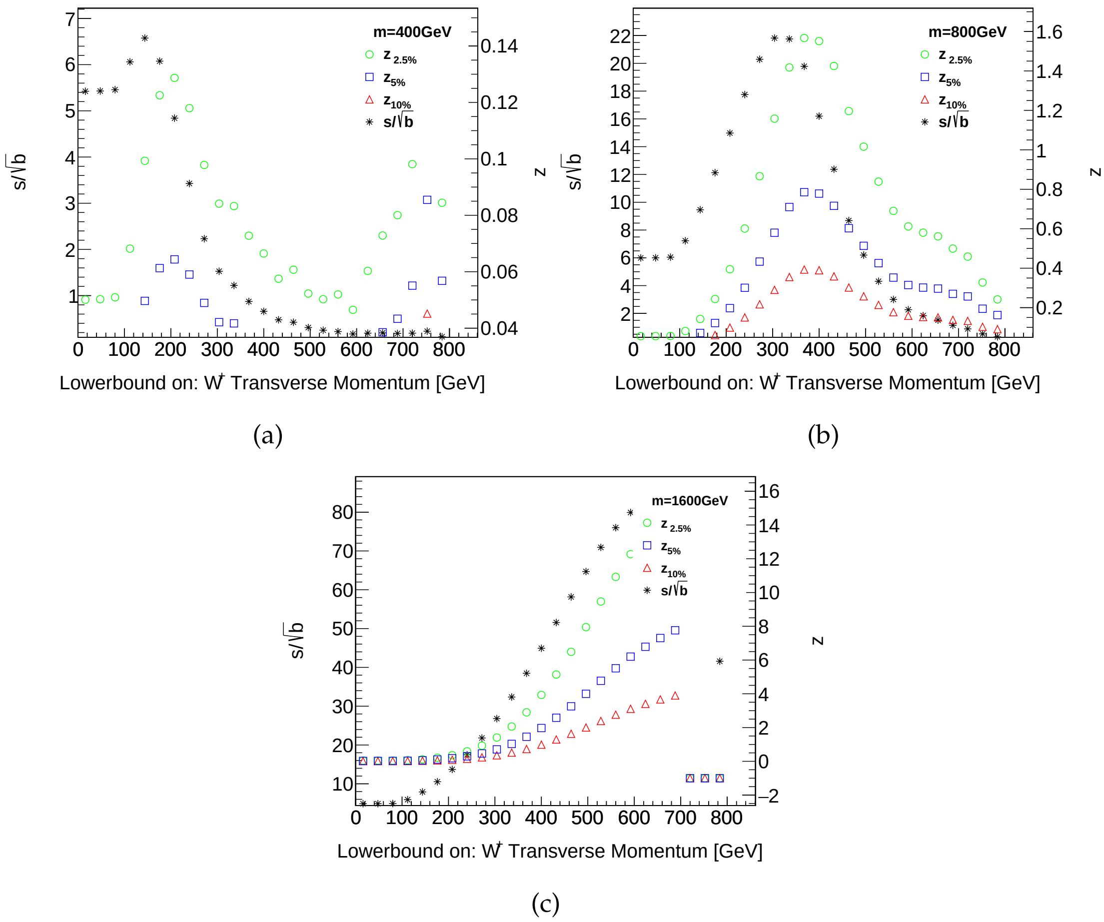

Figure 5.14.: Comparisons of the significance $s\sqrt{b}$, and the z measure as a function of the lower bound on the W boson transverse momentum, presented for different charged Higgs boson masses. The optimal cut corresponding to the peak of the distribution, differs for each mass point.

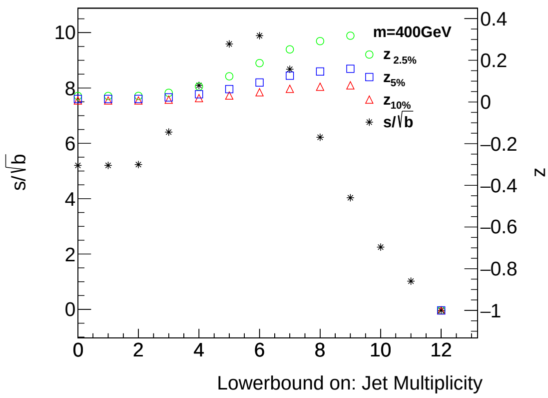

(a) b-tag inclusive

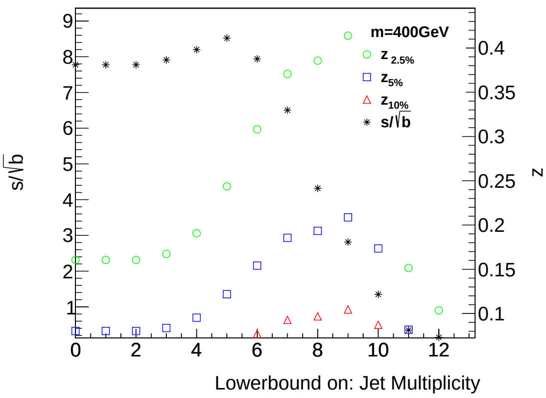

(b) 2 b-tags

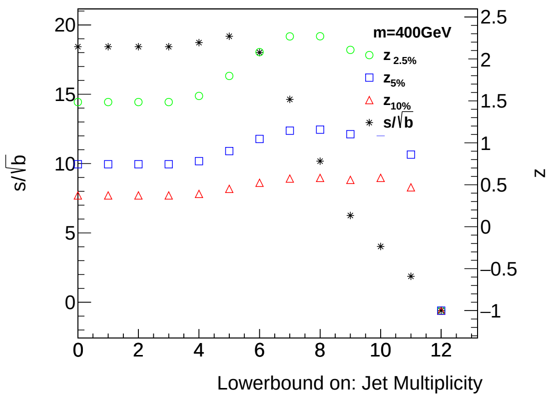

(c) 3 b-tags

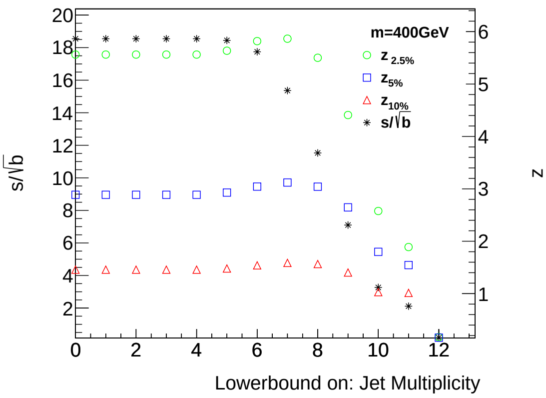

(d) 4+ b-tags

Figure 5.15.: The significance $s\sqrt{b}$, and the z measure in the different b-tag categories for the 400 GeV H^+ mass point. Calculated as a function of lower bounds on the jet multiplicity variable. The optimal cuts corresponding to the peaks of the distribution are almost identical in every b-tag category.

5.5.2. Definition of the Control Region

In order to validate the distribution of the m_{Wh} variable for the dominant background processes, a control region is defined. To ensure similar kinematic properties in the control region as in the signal region, the cuts on the number of jets, the Higgs boson and the W boson p_T are also used to define the control region. The control region is defined by changing the interval in the max BDT score variable.

Figure 5.16 shows the m_{Wh} distribution of the combined standard model backgrounds in the signal region (in red) as well as in various control region candidates. Each region is defined by a different interval in the maximal BDT response (called w_{BDT} in this figure). Whereas in most control region candidates the m_{Wh} distribution is similar to that of the signal region, this is not universally true. E.g for a BDT response between -1.0 and 0 (shown in green) the m_{Wh} distribution is shifted with respect to the m_{Wh} distribution in the signal region. Thus, this particular region is unsuitable as a control region. Furthermore, the control region should contain a minimal amount of signal events and the background should be enhanced over the signal in this region. To identify the control region where this is the case, the fraction of events that fall into the control region normalized to the length of the interval, in the BDT response i.e.

$$\frac{\text{\#Events in CR}}{\text{\# of all Event * Intergral Lenght}} \tag{5.7}$$

is computed. This measure was calculated for the background processes as well as for the H^+ signal mass point in a variety of control region candidates. The results are listed in table 5.8. As the region defined by a max BDT response between -0.5 and +0.3 best fulfills both requirements, it was chosen as the control region.

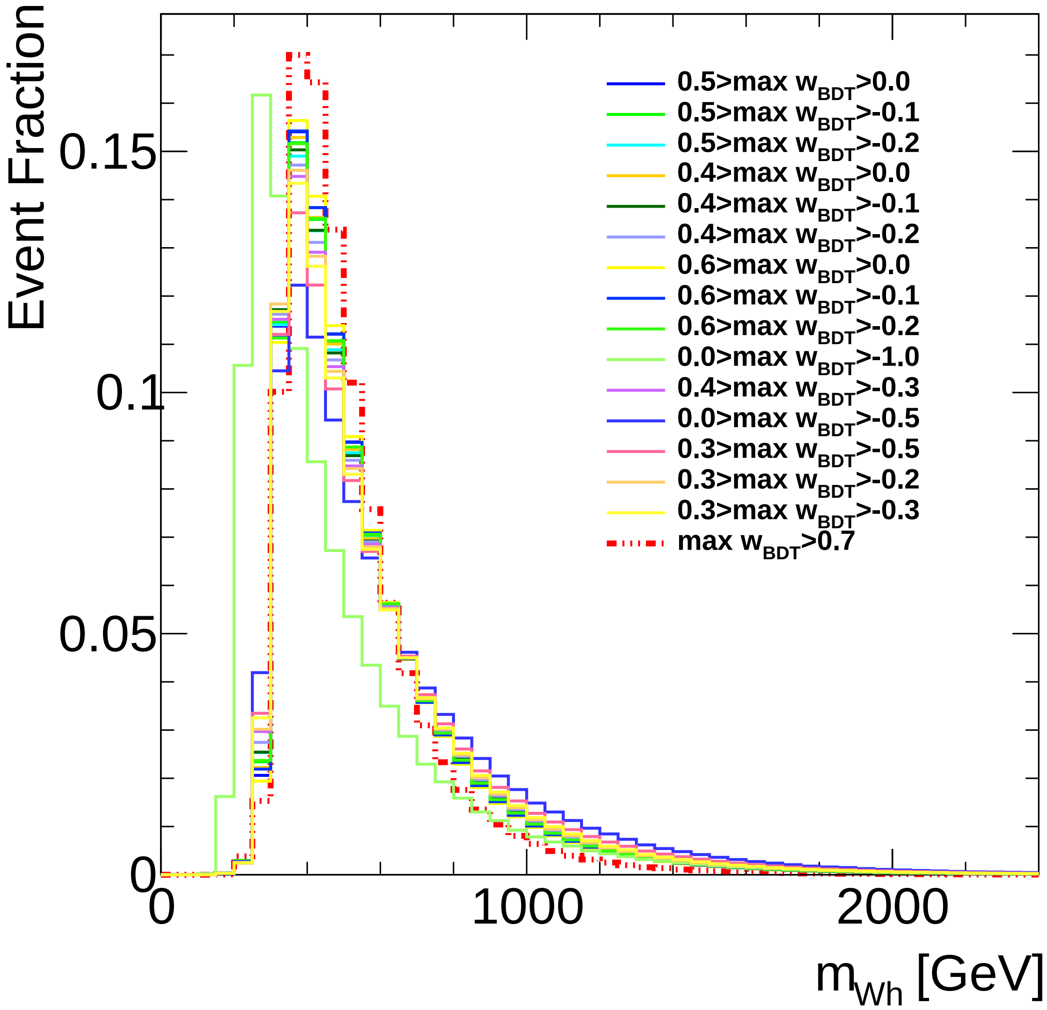

Figure 5.16.: The distribution of the invariant reconstructed charged Higgs boson mass m_{Wh} presented for the sum of all SM-backgrounds, presented in different w_{BDT}^{max} intervals.

Table 5.8.: $\frac{\text{\#Events in CR}}{\text{\# of all Event * Intergral Lenght}}$ for different maximal w_{BDT}^{max} response intervals.

	m=400GeV	m=800GeV	m=1600GeV	Background
$0.0 < w_{BDT}^{max} < 0.5$	0.36	0.24	0.32	0.77
$-0.1 < w_{BDT}^{max} < 0.5$	0.32	0.21	0.28	0.73
$-0.2 < w_{BDT}^{max} < 0.5$	0.28	0.19	0.26	0.699
$0.0 < w_{BDT}^{max} < 0.4$	0.30	0.20	0.26	0.75
$-0.1 < w_{BDT}^{max} < 0.4$	0.27	0.18	0.23	0.7
$-0.2 < w_{BDT}^{max} < 0.4$	0.24	0.16	0.21	0.67
$-0.3 < w_{BDT}^{max} < 0.4$	0.21	0.14	0.19	0.63
$0.0 < w_{BDT}^{max} < 0.6$	0.42	0.29	0.39	0.8
$-0.1 < w_{BDT}^{max} < 0.6$	0.38	0.26	0.35	0.76
$-0.2 < w_{BDT}^{max} < 0.6$	0.34	0.23	0.32	0.72
$-1.0 < w_{BDT}^{max} < 0.0$	0.05	0.02	0.03	0.43
$-0.5 < w_{BDT}^{max} < 0.0$	0.06	0.04	0.06	0.39
$-0.5 < w_{BDT}^{max} < 0.3$	0.13	0.09	0.12	0.51
$-0.2 w_{BDT}^{max} < 0.3$	0.19	0.13	0.17	0.62
$-0.3 < w_{BDT}^{max} < 0.3$	0.17	0.11	0.15	0.58

5.5.3. Event Yields and Cut Flow

The expected number of signal and background events passing the selection requirements of the signal and control regions (SR and CR) are listed separately for each process and b-tag category in table 5.10. In every b-tag category, the dominant background contribution stems from top-quark pair production. The number of charged Higgs boson events are normalized to 1pb. The distributions of these events as a function of the reconstructed mass are given in figure 5.17.

In order to compare the signal sensitivity in the different b-tag regions, the $s/\sqrt{b}$ has been calculated in every signal region around the signal mass peak. Only events with a mass within a $\pm 2\sigma$ window around the charged Higgs boson mass pole are considered, σ is the mass resolution of the mass point (see subsection 5.4.2). The results are given in table 5.9. The 2 b-tag region has the lowest sensitivity. The sensitivity in the 3 or 4+ b-tag region is approximately twice as large. The 3 b-tag region is the most sensitive for the 400 and 800 GeV mass points. For the 1600 GeV mass point, the $s/\sqrt{b}$ is the lowest in the 4+ b-tag region, while the 3 b-tag region is the most sensitive region. The absolute values of the signal significance, correspond to a signal cross-section normalized to 1pb (shown as an example), but are not expected to be realistic.

Cut Flow diagrams for the three signal mass points are presented in figure 5.19 and in figure 5.20-figure 5.21 for the background processes. Each bin in these diagrams shows the number of events that pass the respective selection requirement. The selection requirement with the biggest effect on the background yields is the $N^{Jets} > 4$ requirement. The background process, expected the top-quark pair production are drastically reduced by the, requirement (e.g the number of W+jets events is reduced by 88% of the selection requirement). The number $t\bar{t}$ is reduced to about 50% by this requirement, while the signal yields are reduced by about 20%. The $maxMVA > 0.7$ has the biggest impact on the signal, the number of events is reduced by about 40%. The signal region selection reduces the event yields to about: 50%(H^+ 1600 GeV), 53%(H^+ 800 GeV), 38%(H^+ 400 GeV), 5%(diboson), 4%(single top), 1%(Z+jets), 2%(W+jets) and 10%($\bar{t}t$) of their initial values.

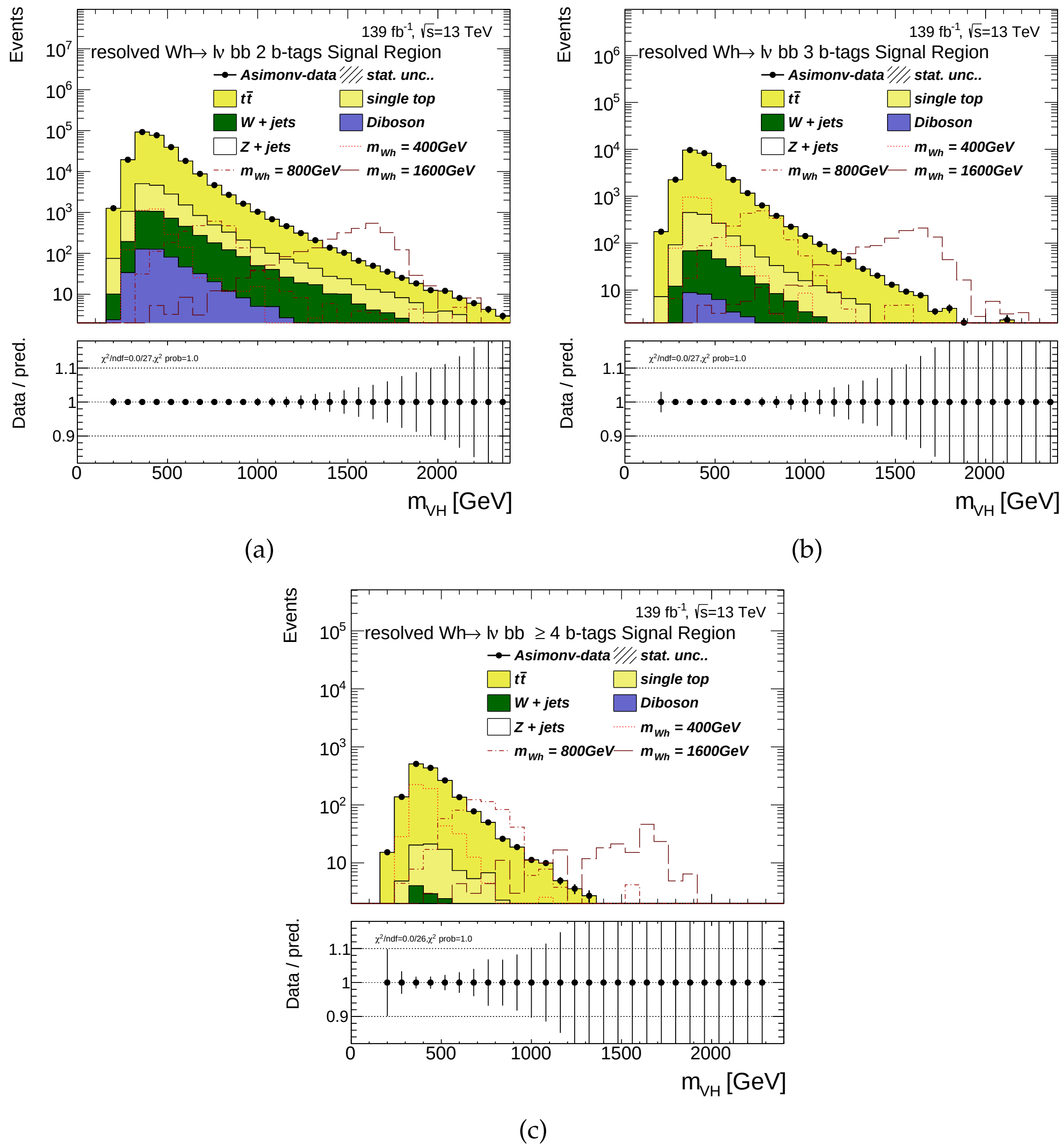

Figure 5.17.: The m_{Wh} distribution of the SM-background and the signal process in the signal region. The distributions are presented for the 2-tag, 3-tag and 4+ tag categories.

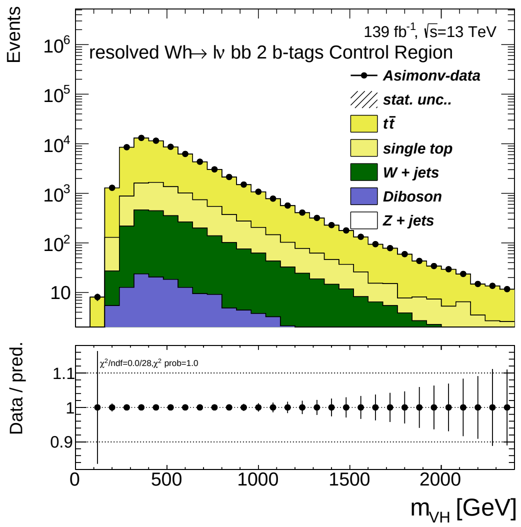

(a)

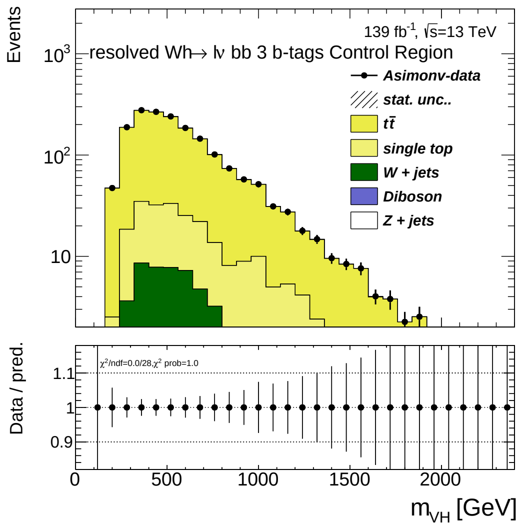

(b)

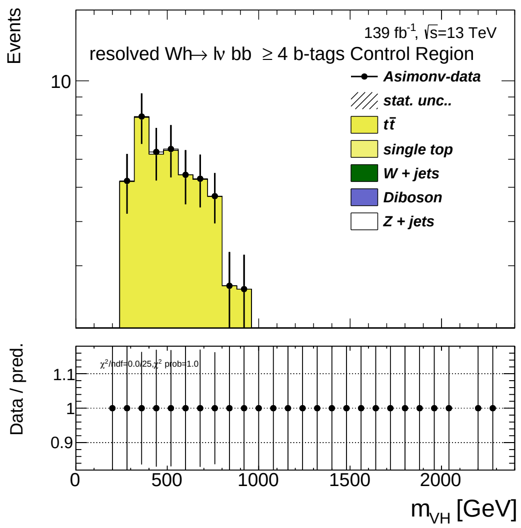

(c)

Figure 5.18.: The m_{Wh} distribution of the SM-background in the control region. The distributions are presented for the 2-tag, 3-tag and 4+ tag categories.

Table 5.9.: The significance $s/\sqrt{b}$ calculated in the signal region in a $\pm 2\sigma$ mass window under the peak. The signals are each normalized to a cross-section of 1 pb.

	m=400GeV	m=800GeV	m=1600GeV
2 b-tags	6.75	9.587	69.19
3 b-tags	16.08	21.60	79.73
4+ b-tags	15.85	24.07	46.57

Table 5.10.: The number of expected events in the signal and control region. The three signal hypotheses are each normalized to 1 pb.

	2 b-tag SR	3 b-tag SR	4+ b-tag SR
$H^+ \to hW \to l\nu rbb$(m=400GeV)	2994±106	2362±92	539±43
$H^+ \to hW \to l\nu bb$(m=800GeV)	2468±100	1954±89	552±44
$H^+ \to hW \to l\nu bb$(m=1600GeV)	2480±104	1099±70	210±29
$t\bar{t}$	250375±182	28265±61	1609±15
t	13193±60	1333±19	75±5
diboson	512±5	36±1	3±0
W+jets	3860±28	254±6	13±1
Z+jets	539±6	43±1	3±0

	2 b-tag CR	3 b-tag CR	4+ b-tag CR
$H^+ \to hW \to l\nu rbb$(m=400GeV)	424±40	63±17	7±4
$H^+ \to hW \to l\nu bb$(m=800GeV)	505±41	112±19	6±5
$H^+ \to hW \to l\nu bb$(m=1600GeV)	181±30	51±14	4±4
$t\bar{t}$	54646±89	1528±15	47±3
t	6841±45	182±8	5±1
diboson	137±3	4±1	0±0
W+jets	2394±21	49±3	1±0
Z+jets	347±5	8±1	0±0

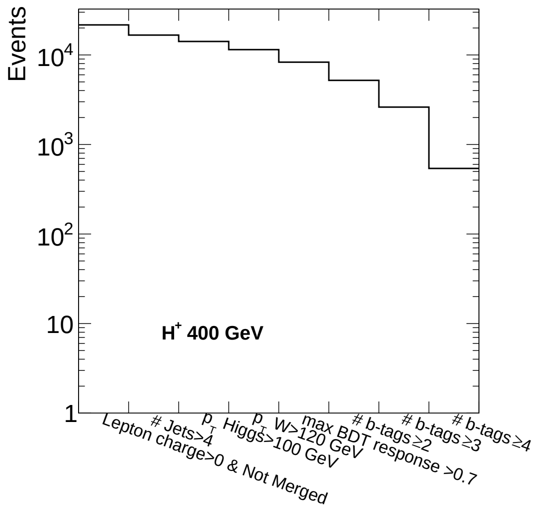

(a) 400 GeV

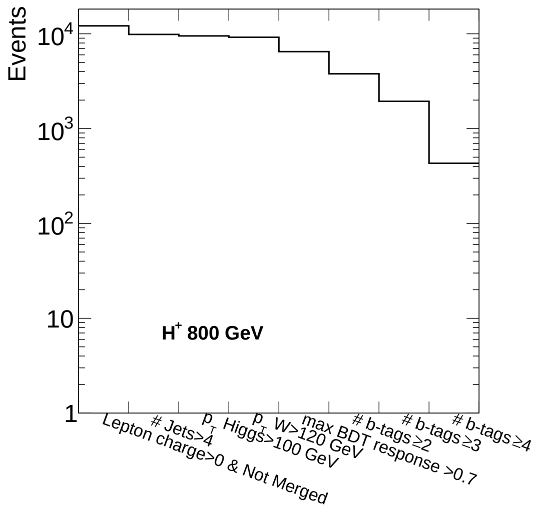

(b) 800 GeV

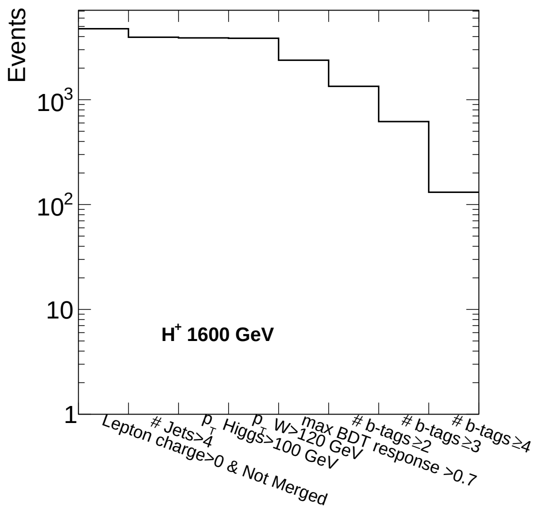

(c) 1600 GeV

Figure 5.19.: Cutflow diagrams of the three H^+ mass points. Each bin shows the number of events passing the respective selection requirement.

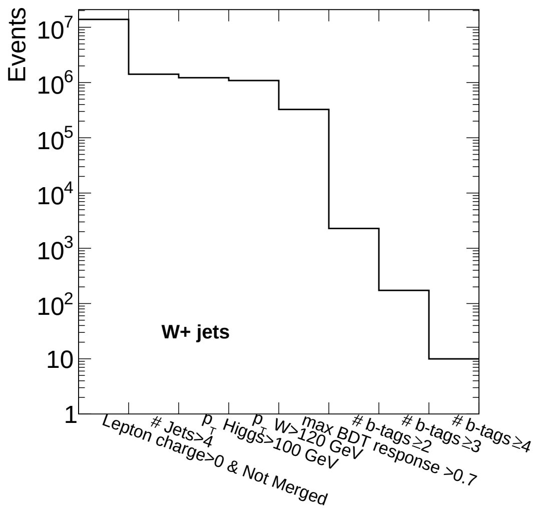

(a) W+ jets

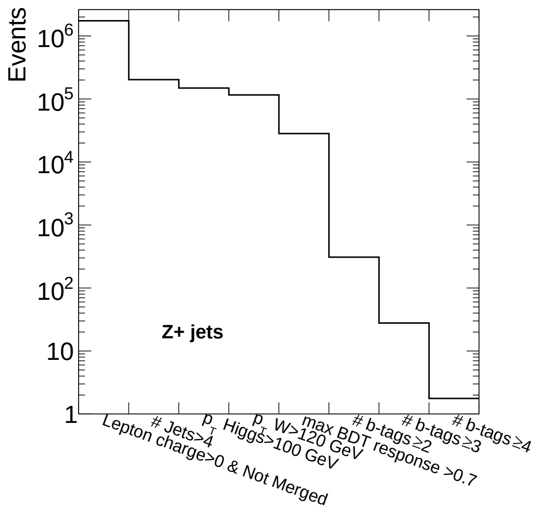

(b) Z+ jets

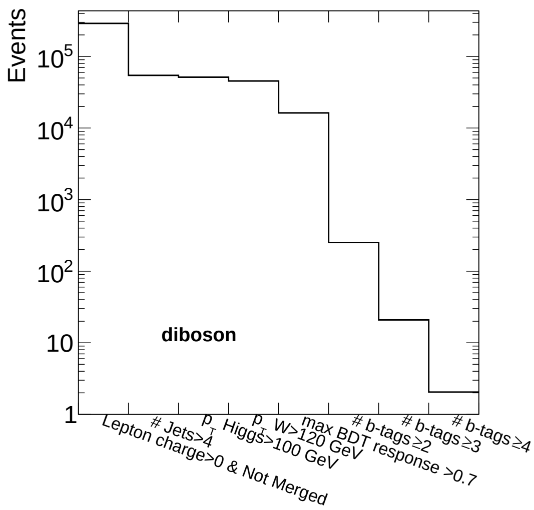

(c) diboson

Figure 5.20.: Cutflow diagrams of the W+jets, the Z+jets and the diboson backgrounds. Each bin shows the number of events passing the respective event selection requirement.

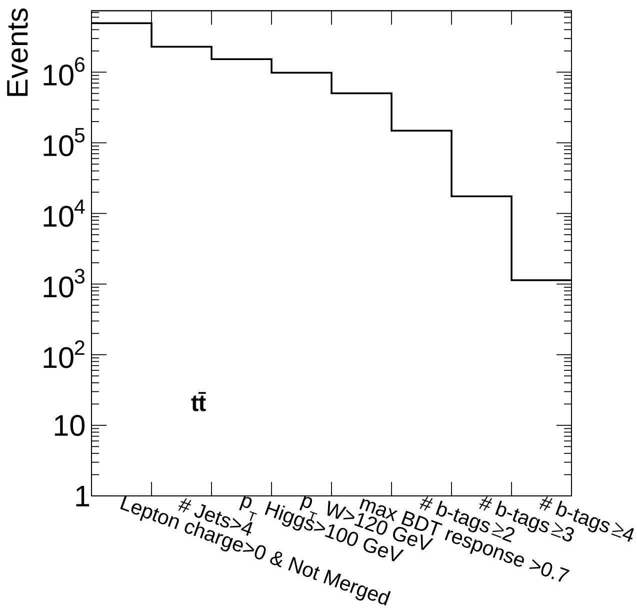

(a) $t\bar{t}$

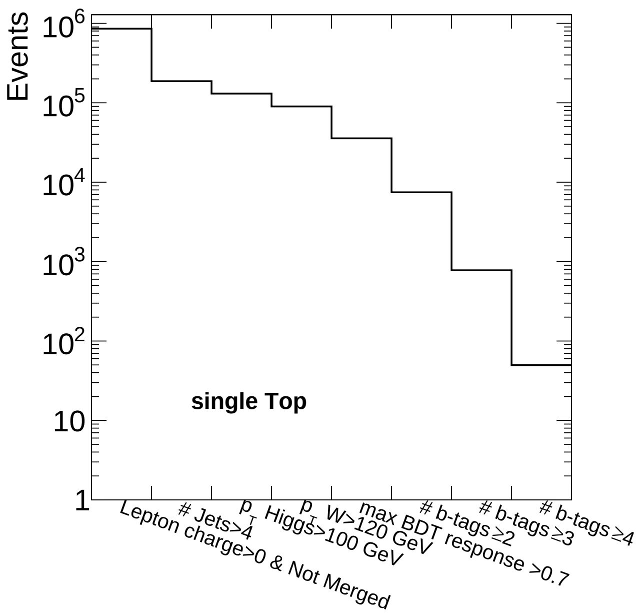

(b) single top

Figure 5.21.: Cutflow diagrams of the single top and top-quark pairs background. Each bin shows the number of events passing the respective event selection requirement.

5.6. Comparisons of Data and Simulation

comparison of data to Monte Carlo prediction are performed in the 2-b tag region. As in this region the signal sensitivity is expected to be the lowest (see subsection 5.5.3), it can be used as a *validation region*. Without any further kinematic selection requirements, defining the signal and control regions, the background modelling is validated. Figure 5.23 and figure 5.24 compares the data to the Monte Carlo prediction in the 2-b tag region for the number of jets, the H_T, the max MVA response, the m_{Wh} variable, the missing transverse energy, the lepton p_T as well as the leading and subleading jet p_T. Beside the b-tag requirement, events are only required to contain at least 4 jets and one positively charged lepton.

Further data-to-simulation comparisons are presented in the appendix (see subsection A.1.3). There are noticeable differences between the data and the Monte Carlo predictions. The discrepancies are most apparent in the number of jets distributions (figure 5.23 a). High jet multiplicities are not very well modeled by the POWHEG+PHYIHA generators. They are generally under predicted, e.g events containing 8 jets are observed 10% more often than predicted, while events with 12 jets are observed about 80% more often than predicted. Also other kinematic variables like the lepton p_T, or E_T^{miss} are miss-modeled. In high level observable such as the max MVA response there is a discrepancy between data and the prediction as well. Similar disagreements between the observed and expected jet multiplicity distribution haven been reported by other analyses (e.g. see Ref. [48]) .

5.6.1. Background correction procedure

In order to improve the background estimation and modelling, a data driven correction procedure is performed by reweighting the Monte Carlo prediction. Weights are derived from the data-to-simulation ratios in the 2 b-tag region. Afterwards, these weights are also applied to the background prediction in the 3 and 4+ tag signal and control regions. A sequential reweighting approach, similar to the one described in Ref. [48] is used. It is assumed that the miss-modelling solely stems from the $t\bar{t}$ background. Consequently only the $t\bar{t}$ predictions gets reweighted. Weight factors are defined as

$$w(x) = \frac{N^{data}(x) - N^{non-t\bar{t}}(x)}{N^{t\bar{t}}(x)}, \tag{5.8}$$

i.e the ratio of the yields in data, (with the contribution of background processes not stemming from $t\bar{t}$ subtracted) to the expected yields of the $t\bar{t}$ background. Where x represents the interval of a certain variable. The first set of weight factors is calculated from the data-to-simulation ratios in the jet multiplicity (N^{Jets}) distributions. In each jet multiplicity bin, a weight factor is extracted. Events containing 11 or more jets are merged into a single bin. Figure 5.22 shows the weights obtained by this procedure.

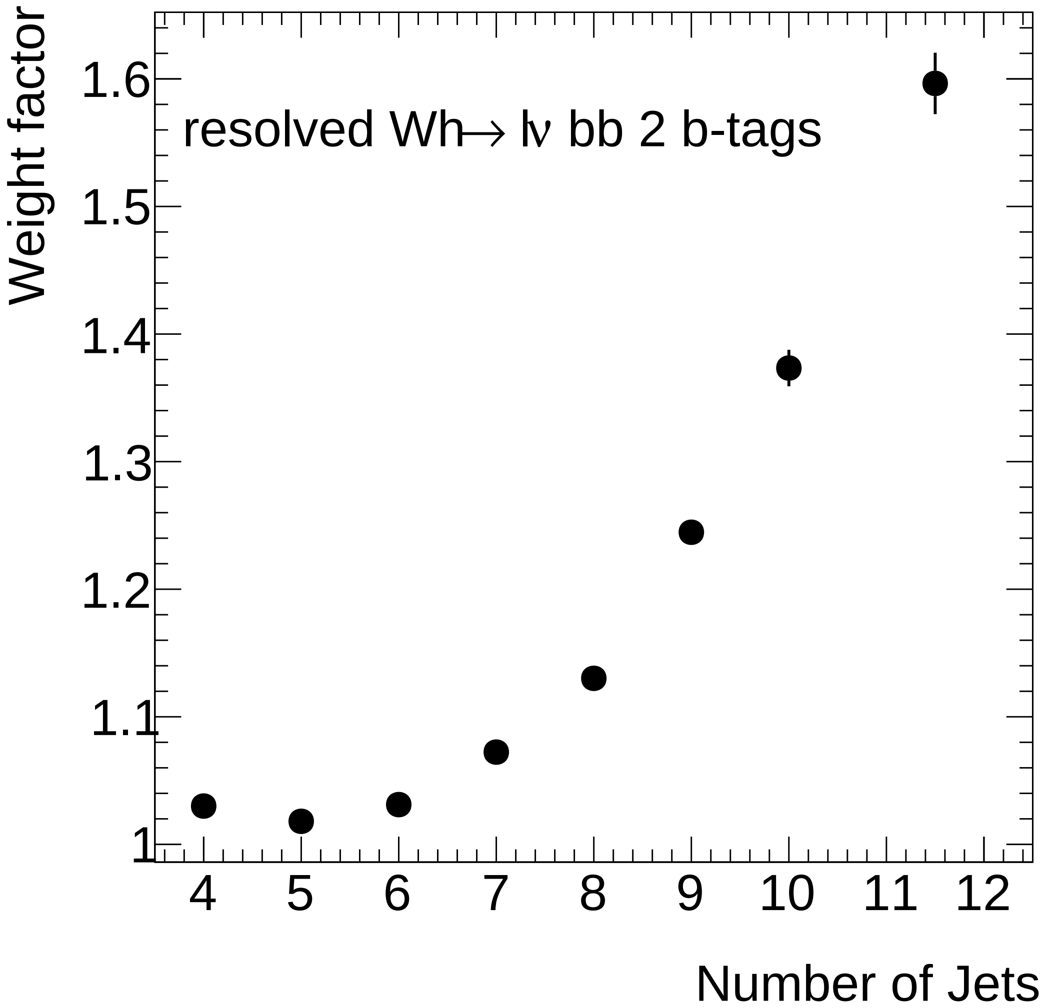

Figure 5.22.: Weight factor obtained from the ratios of the data to the Monte Carlo prediction as a function of the jet multiplicity. Events containing 11 or more jets have been merged into a single bin, for which a single weight factor is calculated.

After the weights are applied, the next set of weight factors is extracted from the H_T distribution, which is the transverse momentum sum of all jets. This is done separately for each jet multiplicity. Finally, a 5th order polynomial is fitted to the weight factors of the H_T distributions. The distribution of the H_T is presented in figure 5.25-figure 5.26 in bins of the corrected N^{Jets} distribution. The weight factors that are obtained from the corrected distributions are presented in figure 5.27-figure 5.28.

Figure 5.29-Figure 5.32 presents data-to-simulation comparisons for the jet multiplicity, H_T, lepton p_T, leading and subleading jet p_T, E_T^{miss} and m_{Wh} distributions before (left column) and after (right column) the sequential reweighting is applied. Due to the reweighting, the agreement between data and the predictions by the simulation improve significantly for the jet multiplicity and H_T distributions. I.e. the χ^2 values obtained from a χ^2 test to the data-to-simulation comparisons decreases from 3051 to 8 (for the jet multiplicity distribution) and from 1367 to 341 (for the H_T distribution). The sequential reweighting also improves the modeling of other kinematic variables like the leading and subleading jet p_T, the E_T^{miss} and the lepton p_T. However, some residual data-to-simulation disagreement persists for some of these observables. Furthermore, the sequential reweighting procedure has some negative impact on the data-to-simulation agreement for the m_{Wh} observable as the corresponding χ^2 value increases from 233 to 839 after the reweighting is applied. As the m_{Wh} observable will be used as input to the limit setting procedure, it is desired to further improve the modelling of the m_{Wh} observable. For this purpose, a third reweighting step is studied. Weights[3] are derived from data-to-simulation ratios of the lepton p_T, the E_T^{miss} and the leading jet distribution. The distributions of these weights are presented in figure 5.33-figure 5.34. These ratios are obtained after the corrections on the jet multiplicity and H_T distribution have been accounted for. A correction function is obtained by fitting a 5th order polynomial through the weight-factor distributions.

Distributions of the leading and subleading jet p_T, the lepton p_T, the E_T^{miss}, the max BDT response, the jet multiplicity and the H_T are presented in figure 5.35-figure 5.46 for different versions of the three step reweighting procedure and the two step reweighting procedure. figure 5.35-figure 5.38 shows data-to-simulation comparisons for the squential reweighting of the jet multiplicity, H_T and E_T^{miss} distributions. While some observables show a mildly improved data-to-simulation comparison with respect to the two-step reweighting procedure, the modelling of the m_{Wh} distribution does not improve. Similar conclusions are drawn from three-step correction procedures based on N^{jets}, H_T and the lepton p_T as well as N^{jets}, H_T and the leading jet p_T. The corre-

[3] The weight factors are defined via equation 5.8

sponding data-to-simulation comparisons are presented in figure 5.39-figure 5.42 and figure 5.43-figure 5.46

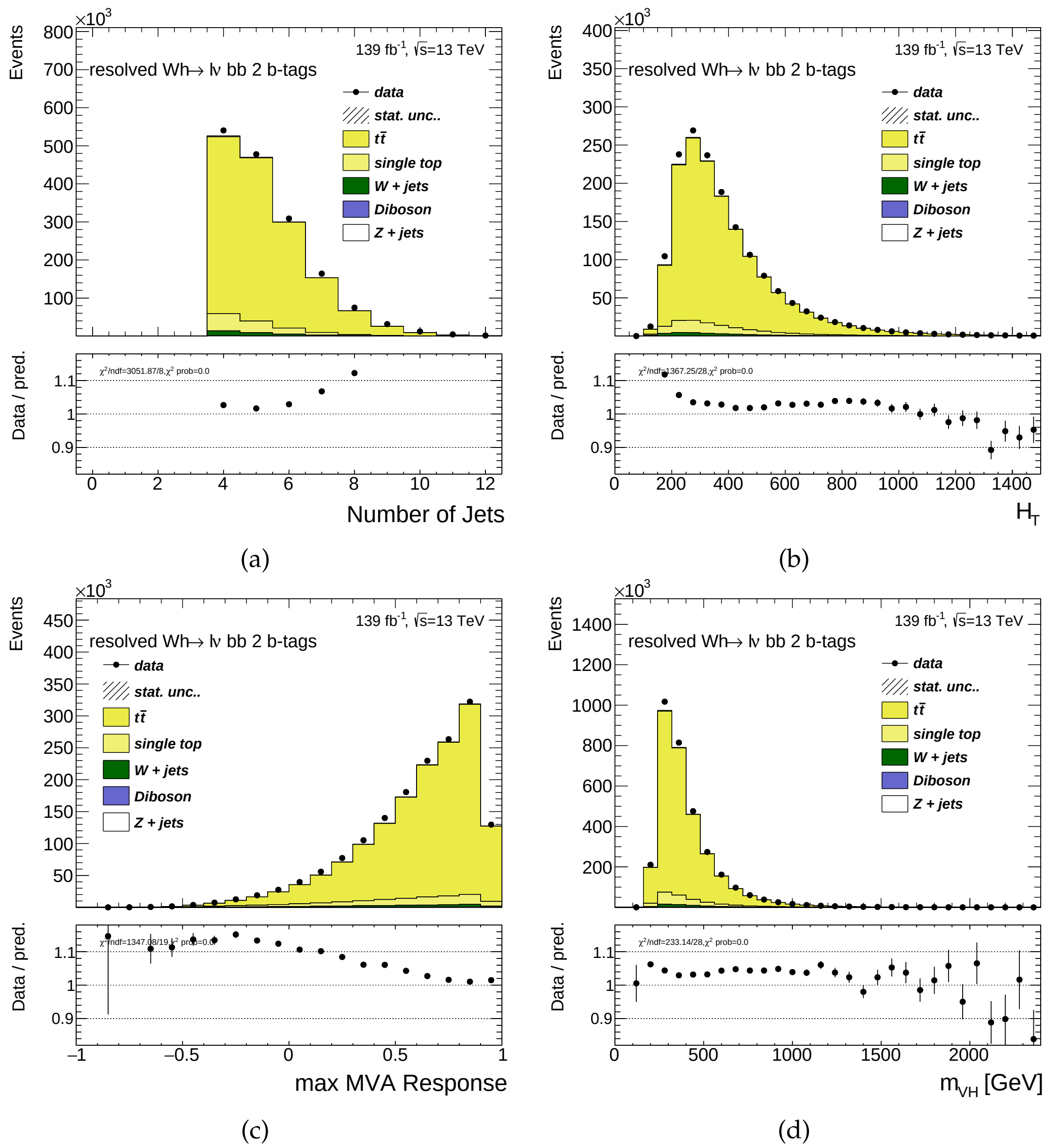

Figure 5.23.: Comparison between the data and the Monte Carlo prediction in the 2 b-tag region.

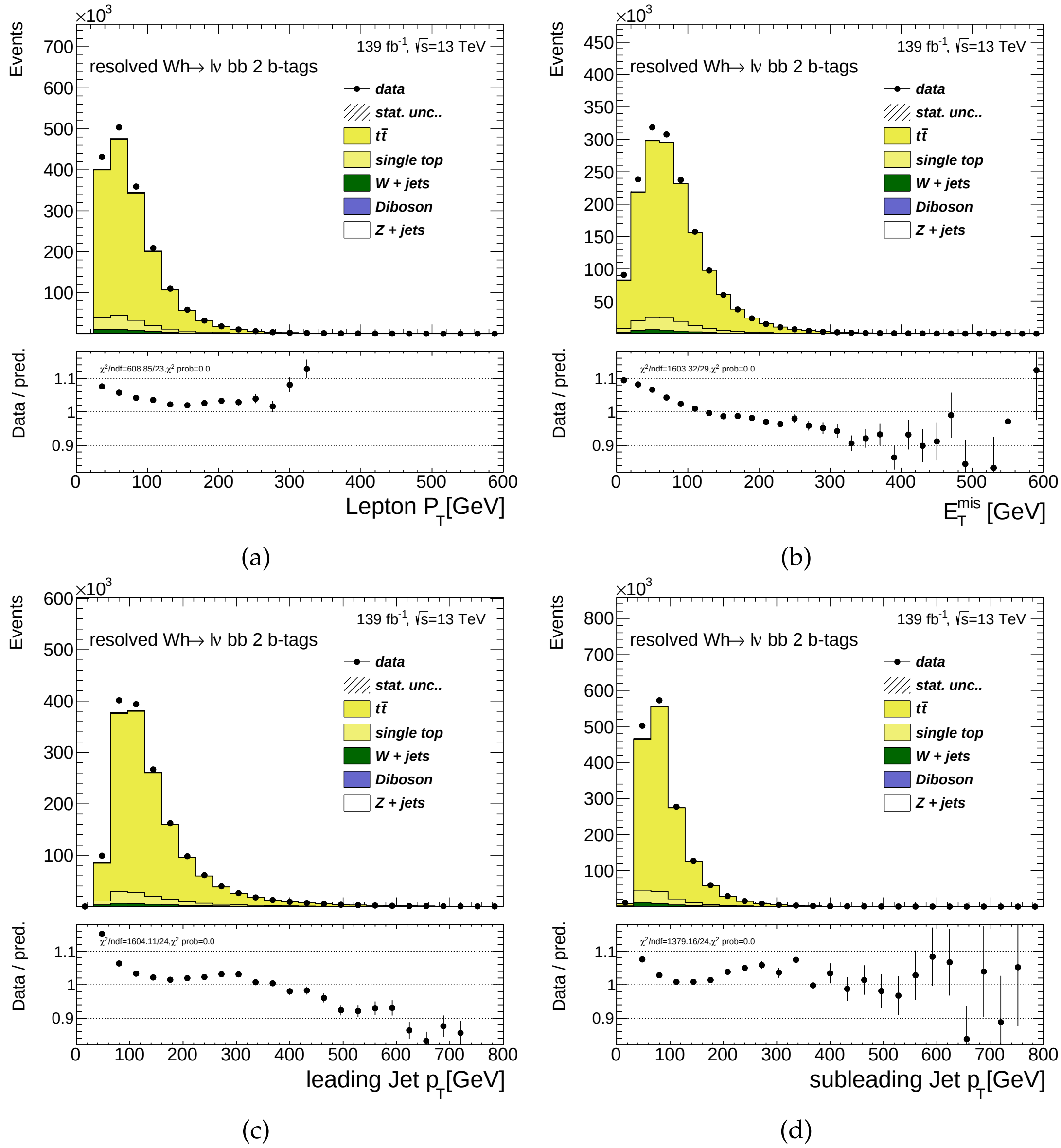

Figure 5.24.: Comparison between the data and the Monte Carlo prediction in the 2 b-tag region.

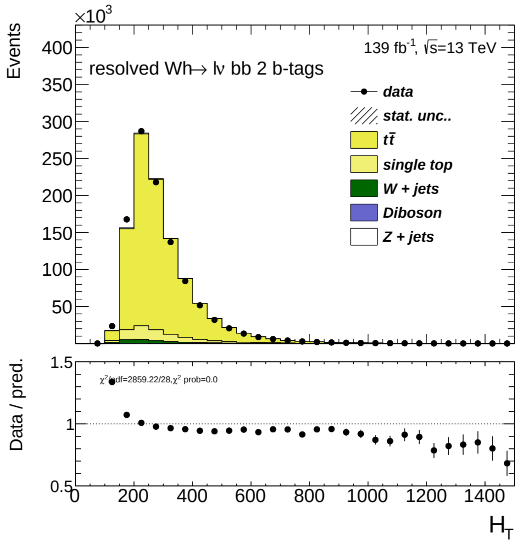

(a) 4 jets

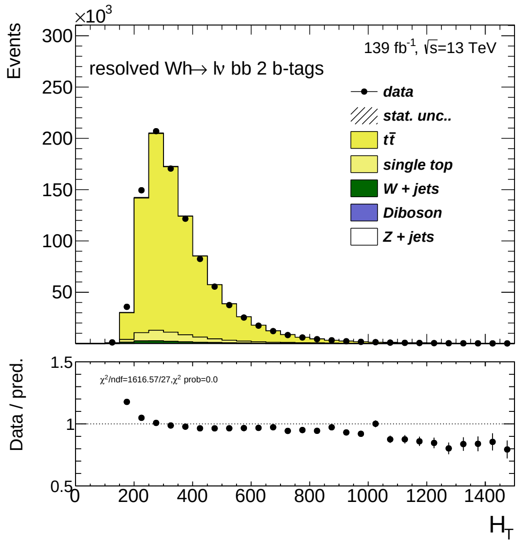

(b) 5 jets

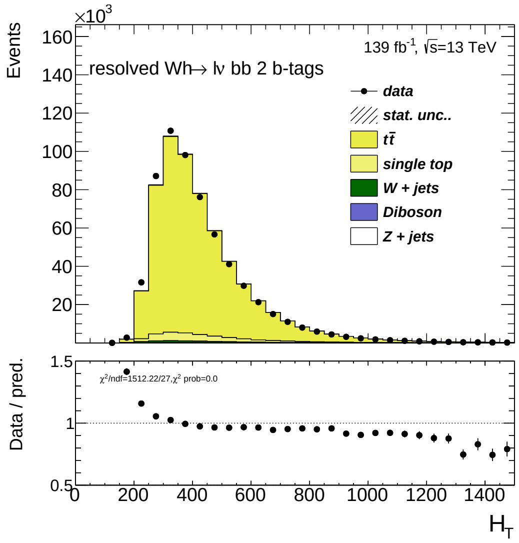

(c) 6 jets

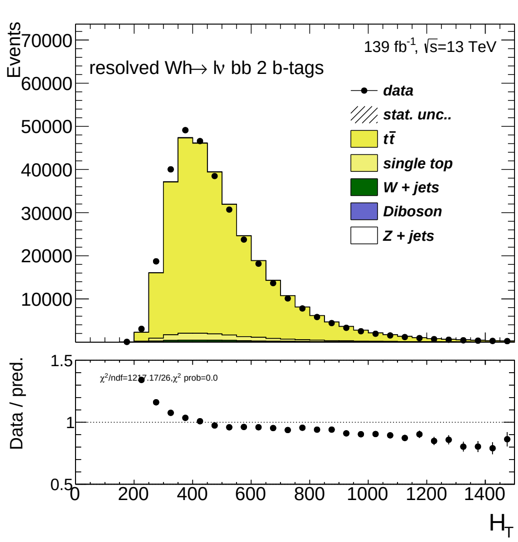

(d) 7 jets

Figure 5.25.: The H_T distribution for each jet multiplicity. The distributions have been reweighted with weights derived from the ratio of the data to the Monte Carlo prediction in the jet multiplicity variable. From the ratio of data to Monte Carlo of these distributions a second set of weights will be calculated.

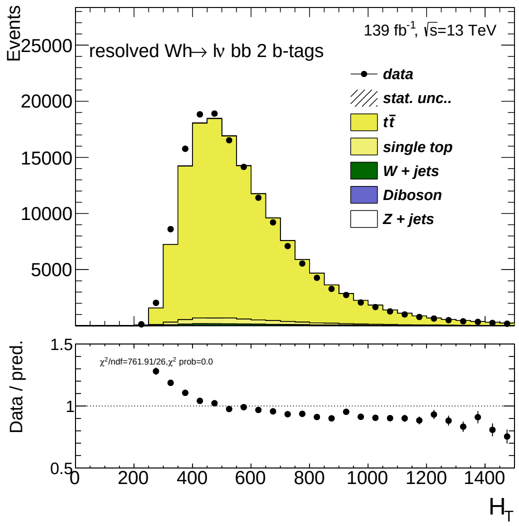

(a) 8 jets

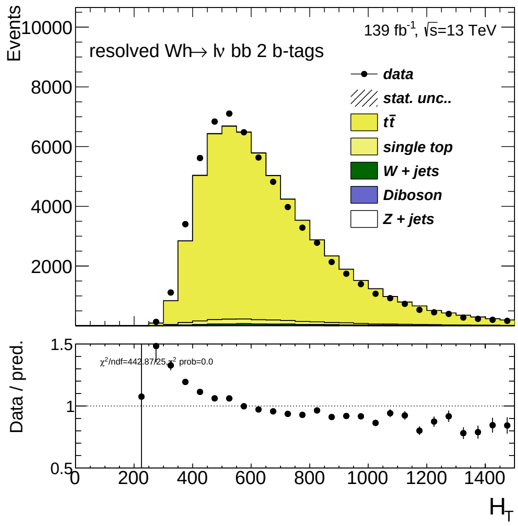

(b) 9 jets

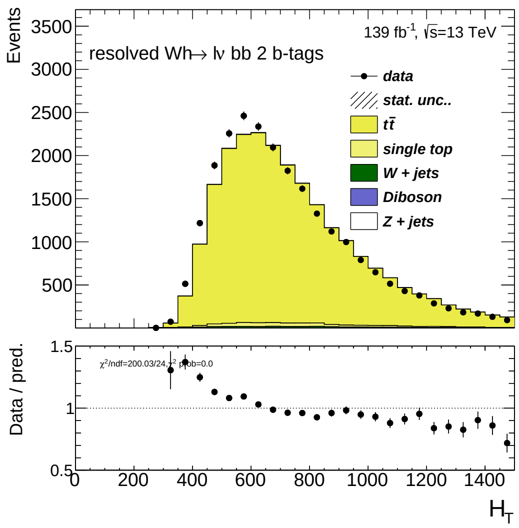

(c) 10 jets

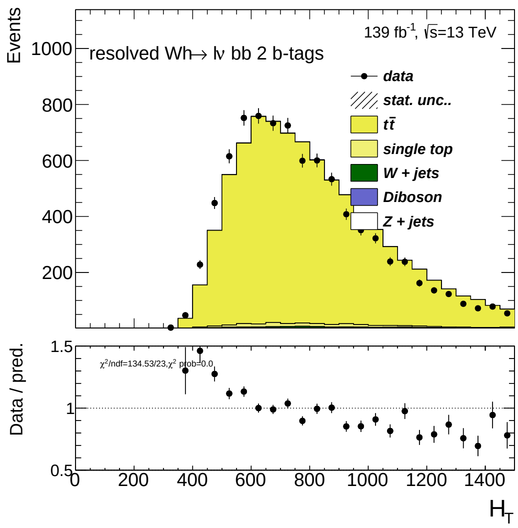

(d) 11 and more jets

Figure 5.26.: The H_T distribution for each jet multiplicity. The distributions have been reweighted with weights derived from the ratio of the data to the Monte Carlo prediction in the jet multiplicity variable. From the ratio of data to Monte Carlo of these distributions a second set of weights will be calculated.

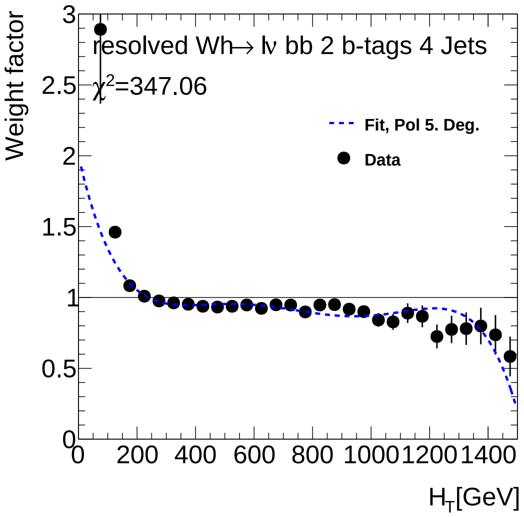

(a) 4 jets

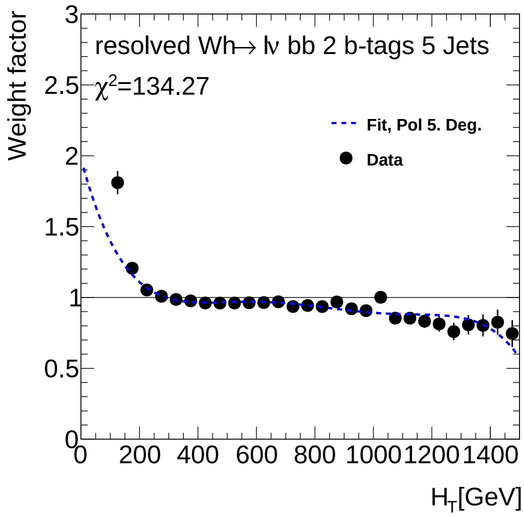

(b) 5 jets

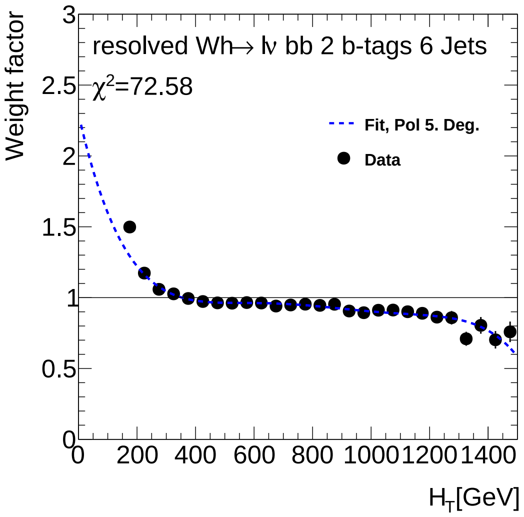

(c) 6 jets

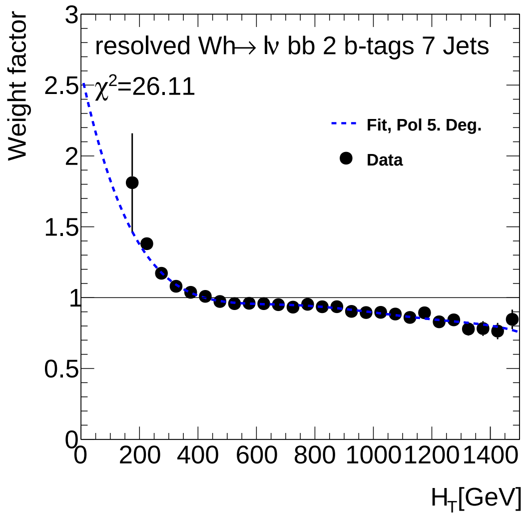

(d) 7 jets

Figure 5.27.: Weight factors, defined as $w = \frac{data - MC_{non-t\bar{t}}}{MC - t\bar{t}}$, as a function of the H_T variable. The weights are calculated for each jet multiplicity after the Monte Carlo predictions have been reweighted by weights extracted from the jet multiplicity distribution. Finally a polynomial function of 5th degree is fitted to the weight factors.

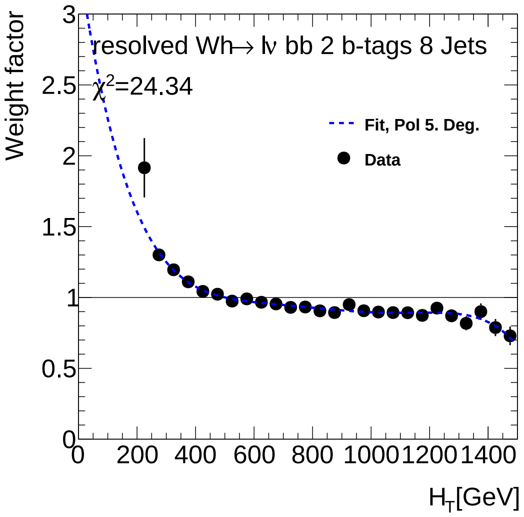

(a) 8 jets

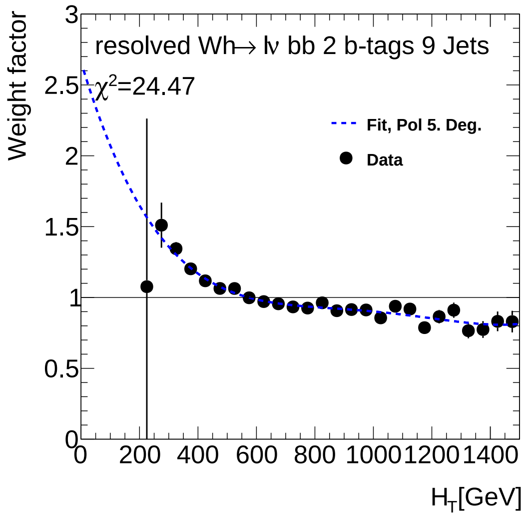

(b) 9 jets

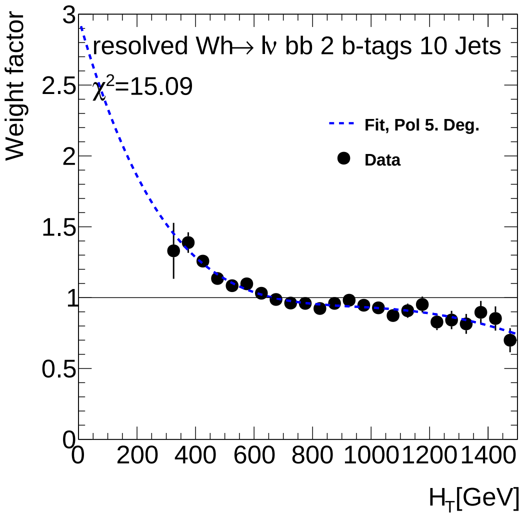

(c) 10 jets

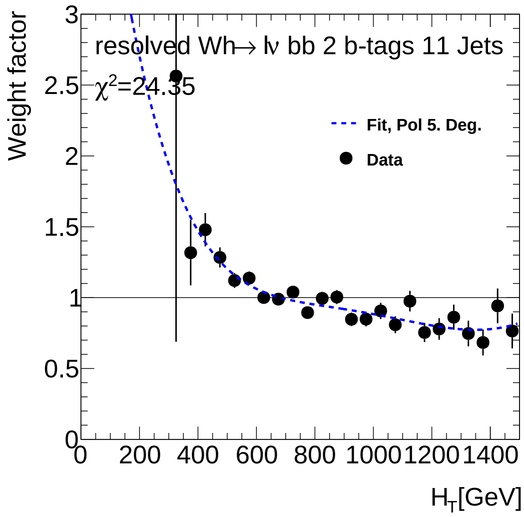

(d) 11+ jets

Figure 5.28.: Weight factors, defined as $w = \frac{data - MC_{non-t\bar{t}}}{MC - t\bar{t}}$, as a function of the H_T variable. The weights are calculated for each jet multiplicity after the Monte Carlo prediction have been reweighted by weights extracted from the jet multiplicity distribution. Finally a polynomial function of 5th degree is fitted to the weight factors.

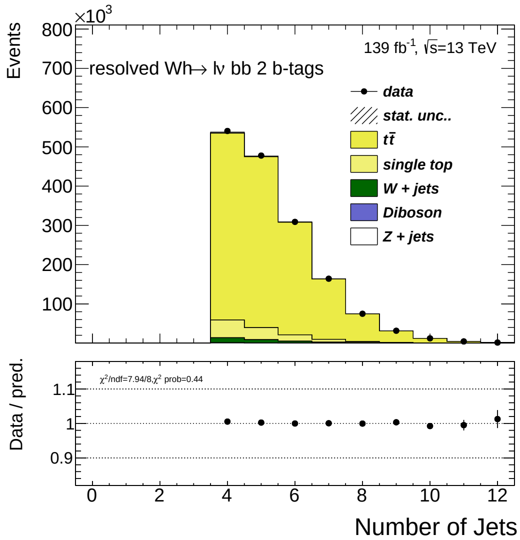

(a) Re-weighted in nJets& H_T

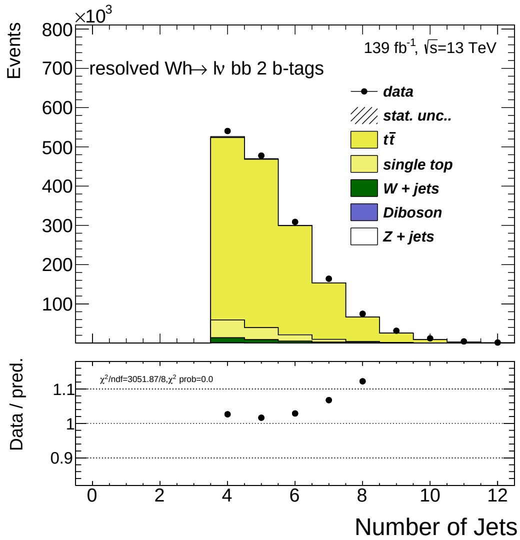

(b) Not Re-weighted

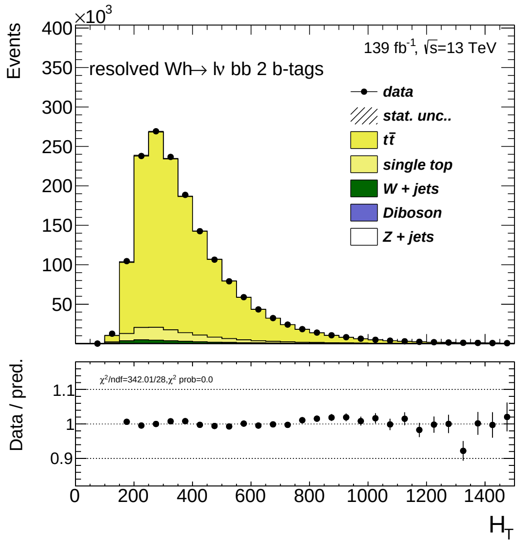

(c) Re-weighted in nJets& H_T

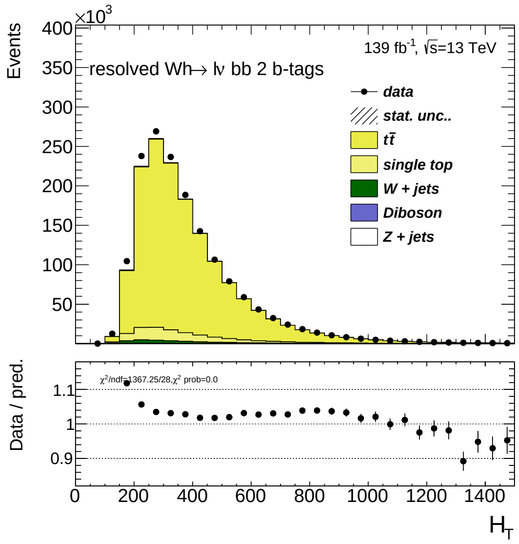

(d) Not Re-weighted

Figure 5.29.: Comparison of different variables before (right column) and after (left column) the sequential reweighting procedure in the 2 b-tag region.

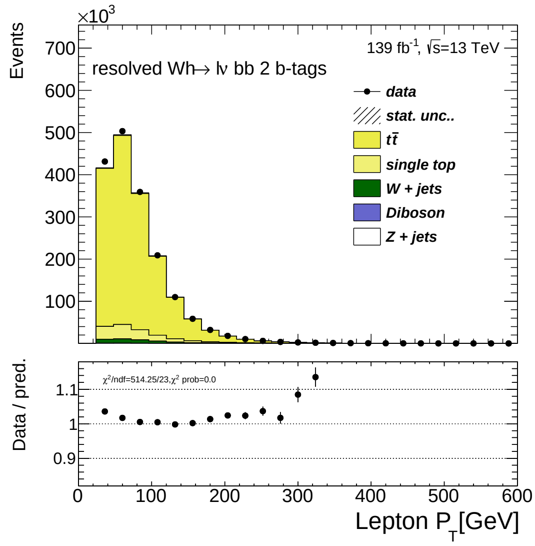

(a) Re-weighted in nJets& H_T

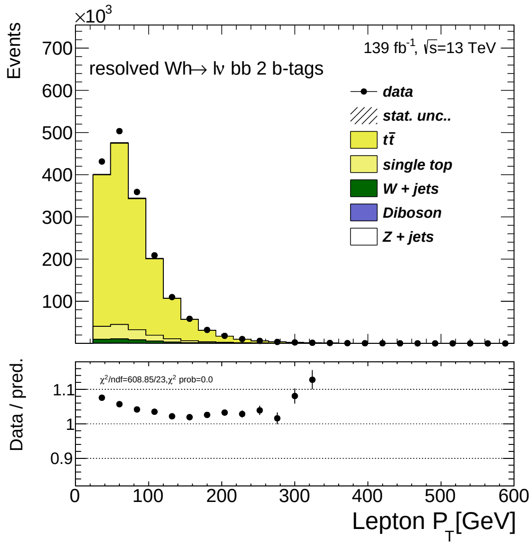

(b) Not Re-weighted

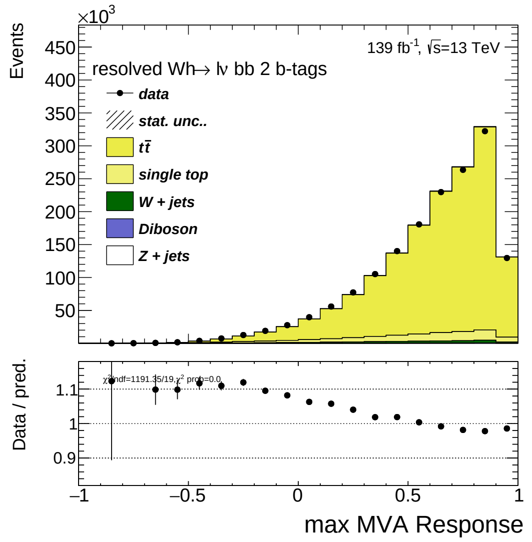

(c) Re-weighted in nJets& H_T

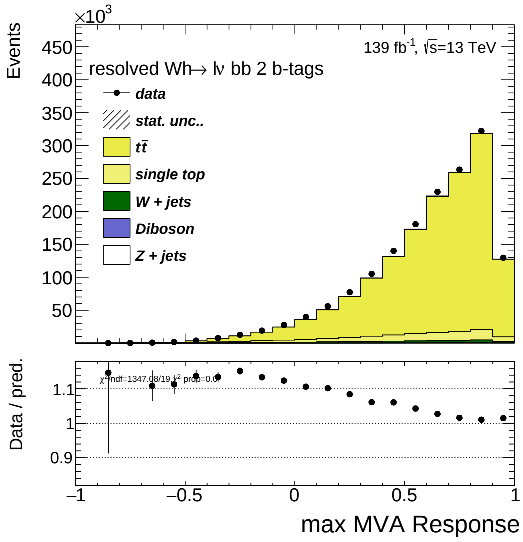

(d) Not Re-weighted

Figure 5.30.: Comparison of different variables before (right column) and after (left column) the sequential reweighting procedure in the 2 b-tag region.

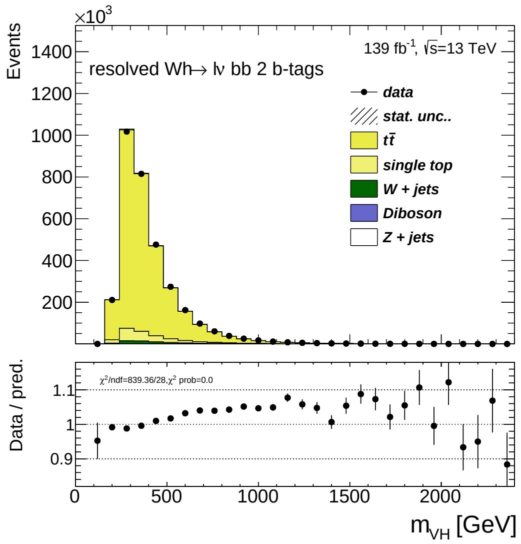

(a) Re-weighted in nJets& H_T

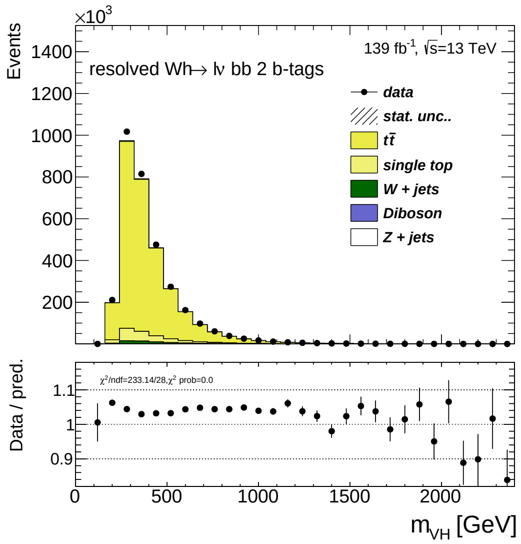

(b) Not Re-weighted

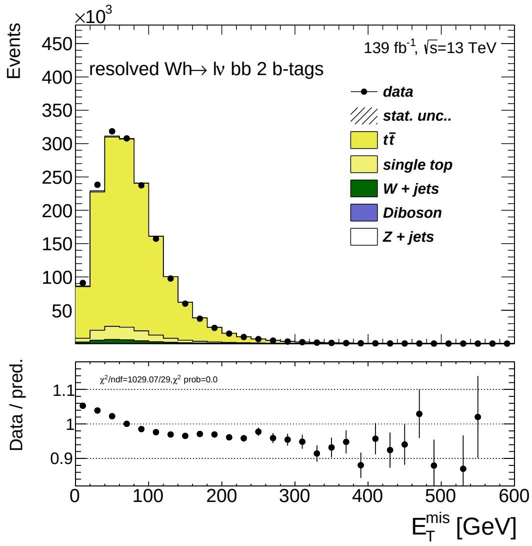

(c) Re-weighted in nJets& H_T

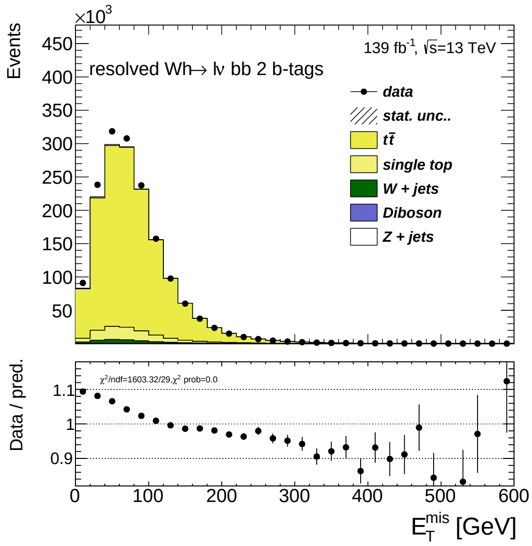

(d) Not Re-weighted

Figure 5.31.: Comparison of different variables before (right column) and after (left column) the sequential reweighting procedure in the 2 b-tag region.

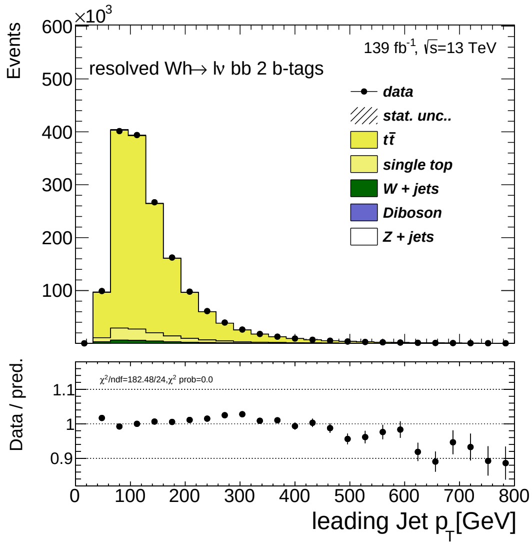

(a) Re-weighted in nJets& H_T

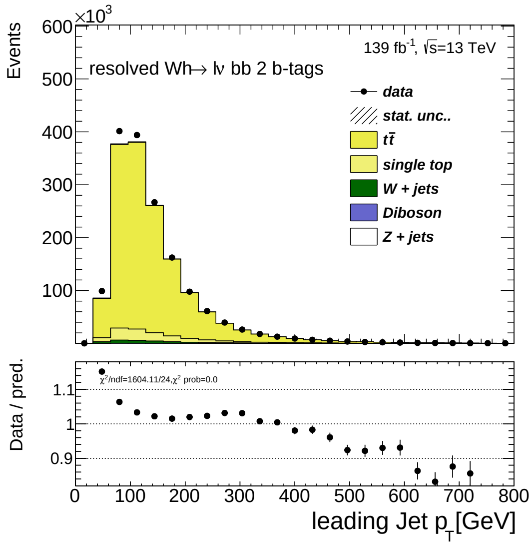

(b) Not Re-weighted

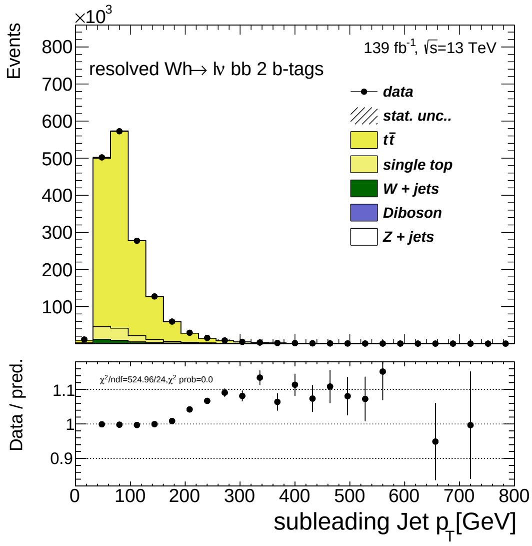

(c) Re-weighted in nJets& H_T

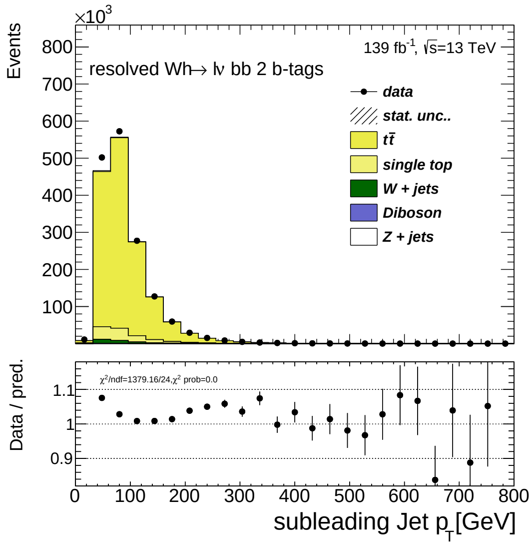

(d) Not Re-weighted

Figure 5.32.: Comparison of different variables before (right column) and after (left column) the sequential reweighting procedure in the 2 b-tag region.

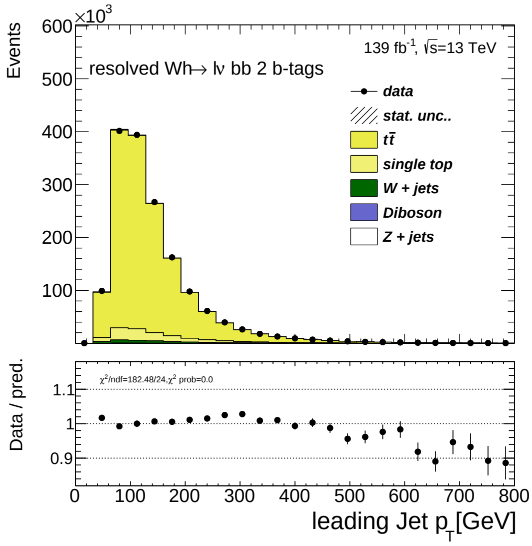

(a) Re-weighted in N^{Jets} & H_T

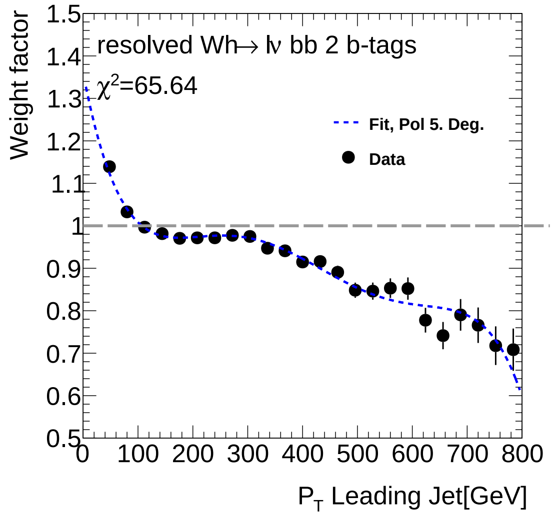

(b)

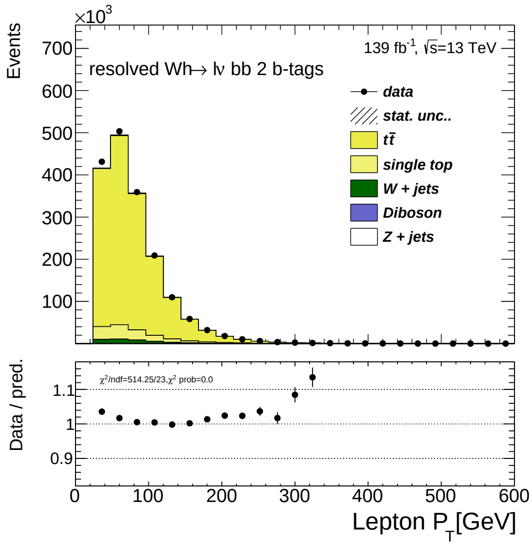

(c) Re-weighted in N^{Jets} & H_T

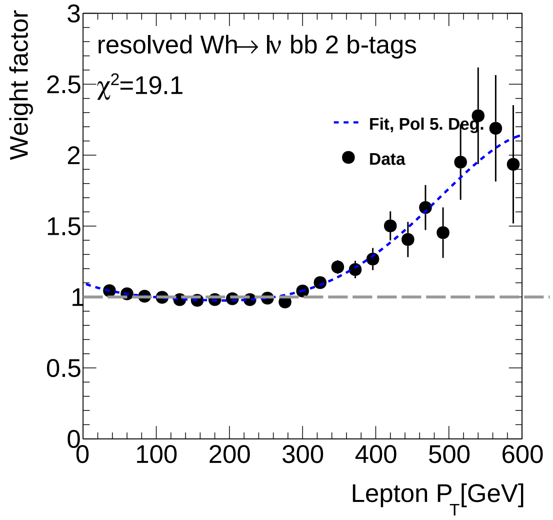

(d)

Figure 5.33.: Distributions of the lepton p_T and leading jet p_T variable after reweighting of the N^{Jets} and H_T spectra (left column) and the weight factors derived from the data-to-simulation ratios, using a 5th order polynomial fit.

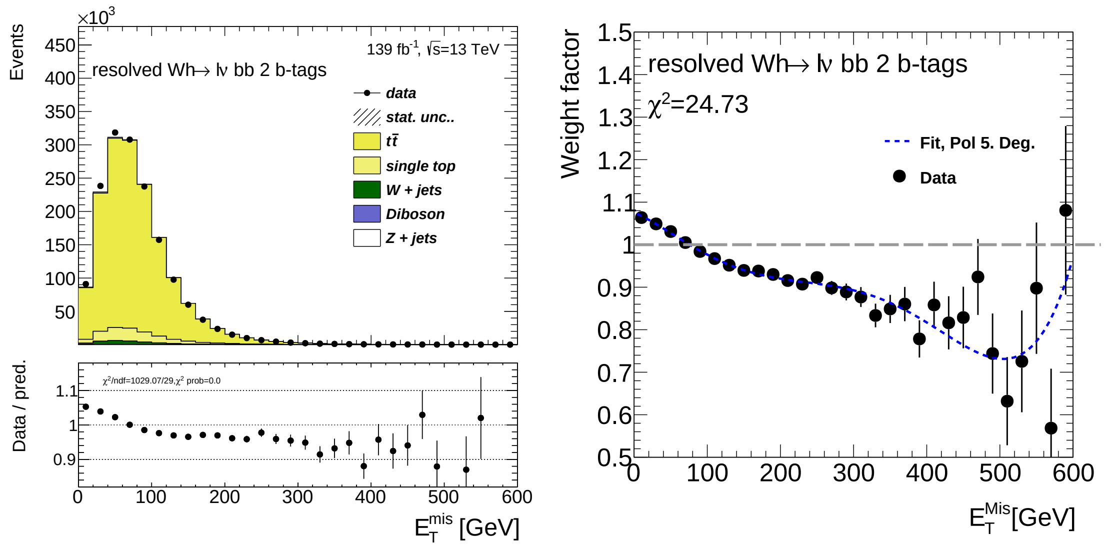

(a) Re-weighted in N^{Jets} & H_T (b)

Figure 5.34.: Distribution of the E_T^{miss} variable after reweighting of the N^{Jets} and H_T spectra (left column) and the weight factors derived from the data-to-simulation ratios, using a 5th order polynomial fit.

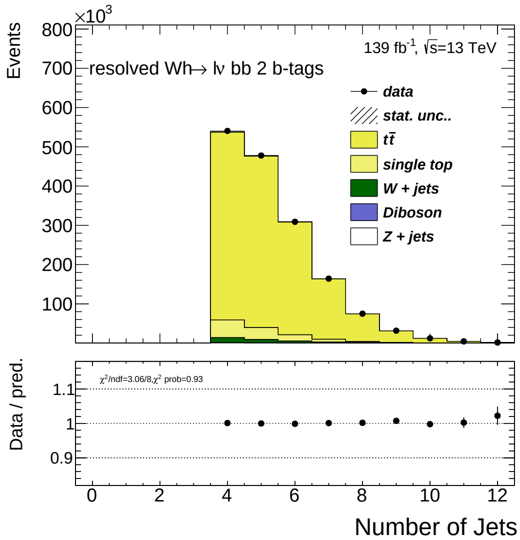

(a) Re-weighted in N^{Jets} & H_T & E_T^{miss}

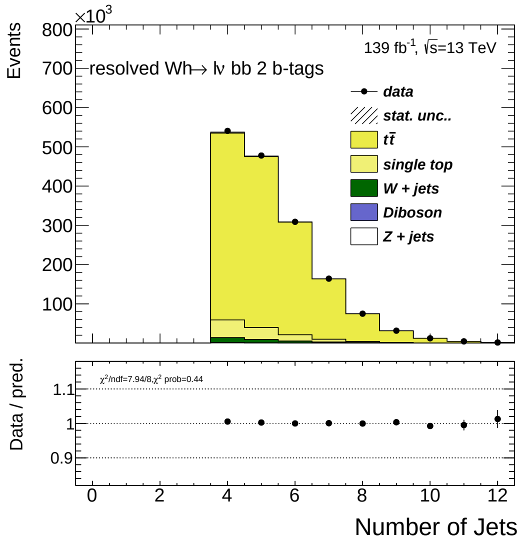

(b) Re-weighted in N^{Jets} & H_T

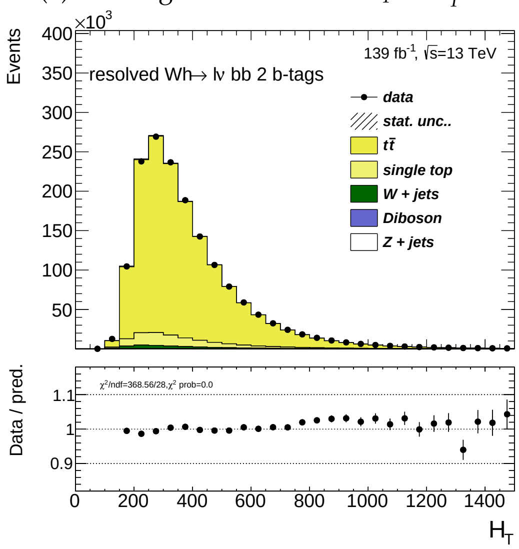

(c) Re-weighted in N^{Jets} & H_T & E_T^{miss}

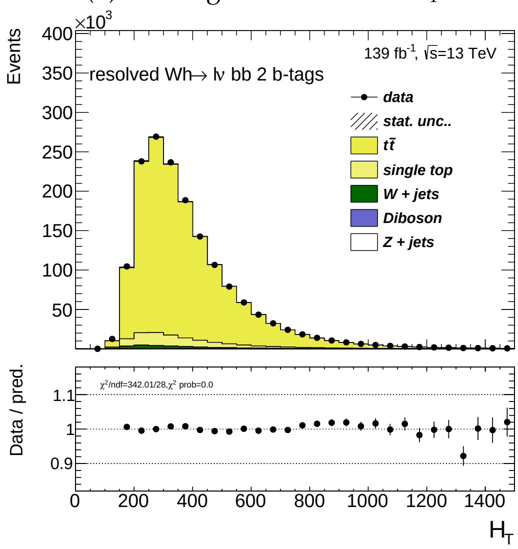

(d) Re-weighted in N^{Jets} & H_T

Figure 5.35.: Comparison of different variables reweighted in the N^{Jets} and H_T (right column) and after reweighting in nJets, H_T and the missing transverse energy (left column) in the 2 b-tag region.

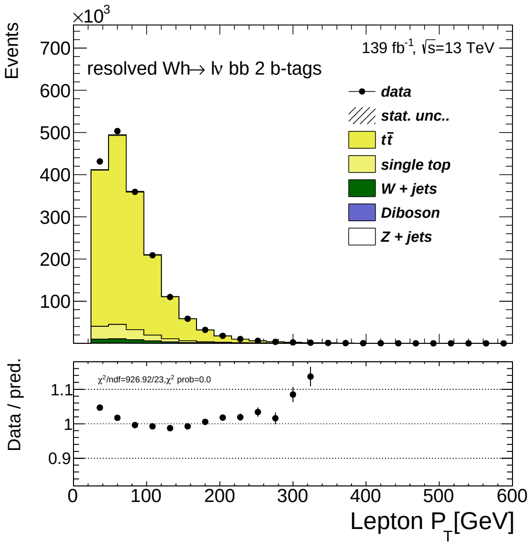

(a) Re-weighted in N^{Jets} & H_T & E_T^{miss}

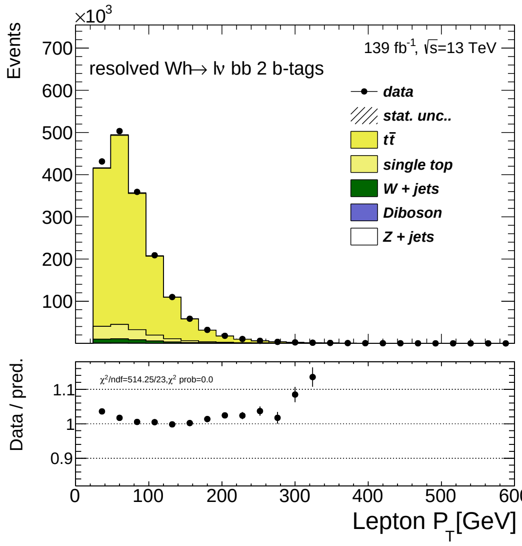

(b) Re-weighted in N^{Jets} & H_T

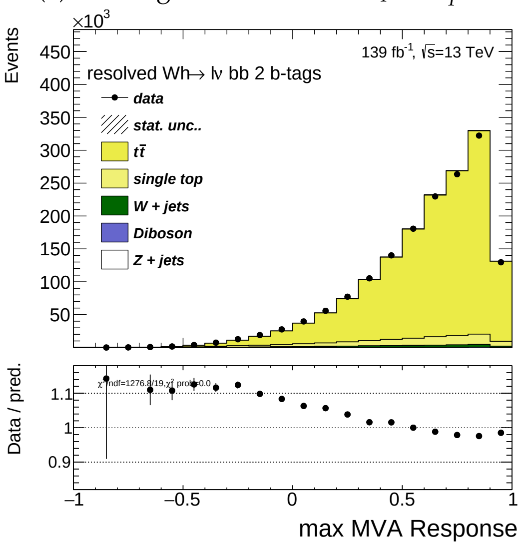

(c) Re-weighted in N^{Jets} & H_T & E_T^{miss}

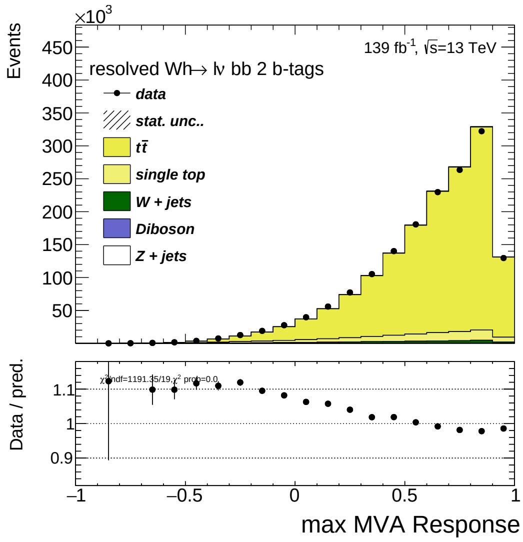

(d) Re-weighted in N^{Jets} & H_T

Figure 5.36.: Comparison of different variables reweighted in the N^{Jets} and H_T (right column) and after reweighting in nJets, H_T and the missing transverse energy (left column) in the 2 b-tag region.

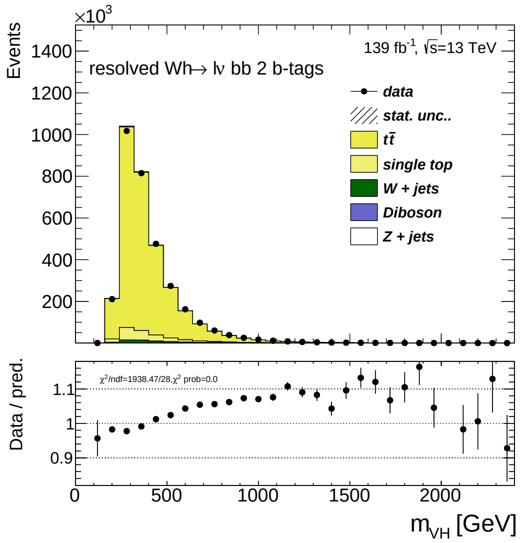

(a) Re-weighted in N^{Jets} & H_T & E_T^{miss}

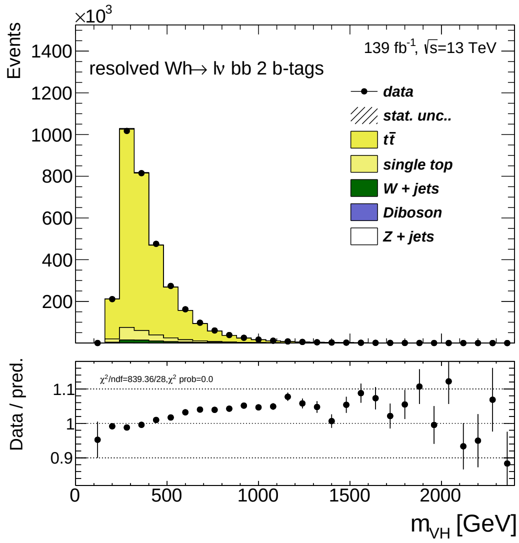

(b) Re-weighted in N^{Jets} & H_T

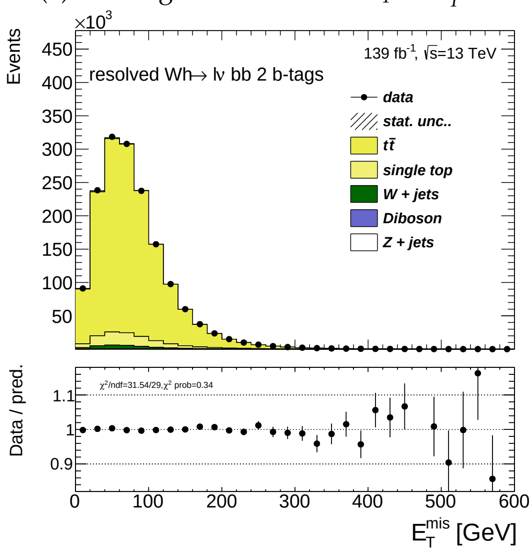

(c) Re-weighted in N^{Jets} & H_T & E_T^{miss}

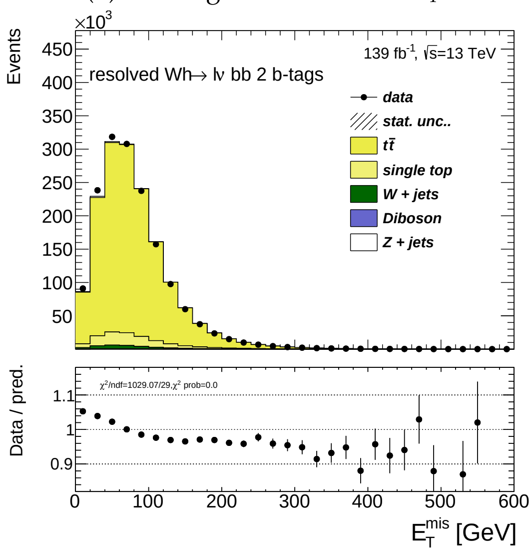

(d) Re-weighted in N^{Jets} & H_T

Figure 5.37.: Comparison of different variables reweighted in the N^{Jets} and H_T (right column) and after reweighting in nJets, H_T and the missing transverse energy (left column) in the 2 b-tag region.

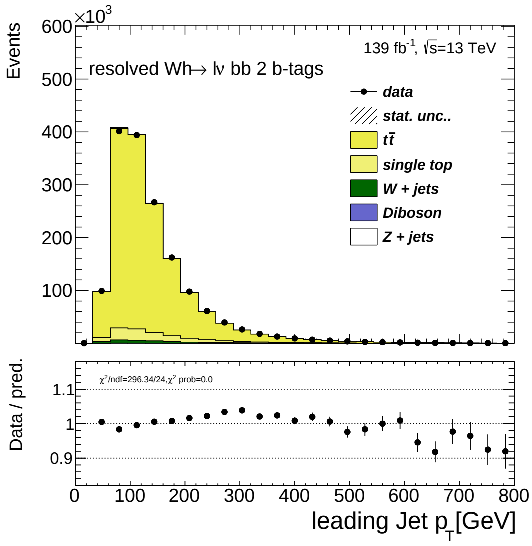

(a) Re-weighted in N^{Jets} & H_T & E_T^{miss}

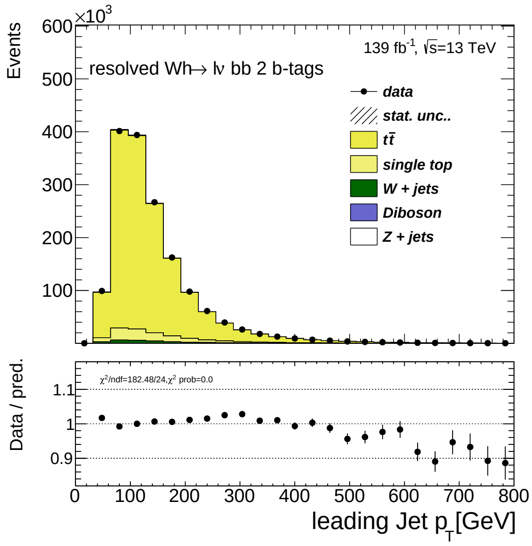

(b) Re-weighted in N^{Jets} & H_T

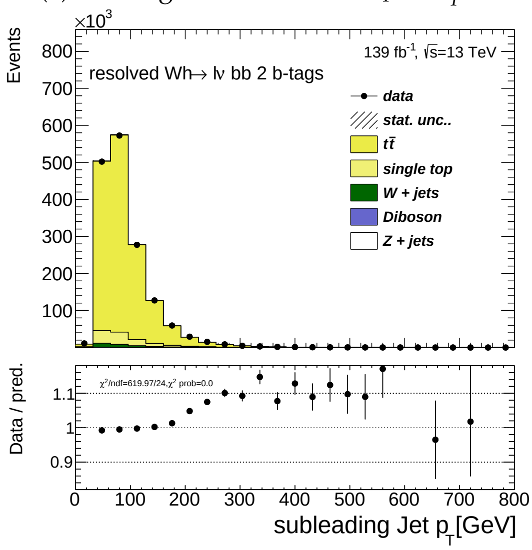

(c) Re-weighted in N^{Jets} & H_T & E_T^{miss}

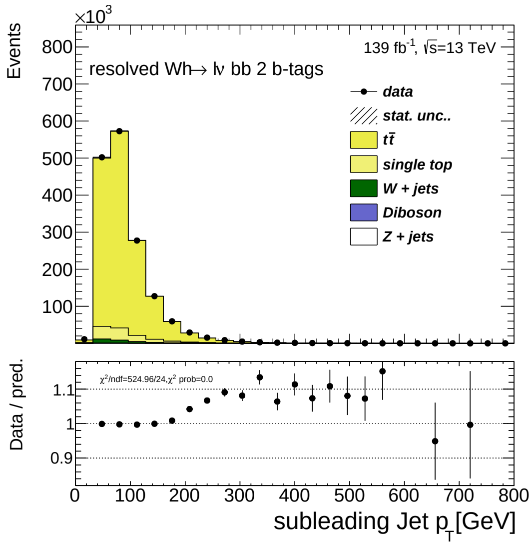

(d) Re-weighted in N^{Jets} & H_T

Figure 5.38.: Comparison of different variables reweighted in the N^{Jets} and H_T (right column) and after reweighting in nJets, H_T and the missing transverse energy (left column) in the 2 b-tag region.

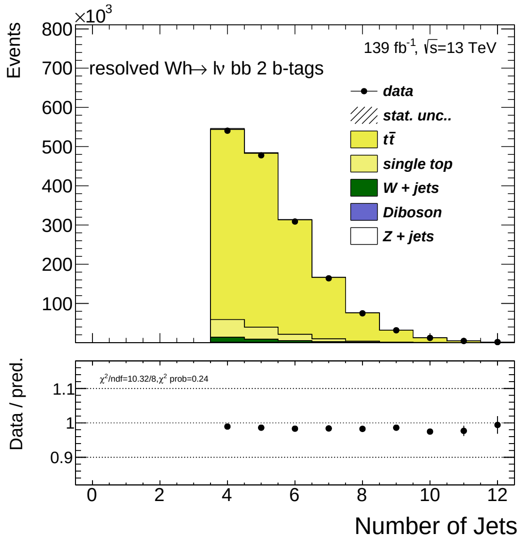

(a) Re-weighted in N^{Jets} & H_T & lepton p_T

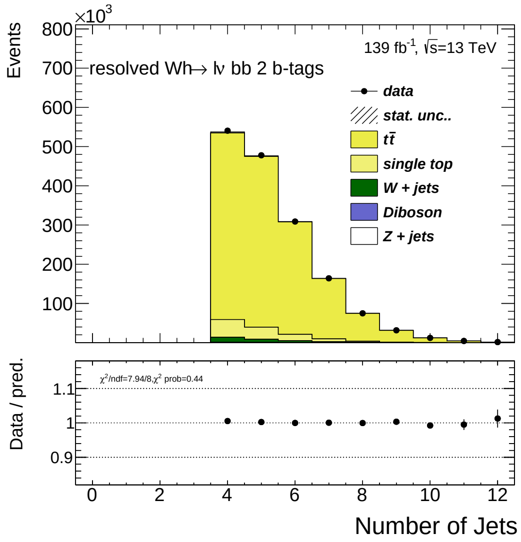

(b) Re-weighted in N^{Jets} & H_T

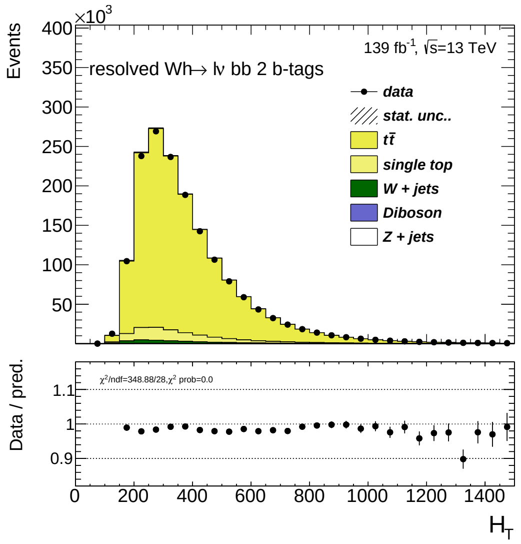

(c) Re-weighted in N^{Jets} & H_T & lepton p_T

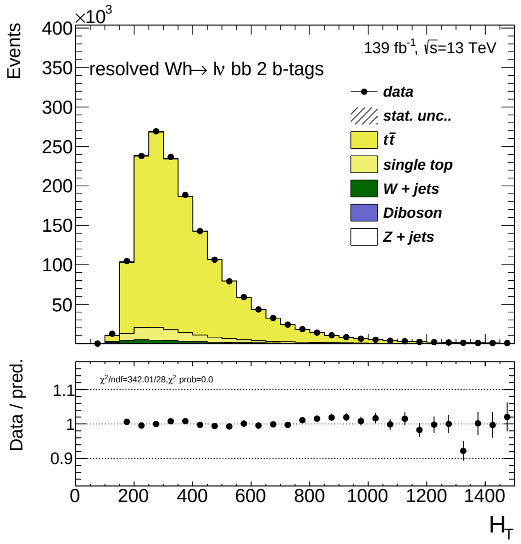

(d) Re-weighted in N^{Jets} & H_T

Figure 5.39.: Data-to-simulation comparison of the jet multiplicity (top row) and the H_T (bottom row) distributions shown for different versions of the reweighting procedure.

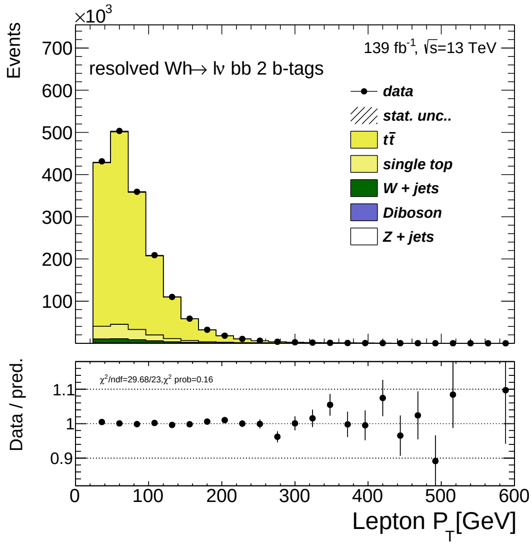

(a) Re-weighted in N^{Jets} & H_T & lepton p_T

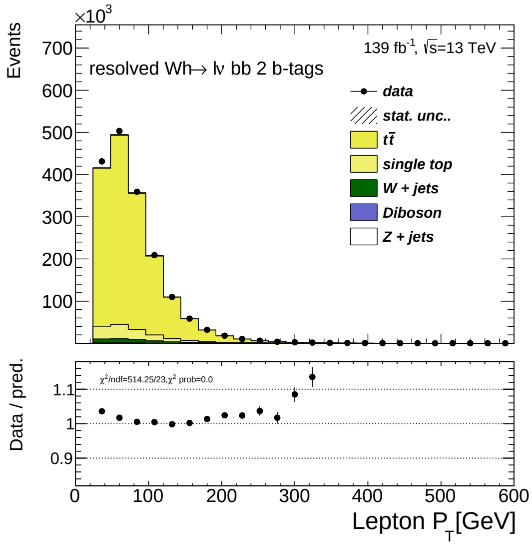

(b) Re-weighted in N^{Jets} & H_T

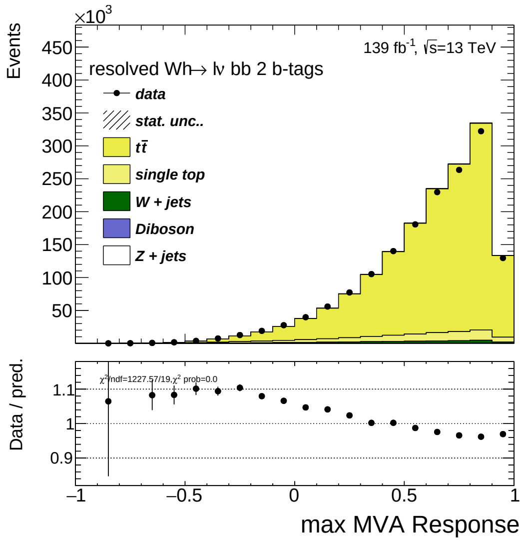

(c) Re-weighted in N^{Jets} & H_T & lepton p_T

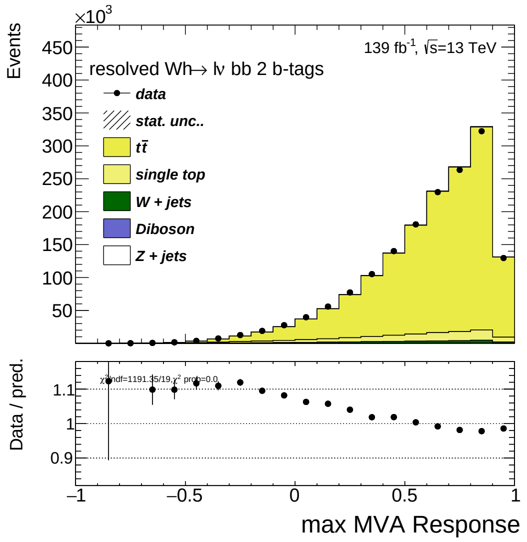

(d) Re-weighted in N^{Jets} & H_T

Figure 5.40.: Data-to-simulation comparison of the lepton p_T (top row) and max MVA Response (bottom row) distributions shown for different versions of the reweighting procedure.

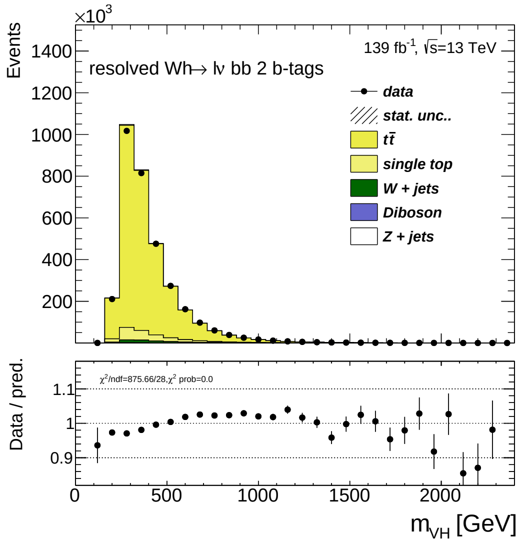

(a) Re-weighted in N^{Jets} & H_T & lepton p_T

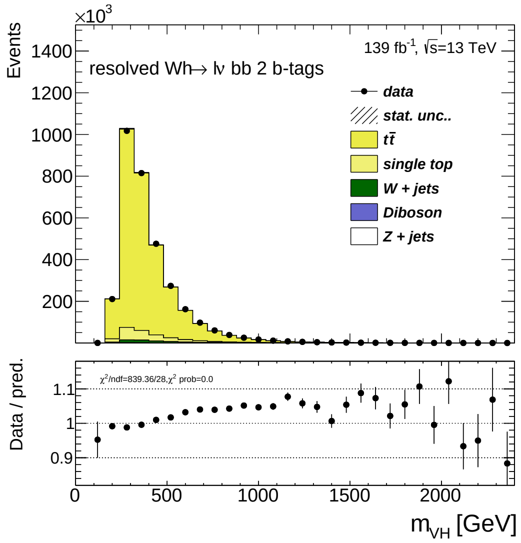

(b) Re-weighted in N^{Jets} & H_T

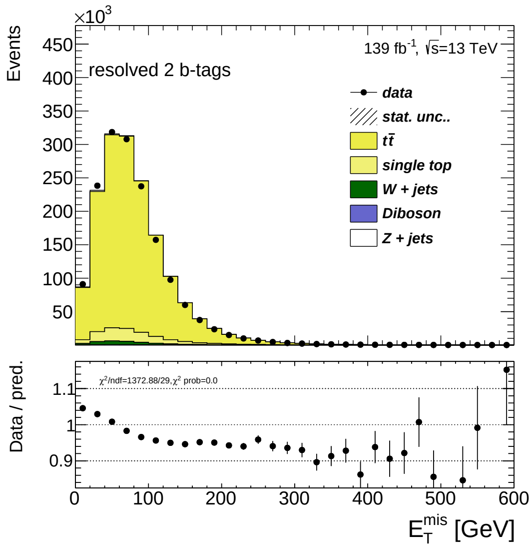

(c) Re-weighted in N^{Jets} & H_T & lepton p_T

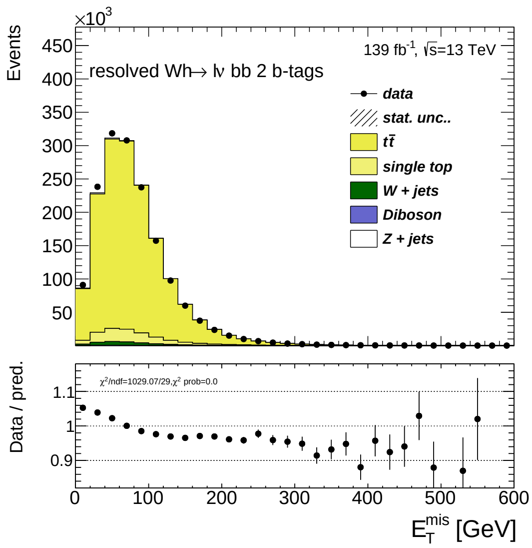

(d) Re-weighted in N^{Jets} & H_T

Figure 5.41.: Data-to-simulation comparison of the m_{Wh}(top row) and missing transverse energy E_T^{miss} (bottom row) distributions shown for different versions of the reweighting procedure.

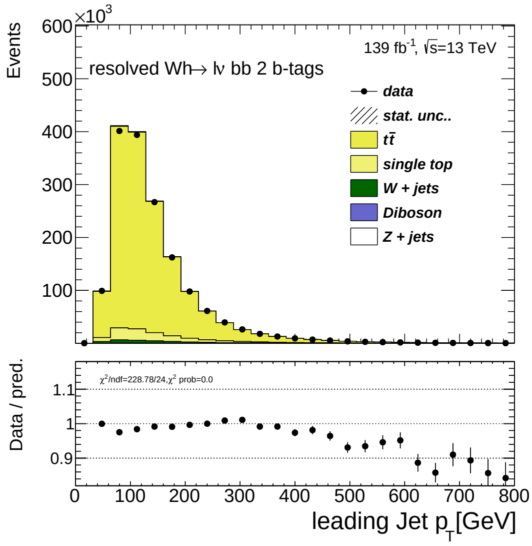

(a) Re-weighted in N^{Jets} & H_T & lepton p_T

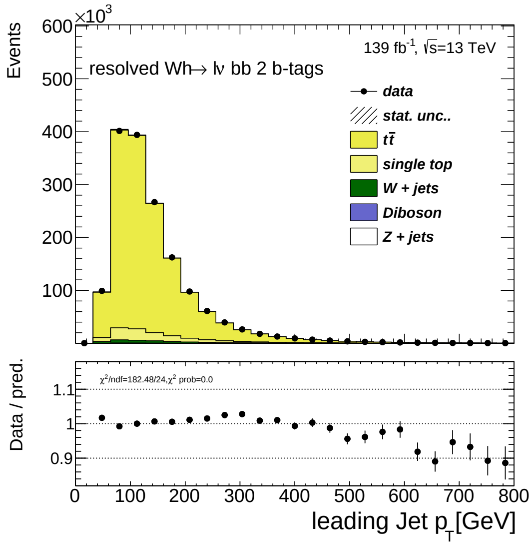

(b) Re-weighted in N^{Jets} & H_T

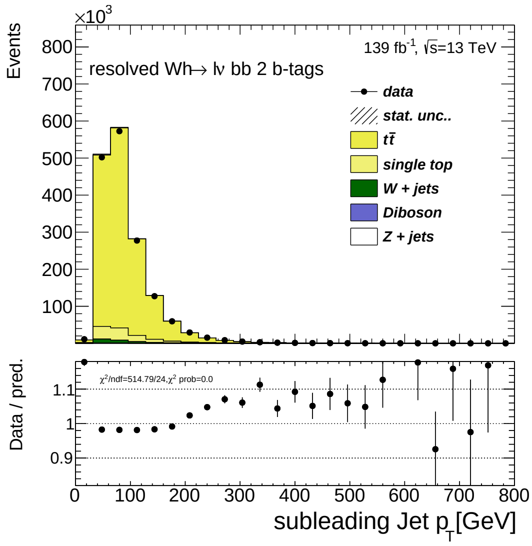

(c) Re-weighted in N^{Jets} & H_T & lepton p_T

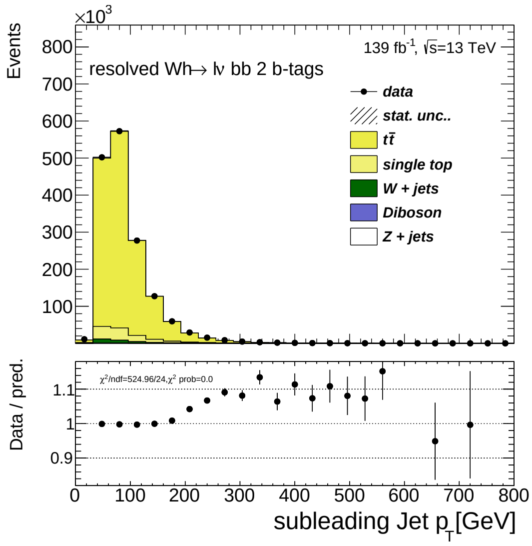

(d) Re-weighted in N^{Jets} & H_T

Figure 5.42.: Data-to-simulation comparison of the leading (top row) and subleading (bottom row) jet p_T distributions shown for different versions of the reweighting procedure.

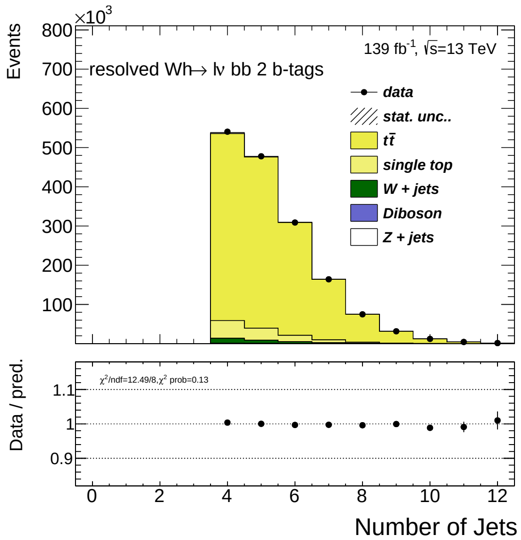

(a) Re-weighted in N^{Jets} & H_T & leading jet p_T

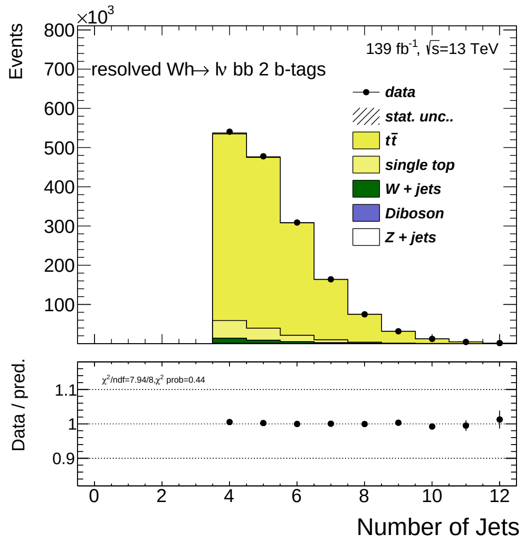

(b) Re-weighted in N^{Jets} & H_T

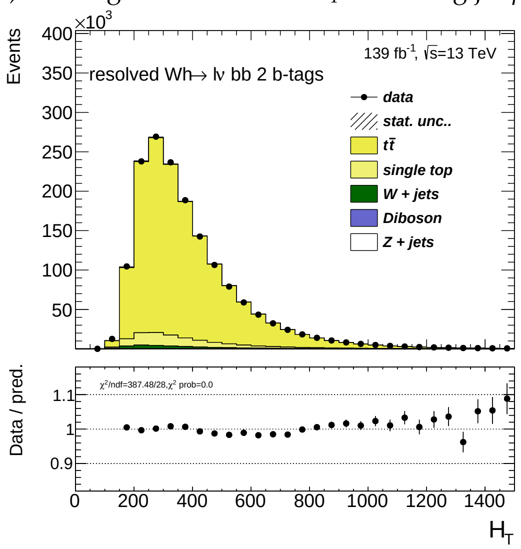

(c) Re-weighted in N^{Jets} & H_T & leading jet p_T

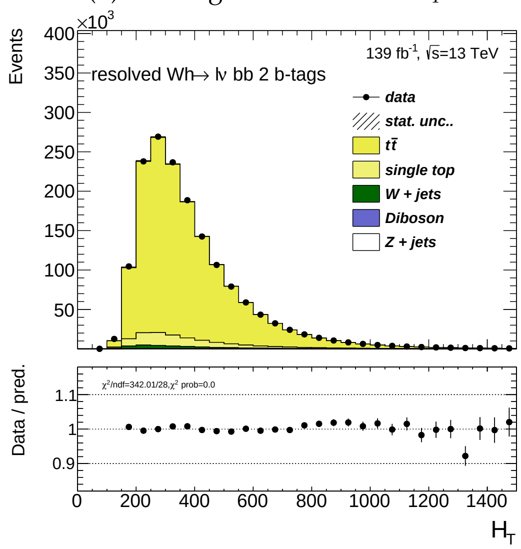

(d) Re-weighted in N^{Jets} & H_T

Figure 5.43.: Data-to-simulation comparison of the jet multiplicity (top row) and the H_T (bottom row) distributions shown for different versions of the reweighting procedure.

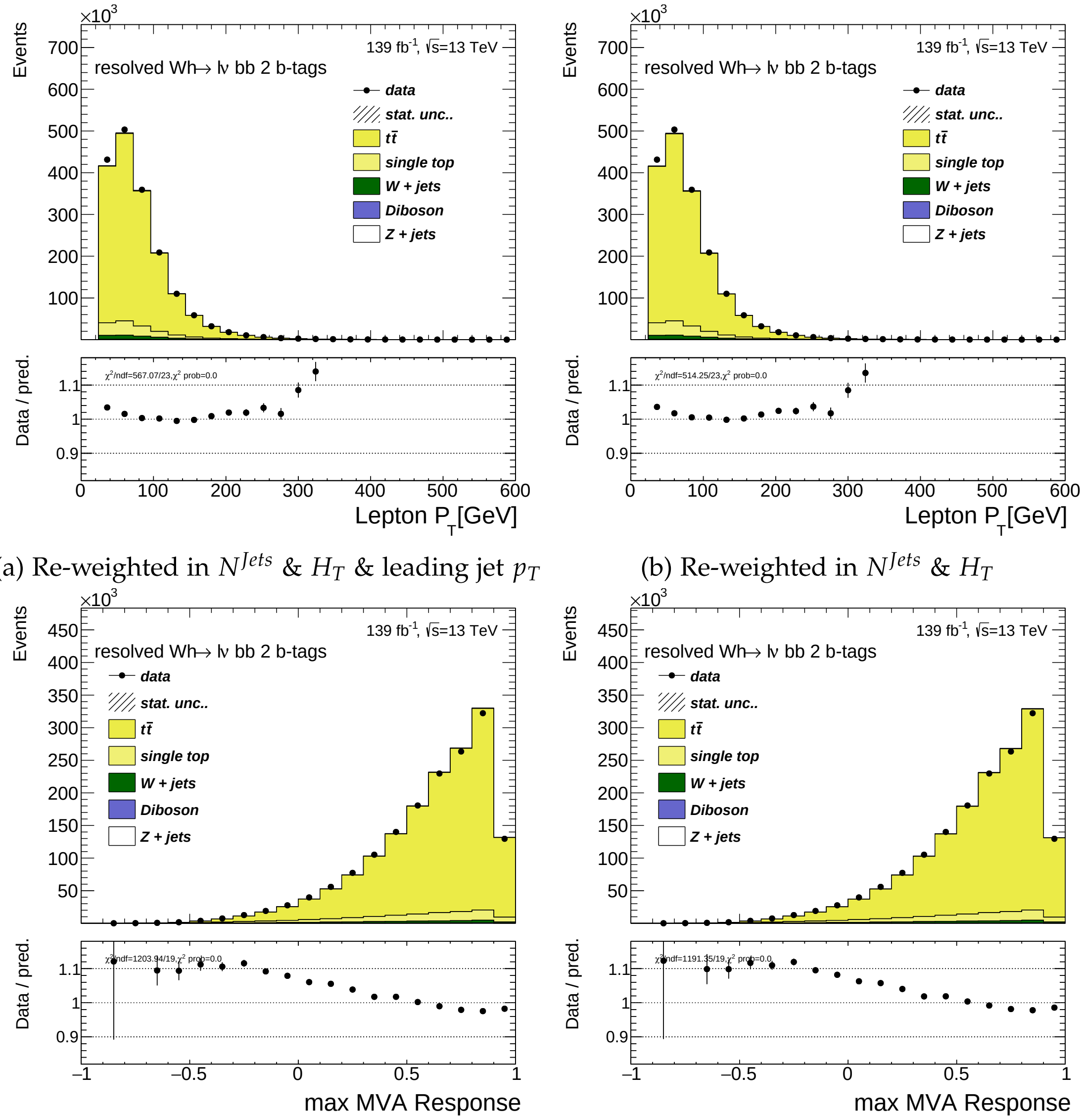

(a) Re-weighted in N^{Jets} & H_T & leading jet p_T

(b) Re-weighted in N^{Jets} & H_T

(c) Re-weighted in N^{Jets} & H_T & leading jet p_T

(d) Re-weighted in N^{Jets} & H_T

Figure 5.44.: Data-to-simulation comparison of the lepton p_T (top row) and max MVA Response (bottom row) distributions shown for different versions of the reweighting procedure.

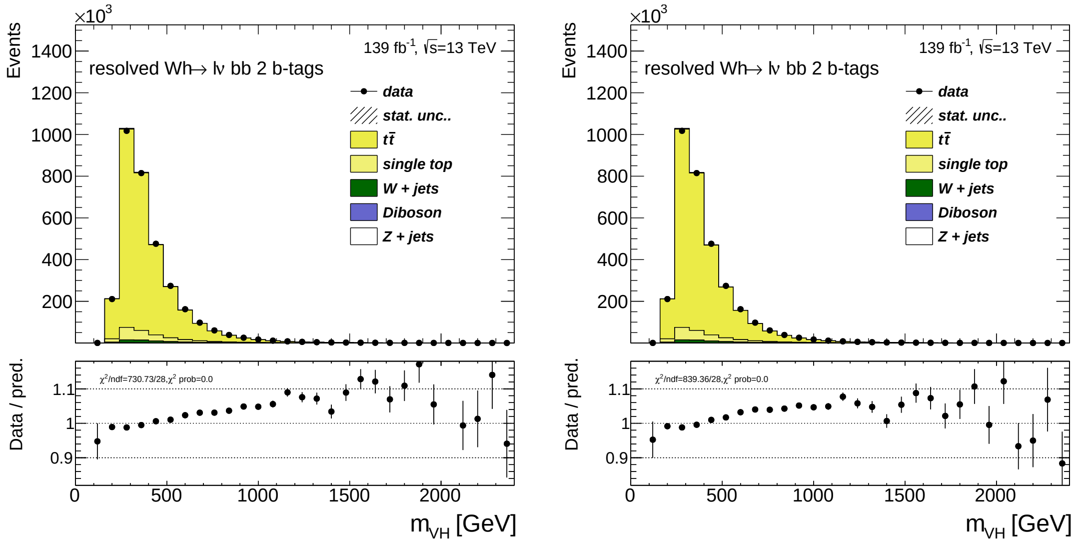

(a) Re-weighted in N^{Jets} & H_T & leading jet p_T (b) Re-weighted in N^{Jets} & H_T

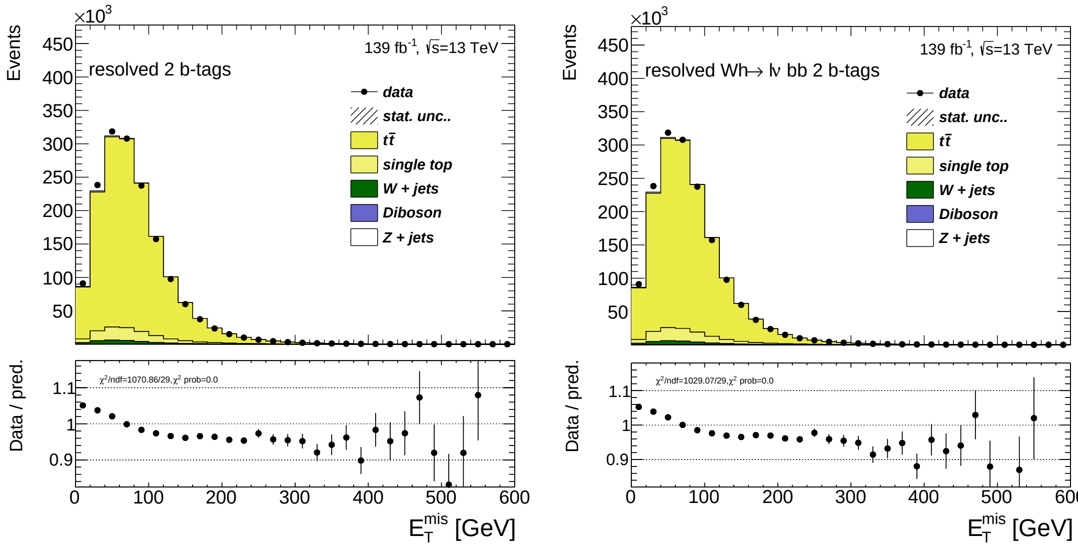

(c) Re-weighted in N^{Jets} & H_T & leading jet p_T (d) Re-weighted in N^{Jets} & H_T

Figure 5.45.: Data-to-simulation comparison of the m_{Wh} (top row) and missing transverse energy E_T^{miss} (bottom row) distributions shown for different versions of the reweighting procedure

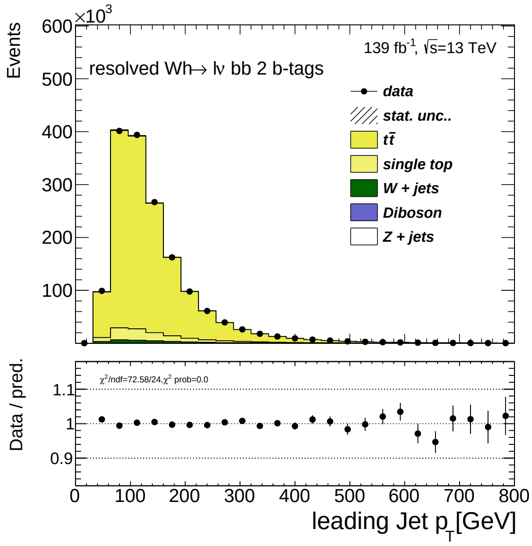

(a) Re-weighted in N^{Jets} & H_T & leading jet p_T

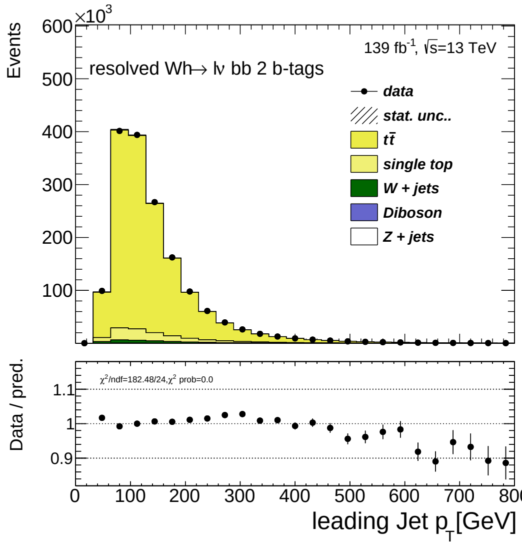

(b) Re-weighted in N^{Jets} & H_T

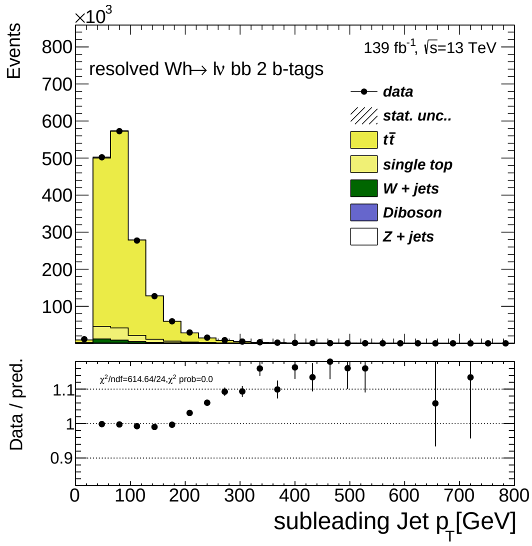

(c) Re-weighted in N^{Jets} & H_T & leading jet p_T

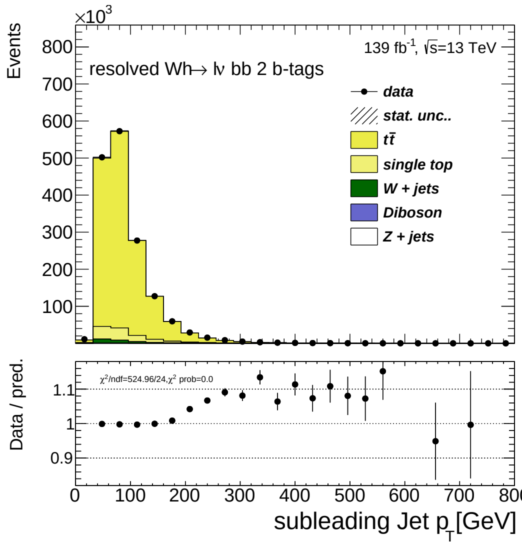

(d) Re-weighted in N^{Jets} & H_T

Figure 5.46.: Data-to-simulation comparison of the leading (top row) and subleading (bottom row) jet p_T distributions shown for different versions of the reweighting procedure

5.7. Systematic Uncertainties

The search for charged Higgs bosons in $H^+ \to Wh$ deacys is affected by many sources of systematic uncertainties. Examples are the uncertainties on the luminosity measurement, the signal and background modelling or uncertainties on the calibration of the energy/momentum scale and resolution for leptons and/or jets as well as the reconstruction and identification efficiencies [23]. However, for this thesis, a simplified approach in the treatment of systematic uncertainties is used. Only uncertainties on the background normalization and on the modelling of the $t\bar{t}$ background are considered as it is know from other analysis studying the same final state that these are the dominating sources of uncertainties [48, 91].

The effects of the uncertainties on the shape of the m_{Wh} distribution are considered. These uncertainties are derived by comparing nominal and alternative event generators and parton shower models. This is done separately in each b-tagging category.

Uncertainties associated with the parton shower model are derived by comparing the shapes of the nominal $t\bar{t}$ sample which is generated with POWHEG BOX 2 [84] and PYTHIA 8 [80] for simulating the parton shower to a sample where the parton shower has been simulated using HERWIG 7 [92]. The corresponding comparison is depicted in figure 5.47. POWHEG BOX 2 + PYTHIA 8 predicts more events for low masses below 500 GeV, here the ratios ranges up to 1.3, while POWHEG BOX 2 + HERWIG 7 predicts more events at higher masses above 500 GeV. The ratio increases with increasing m_{Wh} and goes to about 0.5.

To estimate the uncertainty in the matching between the matrix element and the parton shower generators, the samples generated using POWHEG BOX 2+ PYTHIA 8 have been compared to samples generated using MadGraph5_aMC@NLO [81] and PYHTIA 8, as shown in figure 5.49. The sample with generated with POWHEG BOX 2 predicts more events at low masses (below a m_{Wh} of about 500 GeV), as the ratios go up to about 1.5. Above a m_{Wh} of 500 GeV, MadGraph5_aMC@NLO predicts more events. Here, the ratios range up to about 0.5.

Two further samples produced with POWHEG BOX 2 + PYTHIA 8 are used to study the impact of an increased or decreased amount of initial and final state radiation (ISR/FSR) produced in association with the $t\bar{t}$ system. In these samples, the settings of the renormalisation and factorisation scales μ_N and μ_F as well as the so-called hdamp parameter (which sets the resummation scale) have been adjusted to cover the experimental uncertainties on previous N^{jet} and gap fraction measurements [93]. The scales

μ_N and μ_F are shifted up (down) by a factor of 2 (0.5), while the hdamp parameter is set to 3.0 times the top-quark mass for the sample corresponding to a decreased amount of radiation and to 1.5 times the top-quark mass for the sample corresponding to an increased amount of radiation. The comparison between those two samples is shown in figure 5.48 separately for the 2-tag, 3-tag, and 4-tag categories. The sample with decreased radiation predicts slightly more events at low masses, as the ratios go up to about 1.1. The differences are more pronounced in the tails of the distributions. Here, the ratios range up to about 0.5. I.e. the sample with increased radiation predicts more events at these high m_{Wh} values.

To account for uncertainties associated with the reweighting procedure described in subsection 5.6.1, the m_{Wh} distribution of the nominal $t\bar{t}$ sample is compared to the nominal sample after the sequential reweighting procedure in N^{jets} and H_T was applied. These comparisons are presented in figure 5.50. The reweighting procedure shifts the m_{Wh} distribution to higher masses. In the tail of the distributions the ratio ranges up to about 0.6.

In addition to these modelling uncertainties, uncertainties on the cross-section predictions of the backgrounds and the luminosity measurements are taken into account [74, 94]. Table 5.11 summaries all the systematic uncertainties on the background normalization.

Table 5.11.: The uncertainties on the normalization of the background processes and the luminosity measurement.

Diboson normalization	50%
Single top normalization	50%
W/Z +jets normalization	50%
Luminosity	1.9%

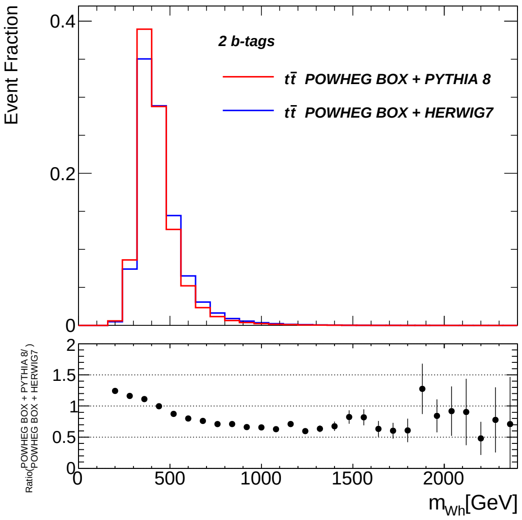

(a)

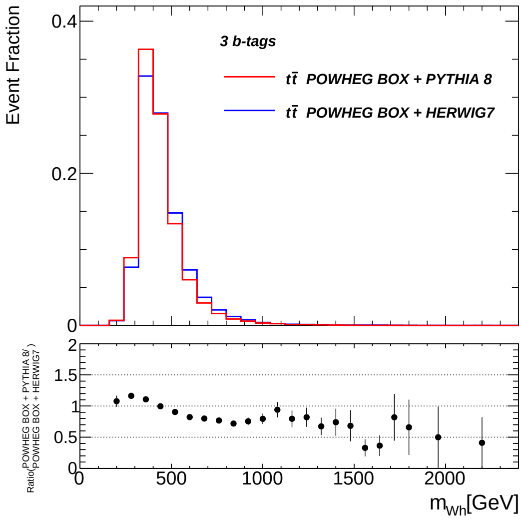

(b)

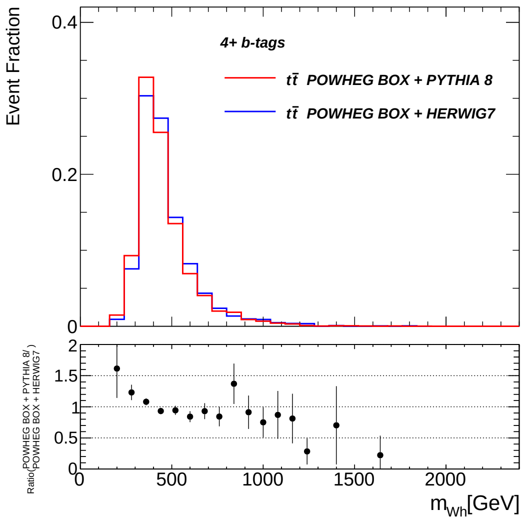

(c)

Figure 5.47.: A comparison between the normalized distributions of two $t\bar{t}$ samples generated using different generators. One using POWHEG BOX 2 and PYTHIA 8, the other one using POWHEG BOX 2 and HERWIG 7. The ratio of these two samples is used to estimate the uncertainty associated with the parton shower model.

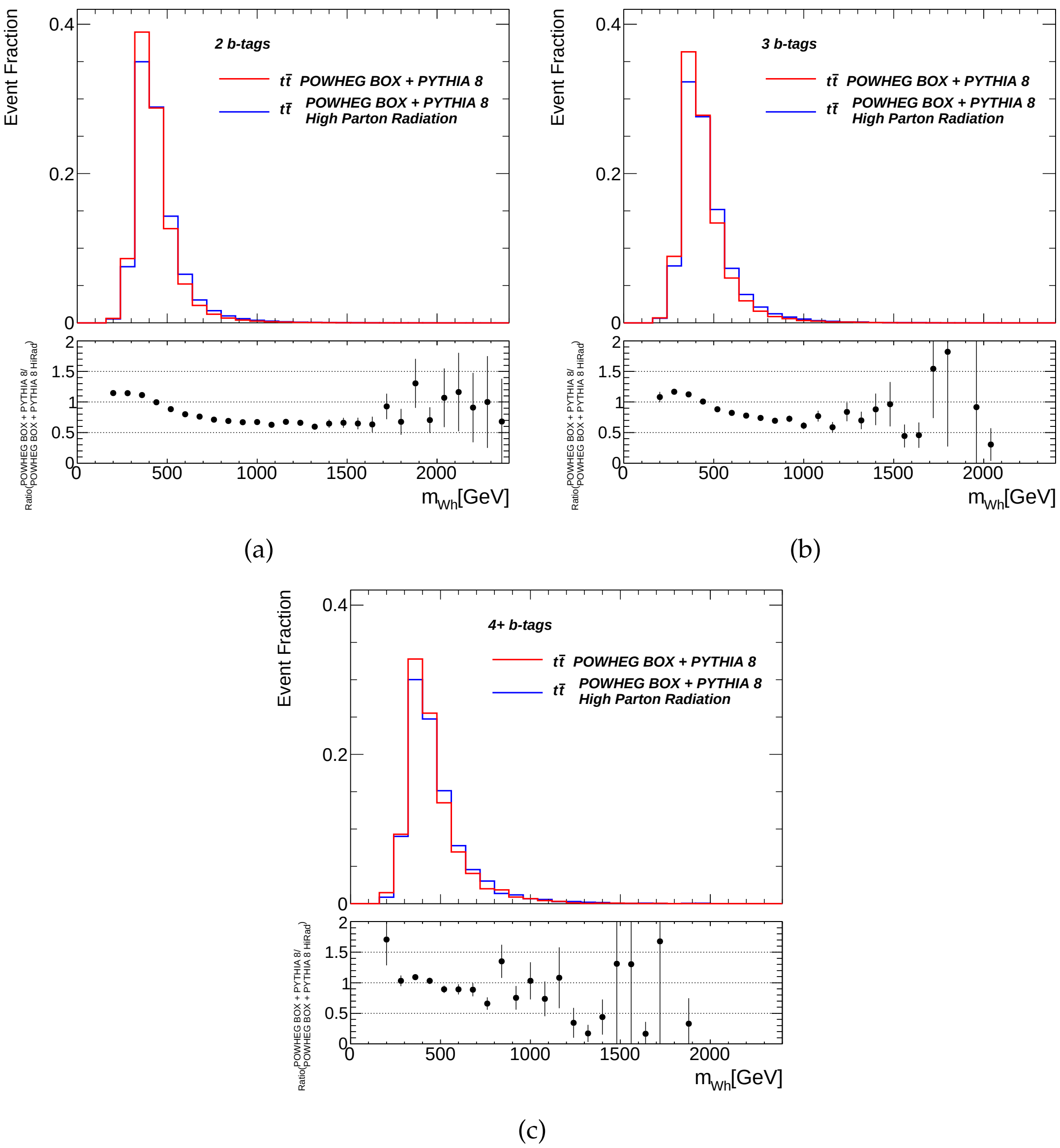

Figure 5.48.: A comparison between the normalized distributions of two $t\bar{t}$ samples generated using different generators. One using POWHEG BOX 2 and PYTHIA 8, the other one using POWHEG BOX 2 and PYTHIA 8 with increased parton radiation. The ratio of these two samples is used to estimate the uncertainty associated with the initial and final state radiation model.

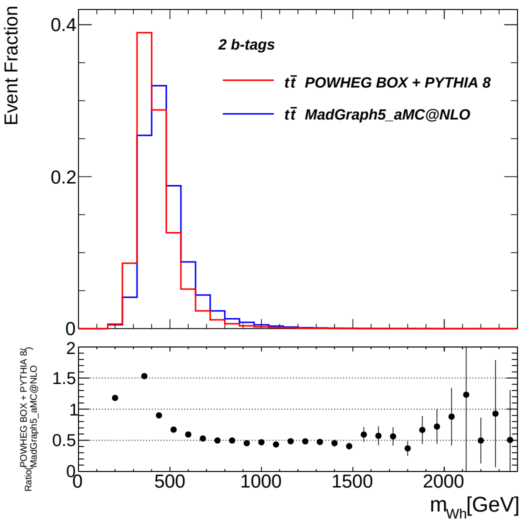

(a)

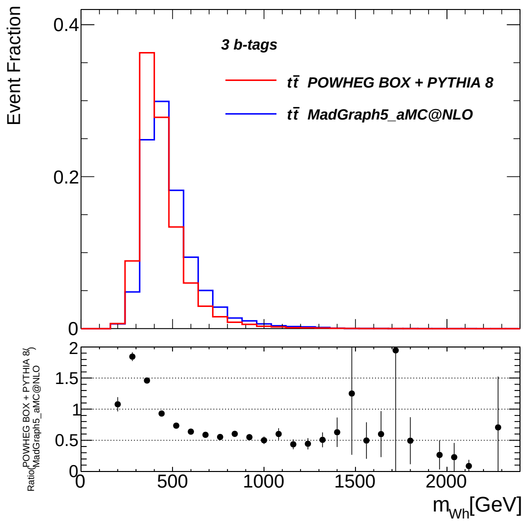

(b)

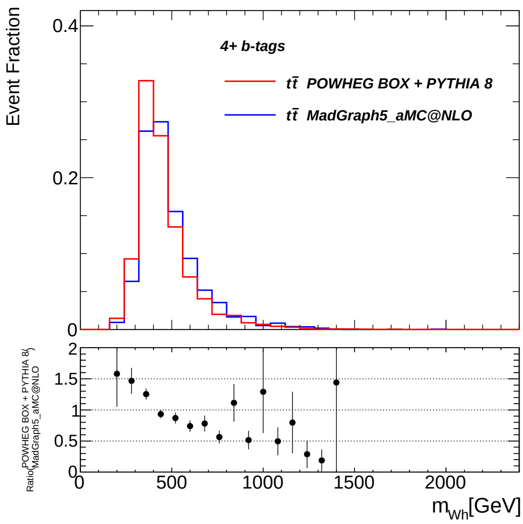

(c)

Figure 5.49.: A comparison between the normalized distributions of two $t\bar{t}$ samples generated using different generators. One using POWHEG BOX 2 and PYTHIA 8, the other one using MadGraph5_aMC@NLO and PYTHIA 8. The ratio of these two samples is used to estimate the uncertainty associated with the matching between the matrix element and the parton shower generator.

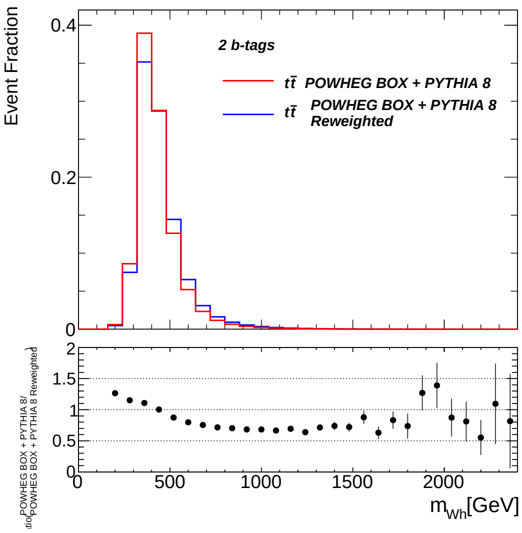

(a)

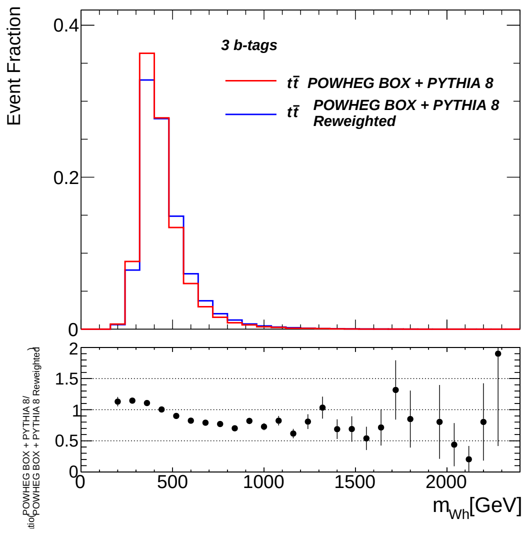

(b)

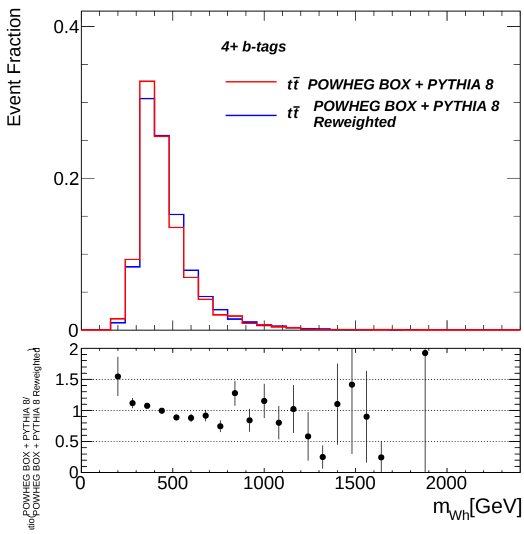

(c)

Figure 5.50.: A comparison between the normalized distributions of two $t\bar{t}$ samples. The first samples is generated using POWHEG BOX 2 and PYTHIA 8, the other one was also generated using POWHEG BOX 2 and PYTHIA 8 and additionally the sequential reweighting procedure described in subsection 5.6.1 was applied The ratio of these two samples is used to estimate the uncertainty associated with the data-correction procedure described in subsection 5.6.1.

5.8. Statistical Analysis

The results of the $H^+ \to Wh$ search are expressed as expected upper limits on the cross-section times branching ratio for the $pp \to tbH^+ \to tbWh$ process. At this stage only expected upper limits are calculated, as the signal regions are still blinded[4]. The expected upper limits are obtained by performing a simultaneous profile likelihood fit [95] on the expected signal and background distributions of the reconstructed charged Higgs boson mass m_{Wh}. These distributions are presented in figure 5.17 and figure 5.18 for the signal and control regions, respectively. The likelihood function $L(\mu, \Theta)$ used for this analysis, is given by the product of 2 poisson probabilities P in each bin j and each category i (i.e. the different b-tagging categories)

$$L(\mu, \Theta) = \prod_{i}^{N_{category}} \prod_{j}^{N_{bins}} P(N_{i,j}|S_{i,j}(\mu, \Theta) + B_{i,j}(\Theta)) \prod_{m} f(\Theta), \tag{5.9}$$

where μ is the parameter of interest (i.e. the signal strength), Θ the nuisance parameters accounting for systematic uncertainties, N is the observed number of events, S the expected number of signal events, and B the expected number of background events. The term $f(\Theta)$ is used to constrain the nuisance parameters by auxiliary measurements.

The m_{Wh} distributions in the 2-tag, 3-tag and 4-tag regions are used as the fit input. The m_{Wh} distributions of the simulated signal and background processes are fitted to an Asimov dataset [95] (i.e the sum of all background predictions). The data correction procedure described in subsection 5.6.1 is not applied to the expected background events. But the effects of the correction procedure on the m_{Wh} distribution are taken into account as an additional uncertainty. All other systematic uncertainties described in section 5.7 are taken into account in the fit. The systematic uncertainties are incorporated in the fit as nuisance parameters with correlations across regions and processes taken into account. The normalization of the $t\bar{t}$ background is allowed to float freely in the fit, while the normalization of the remaining background processes are allowed to vary within their assigned uncertainties (see table 5.11).

The expected upper limits on the cross-section times branching ratio obtained in this manner are shown in figure 5.51 as a function of m_{H^+}, where the green and yellow bands indicate the 68% and 95% confidence level. The limit becomes stronger for larger charged Higgs boson masses. For charged Higgs boson masses of 400 GeV, 800 GeV, and

[4]Currently only the 2 b-tag region and the control regions are unblinded. The 3 b-tag and 4+ b-tag signal regions will be unblinded after CR-only fits have been performed with satisfactory results and all necessary uncertainties have been determined.

1600 GeV, the expected limits are 0.1215 pb, 0.00564 pb, and 0.00179 pb, respectively. To quantify the effects of the data-correction procedure on the expected limits, the fit has been repeated without including the shape uncertainty associated with the reweighting procedure. The expected limit for a charged Higgs boson mass of 1600 GeV improves only very slightly from 0.0179 pb to 0.0177 pb, while the limits for charged Higgs boson mass of 400 GeV and 800 GeV remain the same at 0.1215 pb and 0.0564 pb respectably. I.e the uncertainty on the m_{Wh} shape based on the reweighting procedure has only a very small effect on the expected limits.

The expected model independent limits for the Search for charged Higgs bosons decaying into a top quark and a bottom quark at $\sqrt{s} = 13 TeV$ with the ATLAS detector [96] are show in red in figure 5.51. This search for charged Higgs bosons studies the same final state as the analysis presented in this thesis and is thus challenged by the same background. The expected limits for the search for charged Higgs boson in $H^+ \to Wh$ decays are stronger by 6% to 20% compared to those for the search in $H^+ \to tb$ decays. However, currently not all sources of systematic uncertainty are included in the fit such that the limits of the $H^+ \to Wh$ search may become a bit weaker.

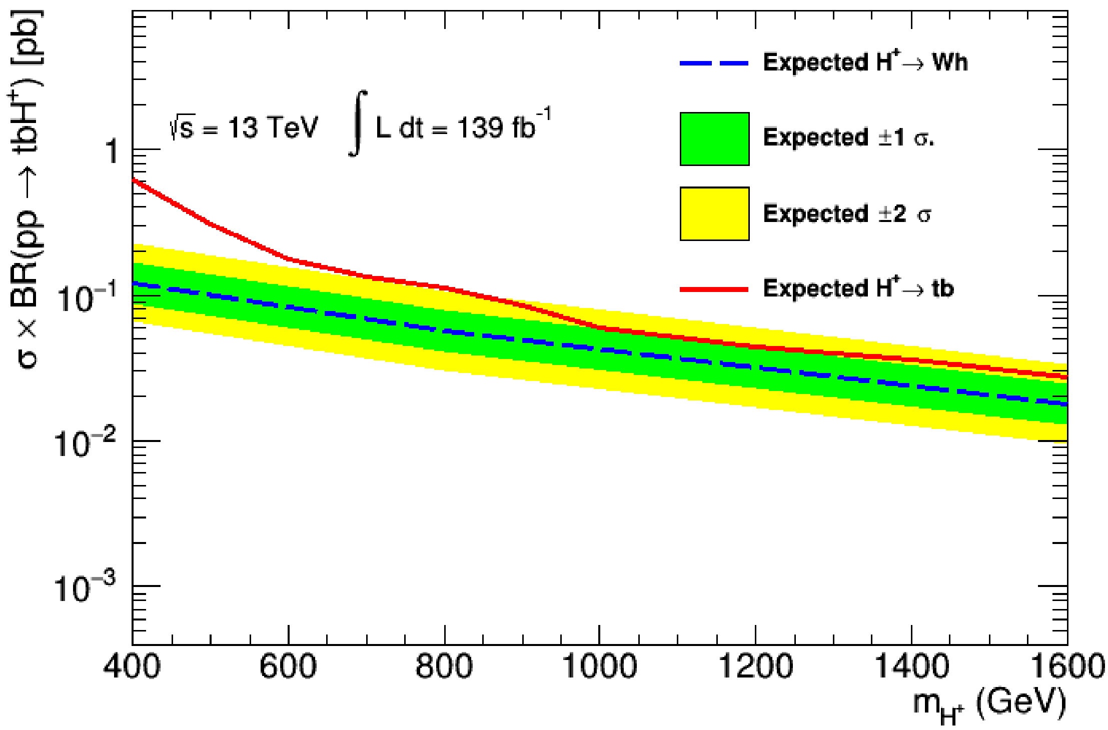

Figure 5.51.: Expected upper limits on the production cross-section times branching ratio for $H^+ \to Wh$ produced in association with a top and bottom quark as a function of the charged Higgs boson mass m_{H^+}. The green and yellow bands indicate the 68% and 95% confidence level intervals. The red line shows the expected limits for the search for charged Higgs boson in $H^+ \to tb$ decays [96].

6. Conclusions

In this thesis, a search for charged Higgs bosons in $H^+ \rightarrow W^+h \rightarrow lvbb$ decays is presented. The search is performed using 139 fb^{-1} of proton-proton collision data, at $\sqrt{s} = 13$ TeV, recorded between 2015-2018 by the ATLAS detector.

The decay of a charged Higgs boson into a W and Higgs boson can acquire significant branching ratios in several extended Higgs models like the N2HDM or the Georgie-Machacek model, as was found by studying the branching ratios of $H^+ \rightarrow W^+h$ in these models. Yet, this decay channel has so far not been covered by searches at the LHC.

At the LHC, charged Higgs bosons are produced in association with a top and bottom quark leading to a complex final state. Thus, a sophisticated method based on boosted decision trees (BDTs) had to be developed to be able to reconstructed the charged Higgs boson from a final state containing multiple jets, a single charged lepton and missing transverse energy.

The BDT was trained to discriminate between the combination of final state particles originating from the charged Higgs boson decay against the combinatorial background from wrong combinations of all final state particles. The 4-momentum of the charged Higgs boson is reconstructed from the jet-jet-lepton-E_T^{miss} combination favored by the BDT. By extensively testing this reconstruction approach, BDTs have proven to be a successful method to reconstruct the H^+ decay. Both the mass resolution, corresponding to the reconstruction procedure as well the matching efficiency between the generator level and the reconstructed charged Higgs boson have been tested and yielded satisfactory results.

To suppress the Standard Model background and to maximize the sensitivity of the search for charged Higgs bosons in $H^+ \rightarrow Wh \rightarrow lvbb$ decays, a signal region was defined by introducing selection requirements on certain kinematic variables aiming to maximize the signal over the Standard Model background. The dominant background source is the top quark pairs production. A simple cut based approach is used i.e. the shapes of different kinematic variables are compared between signal and background processes allowing for the identification of variables that are distinct between the signal and backgrounds. Here the BDT is utilized again. The maximal BDT response provides a effective variable to distinguish between signal and background processes. The selection criteria are derived by maximizing the signal significance $s/\sqrt{b}$.

In addition, a control region depleted in signal was defined allowing for an unbiased comparison of the background simulation to the data. In the control region, a moderate difference between the simulated background predictions and the data was found. To improve the background prediction, a multi level data-based correction procedure was explored. Weight factors are extracted from the ratio of the Monte Carlo predictions to the data as a function of the jet multiplicity. After these corrections are applied, a second set of weights was derived as a function of H_T. Finally, to correct for residual missmodelling the distribution of a third observable is reweighed. This procedure has been explored for the lepton transverse momentum, the leading jet transverse momentum as well as the missing transverse energy. These method did not yield the desired improvement in the data-simulation agreement for all observables of interest. In future iterations on this work, the data-simulation agreement might be improved by using a more sophisticated correction approach. While the correction procedure is currently unused, it will be of useful in later stages of the analysis, potentially improving fits to data. Furthermore, the correction procedure has only a very small effect on the shape of the m_{Wh} distribution. The shape uncertainties associated with the reweighting procedure barley change the expected limits.

Finally, the search sensitivity was evaluated in terms of expected upper limits on the production cross-section $\times$ branching ratio by performing a maximum likelihood fit. The expected signal and background m_{Wh} distributions are fitted to an Asimov data-set. The expected limits depend on the charged Higgs boson mass. The expected limits for a charged Higgs boson mass of 400 GeV is 0.1215 pb, for a charged Higgs boson mass of 800 GeV 0.0564 pb and 0.00179 pb for a charged Higgs boson mass of 1600 GeV. The obtained expected limit are competitive with the expected limits in similar searches for charged Higgs bosons.

In this thesis, an effective analysis strategy for the search for charged Higgs bosons in the $H^+ \to Wh \to l\nu bb$ decay channel was develop. Still this thesis does not constitute a comprehensive search for a charged Higgs boson in $H^+ \to Wh$ decays, but rather describes a selection of certain aspect of such a search. Based on the studies, presented in this thesis, a publication by the ATLAS collaboration is planned within the next year. This would include findings of this thesis and new developments on these as well as additional findings. For example, for high charged Higgs boson masses, the decay products are strongly boosted, such that the individual jets of the Higgs boson decay cannot be resolved by the detector, but rather get merged into a single large radius jet. For such an event topology, the charged Higgs boson reconstruction approach used in this thesis is no longer feasible. Thus, a dedicated approach for such boosted event topologies might be crucial for the search for charged Higgs bosons with masses at the TeV scale. In addition to the leptonically decaying W boson, also hadronic W boson decays should be considered in future iterations of this analysis. A similar approach based on BDTs as developed in this thesis could be used to reconstruct the charged Higgs boson decay from 4 jets.

A. Appendix

A.1. Additional Figures from the Analysis

A.1.1. Additional Figures for Subsection 5.4.2

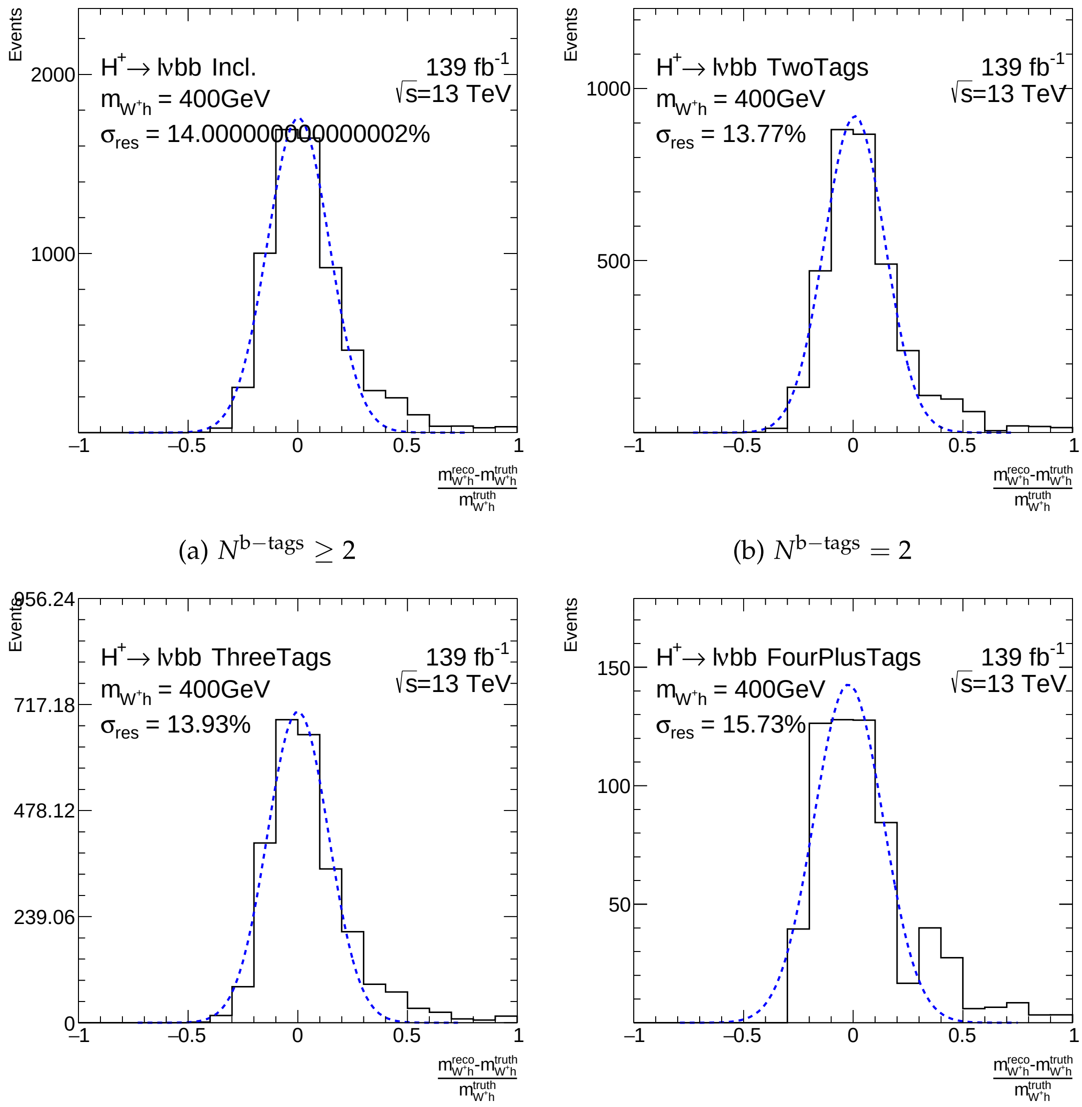

(a) $N^{\text{b-tags}} \geq 2$

(b) $N^{\text{b-tags}} = 2$

(c) $N^{\text{b-tags}} = 3$

(d) $N^{\text{b-tags}} \geq 4$

Figure A.1.: The *mass resolution*, $m_{Wh}^{recon} - m_{Wh}^{truth} / m_{Wh}^{truth}$ for the 400 GeV mass point. A Gaussian function is fitted to the histograms.

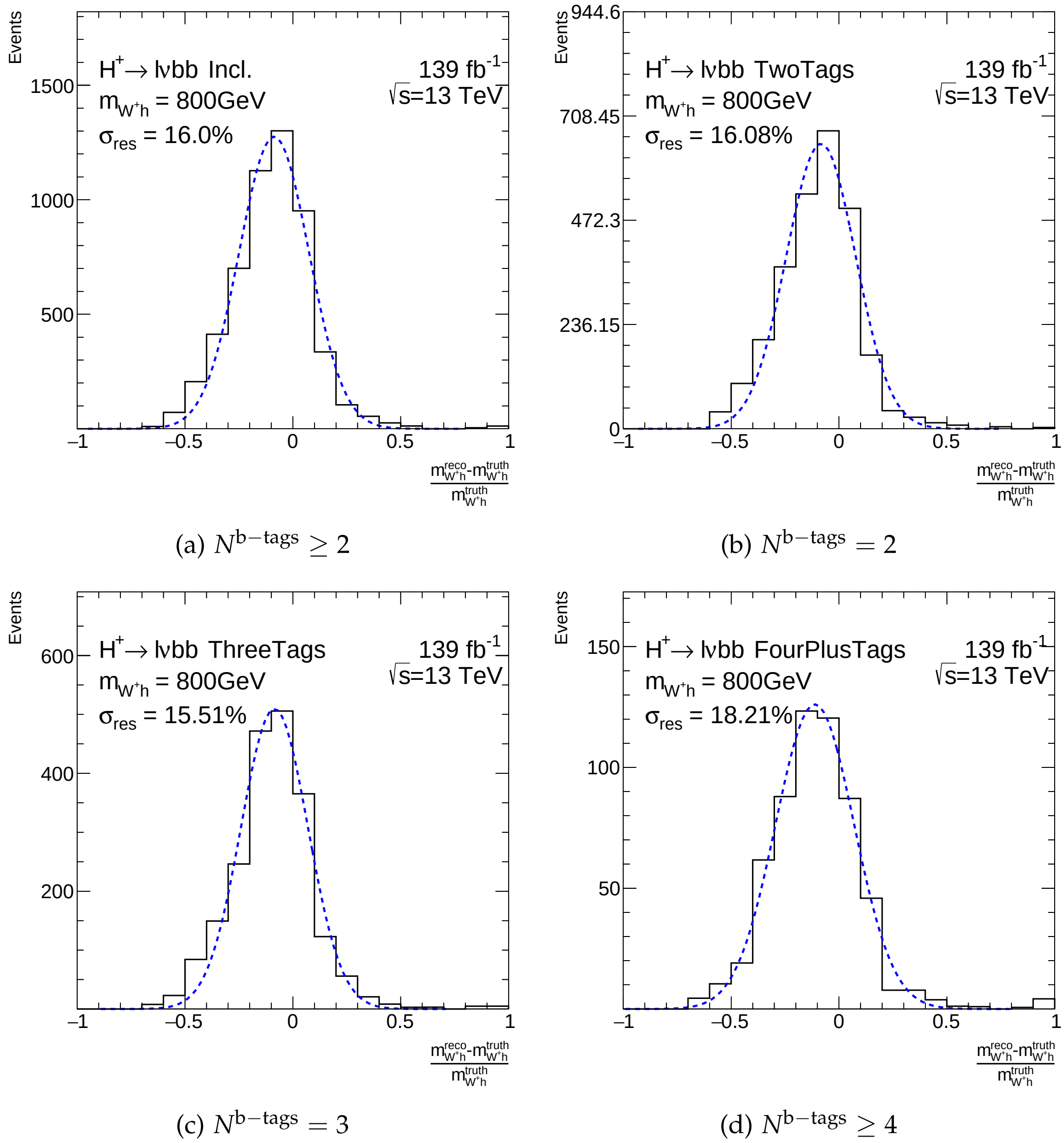

(a) $N^{\mathrm{b-tags}} \geq 2$

(b) $N^{\mathrm{b-tags}} = 2$

(c) $N^{\mathrm{b-tags}} = 3$

(d) $N^{\mathrm{b-tags}} \geq 4$

Figure A.2.: The *mass resolution*, $m^{recon}_{Wh} - m^{truth}_{Wh} / m^{truth}_{Wh}$ for the 800 GeV mass point. A Gaussian function is fitted to the histograms.

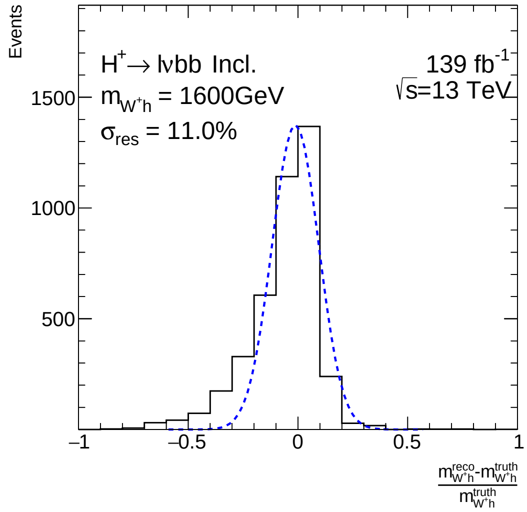

(a) $N^{\text{b-tags}} \geq 2$

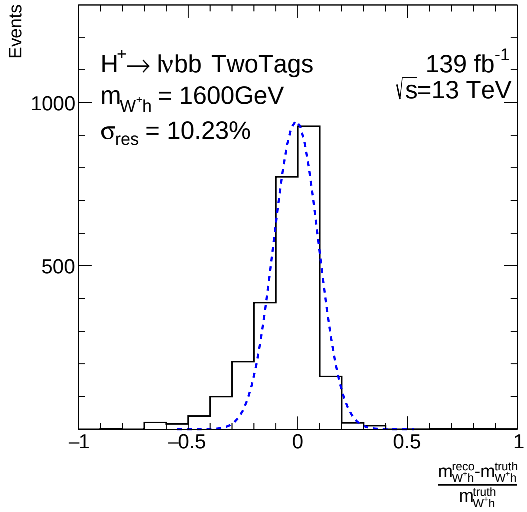

(b) $N^{\text{b-tags}} = 2$

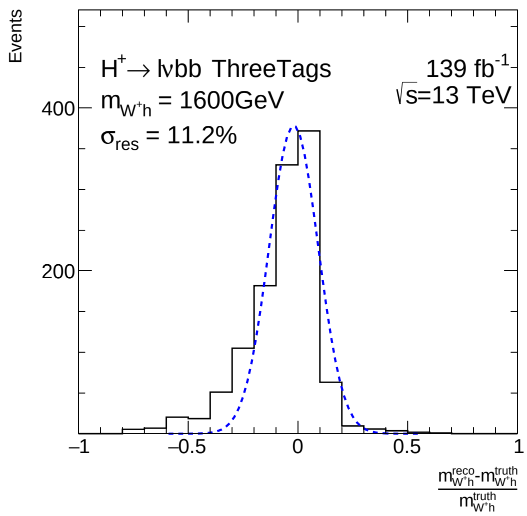

(c) $N^{\text{b-tags}} = 3$

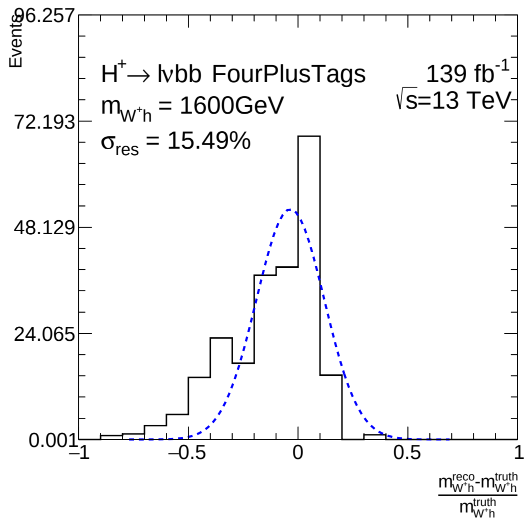

(d) $N^{\text{b-tags}} \geq 4$

Figure A.3.: The *mass resolution*, $m_{Wh}^{recon} - m_{Wh}^{truth} / m_{Wh}^{truth}$ for the 1600 GeV mass point. A Gaussian function is fitted to the histograms.

A.1.2. Additional Figure for Section 5.5

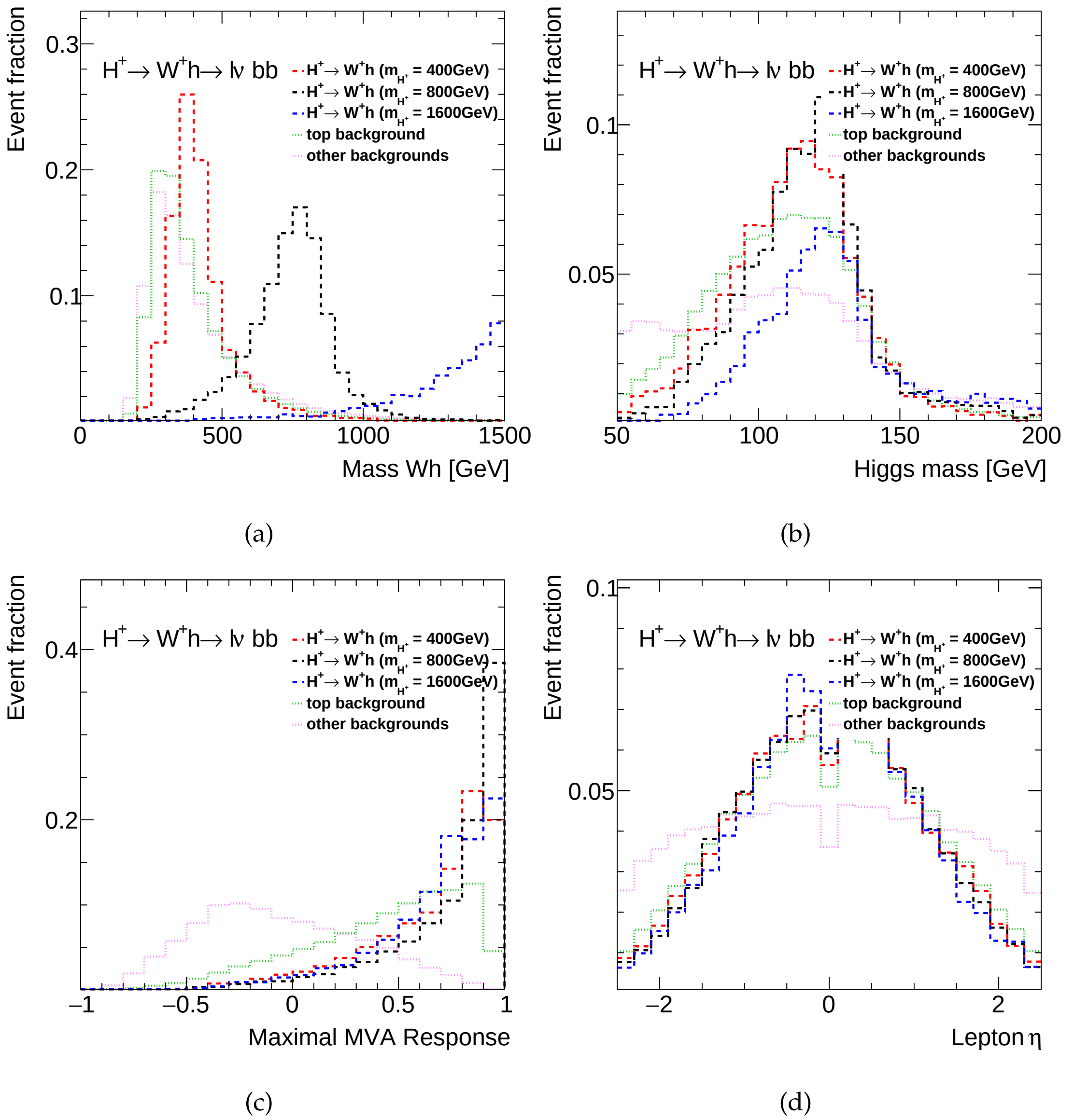

Figure A.4.: A comparison of the distributions of different variable for the signal and the background, separated into background stemming from top quarks and all other background process presented in the b-tag inclusive region. All the histograms are normalized.

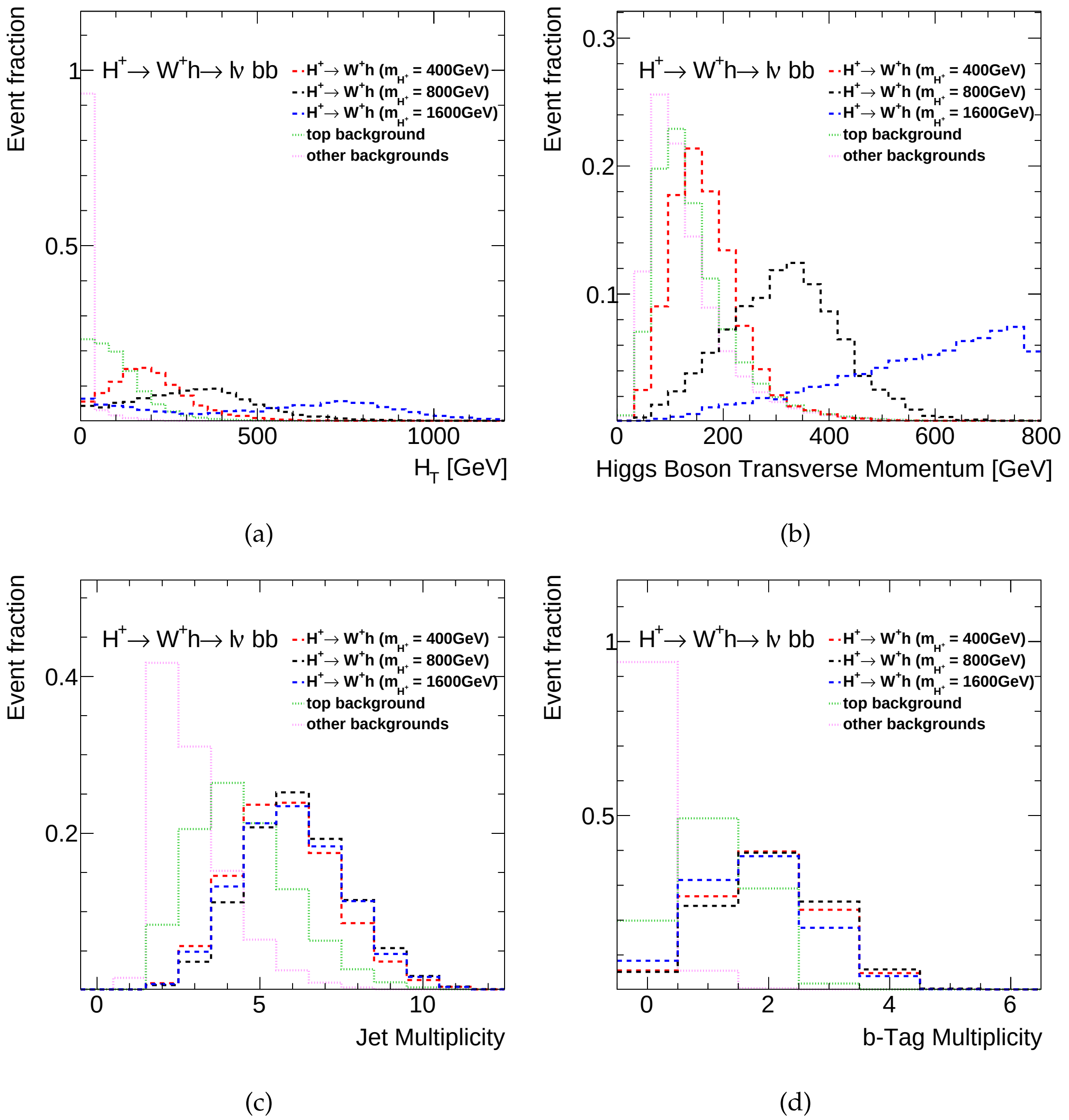

Figure A.5.: A comparison of the distributions of different variable for the signal and the background, separated into background stemming from top quarks and all other background process presented in the b-tag inclusive region. All the histograms are normalized.

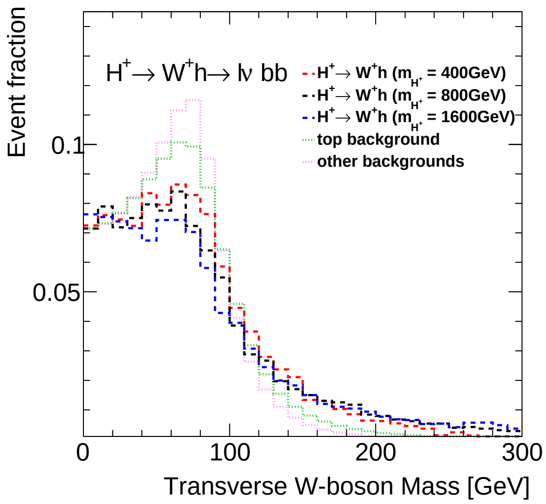

(a)

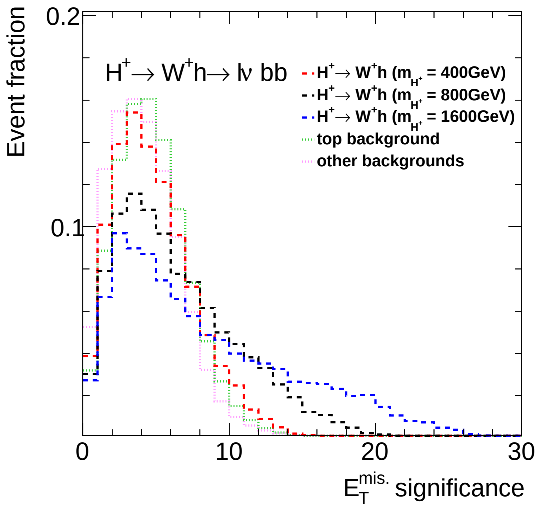

(b)

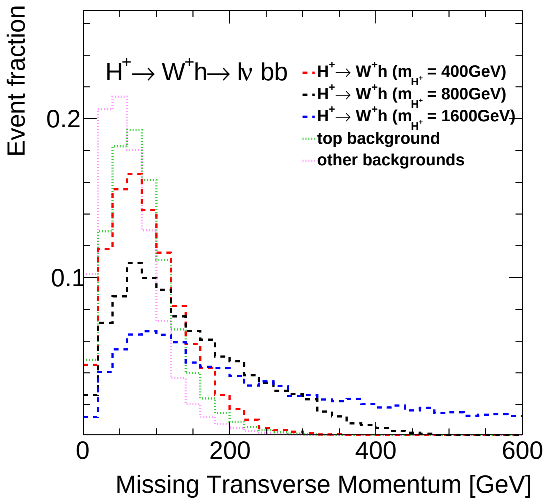

(c)

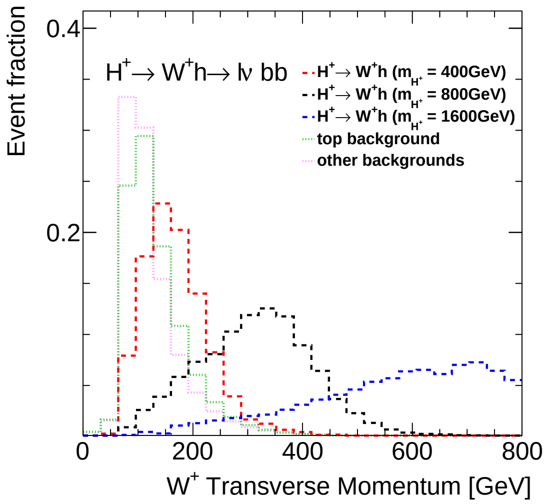

(d)

Figure A.6.: A comparison of the distributions of different variable for the signal and the background, separated into background stemming from top quarks and all other background process presented in the b-tag inclusive region. All the histograms are normalized.

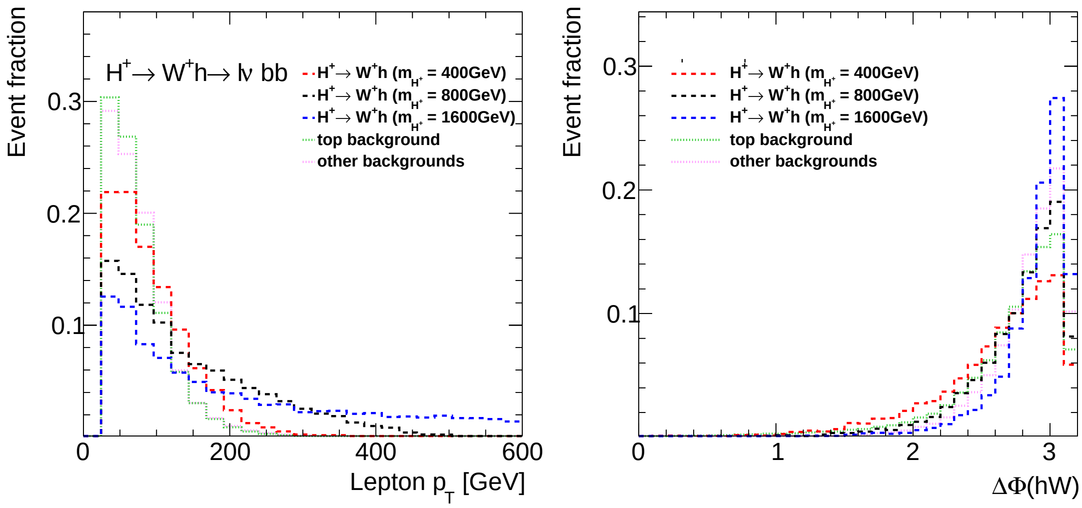

(a) (b)

Figure A.7.: A comparison of the distributions of different variable for the signal and the background, separated into background stemming from top quarks and all other background process presented in the b-tag inclusive region. All the histograms are normalized.

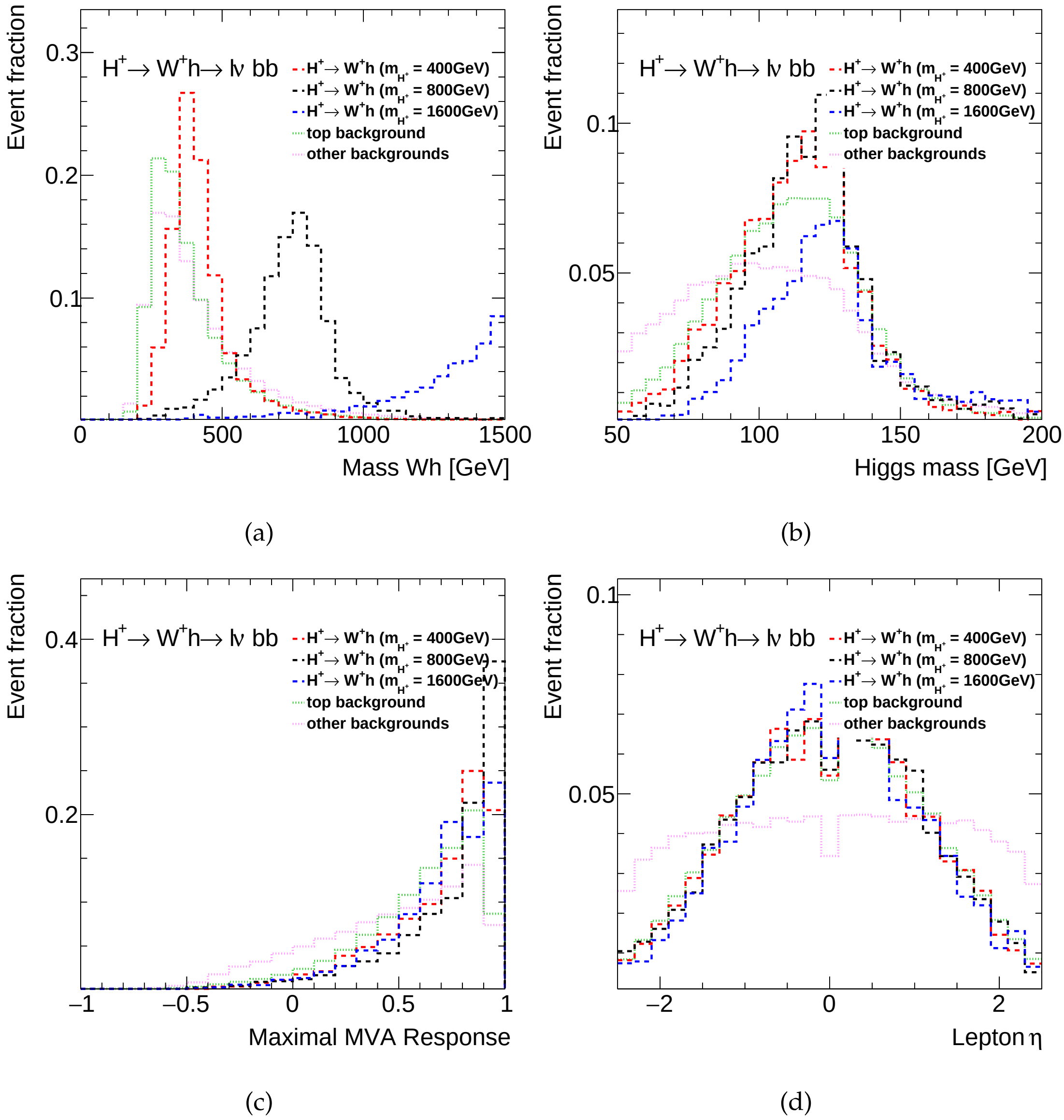

Figure A.8.: A comparison of the distributions of different variable for the signal and the background, separated into background stemming fro top quarks and all other background process, in the 2 b-tag region. All the histograms are normalized.

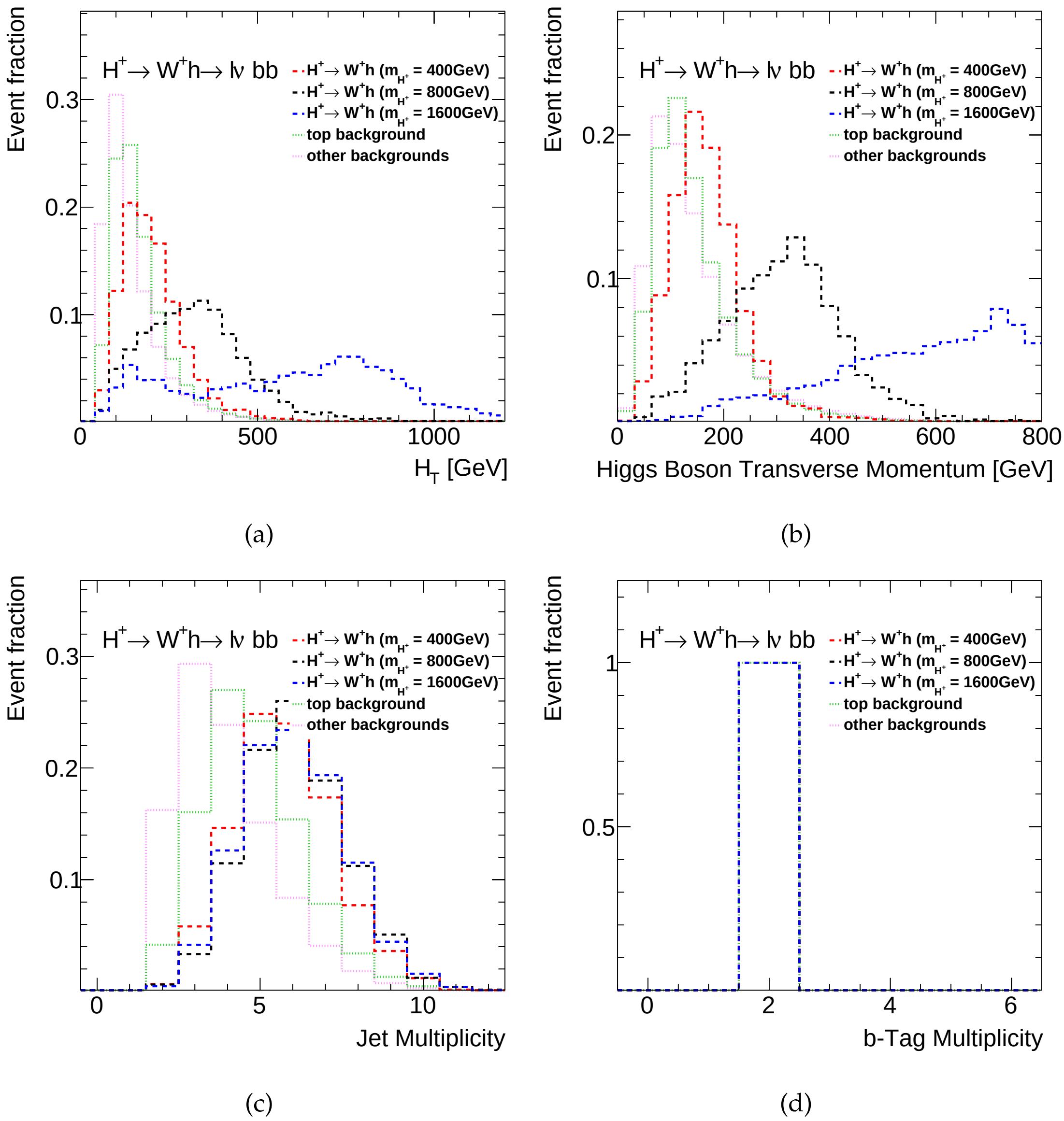

Figure A.9.: A comparison of the distributions of different variable for the signal and the background, separated into background stemming fro top quarks and all other background process, in the 2 b-tag region. All the histograms are normalized.

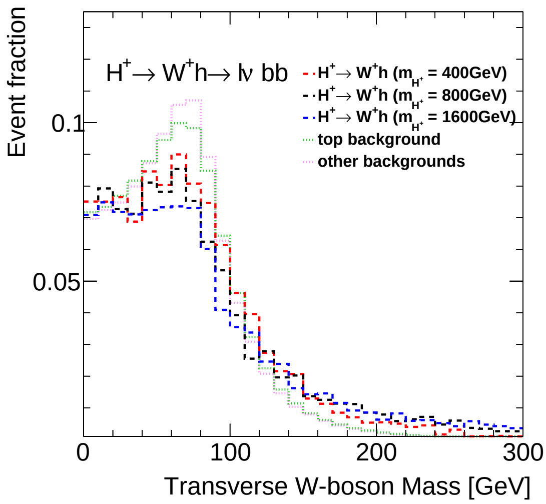

(a)

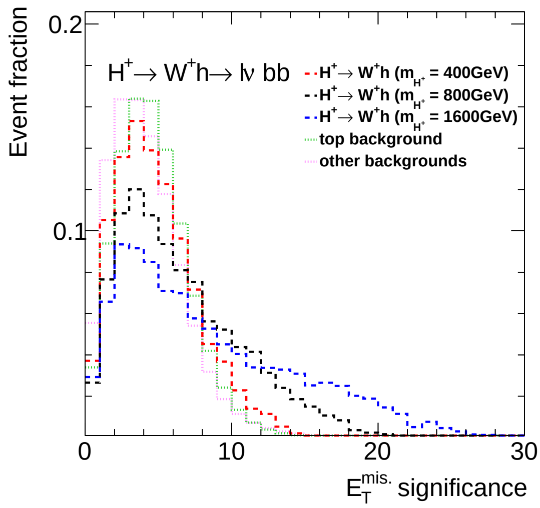

(b)

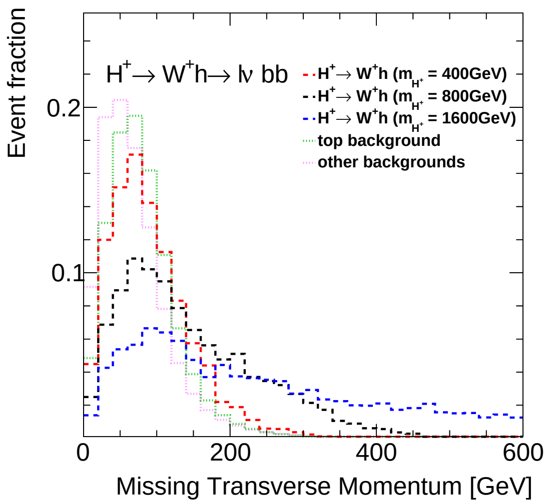

(c)

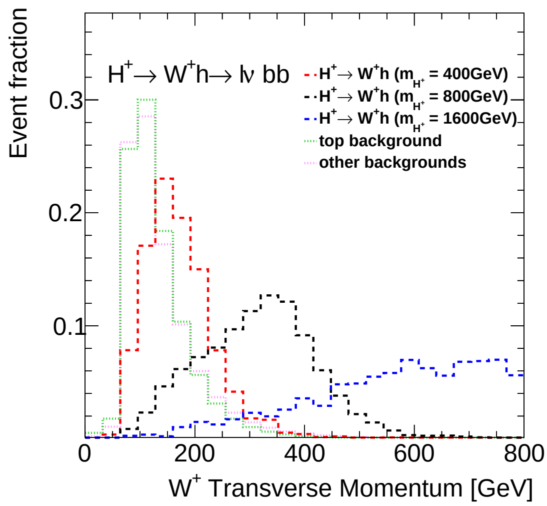

(d)

Figure A.10.: A comparison of the distributions of different variable for the signal and the background, separated into background stemming fro top quarks and all other background process, in the 2 b-tag region. All the histograms are normalized.

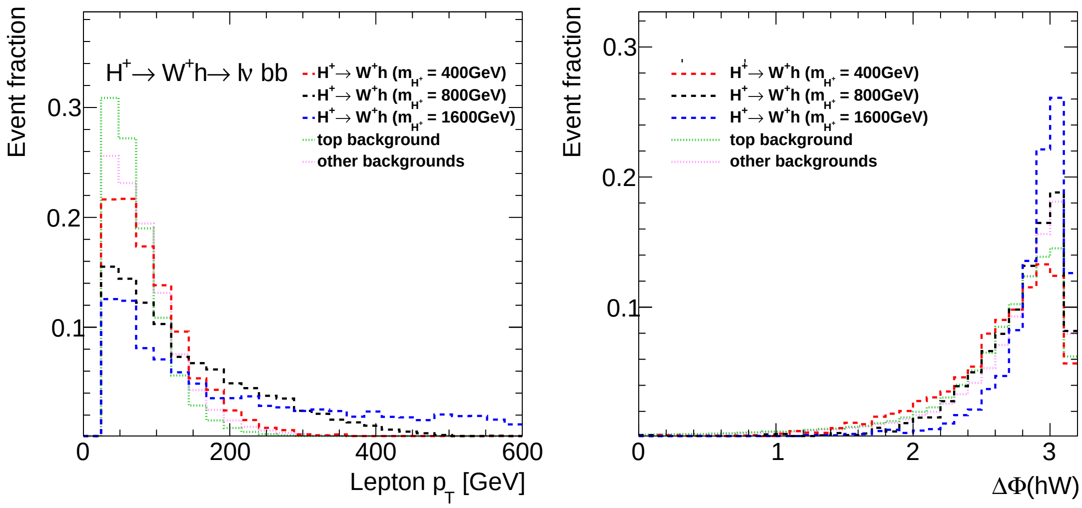

(a) (b)

Figure A.11.: A comparison of the distributions of different variable for the signal and the background, separated into background stemming fro top quarks and all other background process, in the 2 b-tag region. All the histograms are normalized.

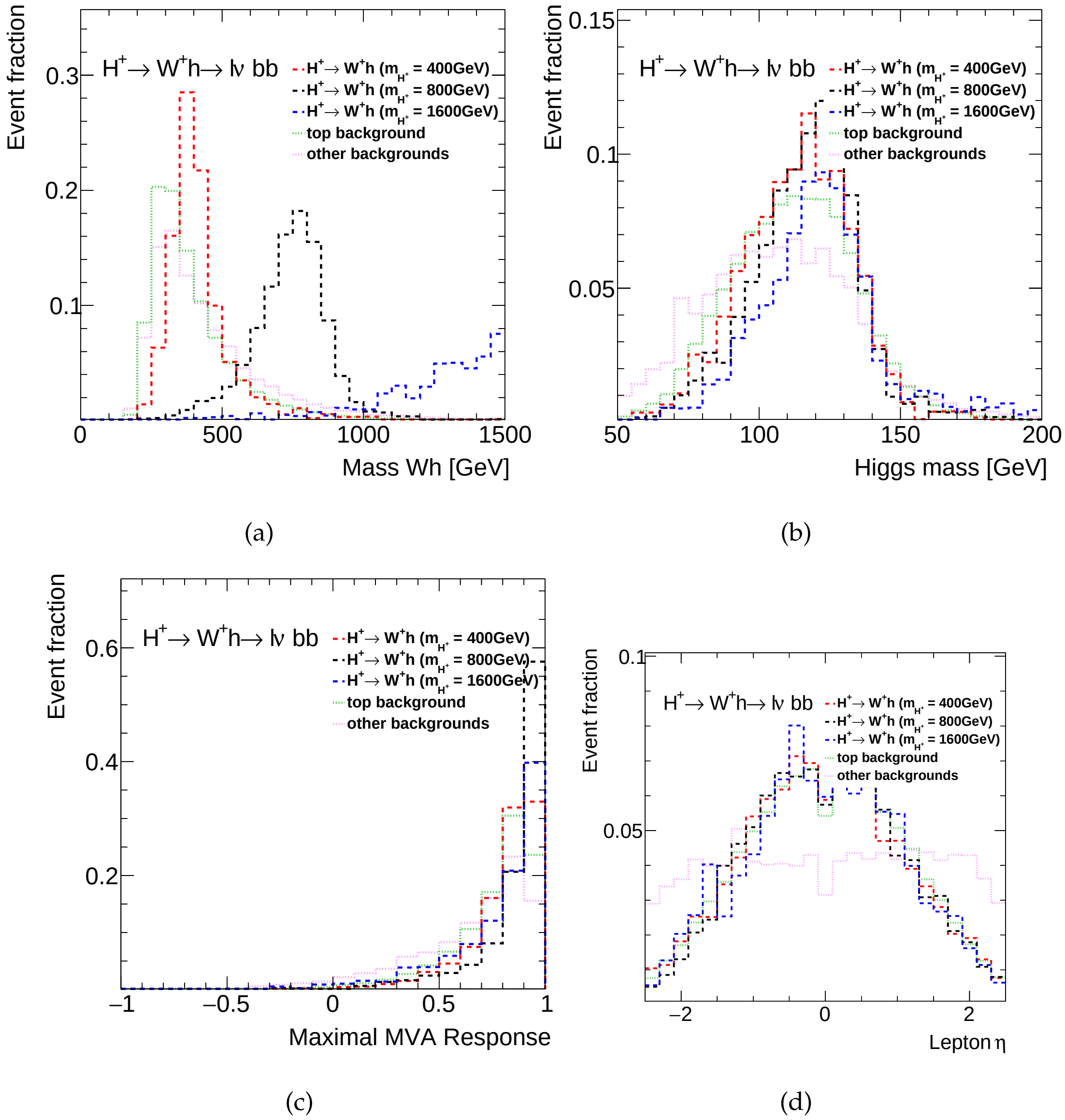

Figure A.12.: A comparison of the distributions of different variable for the signal and the background, separated into background stemming from top quarks and all other background process, in the 3 b-tag region. All the histograms are normalized.

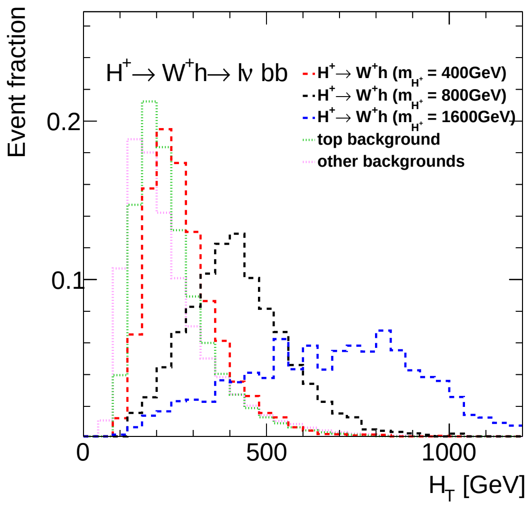

(a)

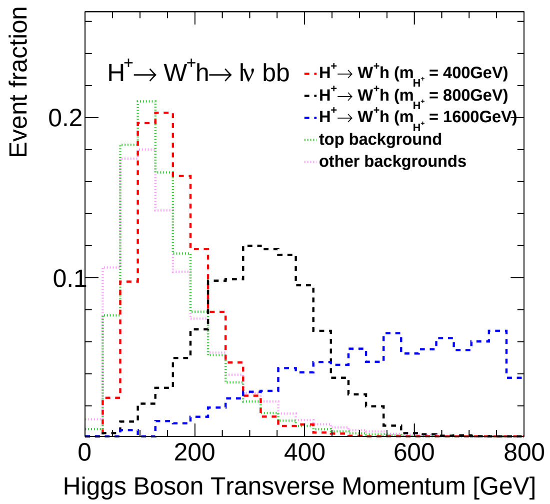

(b)

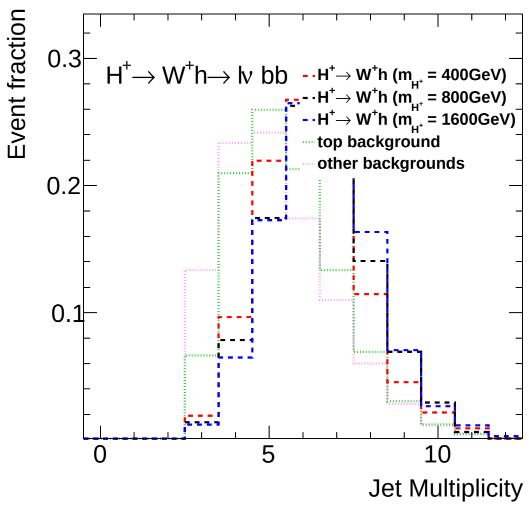

(c)

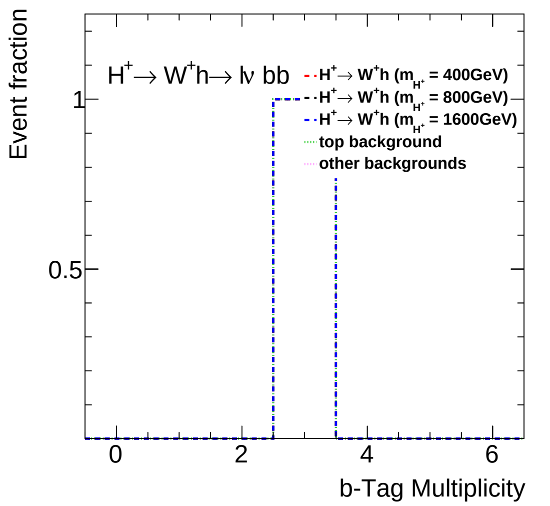

(d)

Figure A.13.: A comparison of the distributions of different variable for the signal and the background, separated into background stemming from top quarks and all other background process, in the 3 b-tag region. All the histograms are normalized.

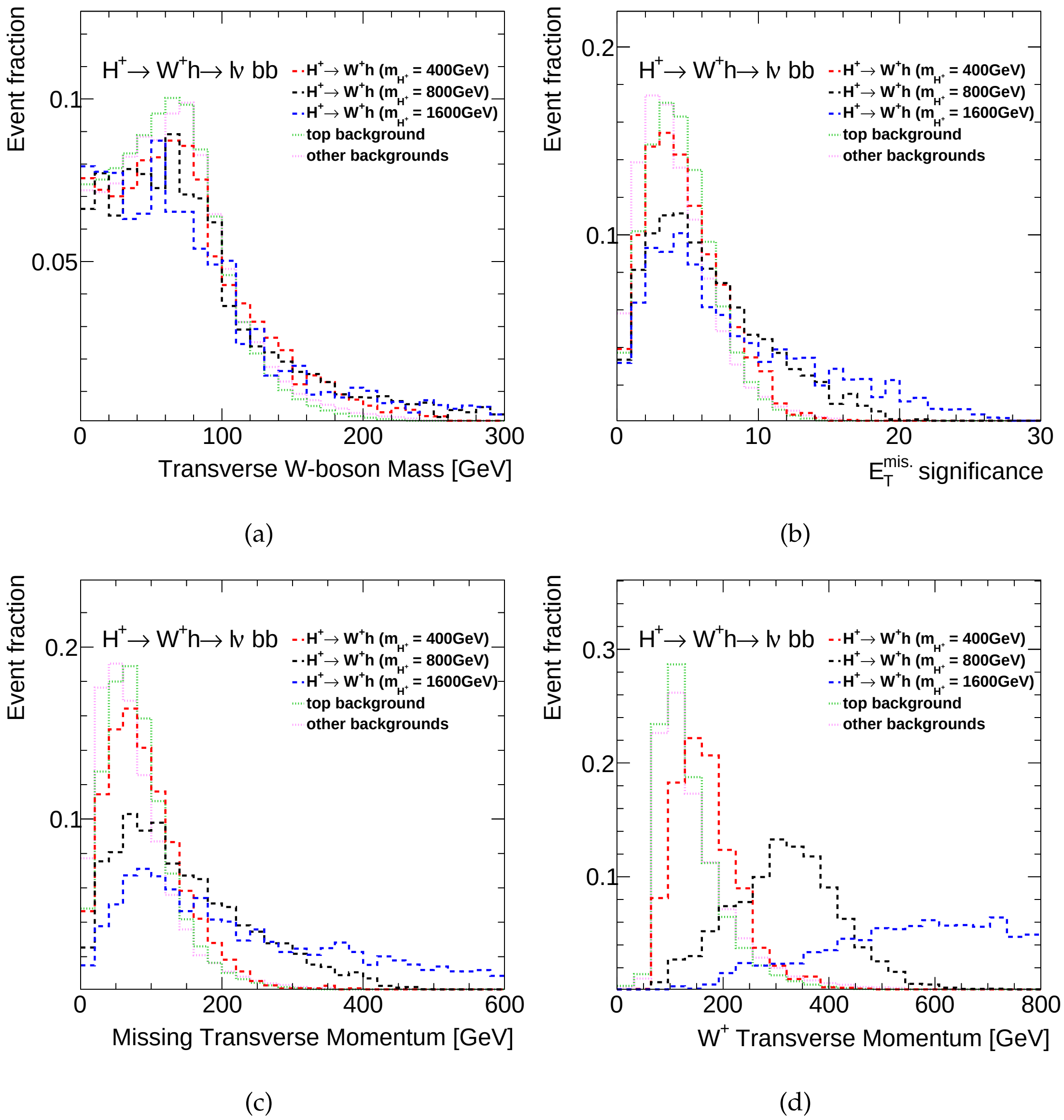

(a) (b) (c) (d)

Figure A.14.: A comparison of the distributions of different variable for the signal and the background, separated into background stemming from top quarks and all other background process, in the 3 b-tag region. All the histograms are normalized.

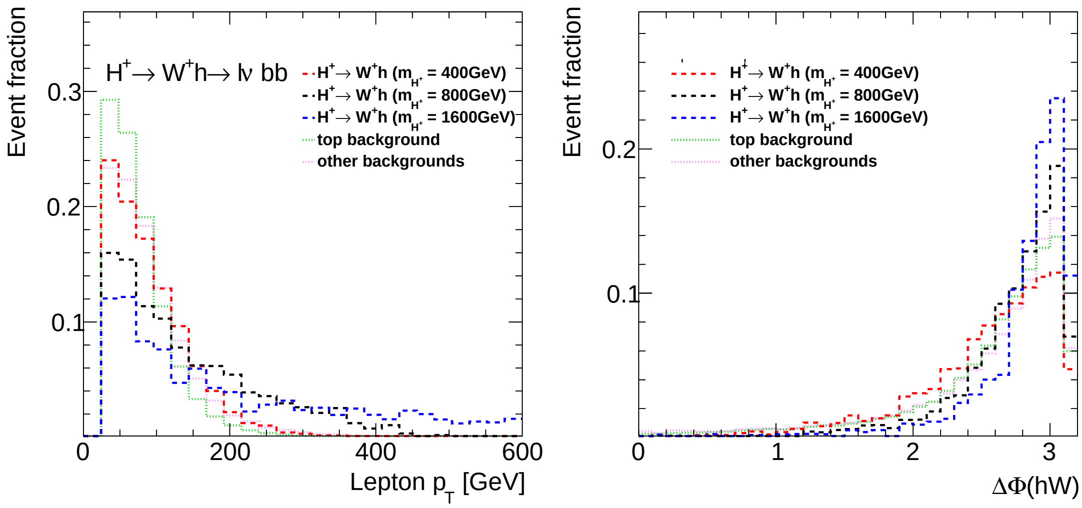

(a)

(b)

Figure A.15.: A comparison of the distributions of different variable for the signal and the background, separated into background stemming from top quarks and all other background process, in the 3 b-tag region. All the histograms are normalized.

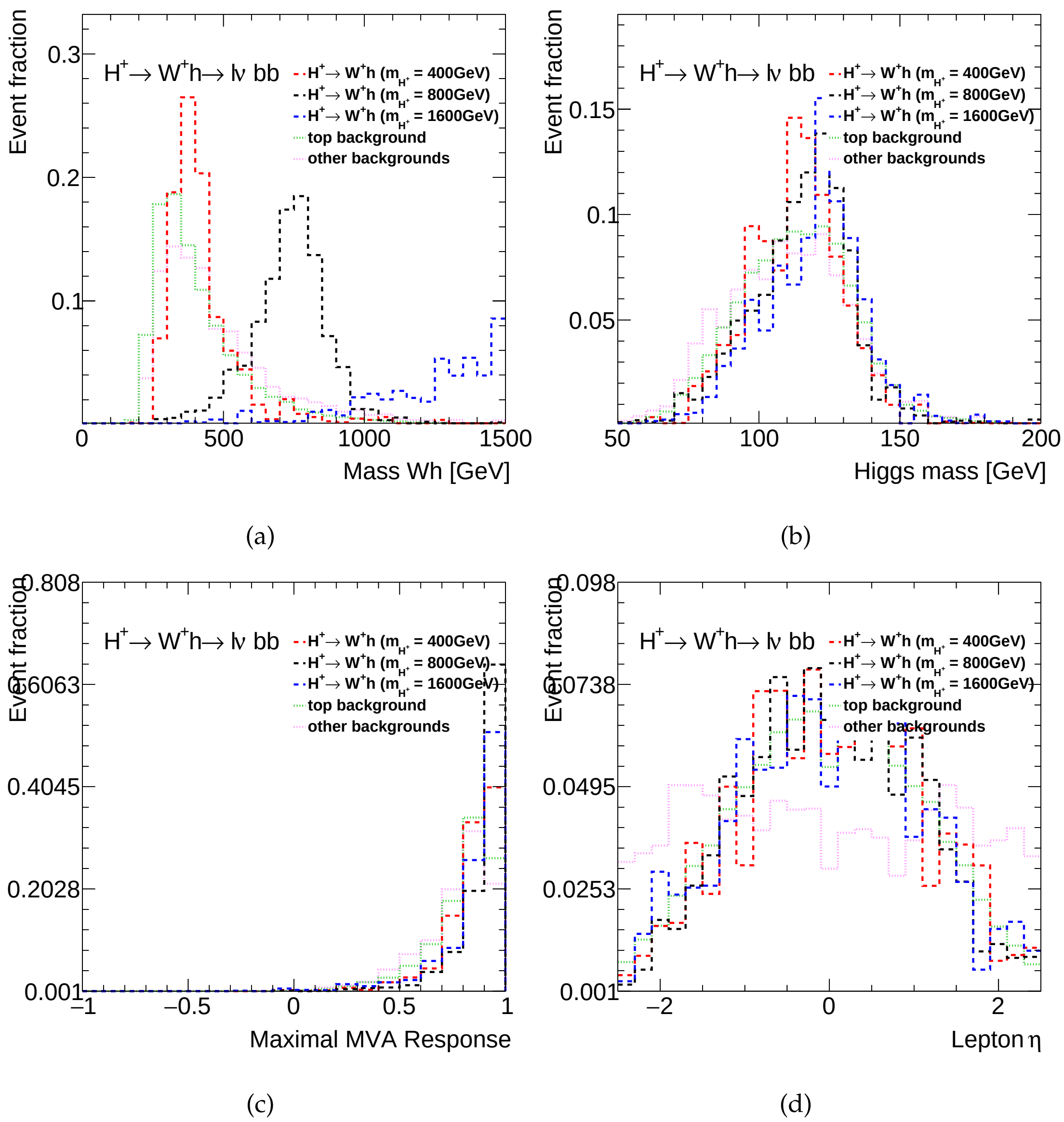

Figure A.16.: A comparison of the distributions of different variable for the signal and the background, separated into background stemming fro top quarks and all other background process, in the 4+ b-tag region. All the histograms are normalized.

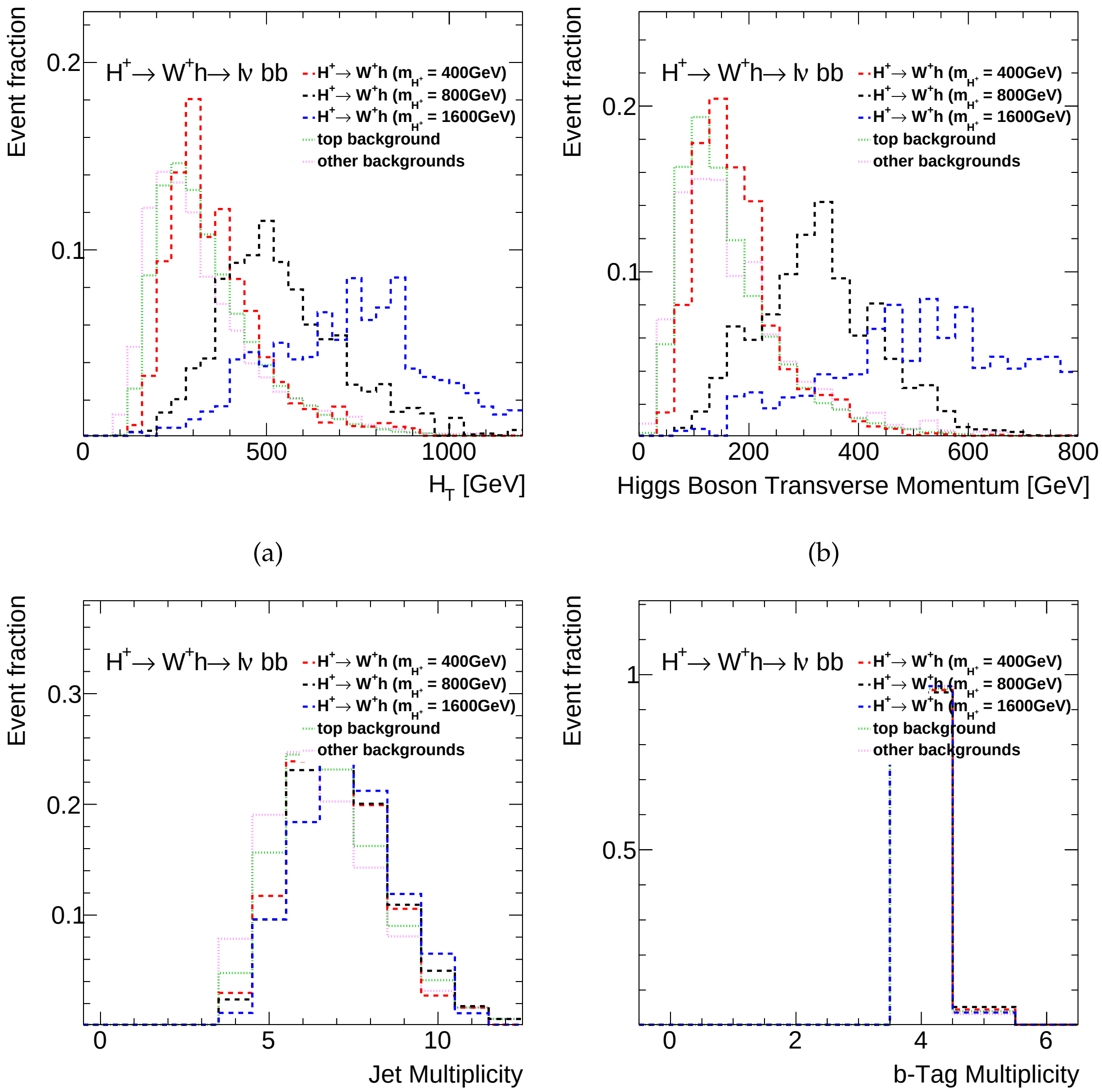

(a) (b) (c) (d)

Figure A.17.: A comparison of the distributions of different variable for the signal and the background, separated into background stemming fro top quarks and all other background process, in the 4+ b-tag region. All the histograms are normalized.

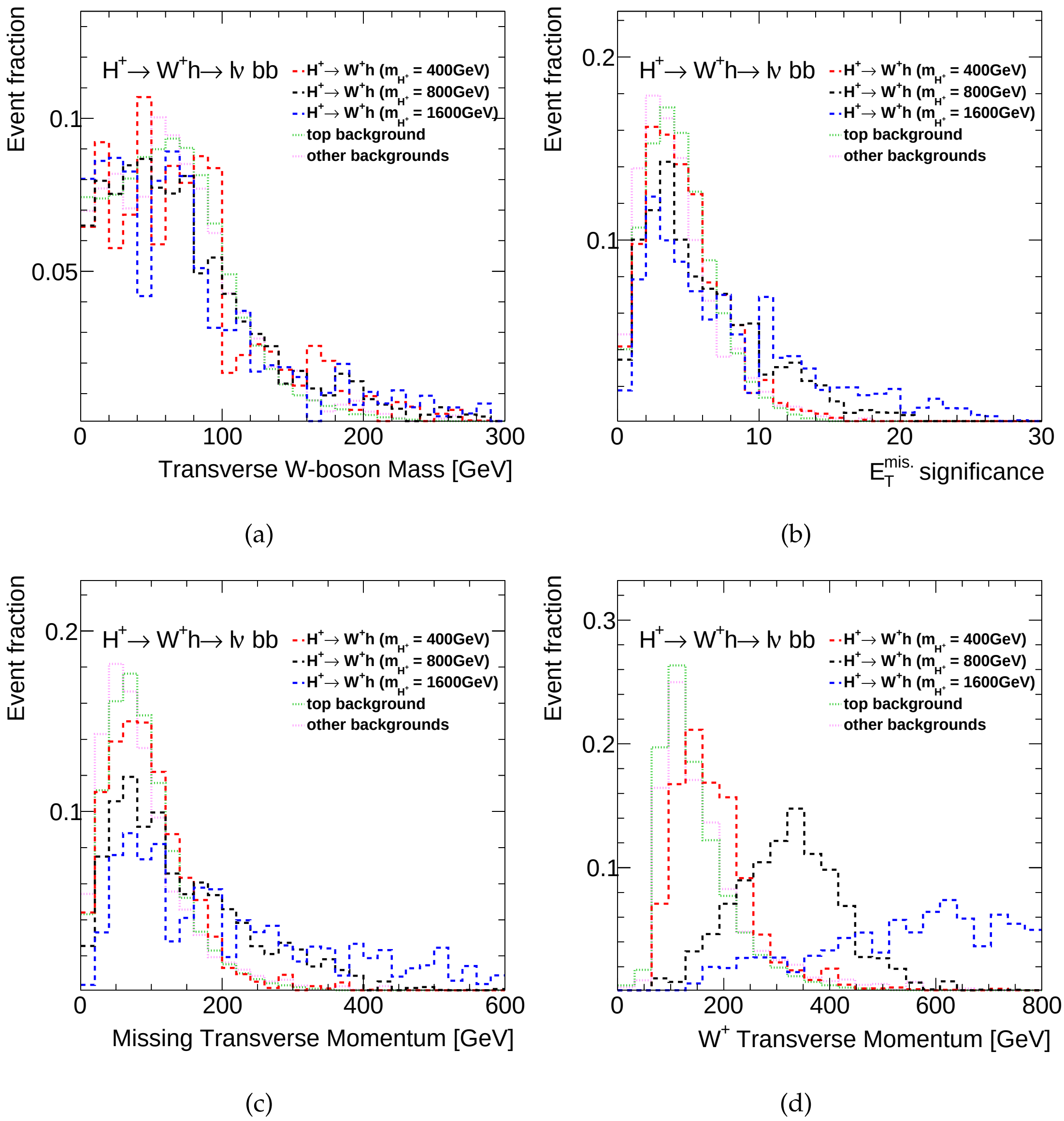

Figure A.18.: A comparison of the distributions of different variable for the signal and the background, separated into background stemming fro top quarks and all other background process, in the 4+ b-tag region. All the histograms are normalized.

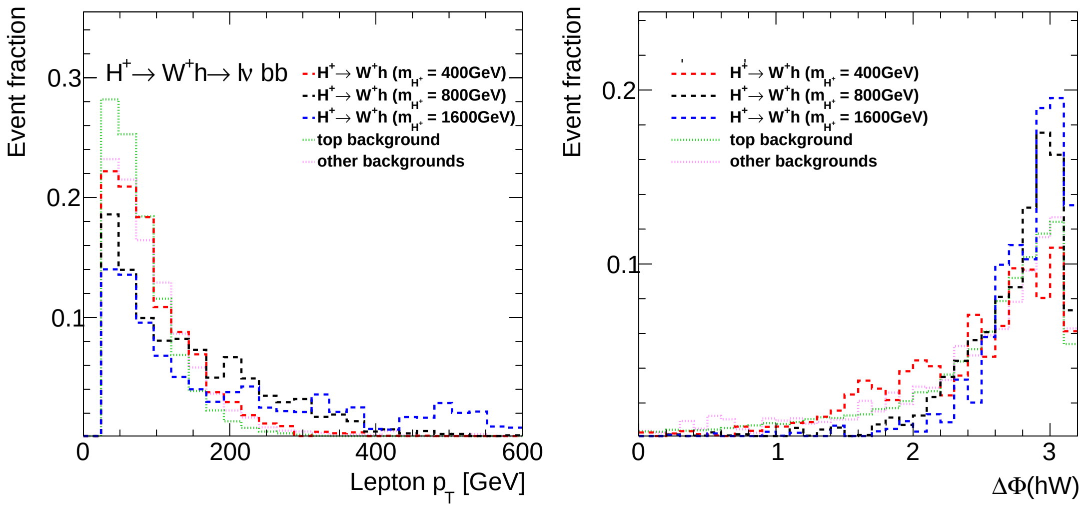

(a) (b)

Figure A.19.: A comparison of the distributions of different variable for the signal and the background, separated into background stemming fro top quarks and all other background process, in the 4+ b-tag region. All the histograms are normalized.

A.1.3. Additional Figures for Section 5.6

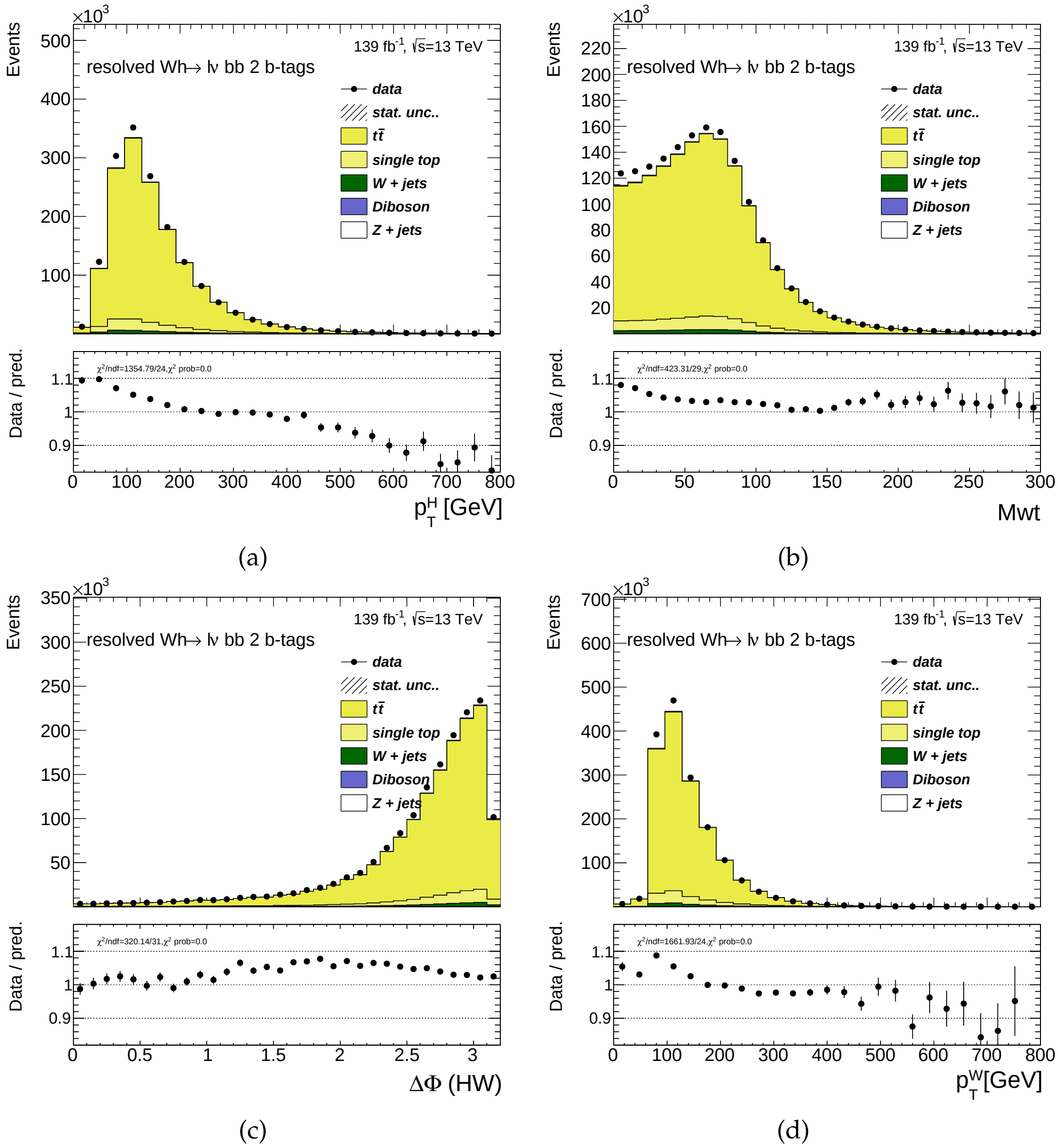

Figure A.20.: Comparison between the data and the Monte-Carlo prediction in the 2 b-tag region.

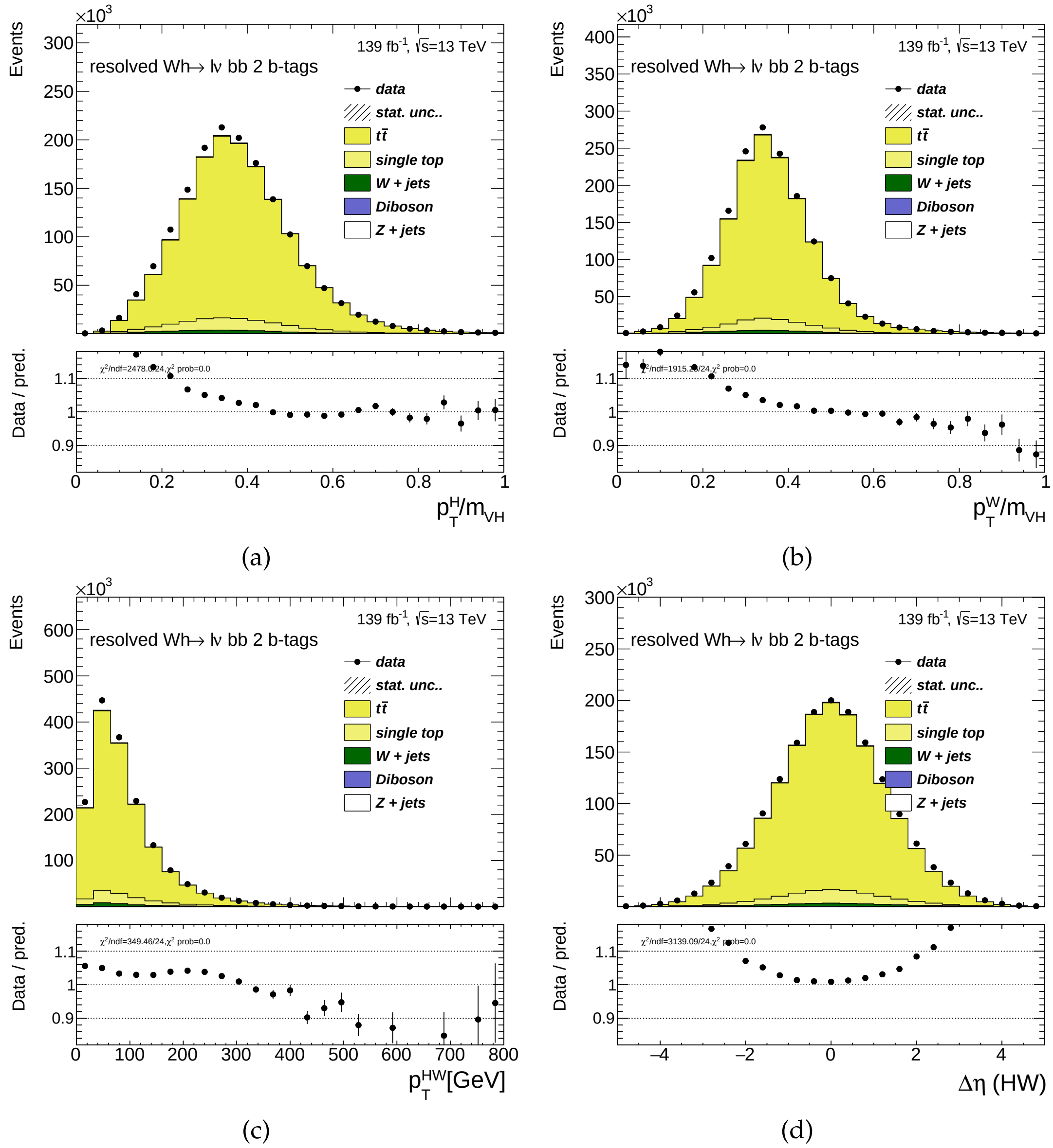

Figure A.21.: Comparison between the data and the Monte-Carlo prediction in the 2 b-tag region.

List of Figures

List of Tables

Bibliography

[1]G. Aad et al. (ATLAS Collaboration), "Observation of a new particle in the search for the Standard Model Higgs boson with the ATLAS detector at the LHC," Phys. Lett. B **716**, 1–29 (2012).

[2]S. Chatrchyan et al. (CMS Collaboration), "Observation of a New Boson at a Mass of 125 GeV with the CMS Experiment at the LHC," Phys. Lett. B **716**, 30–61 (2012).

[3]G. Aad et al. (ATLAS Collaboration), "Test of the universality of τ and μ lepton couplings in W-boson decays from $t\bar{t}$ events with the ATLAS detector," (2020).

[4]P. Zyla et al. (Particle Data Group), "Review of Particle Physics," PTEP **2020**, 083C01 (2020).

[5]G. Pásztor (ATLAS Collaboration, CMS Collaboration), "Precision tests of the Standard Model at the LHC with the ATLAS and CMS detectors," PoS **FFK2019**, 005 (2020).

[6]H. Haber and G. Kane, "The search for supersymmetry: probing physics beyond the standard model," Physics Reports **117**, 75–263 (1985).

[7]P. Gutierrez (CDF, D0), "Review of Charged Higgs Searches at the Tevatron," PoS **CHARGED2010**, edited by R. Enberg and A. Ferrari, 004 (2010).

[8]G. Abbiendi et al. (ALEPH, DELPHI, L3, OPAL, LEP), "Search for Charged Higgs bosons: Combined Results Using LEP Data," Eur. Phys. J. C **73**, 2463 (2013).

[9]R. Enberg, W. Klemm, S. Moretti, S. Munir, and G. Wouda, "Charged Higgs boson in the $W^{\pm}$ Higgs channel at the Large Hadron Collider," Nucl. Phys. B **893**, 420–442 (2015).

[10]K. A. Assamagan, Y. Coadou, and A. Deandrea, "ATLAS discovery potential for a heavy charged Higgs boson," Eur. Phys. J. direct **4**, 9 (2002).

[11]M. Drees, M. Guchait, and D. P. Roy, "Signature of charged to neutral Higgs boson decay at the LHC in SUSY models," Phys. Lett. B **471**, 39–44 (1999).

[12]B. Coleppa, F. Kling, and S. Su, "Charged Higgs search via $AW^{\pm}/HW^{\pm}$ channel," JHEP **12**, 148 (2014).

[13]G. Aad et al. (ATLAS Collaboration), "The ATLAS Experiment at the CERN Large Hadron Collider," JINST **3**, S08003 (2008).

[14]S. Chatrchyan et al. (CMS Collaboration), "The CMS Experiment at the CERN LHC," JINST **3**, S08004 (2008).

[15]K. Aamodt et al. (ALICE Collaboration), "The ALICE experiment at the CERN LHC," JINST **3**, S08002 (2008).

[16]A. A. Alves Jr. et al. (LHCb Collaboration), "The LHCb Detector at the LHC," JINST **3**, S08005 (2008).

[17]E. Mobs, "The CERN accelerator complex - 2019. Complexe des accélérateurs du CERN - 2019," General Photo (2019).

[18]L. Evans and P. Bryant, "LHC Machine," JINST **3**, S08001 (2008).

[19]M. Capeans, G. Darbo, K. Einsweiller, M. Elsing, T. Flick, M. Garcia-Sciveres, C. Gemme, H. Pernegger, O. Rohne, and R. Vuillermet (ATLAS Collaboration), *ATLAS Insertable B-Layer Technical Design Report*, tech. rep. (Sept. 2010).

[20]B. Abbott et al. (ATLAS Collaboration), "Production and Integration of the ATLAS Insertable B-Layer," JINST **13**, T05008 (2018).

[21]G. Aad et al. (ATLAS Collaboration), "Operation of the ATLAS trigger system in Run 2," JINST **15**, P10004 (2020).

[22]M. Aaboud et al. (ATLAS Collaboration), "Performance of the ATLAS Track Reconstruction Algorithms in Dense Environments in LHC Run 2," Eur. Phys. J. C **77**, 673 (2017).

[23]M. Aaboud et al. (ATLAS Collaboration), "Electron reconstruction and identification in the ATLAS experiment using the 2015 and 2016 LHC proton-proton collision data at $\sqrt{s}$ = 13 TeV," Eur. Phys. J. C **79**, 639 (2019).

[24]G. Aad et al. (ATLAS Collaboration), "Muon reconstruction performance of the ATLAS detector in proton–proton collision data at $\sqrt{s}$ =13 TeV," Eur. Phys. J. C **76**, 292 (2016).

[25]ATLAS Collaboration, *E_T^{MISS} PERFORMANCE IN THE ATLAS DETECTOR USING 2015–2016 LHC PP COLLISIONS*, ATLAS-CONF-2018-023, 2018.

[26]ATLAS Collaboration, *Performance of missing transverse momentum reconstruction with the ATLAS detector in the first proton–proton collisions at $\sqrt{s} = 13$ TeV*, ATL-PHYS-PUB-2015-027, 2015.

[27]G. Aad et al. (ATLAS Collaboration), "Topological cell clustering in the ATLAS calorimeters and its performance in LHC Run 1," Eur. Phys. J. C **77**, 490 (2017).

[28]M. Cacciari, G. P. Salam, and G. Soyez, "The anti-k_t jet clustering algorithm," JHEP **04**, 063 (2008).

[29]M. Cacciari, G. P. Salam, and G. Soyez, “FastJet user manual,” Eur. Phys. J. C **72**, 1896 (2012).

[30]ATLAS Collaboration, *Properties of jets and inputs to jet reconstruction and calibration with the ATLAS detector using proton–proton collisions at* $\sqrt{s} = 13$ *TeV*, ATL-PHYS-PUB-2015-036, 2015.

[31]ATLAS Collaboration, *Optimisation and performance studies of the ATLAS b-tagging algorithms for the 2017-18 LHC run*, ATL-PHYS-PUB-2017-013, 2017.

[32]G. Aad et al. (ATLAS Collaboration), “ATLAS b-jet identification performance and efficiency measurement with $t\bar{t}$ events in pp collisions at $\sqrt{s} = 13$ TeV,” Eur. Phys. J. C **79**, 970 (2019).

[33]ATLAS Collaboration, *Optimisation of the ATLAS b-tagging performance for the 2016 LHC Run*, ATL-PHYS-PUB-2016-012, 2016.

[34]F. Englert and R. Brout, “Broken symmetry and the masses of gauge vector mesons,” Phys. Rev. Lett. **13**, 321–323 (1964).

[35]P. W. Higgs, “Broken symmetries and the masses of gauge bosons,” Phys. Rev. Lett. **13**, 508–509 (1964).

[36]J. Ellis, “Higgs Physics,” 52 pages, 45 figures, Lectures presented at the ESHEP 2013 School of High-Energy Physics, to appear as part of the proceedings in a CERN Yellow Report, 117–168. 52 p (2013).

[37]G. Aad et al. (ATLAS Collaboration), “Observation of a new particle in the search for the Standard Model Higgs boson with the ATLAS detector at the LHC,” Phys. Lett. B **716**, 1–29 (2012).

[38]R. K. Ellis, W. J. Stirling, and B. R. Webber, *Qcd and collider physics*, Cambridge Monographs on Particle Physics, Nuclear Physics and Cosmology (Cambridge University Press, 1996).

[39]G. Aad et al. (ATLAS Collaboration), “Combined measurements of Higgs boson production and decay using up to 80 fb^{-1} of proton-proton collision data at $\sqrt{s} = 13$ TeV collected with the ATLAS experiment,” Phys. Rev. D **101**, 012002 (2020).

[40]D. Espriu, F. Mescia, and A. Renau, “Axion-Higgs interplay in the two Higgs-doublet model,” Phys. Rev. D **92**, 095013 (2015).

[41]D. A. Camargo, M. D. Campos, T. B. de Melo, and F. S. Queiroz, “A Two Higgs Doublet Model for Dark Matter and Neutrino Masses,” Phys. Lett. B **795**, 319–326 (2019).

[42]N. G. Deshpande, J. F. Gunion, B. Kayser, and F. I. Olness, “Left-right symmetric electroweak models with triplet Higgs,” Phys. Rev. D **44**, 837–858 (1991).

[43]E. Ma and U. Sarkar, "Neutrino masses and leptogenesis with heavy Higgs triplets," Phys. Rev. Lett. **80**, 5716–5719 (1998).

[44]A. Tranberg and B. Wu, "Cold Electroweak Baryogenesis in the Two Higgs-Doublet Model," JHEP **07**, 087 (2012).

[45]G. C. Dorsch, S. J. Huber, T. Konstandin, and J. M. No, "A Second Higgs Doublet in the Early Universe: Baryogenesis and Gravitational Waves," JCAP **05**, 052 (2017).

[46]S. Iguro and Y. Omura, "The direct CP violation in a general two Higgs doublet model," JHEP **08**, 098 (2019).

[47]R. D. Peccei and H. R. Quinn, "CP conservation in the presence of pseudoparticles," Phys. Rev. Lett. **38**, 1440–1443 (1977).

[48]M. Aaboud et al. (ATLAS Collaboration), "Search for charged Higgs bosons decaying into top and bottom quarks at $\sqrt{s}$ = 13 TeV with the ATLAS detector," JHEP **11**, 085 (2018).

[49]M. Aaboud et al. (ATLAS Collaboration), "Search for charged Higgs bosons decaying via $H^{\pm} \to \tau^{\pm}\nu_{\tau}$ in the τ+jets and τ+lepton final states with 36 fb^{-1} of pp collision data recorded at $\sqrt{s} = 13$ TeV with the ATLAS experiment," JHEP **09**, 139 (2018).

[50]A. M. Sirunyan et al. (CMS Collaboration), "Search for a charged Higgs boson decaying into top and bottom quarks in events with electrons or muons in proton-proton collisions at $\sqrt{s}$ = 13 TeV," JHEP **01**, 096 (2020).

[51]A. M. Sirunyan et al. (CMS Collaboration), "Search for charged Higgs bosons in the $\mathrm{H}^{\pm} \to \tau^{\pm}\nu_{\tau}$ decay channel in proton-proton collisions at $\sqrt{s} = 13$ TeV," JHEP **07**, 142 (2019).

[52]G. C. Branco, P. M. Ferreira, L. Lavoura, M. N. Rebelo, M. Sher, and J. P. Silva, "Theory and phenomenology of two-Higgs-doublet models," Phys. Rept. **516**, 1–102 (2012).

[53]J. F. Gunion, H. E. Haber, G. L. Kane, and S. Dawson, *The Higgs Hunter's Guide*, Vol. 80, Frontiers in physics (2000).

[54]T. Stefaniak, "Higgs physics beyond the Standard Model," in An Alpine LHC Physics Summit 2019 (Aug. 2019).

[55]A. Arbey, F. Mahmoudi, O. Stal, and T. Stefaniak, "Status of the Charged Higgs Boson in Two Higgs Doublet Models," Eur. Phys. J. C **78**, 182 (2018).

[56]M. Muhlleitner, M. O. P. Sampaio, R. Santos, and J. Wittbrodt, "The N2HDM under Theoretical and Experimental Scrutiny," JHEP **03**, 094 (2017).

[57]T. Biekötter, M. Chakraborti, and S. Heinemeyer, "A 96 GeV Higgs boson in the N2HDM," Eur. Phys. J. C **80**, 2 (2020).

[58]I. Engeln, M. Mühlleitner, and J. Wittbrodt, "N2HDECAY: Higgs Boson Decays in the Different Phases of the N2HDM," Comput. Phys. Commun. **234**, 256–262 (2019).

[59]C.-Y. Chen, M. Freid, and M. Sher, "Next-to-minimal two Higgs doublet model," Phys. Rev. D **89**, 075009 (2014).

[60]H. Georgi and M. Machacek, "Doubly charged higgs bosons," Nuclear Physics B **262**, 463–477 (1985).

[61]N. Ghosh, S. Ghosh, and I. Saha, "Charged Higgs boson searches in the Georgi-Machacek model at the LHC," Phys. Rev. D **101**, 015029 (2020).

[62]M. S. Chanowitz and M. Golden, "Higgs Boson Triplets With M (W) = M (Z) cos $\theta\omega$," Phys. Lett. B **165**, 105–108 (1985).

[63]J. F. Gunion, R. Vega, and J. Wudka, "Higgs triplets in the standard model," Phys. Rev. D **42**, 1673–1691 (1990).

[64]K. Hartling, K. Kumar, and H. E. Logan, "The decoupling limit in the Georgi-Machacek model," Phys. Rev. D **90**, 015007 (2014).

[65]G. Aad et al. (ATLAS Collaboration), "Search for a Charged Higgs Boson Produced in the Vector-Boson Fusion Mode with Decay $H^{\pm} \to W^{\pm}Z$ using pp Collisions at $\sqrt{s} = 8$ TeV with the ATLAS Experiment," Phys. Rev. Lett. **114**, 231801 (2015).

[66]G. Aad et al. (ATLAS Collaboration), "Search for a light charged Higgs boson in the decay channel $H^{+} \to c\bar{s}$ in $t\bar{t}$ events using pp collisions at $\sqrt{s}$ = 7 TeV with the ATLAS detector," Eur. Phys. J. C **73**, 2465 (2013).

[67]A. M. Sirunyan et al. (CMS Collaboration), "Search for a light charged Higgs boson in the $\mathrm{H}^{\pm} \to$ cs channel in proton-proton collisions at $\sqrt{s} = 13$ TeV," Phys. Rev. D **102**, 072001 (2020).

[68]A. M. Sirunyan et al. (CMS Collaboration), "Search for charged Higgs bosons decaying into a top and a bottom quark in the all-jet final state of pp collisions at $\sqrt{s}$ = 13 TeV," JHEP **07**, 126 (2020).

[69]A. M. Sirunyan et al. (CMS Collaboration), "Search for a light charged Higgs boson decaying to a W boson and a CP-odd Higgs boson in final states with e$\mu\mu$ or $\mu\mu\mu$ in proton-proton collisions at $\sqrt{s} = 13$ TeV," Phys. Rev. Lett. **123**, 131802 (2019).

[70]A. M. Sirunyan et al. (CMS Collaboration), "Search for Charged Higgs Bosons Produced via Vector Boson Fusion and Decaying into a Pair of W and Z Bosons Using pp Collisions at $\sqrt{s} = 13$ TeV," Phys. Rev. Lett. **119**, 141802 (2017).

[71]M. Krause, M. Mühlleitner, and M. Spira, "2HDECAY —A program for the calculation of electroweak one-loop corrections to Higgs decays in the Two-Higgs-Doublet Model including state-of-the-art QCD corrections," Comput. Phys. Commun. **246**, 106852 (2020).

[72]K. Hartling, K. Kumar, and H. E. Logan, "GMCALC: a calculator for the Georgi-Machacek model," (2014).

[73]H. E. Logan and M. B. Reimer, "Characterizing a benchmark scenario for heavy Higgs boson searches in the Georgi-Machacek model," Phys. Rev. D **96**, 095029 (2017).

[74]ATLAS Collaboration, *Luminosity determination in pp collisions at* $\sqrt{s} = 13$ *TeV using the ATLAS detector at the LHC*, ATLAS-CONF-2019-021, 2019.

[75]G. Aad et al. (ATLAS Collaboration), "ATLAS data quality operations and performance for 2015–2018 data-taking," JINST **15**, P04003 (2020).

[76]ATLAS Collaboration, *Trigger Menu in 2016*, ATL-DAQ-PUB-2017-001, 2017.

[77]G. Aad et al. (ATLAS Collaboration), "Performance of the missing transverse momentum triggers for the ATLAS detector during Run-2 data taking," JHEP **08**, 080 (2020).

[78]GEANT4 Collaboration, S. Agostinelli, et al., "GEANT4 – A SIMULATION TOOLKIT," Nucl. Instrum. Meth. A **506**, 250 (2003).

[79]G. Aad et al. (ATLAS Collaboration), "The ATLAS Simulation Infrastructure," Eur. Phys. J. C **70**, 823–874 (2010).

[80]T. Sjöstrand, S. Ask, J. R. Christiansen, R. Corke, N. Desai, P. Ilten, S. Mrenna, S. Prestel, C. O. Rasmussen, and P. Z. Skands, "An introduction to PYTHIA 8.2," Comput. Phys. Commun. **191**, 159 (2015).

[81]J. Alwall, R. Frederix, S. Frixione, V. Hirschi, F. Maltoni, O. Mattelaer, H. .-S. Shao, T. Stelzer, P. Torrielli, and M. Zaro, "The automated computation of tree-level and next-to-leading order differential cross sections, and their matching to parton shower simulations," JHEP **07**, 079 (2014).

[82]R. D. Ball et al., "Parton distributions with LHC data," Nucl. Phys. B **867**, 244 (2013).

[83]ATLAS Collaboration, *ATLAS Pythia 8 tunes to 7 TeV data*, ATL-PHYS-PUB-2014-021, 2014.

[84]S. Alioli, P. Nason, C. Oleari, and E. Re, "A general framework for implementing NLO calculations in shower Monte Carlo programs: the POWHEG BOX," JHEP **06**, 043 (2010).

[85]R. D. Ball et al. (NNPDF), "Parton distributions for the LHC run II," JHEP **04**, 040 (2015).

[86]T. Ježo, J. M. Lindert, P. Nason, C. Oleari, and S. Pozzorini, "An NLO+PS generator for $t\bar{t}$ and Wt production and decay including non-resonant and interference effects," Eur. Phys. J. C **76**, 691 (2016).

[87]E. Bothmann et al., "Event generation with Sherpa 2.2," SciPost Phys. **7**, 034 (2019).

[88]S. Höche, F. Krauss, M. Schönherr, and F. Siegert, "QCD matrix elements + parton showers. The NLO case," JHEP **04**, 027 (2013).

[89]A. Hoecker et al., *TMVA - Toolkit for Multivariate Data Analysis*, 2007.

[90]A. D. Bukin, *Fitting function for asymmetric peaks*, 2007.

[91]G. Aad et al. (ATLAS Collaboration), "Muon reconstruction and identification efficiency in ATLAS using the full Run 2 pp collision data set at $\sqrt{s} = 13$ TeV," (2020).

[92]J. Bellm et al., "Herwig 7.1 Release Note," (2017).

[93]ATLAS Collaboration, *Studies on top-quark Monte Carlo modelling for Top2016*, ATL-PHYS-PUB-2016-020, 2016.

[94]G. Avoni et al., "The new LUCID-2 detector for luminosity measurement and monitoring in ATLAS," JINST **13**, P07017 (2018).

[95]G. Cowan, K. Cranmer, E. Gross, and O. Vitells, "Asymptotic formulae for likelihood-based tests of new physics," The European Physical Journal C **71**, `10.1140/epjc/s10052-011-1554-0` (2011).

[96]G. Aad et al. (ATLAS Collaboration), "Search for charged Higgs bosons decaying into a top quark and a bottom quark at $\sqrt{s}$=13 TeV with the ATLAS detector," (2021).